Micromechanistic study of hydrogen embrittlement in pipeline steels

THE UNIVERSITY OF SYDNEY

Hanyu Li

Supervised by

Professor Julie M. Cairney

Dr Yi-Sheng (Eason) Chen

Dr Ranming Niu

A thesis submitted in fulfilment of the requirements for the degree of Doctor of Philosophy

School of Aerospace, Mechanical and Mechatronic Engineering

Faculty of Engineering

The University of Sydney

June 2023

Authorship attribution statements

Candidate's statement

I certify that I understand if my candidature is successful, my thesis will be lodged with the University Libraries and made available for use. I certify that to the best of my knowledge the intellectual content of this thesis is my own work. This thesis has not been submitted for any degree or other purposes. ChatGPT was occasionally used only for language polishing.

Some of the content in Chapter 2 is published as part of this review article, where I reviewed the literature and wrote the drafts of the manuscript:

H. Li, R. Niu, W. Li, H. Lu, J. M. Cairney, and Y.-S. Chen (corresponding author), 'Hydrogen in pipeline steels: Recent advances in characterization and embrittlement mitigation' *Journal of Natural Gas Science and Engineering* **105** (2022) 104709.

Some of the content in Chapter 4 is published as part of this conference paper, where I conducted the experiments, analyzed the experimental results, and wrote the manuscript:

H. Li (corresponding author), R. Niu, J. Cairney, Y.-S. Chen, 'In-situ Micromechanics of Hydrogen-induced Deformation in Pearlitic Steels' *Microscopy and Microanalysis* **28** (S1) 1642-1644.

Atom probe tomography results as in Figure 3.18, Figure 4.5, Figure 4.12, and Figure 4.13 are provided by Dr Ranming Niu. Figure 4.7 for thermal desorption analysis is provided by Mr Pang-Yu Liu.

All the assistance received in preparing this thesis and sources have been acknowledged. In addition to the statements above, in cases where I am not the corresponding author of a published item or the person conducting the experiments, permission to include the results and figures has been granted by the related personnel.

_____ (signature) _____ (Date)

Hanyu Li

Lead supervisor's statement

This thesis is well presented to be examined and does not exceed the prescribed word limit.

The student started this project 6 months after his enrollment in Q4 2019, and the progress of this experimental research was significantly affected by COVID19 lockdowns in 2020-2021, which limited the student's access to key facilities for 13 months (about 36% of the overall 36-month research period).

As the supervisor for the candidature upon which this thesis is based, I can confirm that the authorship attribution and other statements above are correct.

_____(signature) _____ (Date)

Julie Cairney, Professor

Statement of originality

I hereby provide an attestation, in accordance with academic standards, that the information presented in this thesis is a genuine reflection of my own knowledge and efforts. I affirm that this thesis has not been previously submitted for the fulfillment of any academic degree or utilized for any other purposes. I confirm that the intellectual content contained within this thesis is the outcome of my independent scholarly work, and I have duly acknowledged all sources utilized and any assistance received in its preparation.

_____ (signature)

Hanyu Li

Acknowledgments

At the outset of this acknowledgment section, I would like to extend my sincere gratitude to the individuals who have contributed to the completion of this thesis. Their unwavering support, invaluable guidance, and encouragement have been pivotal in navigating the complexities of this research journey. Through their contributions, this thesis has been enriched and made possible.

Foremost, I would like to express my sincere appreciation to my supervisor, Prof. Julie Cairney. The guidance, expertise, and unwavering support have been invaluable throughout my doctoral journey. The open-door policy and willingness to listen and provide guidance, even during the busiest of times, have been deeply appreciated.

I would like to thank my co-supervisors, Dr. Yi-Sheng (Eason) Chen and Dr. Ranming Niu for the countless hours that they dedicated to discussing and refining my research. Their constructive feedback, thought-provoking questions, and insightful suggestions have consistently elevated the quality and rigor of my work.

This project received funding from the Australian Research Council (ARC) Linkage Project (LP180100431). I would like to thank Dr. Hongzhou Lu and Dr. Aimin Guo from CITIC Metal for their support. I also would like to acknowledge the Faculty of Engineering and School of Aerospace, Mechanical and Mechatronic Engineering for providing a scholarship for my PhD project.

This work was performed in the Australia Centre for Microscopy and Microanalysis at the University of Sydney. I would like to thank Dr. Vijay Bhatia, Mr. Jacob Byrnes, Dr. Hongwei Liu, Ms. Ashalatha I.K, Dr. Takanori Sato, Dr. Magnus Garbrecht, Dr. Limei Yang, Mrs. Ellie Kable, and Dr. Mattew Foley for scientific and technical support.

I would like to thank Dr. Chang Li for referring me to Prof. Julie Cairney, who secured a full scholarship to support my PhD studies.

I would like to thank members of the research group for their generous help including Dr. Ingrid McMarroll, Dr. Jiangtao Qu, Dr. Matthew Griffith, Dr. Levi Tegg, Dr. Natalie Holmes, Dr. Jessie Posar, Dr. Halsey Ostergaard, Mr. Siyu Huang, Mr. Pang-Yu Liu, and Mr. Nathan Brichta.

I would like to thank friends around me in the University of Sydney including Dr. Xianghai An, Dr. Feng Li, Dr. Zibin Chen, Dr. Hansheng Chen, Dr. Tiebin Yang, Dr. Qi Wang, Mr. Jinqiao Liu, Ms. Heqing Li.

Lastly, I would like to thank my family. The unwavering support of my parents compelled me to return to Sydney once again to pursue academic research. In particular, I would like to express my heartfelt appreciation to my wife, Ms. Yuqing Zhang, for her unwavering support and remarkable understanding throughout my journey as a PhD student. Let us hold each other's hand and journey through life together until old age.

Abstract

Hydrogen embrittlement (HE), which can cause the premature failure of steel transmission pipelines, poses a long-standing challenge to bloom the utilization of hydrogen energy. Ferrite-pearlite steels dominate the market of in-service hydrogen pipelines. Yet hydrogen embrittlement mechanisms for the highly susceptible pearlite phase have remained inconclusive since the complicated microstructures in the bulk ferrite-pearlite steels interfere with categorizing the contribution of pearlite to hydrogen-induced failure. Here we provide a protocol combining in-situ micromechanical testing and ex-situ electrochemical hydrogen charging to successfully examine the effects of hydrogen on the mechanical behavior of pearlite and ferrite micropillars.

In this project atom probe tomography with cryogenic-sample-transfer technique was conducted on hydrogen-charged pearlite samples and observed that hydrogen is trapped in the cementite lamellae rather than at the ferrite-cementite interfaces. The introduction of hydrogen reduces the yield strength of pearlite micropillars to a narrow range, which means that hydrogen weakens the anisotropic yielding of pearlite. Slip occurs at the ferrite-cementite interface for uncharged micropillars with inclined lamellae but after hydrogen charging it takes place in the ferrite matrix, rather than at the interface. Shear deformation dominates in micropillars with vertical and horizontal lamellae, in which fracture occurs in the presence of hydrogen. Unlike pearlite, hydrogen only slightly reduces the yield strength of ferrite but has a greater impact on plasticity. Hydrogen softens ferrite micropillars and weakens intermittency during plastic deformation. These phenomena are attributed mainly to the hydrogen-enhanced local plasticity mechanism.

In addition to the findings about the deformation behavior of pearlite in the presence of hydrogen, this thesis also provides a new scanning electron microscope-based protocol to test the effect of hydrogen on the mechanical behavior of ferrite-pearlite steels that can facilitate fundamental studies on the interactions between hydrogen, microstructure, and deformation behavior.

Table of acronyms

ABF	Annular bright-field
AcC	Accelerated cooling
ADF	Annular dark-field
AIDE	Adsorption-induced dislocation emission
API	American Petroleum Institute
APT	Atom probe tomography
BCC	Body-cantered cubic
BSE	Backscattered electrons
DP	Diffraction patterns
EBSD	Electron backscattering diffraction
EDX	Energy dispersive X-ray
EELS	Electron energy loss spectroscopy
Environmental SEM	E-SEM
Environmental TEM	E-TEM
FCC	Face-cantered cubic
FIB	Focused ion beam
GB	Grain boundary
HAADF	High-angle annular dark-field
HAGB	High-angle grain boundary
HAZ	Heat-affected zones
HE	Hydrogen embrittlement
HEDE	Hydrogen-enhanced decohesion
HELP	Hydrogen-enhanced local plasticity
HESIV	Hydrogen-enhanced strain-induced vacancies
HSLA	High-strength low-alloy
IPF	Inverse pole figure
KAM	Kernel average misorientation map
LAGB	Low-angle grain boundary
LIST	Linearly increasing stress test
LME	Liquid-metal embrittlement
NTS	Notch tensile strength
OR	Orientation relationships

O-site	Octahedral interstitial sites
PFIB	Plasma FIB
RA	Reduction of area
ROI	Region of interest
SEM	Scanning electron microscope
SSRT	Slow strain rate test
STEM	Scanning TEM
TDA	Thermal desorption analysis
TEM	Transmission electron microscopy
TMCP	Thermomechanical controlled processing
TKD	Transmission Kikuchi diffraction
T-site	Tetrahedral interstitial sites
wppm	Part per million in weight

Table of Contents

1 Introduction

1.1 Research background

The world's demand for energy has been steadily increasing due to the growth of global population and economic activity [1]. This demand has been met by using fossil fuels, which result in significant carbon emissions and the consequential climate change [2]. Hydrogen energy is regarded as one of the potential solutions. The conversion of hydrogen to energy emits no carbon but only water vapor. In addition, hydrogen has a high energy density by weight, and it can be used on demand, making it suitable to complement the intermittent nature of wind and solar power in the renewable energy portfolio [3]. A summary of this aspect of versatility is shown in Figure 1.1, highlighting that hydrogen can be produced from a variety of industrially ready methods, such as electrolysis powered by solar [4] and/or geothermal [5] and biomass transformation [6]. Hydrogen produced with zero carbon footprint is termed "green hydrogen", as opposed to "grey hydrogen", which refers to conventional hydrogen production from fossil fuels, and "blue hydrogen" which uses these conventional methods in combination with carbon capture [7]. To enable a hydrogen-fueled society, infrastructure will be required to transport and store low-carbon hydrogen at scale.

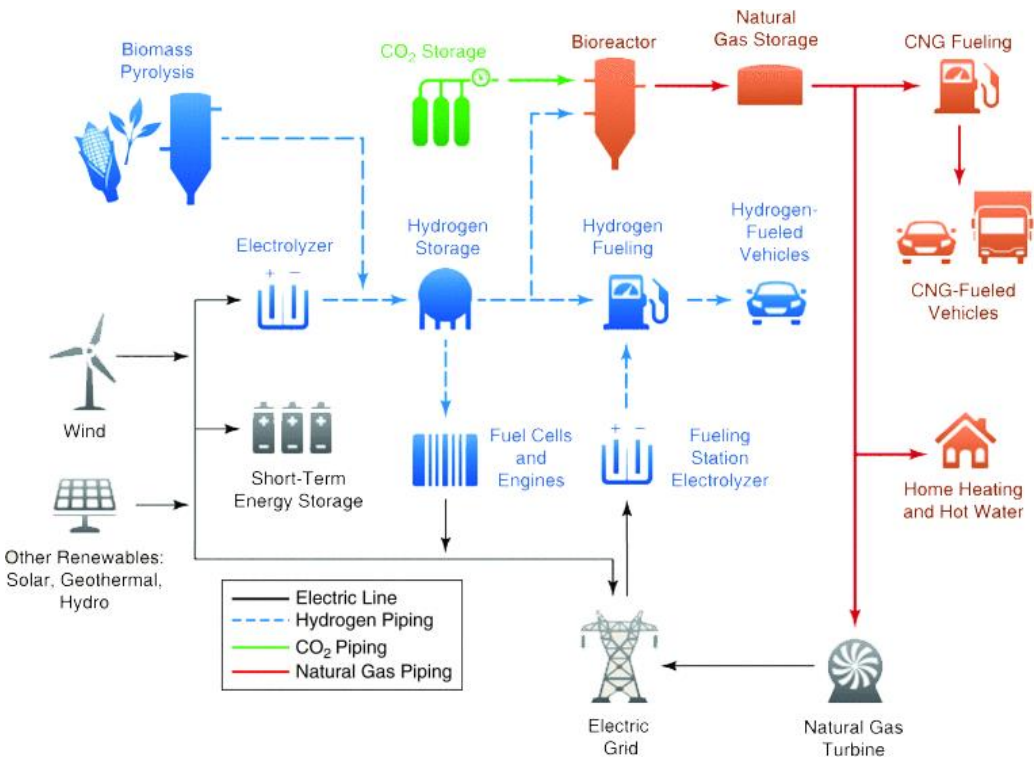

Figure 1.1 Prospective logistics for hydrogen production, transportation, and utilization [7].

For the transportation and storage of hydrogen (and its derivative forms such as ammonia and methane/natural gas), pipes and vessels are considered to be most the scalable approach, although extra energy (and cost) is required for compression and liquification [8, 9]. As of 2017, in the USA alone 1,600 miles of gas pipe already operate for hydrogen transmission and over 300,000 miles for natural gas [10, 11]. Considering the existing scale of natural gas infrastructure, a business case has been created to enable a hydrogen economy by repurposing the natural gas infrastructure for hydrogen use [12]. These pipelines are expected to carry natural gas blended with 5-10% (volume) hydrogen in the short term and 100% hydrogen in the long term [11, 12]. However, hydrogen is highly flammable at only 4% (volume) in air [13]. An incident on piping systems with high-pressure hydrogen could lead to leakage in air, which could cause fire. In fact, according to the USA's Department of Energy, the piping system is the sector most vulnerable to incidents in the entire chain of hydrogen production and utilization (Figure 1.2) [14]. As such, ensuring safe hydrogen transportation is paramount when it comes to repurposing the gas pipeline network for hydrogen.

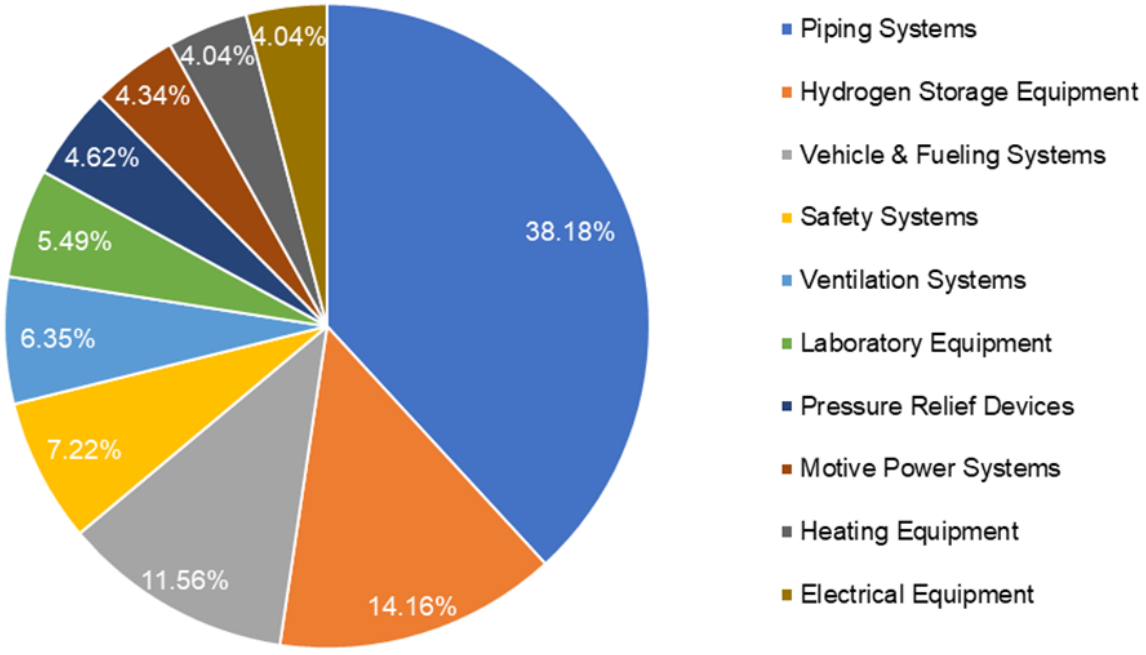

Figure 1.2 Statistics of hydrogen incidents [14].

The structural components in the existing gas infrastructure are mainly comprised of steels due to their high cost-effectiveness compared to other structural materials [11, 15]. Among steels, low-carbon low-alloying mid-strength steels are the most commonly used for gas pipes. The American Petroleum Institute (API) developed a series of materials for gas pipes, such as X42, X46, and X52, which allow operation up to 13 mega pascal (MPa) of gas pressure

[12, 16]. There are also higher-grade pipeline steels such as X60, X70, and X80, which can carry higher-pressure gas with higher strengths [17]. Their different strengths are mainly due to the use of different metallurgical processes during manufacturing. For example, thermomechanical controlled processing (TMCP) and accelerated cooling (AcC) are used for making higher-grade steels (X60 and above) [18, 19]. These techniques generally aim to create fine grains and specific microstructures that improve mechanical properties [20], such as acicular ferrite [21], bainite [22], and lath martensite [23]. Figure 1.3 shows the microstructure of a high-strength X90 pipeline steel with the different fine microstructural features labelled. Figure 1.4 summarizes the common pipeline steels and their corresponding strengths, microstructural components, and manufacturing techniques.

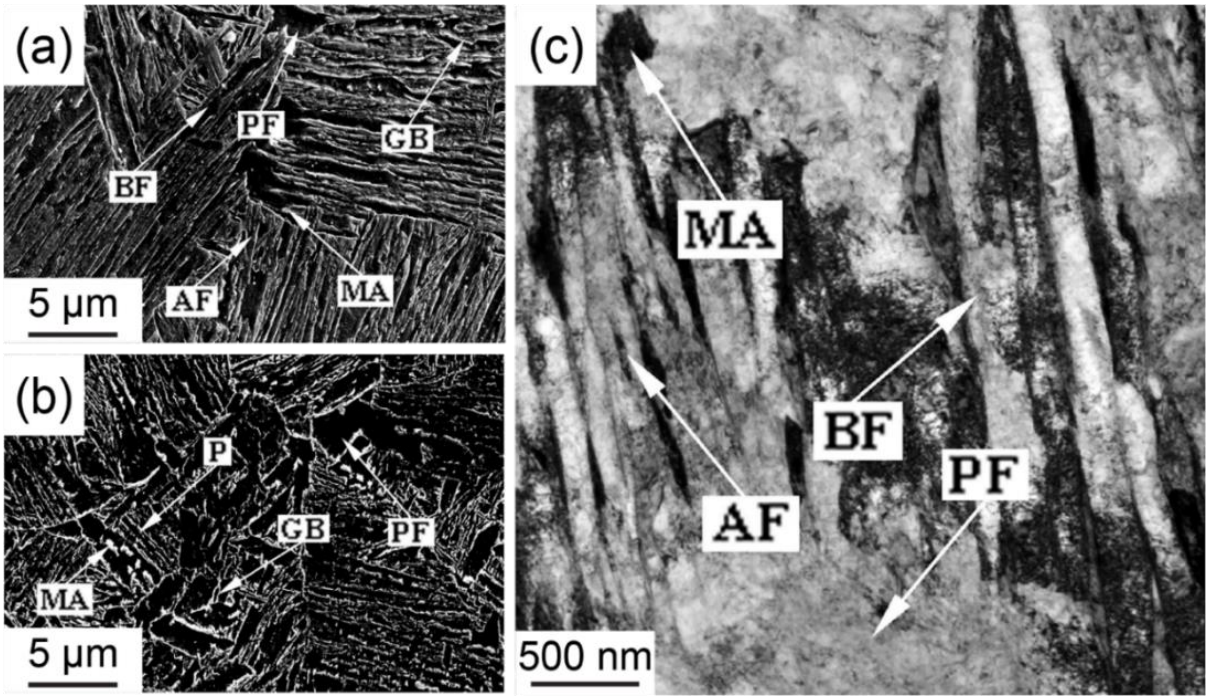

Figure 1.3 Common microstructures of X90 pipeline steel: (a) and (b) are scanning electron micrographs; (c) is from a transmission electron microscope. MA: martensite/austenite constituent; BF: bainitic ferrite; GB: granular bainite; AF: acicular ferrite; PF: polygonal ferrite; P: pearlite [24].

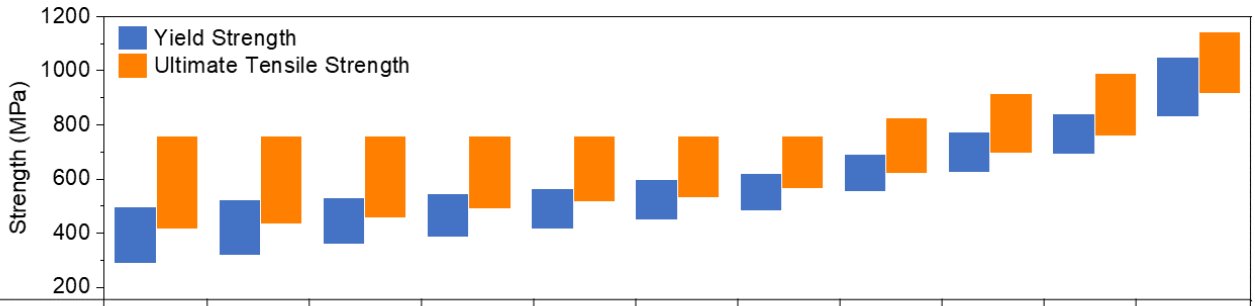

API 5L	X42	X46	X52	X56	X60	X65	X70	X80	X90	X100	X120
ISO 3183	L290	L320	L360	L390	L415	L450	L485	L555	L625	L690	L830
Invention year	1940s	1950s			1960s		1970s	1980s			1990s
Metallurgical technique	Hot rolled + Normalized						TMCP	TMCP + AcC			
Specific microstructure	Ferrite/Pearlite						Acicular Ferrite/ Bainite	Dual Phase/Martensite-Austenite			Lath Martensite

Figure 1.4 Strengths, microstructures, and manufacturing techniques of common pipeline steels. Data sources: [18, 25].

When steels absorb hydrogen, early failure, strength reduction, and ductility loss can take place, known as hydrogen embrittlement (HE) [26]. HE in steels has four requirements: i) sufficient diffusible hydrogen solutes within the microstructure, ii) intense mechanical load (with respect to material's yield strength), iii) the presence of HE-susceptible microstructural defects such as micro-cracks, and iv) sufficient time for hydrogen solute to diffuse and reach the susceptible features [27, 28]. In-service pipeline steels for high-pressure hydrogen transmission meet all these requirements and are therefore susceptible to HE. As such, it is crucial to understand HE problems in pipeline steels for the development of better materials or the implementation of safer operation protocols for a safe hydrogen-fueled society.

1.2 Aims of study and thesis overview

This thesis aims to contribute knowledge of how hydrogen influences the deformation mechanisms of steels. Considering conventional pipeline steels (X60 and older ones, Figure 1.4) generally contain ferrite and pearlite, we focused on the effect of hydrogen on these microstructural phases. Conventional studies of these behviours use macroscale mechanical testing. In contrast, this project involved the development and application of new electron-microscopy-based micromechanical methods to investigate the hydrogen effect at microscale. Overall, the aims of this thesis include:

1. Examine hydrogen distributions and content in steel specimens.
2. Investigate hydrogen effects on mechanical properties and deformation of pearlite.

3. Study the effect of hydrogen on mechanical properties and deformation of ferrite.
4. Through detailed analyses of the deformed microstructures, determine the mechanisms by which hydrogen affects material deformation.

Chapter 2 describes the background knowledge around pipeline steels and hydrogen embrittlement, highlighting the knowledge gap around hydrogen embrittlement in pearlite. Chapter 3 introduces the experimental techniques used in this thesis, including electron microscopy and in-situ microscale mechanical testing in electron microscopes. Chapter 4 examines the microstructure of the pearlitic samples, containing lamellar cementite in a ferrite matrix, as well as the effect of hydrogen on the deformation of this microstructure. Chapter 5 discusses the effect of hydrogen on the deformation and directions of dislocation slipping planes in pearlites. Chapter 6 continues the discussion on dislocation slipping, using ferrite specimens that were uncharged and charged with hydrogen. Chapter 7 provides conclusions and suggested future work.

2 Literature review

2.1 Pearlite

Steel is iron (Fe) with carbon (C) added as a major alloying element. Figure 2.1 is a Fe-C phase diagram, foundational information for steel research and production, showing the phases that are stable at given temperatures and carbon compositions, providing a guideline for fabricating steels with the desired fraction of phases and corresponding mechanical properties [29]. It is worth noting that Figure 2.1 only refers to the thermodynamic equilibrium in a simple Fe-C binary alloy system. The exact microstructures of steels are largely controlled by adding other alloying elements and applying different heating or cooling rates to create metastable microstructures that can provide better mechanical performances [30].

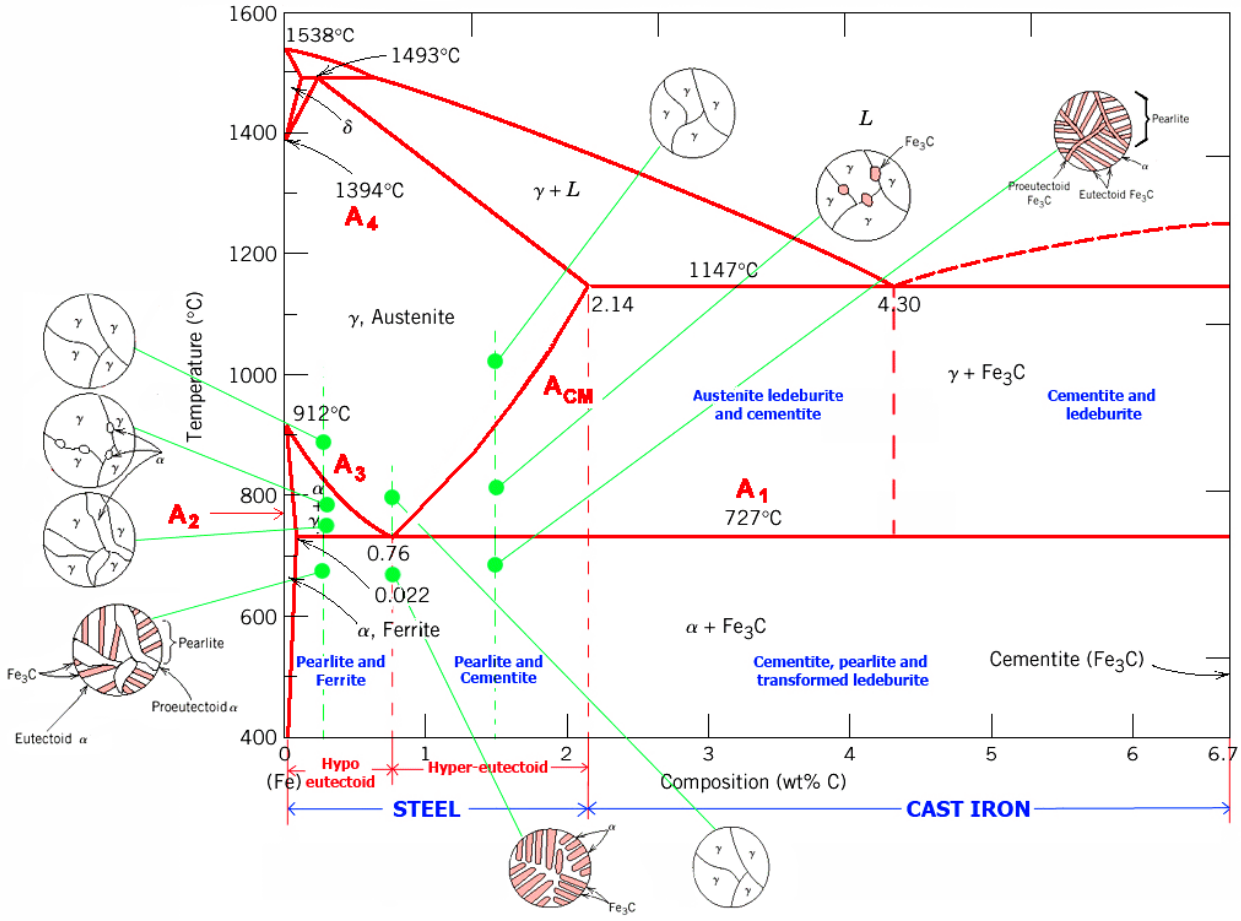

Figure 2.1 Fe-C phase diagram up to 6.7% carbon mass content (Source: https://www.tf.uni-kiel.de/matwis/amat/iss/kap_6/illustr/s6_1_2.html)

On the left side of Figure 2.1, one can see ferrite (α phase) and austenite (γ phase) are the primary phases for steels. There is also a high-carbon-content phase 'cementite' (Fe_3C, i.e.,

25% carbon and 75% iron), noted in the right side of Figure 2.1. The carbon solubility in austenite can be as high as 2.14 wt.% (at 1147 °C), which is significantly higher than that of ferrite (up to 0.022 wt.% at 727 °C). For steels with carbon content greater than 0.022 wt.%, during slow cooling from the high temperature (> 727 °C, where austenite is stable) to room temperature, the carbon atoms in solution in austenite diffuse and cluster during the austenite-ferrite phase transformation, forming cementite. The formation of cementite accommodates the carbon that exceeds the ferrite solubility limit from the surrounding ferrite regions, and this characteristic microstructure of cementite surrounded by ferrite is called pearlite [31]. For steels that have carbon content less than 0.76 wt.% (i.e., bottom left corner in Figure 2.2, referred as hypo-eutectoid steels), a mixture of pearlite with ferrite forms via slow cooling from the austenite temperatures. This kind of microstructure is common in pipeline steels, as shown in Figure 2.2. For steels having more than 0.76 wt.% of carbon (but less than the 2.14 wt.% solubility limit of austenite, referred to as hyper-eutectoid steel), a mixture of pearlite and cementite forms [32].

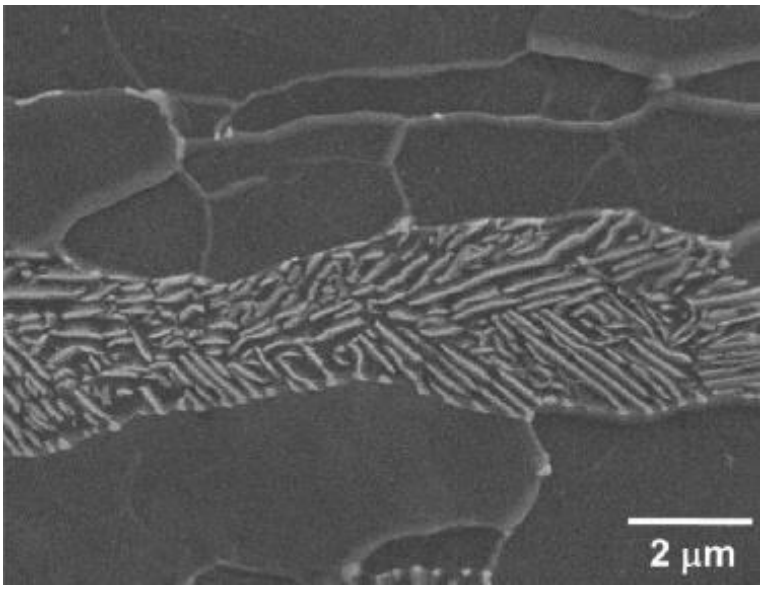

Figure 2.2 SEM image of an X65 pipeline steel, showing a pearlitic grain with cementite (bright lines) in a ferrite matrix, surrounded by ferritic grains [33].

Pearlite is used in pipeline steels to improve their mechanical properties. Figure 2.2 exhibits the characteristic pearlite microstructure with alternated cementite lamellae in ferrite. These cementite lamellae exhibit several crystallographic orientation relationships (OR) with the ferrite matrix, as summarized in Table 2.1. Reducing the distance between the lamellae in pearlitic steels through drawing can lead to an increase in the strength of the steel up to 6 giga pascal (GPa) [34].

Table 2.1 The orientation relationship between ferrite and cementite in pearlite [35]

Name	Orientation relationships	Reference
Isaichev	$[010]_{\text{cementite}} \parallel [111]_{\text{ferrite}}$ $(103)_{\text{cementite}} \parallel (01\bar{1})_{\text{ferrite}}$ $(101)_{\text{cementite}} \parallel (11\bar{2})_{\text{ferrite}}$	[35, 36]
Bagaryatsky	$[100]_{\text{cementite}} \parallel [1\bar{1}0]_{\text{ferrite}}$ $[010]_{\text{cementite}} \parallel [111]_{\text{ferrite}}$ $(001)_{\text{cementite}} \parallel (11\bar{2})_{\text{ferrite}}$	[37]
Pitsch-Petch	$[100]_{\text{cementite}}$ 2.6° from $[\bar{3}1\bar{1}]_{\text{ferrite}}$ $[010]_{\text{cementite}}$ 2.6° from $[131]_{\text{ferrite}}$ $(001)_{\text{cementite}} \parallel (\bar{2}\bar{1}5)_{\text{ferrite}}$	[38, 39]

2.2 Hydrogen behavior in steels

2.2.1 Hydrogen entry

Like other metallic materials, hydrogen uptake in pipeline steels involves three steps: physisorption, chemisorption, and absorption, as illustrated in Figure 2.3 [40, 41]. Physisorption originates from the Van der Waals forces between hydrogen molecules and metal surfaces. Chemisorption refers to the dissociation of hydrogen molecules and the subsequent chemical hydrogen binding onto metal surfaces. Since hydrogen solution in iron is endothermic, this step is less favorable than that of other metals that have higher affinity to hydrogen such as titanium, zirconium, vanadium, and magnesium [42, 43].

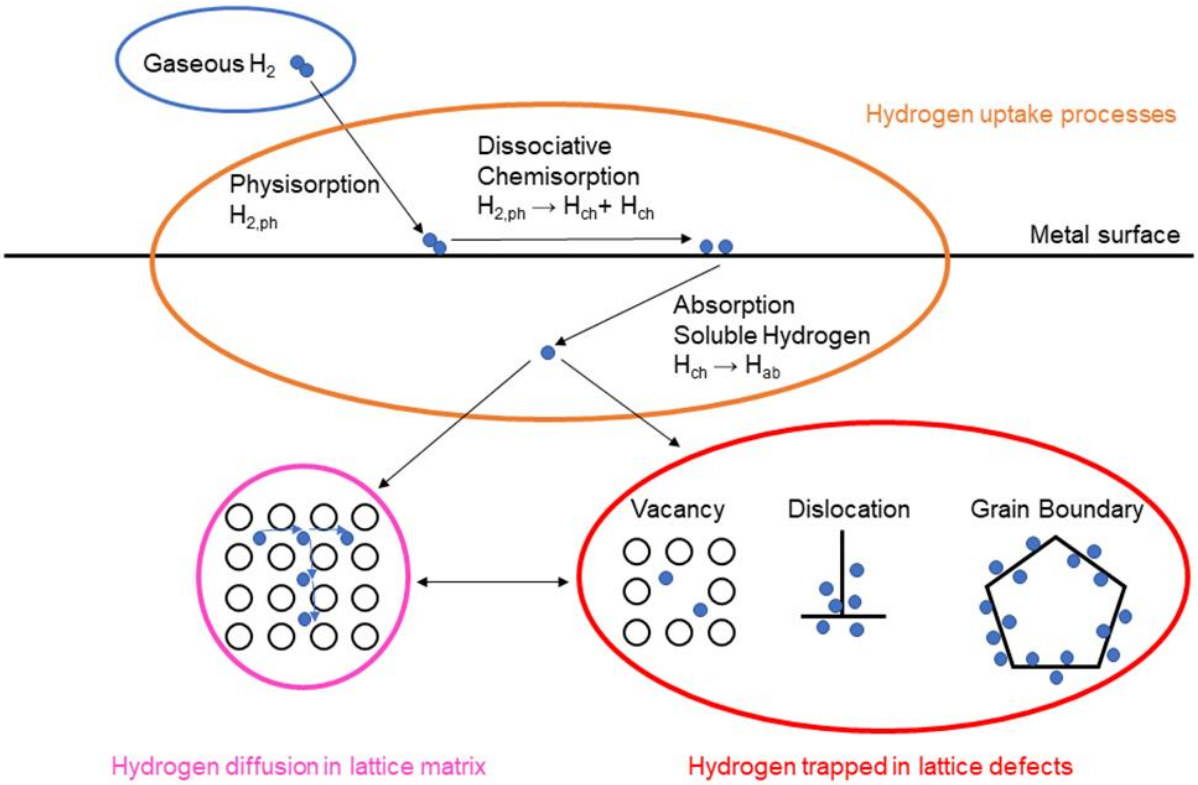

Figure 2.3 Schematic illustration of hydrogen uptake, diffusion, and trapping [40, 41].

The concentration of absorbed hydrogen in steels (C_H) is related to environmental hydrogen pressure or, more precisely, fugacity (f_H) which considers the deviation of hydrogen from an ideal gas. For hydrogen, fugacity can be approximated to pressure for pressures up to 20 MPa [44]. The concentration-fugacity relationship can be described below, following Sievert's law [45]:

$$C_H = S\sqrt{f_H}$$

where S is the solubility constant related to temperature.

2.2.2 Hydrogen in the lattice and in traps

Pipeline steels generally have body-cantered cubic (BCC) lattice structures, and interstitial hydrogen solute in this lattice sits at the tetrahedral interstitial sites (T-site) [46]. This is in contrast with the case of face-cantered cubic (FCC) alloys, where hydrogen solute prefers the octahedral interstitial sites (O-site) [47]. This difference of occupant site between BCC and FCC lattice leads to the higher diffusivity of hydrogen in BCC than that in FCC, due to the shorter diffusion distance between the nearest BCC T-sites than for FCC O-sites [48]. At room temperature, hydrogen diffusivity in pure BCC iron is approximately 10^{-5} to 10^{-4} cm^2/s [49, 50].

Also, the overall number of BCC T-sites is lower than that of FCC O-sites, resulting in a lower hydrogen solubility for BCC iron than FCC iron. At 298 K, an X70 pipeline steel with BCC lattice can accommodate approximately 1 part per million in weight (wppm) of hydrogen [51], which is significantly lower than that of an FCC-based 304 austenitic steel, at 100 wppm [52].

In addition to interstitial lattice sites, hydrogen atoms are trapped at various microstructural defects in steels. Figure 2.4 provides a schematic illustration of the trapping and detrapping of hydrogen atoms around an energetic sink in a metal lattice [53]. A trap in a material is defined as 'irreversible' if it has a strong binding energy to trap hydrogen firmly throughout the component's lifetime at a specific service temperature [54]. At 298 K, a trap with a trapping energy over 50 kJ/mol is generally considered to be irreversible [55]. Trapping energy can be theoretically calculated [56] or experimentally measured by thermal desorption analysis (TDA) [57] or a hydrogen permeation test [58].

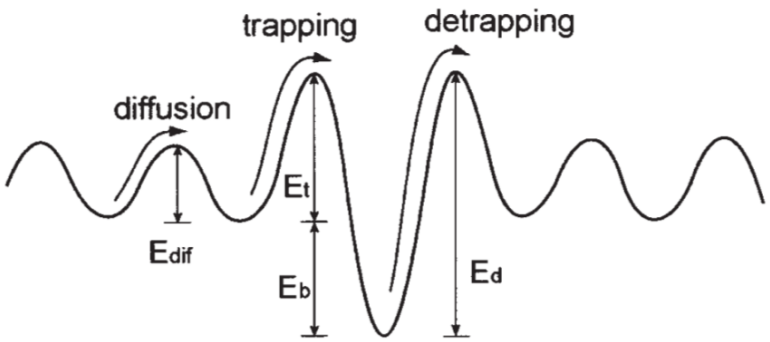

Figure 2.4 Schematic illustration of the potential energy associated with interstitial diffusion sites. E_{dif}: diffusion energy; Et: trapping activation energy; E_b: trap site binding energy; E_d: detrapping activation energy [53].

Table 2.3 provides the trap densities and the hydrogen solubilities of common pipeline steels. Increasing the number of microstructural trapping sites leads to a higher amount of soluble hydrogen in steels, but does not necessarily increase the HE susceptibility [47, 48]. It was found that the HE susceptibility of materials with hydrogen traps depends on the characteristics of the incorporated traps. For instance, more weak traps increase the HE susceptibility [59, 60]. A sound HE mitigation strategy must be established upon a clear understanding of where and how hydrogen atoms are trapped and their influence on the load resistance of materials. The following section provides an overview of the characteristics of common hydrogen traps in relation to HE susceptibility.

Table 2.2 Common hydrogen traps and their trapping energies (E_b) in BCC steels. A negative value means repulsive.

Trap type	-E_b (kJ/mol)	Characterization technique	Reference
Solute elements			
Si, Cr, Mn, Co, and Mo	~0	First Principle	[56]
C (interstitial)	9	First Principle	[56]
N (interstitial)	13	Magnetic Relaxation	[61]
Nb	-7	First Principle	[56]
Ti	-8	First Principle	[56]
Mg	-15	First Principle	[56]
Sc	-20	First Principle	[56]
Y	-25	First Principle	[56]
Crystal defects			
Single vacancy	24-78	First Principle, Permeation	[56, 62-65]
Micro-voids	40	TDA	[66]
Dislocations (bulk)	60	Permeation	[58]
Screw dislocations	26	First Principle	[67]
Dislocation strain field	12-27	Permeation, TDA	[57, 68, 69]
GB	9-49	Mechanical Analysis, TDA	[57, 70-72]
Prior austenite GB	47	Permeation	[73]
Second phases			
Incoherent TiC	60–129	Permeation, TDA	[59, 74-77]
Semi-coherent TiC	48	TDA	[77]
Incoherent V_4C_3	40	TDA	[78]
Semi-coherent V_4C_3	25-28	TDA	[79, 80]
Incoherent NbC	55-60	TDA	[81]
Semi-coherent NbC	28-56	TDA	[81, 82]
Coherent Mo_2C	11-34	TDA	[83-85]
Cementite/α interface	11-18	Permeation, TDA	[57, 86, 87]
ε carbide	12-65	Permeation, TDA	[88, 89]
ε copper	27	TDA	[71]
Dispersed oxide	45	Permeation, First Principle	[90, 91]
MnS interface	64	TDA	[66, 69]
Austenite/Ferrite interface	44	Permeation	[92]
Iron oxide interface	43-62	TDA	[93]
Al_2O_3 interface	71	TDA	[94]

Table 2.3 Trap density and hydrogen solubility of common pipeline steels.

Materials	**Trap site density (cm^{-3})**		**Hydrogen solubility (mol/cm^3)**	
X65	2.35×10^{20}	[95]	8.92×10^{-6}	[96]
X70	2.37×10^{24}	[97]	8.91×10^{-6}	[98]
X80	1.61×10^{27}	[99]	1.07×10^{-5}	[100]
X100	9.25×10^{27}	[101]	1.88×10^{-5}	[102]

2.2.3 Hydrogen interactions with lattice defects

Vacancies are generally strong hydrogen traps [64, 103]. A vacancy can be stabilized when it combines with hydrogen atom(s), while multiple vacancies often form vacancy clusters or hydrogen-vacancy complexes in the presence of hydrogen [47, 104, 105]. Similarly, dislocations can combine with hydrogen, in a similar effect to the well-understood Cottrell atmosphere formed by interstitial carbon atoms, to mediate or 'shield' the surrounding elastic stress field [106]. This change to the stress field means that the motion of dislocations can be enhanced with trapped hydrogen atoms [107-110]. Hydrogen-enhanced dislocation motion was first observed in a 310S stainless steel with in-situ transmission electron microscopy (TEM) [111], and the existence of this phenomenon is also supported by other literature [112, 113]. Edge dislocations are particularly sensitive to this shielding effect in the presence of long-range hydrostatic stresses [27, 47]. For screw dislocations, hydrogen can reduce the formation energy, so the presence of hydrogen enhances the nucleation rate of dislocation kink-pairs, increasing the dislocation mobility, especially in a BCC matrix [114-116]. In addition, the hydrogen atmosphere around dislocations can weaken the interaction between dislocations and microstructural obstacles [107, 109, 117]. A moving dislocation carrying hydrogen might penetrate obstacles that block ordinary dislocations [118, 119]. During material deformation, the dynamic dislocation movements can facilitate the redistribution of hydrogen in materials, and hydrogen transport can be faster along dislocation networks than in a perfect lattice [120].

Grain boundaries (GB) are also a common hydrogen trap in BCC steels. The presence of hydrogen at a GB can decrease its cohesive strength, leading to its decohesion which contributes to intergranular crack propagation at the bulk scale, widely observed as a result of HE [121, 122]. However, the exact effect of hydrogen on GBs is more complicated due to the possible interaction of hydrogen with local defects and decorated impurities. The precise determination of GB trapping energy is difficult if the exact configuration of local defects is not sufficiently known. This discrepancy can lead to a significant difference in the measured hydrogen trapping energies [57, 58]. GB characteristics can also influence the HE susceptibility of materials. It has been found that hydrogen-enhanced crack propagation is less for low-angle GBs (LAGBs) compared to high-angle GBs (HAGBs) (Figure 2.5a) [123]. It has also been demonstrated that hydrogen-enhanced crack propagation in X60 pipeline steels is less severe for $\sum$11, $\sum$13b, and $\sum$29 GBs (Figure 2.5b) [124].

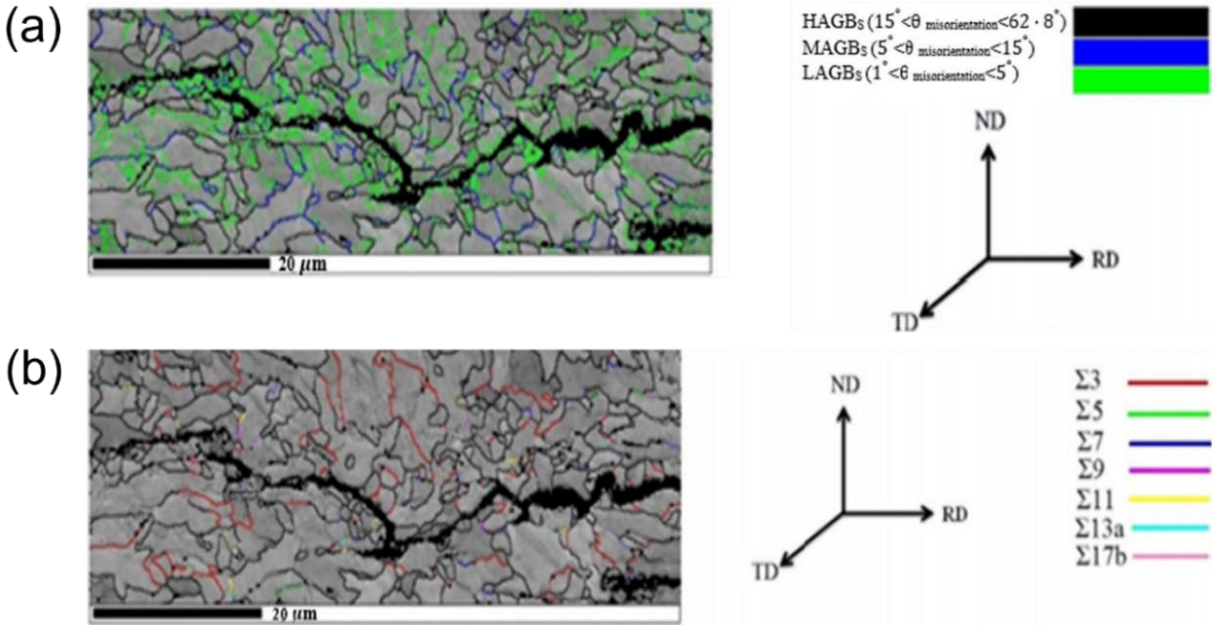

Figure 2.5 Cross-section of hydrogen-embrittled X60 pipeline steels: (a) EBSD reconstructed grain boundary map, (b) Coincidence site lattice boundaries [123, 124].

2.2.4 Second phase hydrogen traps

Second phases are often added into the microstructure of pipeline steels to increase their mechanical performance [47, 122]. It is known that finely dispersed precipitates with high hydrogen trapping energy can reduce hydrogen mobility in steels and improve their overall HE resistance, such as titanium carbide (TiC) and niobium carbide (NbC) [125-127]. In contrast, the presence of large, brittle inclusions such as manganese sulfide (MnS) [128], large Ti/Nb/V carbonitride [129], aluminum oxides [101], and silicon oxides [130, 131], can increase HE susceptibility of steels because the hydrogen trapped at the interfaces between matrix and inclusions can weaken the load resistance of the microstructure [104, 132]

As an FCC lattice has a higher hydrogen solubility and lower diffusivity than a BCC lattice, austenite is a stronger hydrogen trapping phase than ferrite, which can influence HE in steels. Sun et al. [133] compared the hydrogen-induced cracking mechanisms of two steels with different fractions of ferrite and austenite. They found that ferrite-based steel has more post-fracture characteristics consistent with hydrogen-enhanced local plasticity (HELP) (the top of Figure 2.6). In contrast, the HE of austenite-based steel is more consistent with hydrogen-enhanced decohesion (HEDE) because austenite can make hydrogen less accessible across grains, leading to a local hydrogen concentration (and austenite-martensite strain-induced phase transformation) that increases the local HE susceptibility (the bottom of Figure 2.6).

Later Sun et al. [134] further found the presence of local chemical heterogeneity in steel grains can also influence the characteristics of hydrogen-induced cracking. They found that manganese-rich zones in austenite are more crack-resistant and can blunt the crack tip in the presence of hydrogen as compared with a homogeneous counterpart (Figure 2.7). These results demonstrate the possibility to develop by-design steel microstructures for HE resistance.

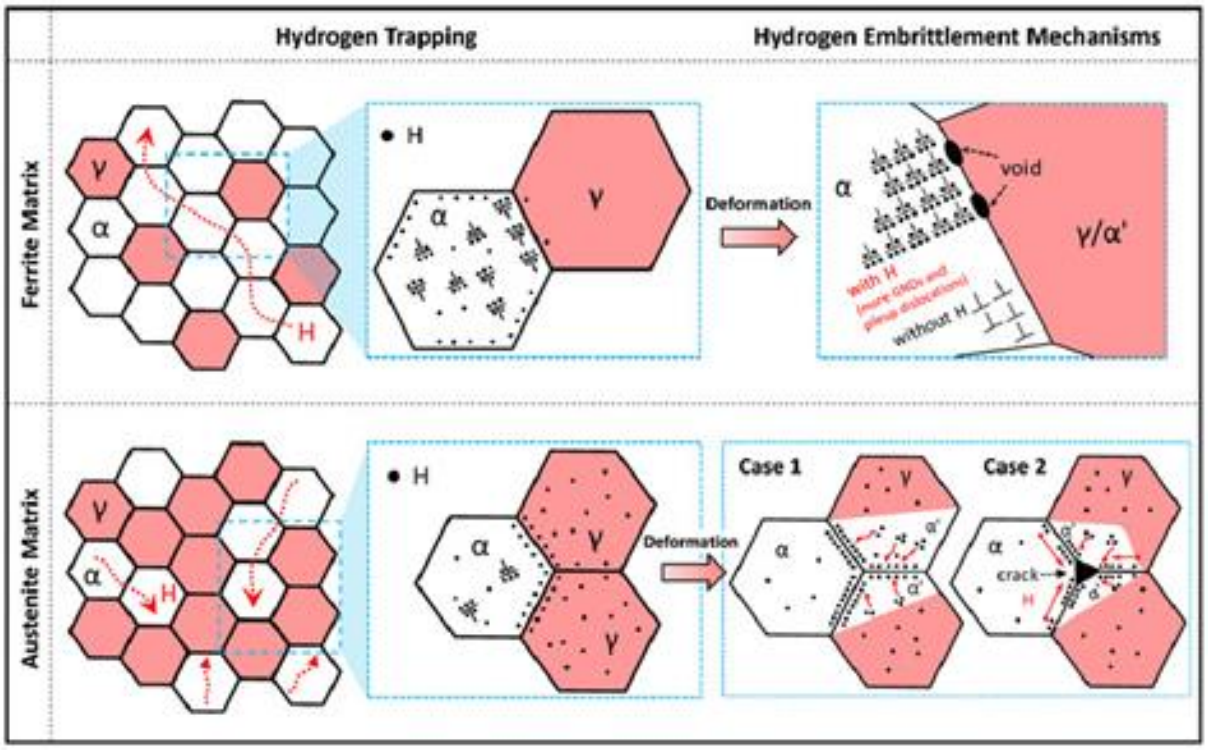

Figure 2.6 Schematic illustrations of hydrogen distribution in microstructures with corresponding HE mechanisms for ferrite- and austenite- dominated steels [133].

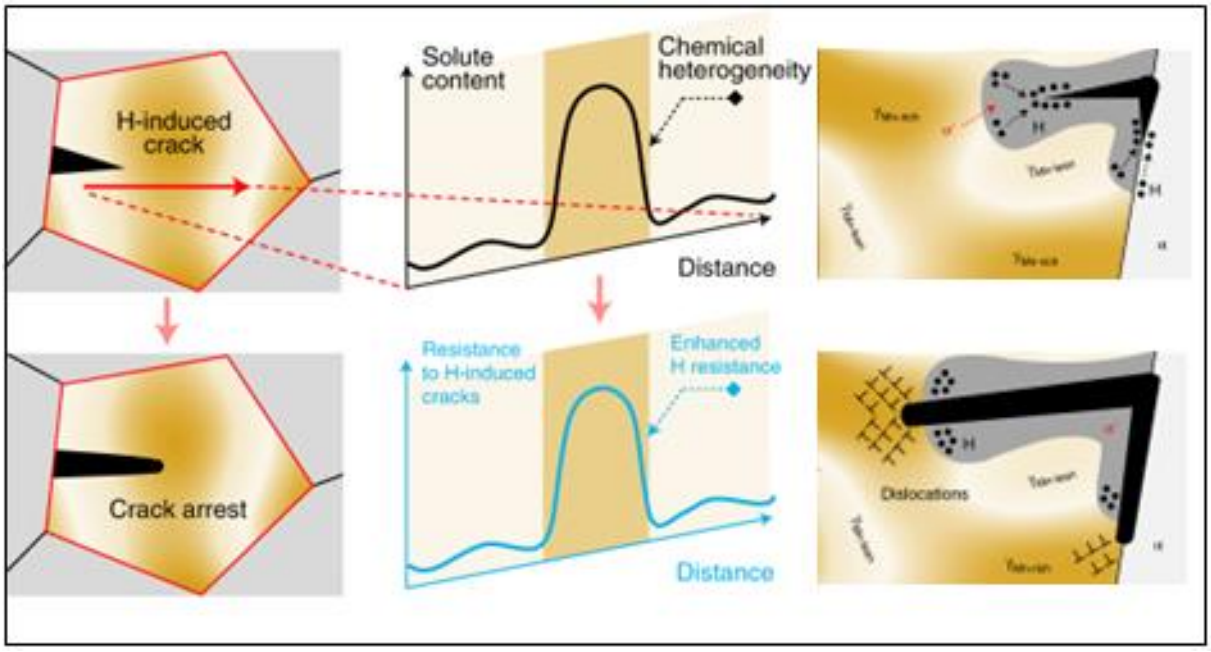

Figure 2.7 Schematic illustrations showing a hydrogen-induced crack propagation crossing a designed manganese-rich zone with the manganese concentration profile and the crack-arresting mechanisms [134].

2.2.5 Hydrogen in pearlite

Hydrogen interaction with the phases (ferrite and cementite) in pearlite is complicated. Regarding trapping, undeformed pearlite with pristine ferrite-cementite interface can trap hydrogen weakly [135], whereas a deformed pearlitic steel in which the ferrite-cementite interface has a high-density dislocations can trap a high content of hydrogen [136, 137]. Literature has reported that increasing cementite density (i.e., lower interlamellar spacing) can increase the content of trapped hydrogen and hence increase the HE resistance [137]. Cementite can also act as a barrier of hydrogen migration in microstructure, resulting in a lower apparent diffusivity of steels with more cementite [138]. Regarding hydrogen-assisted failure, the presence of hydrogen can influence the cracking behaviors of materials with cementite lamella, leading to a preferred cracking direction in pearlite [139]. In the absence of hydrogen, a failed pearlite specimen has numerous cracks through the cementite lamellae (Figure 2.8a). When the concentration of hydrogen in the environment increases, a change of cracking direction with respect to cementite direction is observed in pearlite [140]. In an environment with low hydrogen partial pressure (0.7 MPa), hydrogen-induced crack propagation is mixed with cross-cementite and along-cementite-ferrite-interfaces (Figure 2.8b). In a high hydrogen concentration (90 MPa), cracks along the cementite-ferrite-interfaces dominate (Figure 2.8c).

By using kernel average misorientation map (KAM), which presents the dislocation structures in the specimen, it has been found that high hydrogen concentration resulted in less developed dislocation structures after cracking (Figure 2.8f), as compared to the cases in lower hydrogen partial pressure Figure 2.8e) and the absence of hydrogen (Figure 2.8d). These results suggest the deformation behaviors of pearlite can be strongly influenced by the presence of hydrogen in the specimens. Further insight is needed to develop the fundamental science of this phenomenon.

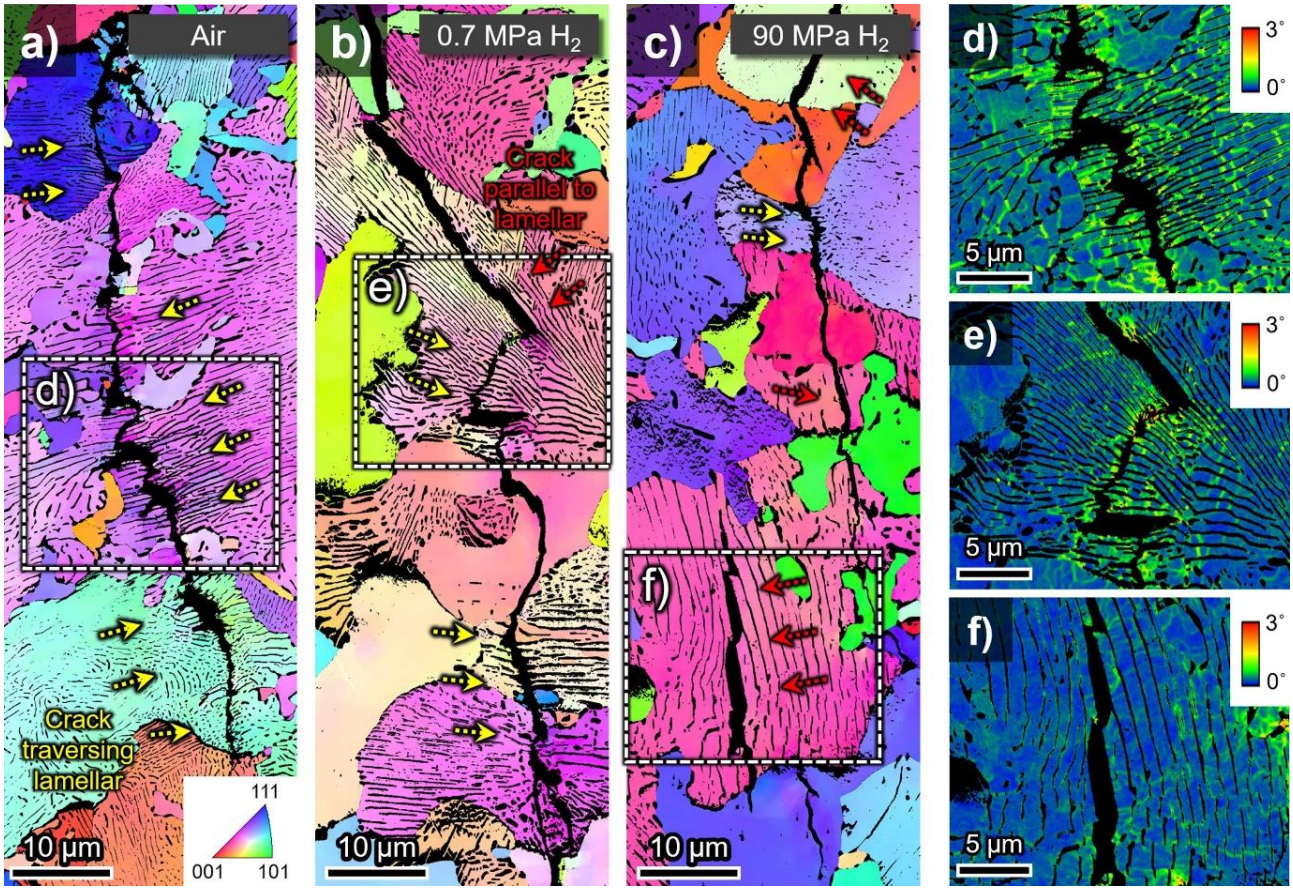

Figure 2.8 Fracture paths of pearlitic steels tested in hydrogen and in air. (a) and (d) were in air. (b) and (e) were in 0.7 MPa of hydrogen. (c) and (f) were in 90 MPa of hydrogen. (a)-(c) are the crystallographic orientation (IPF) maps. (d), (e), and (f) are the KAM maps of the regions surrounded by dashed rectangles in (a), (b), and (c), respectively. The crack growth direction is from top to bottom [140].

2.3 Variables of hydrogen embrittlement in pipeline steels

HE in steel pipes involves environmental, material, and mechanical factors, as illustrated in Figure 2.9 [141]. This section is dedicated to the discussions of these variables.

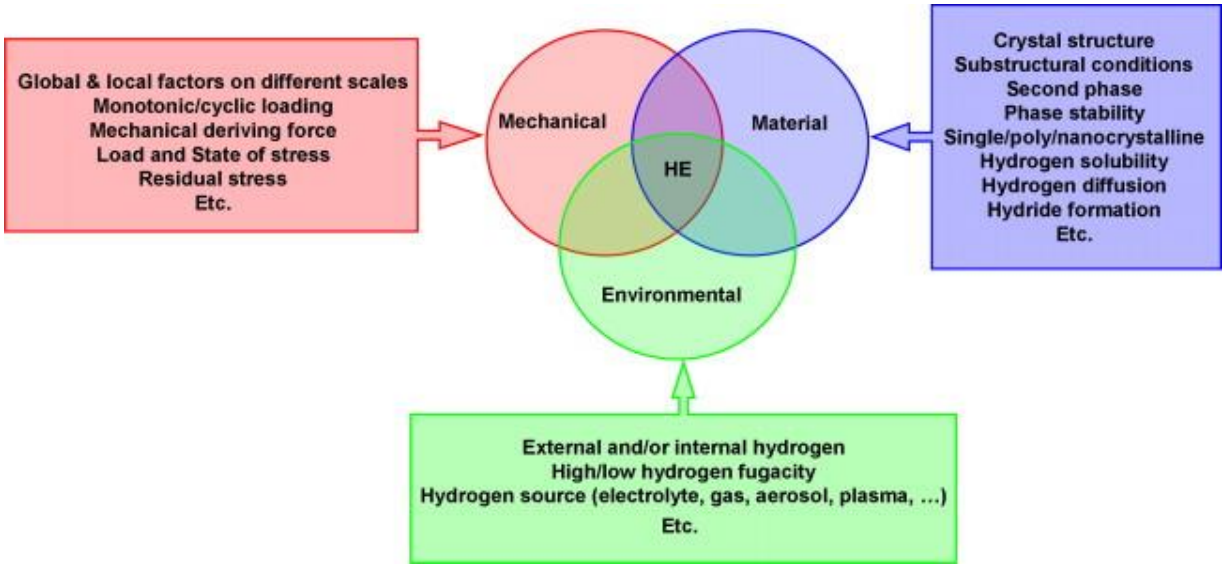

Figure 2.9. Three main factors for the occurrence of hydrogen embrittlement [141].

2.3.1 Hydrogen content

HE requires the presence of enough hydrogen in materials. This threshold concentration is generally low, given the low hydrogen solubility of steels. Based on Sievert's law, the threshold concentration of a steel can be linked with a threshold hydrogen fugacity/pressure in the environment, which is typically at a level of few-to-tens MPa [27, 142]. The increase of hydrogen pressure can lead to the losses of ductility in pipeline steels (Figure 2.10a). Figure 2.10b displays another example showing the decreases of tensile stress resistances of pipeline steels with the increase of hydrogen pressure at various stress intensity factors (K_t) [143]. Figure 2.10c compares the fatigue crack growth rates of an X42 pipeline steel at various stresses in hydrogen with that in nitrogen, demonstrating the degradation due to hydrogen [144]. Figure 2.10d shows increasing hydrogen partial pressure in a gas mixture with nitrogen can lead to an increase in fatigue crack growth rate [145].

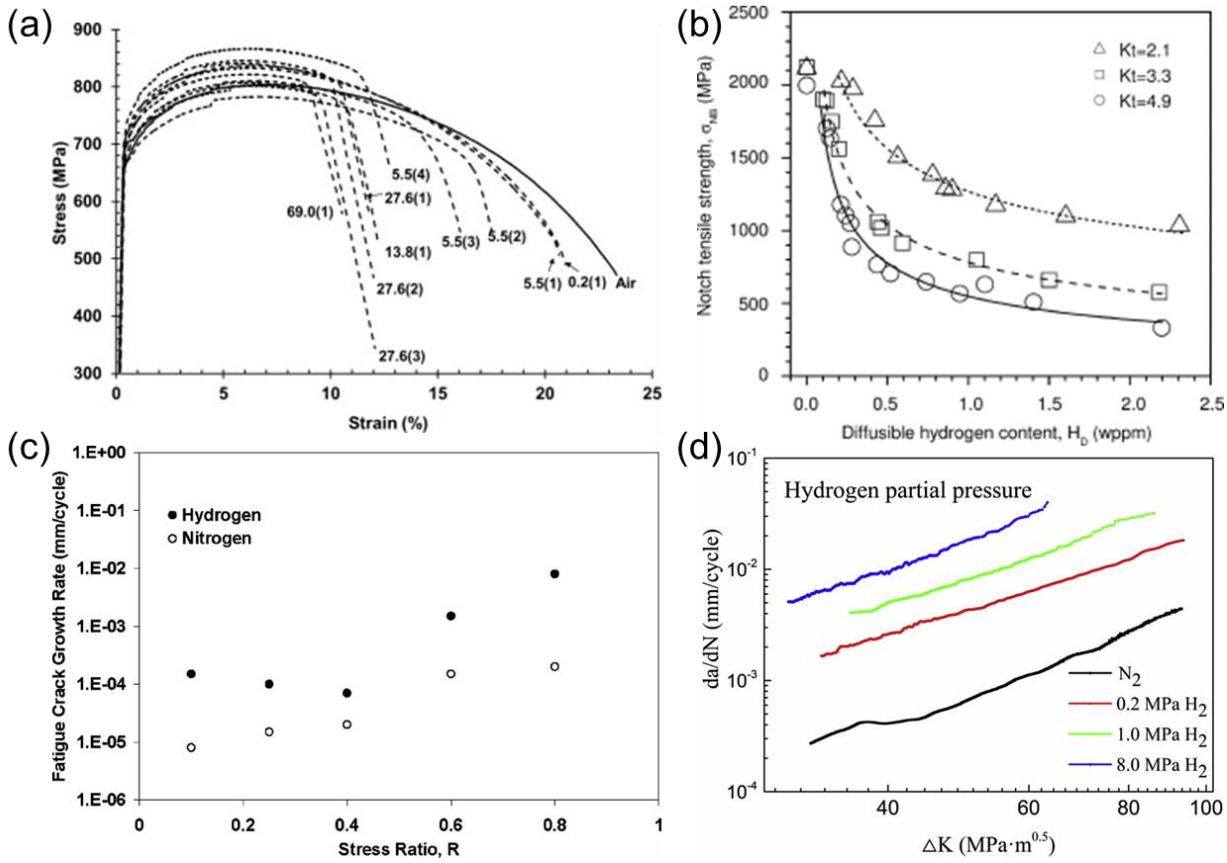

Figure 2.10. Effects of hydrogen content on HE of pipeline steels. (a) Stress-strain curves from X100 steel specimens tested at different hydrogen gas pressures [146]. (b) Resistance of notched samples to tensile load as a function of hydrogen concentration under different stress intensity factors (K_t) [143]. (c) Fatigue crack growth of X42 pipeline steel in hydrogen and nitrogen as a function of stress ratio to yield strength [144]. (d) Fatigue crack growth rate of X80 steel versus stress intensity factor at different hydrogen partial pressures in 12 MPa of a total pressure [145].

The access to high-pressure hydrogen charging is essential for the examination of HE. However, this is sometimes difficult to achieve by using a high-pressure gaseous hydrogen charging setup, which requires a sophisticated management for laboratory safety considering the high flammability of hydrogen [146, 147]. An alternative method is electrolytic charging, which refers to placing a conductive metallic specimen at the cathode in a water electrolysis cell to generate hydrogen around the specimen for uptake. This approach is less experimentally demanding than gas charging and is thus commonly used in laboratories [44, 48]. Adding an electrolyte in water can increase the conductivity of the charging solution, leading to more efficient hydrogen generation. An electrolyte can be either acid or alkaline, and the respective electrolytic reactions are presented as below [122, 148]:

$$H_3O^+ + M + e^- \rightleftharpoons MH_{ads} + H_2O \ (acid\ solution)$$

$$H_2O + M + e^- \rightleftharpoons MH_{ads} + OH^- \ (alkaline\ solution)$$

In electrolytic charging, a longer time of charging can lead to a more uniform distribution of hydrogen within the specimen, allowing more robust measurement. As shown in Figure 2.11, hydrogen-induced ductility loss of an X100 pipeline steel is more significant in the tests with longer charging time. However, it is expected that once the solubility limit of the tested material is reached, further longer charging will not lead to a proportional increase of HE susceptibility.

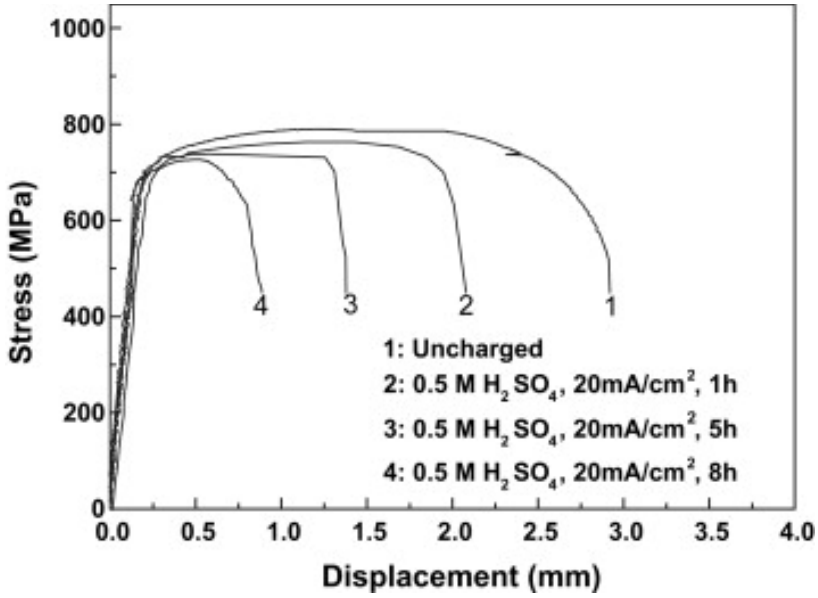

Figure 2.11 Stress-strain curves of an X100 pipeline steel after various durations of hydrogen charging [101].

Increasing the voltage during electrolytic charging can increase the generated hydrogen fugacity around the specimen. However, the level of HE may not proportionally increase with the voltage since excess hydrogen generated at the sample surface during electrolytic charging can recombine and leave the specimen without contributing to the actual uptake [101]. In addition, it has been reported that electrolytic charging at excessively high fugacity can induce blisters and surface cracks, resulting in failures that have the contributions of both HE in the specimen and cracking at the surface [99]. The selection of charging parameters is a key consideration to provide a meaningful HE assessment.

2.3.2 Material strength and microstructures

It is established that the HE susceptibility of steels is related to their strength, i.e., stronger steels are generally more susceptible to HE [27]. As the strength of a material is determined by its microstructure, HE susceptibility can be correlated with material microstructure. As shown in Figure 1.4, pipeline steels that were developed more recently generally have higher strengths due to the incorporation of a higher fraction of martensite. Martensite is known to be susceptible to HE due to the presence of high densities of lath boundaries and dislocations that are prone to HE initiation [149, 150]. This drawback of martensite limits the application of more modern pipeline steels [151]. Considering material properties and HE susceptibility, X70 and X80 pipeline steels are generally considered to be the best existing candidates for high-pressure hydrogen transport in the industry [152].

2.3.3 Welding

Welding is essential for the construction of pipeline systems. However, the welding process can expose base materials with a complicated thermal history, increasing HE susceptivity in the subsequent service in a hydrogen-containing environment [153, 154]. As shown in Figure 2.12a, a welded pipe contains heat-affected zones (HAZ) near the joint. This part can attract a significant amount of hydrogen and be the most HE susceptible part in the component [151, 155]. The HE susceptibilities of base metal and the HAZ of an X80 pipeline steel are presented in Figure 2.12b and c, respectively. It is shown that HAZ is more prone to toughness reduction in the presence of hydrogen [156]. HAZ generally has a complicated microstructure, which can contain martensite, retained austenite, bainite, and high-densities of misfit dislocations and phase boundaries, providing many susceptible sites for hydrogen to reside and embrittle [157, 158]. These sites in HAZ are in addition to the presence of inclusions or common contaminants such as MnS or dirt in the welded regions, which are also susceptible to HE [159]. The coarsened grains in the HAZ can also increase the HE susceptibility of welded steel pipe [160, 161]. To mitigate the HE problem in welding, the use of inert shielding gas for minimal hydrogen uptake during welding is critical [162]. It is also important to select feeding metals that allow low residual stress in the welded region so the inevitable pickup of hydrogen from the environment can be less harmful [163, 164].

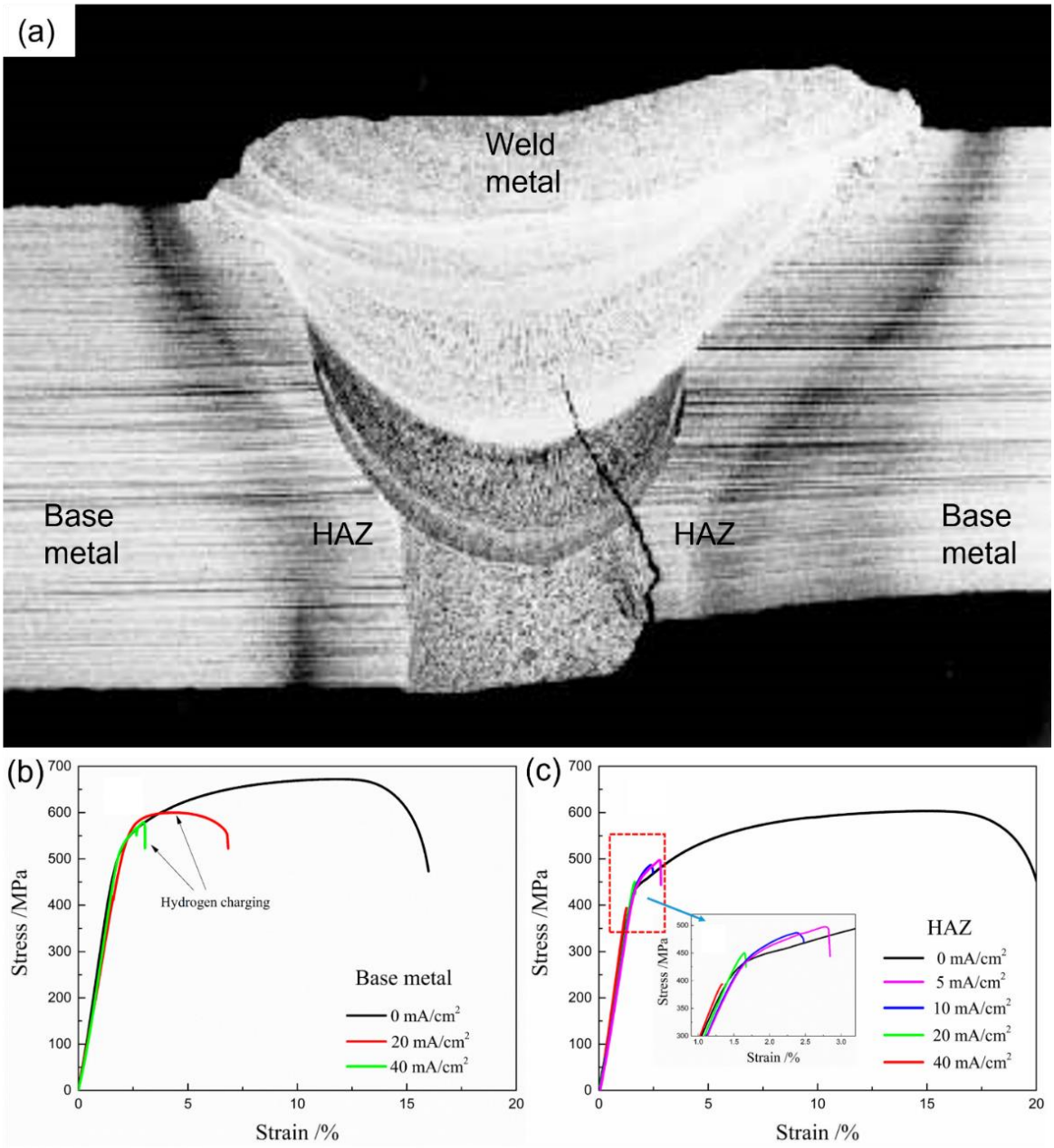

Figure 2.12. HE for welding: (a) HE initiated in HAZ and propagating in weld metal [154]; Stress-strain curves of X80 pipeline steels for (b) base metal and (c) HAZ at different hydrogen charging current densities at various hydrogen charging conditions [156].

2.4 Hydrogen embrittlement mechanisms in pipeline steels

2.4.1 Hydrogen-enhanced plasticity

The theory of hydrogen-enhanced local plasticity (HELP) was first proposed by Beachem [165] on the basis of the observation of ductile fracture surfaces in hydrogen-embrittled mid-carbon steels. Birnbaum, Robertson, and Sofronis then developed the theory [166] and verified the hydrogen effects on dislocation motion acceleration via the in-situ environmental TEM (E-

TEM) [167, 168]. As illustrated in Figure 2.13, HELP postulates that interstitial hydrogen solutes in the metal matrix prefer to concentrate at highly-stressed regions where the lattice spacing is larger [166]. The hydrogen solutes in this region then further concentrate at dislocation cores (as Cottrell atmospheres) [118, 169]. This hydrogen concentration at the dislocation core can shield the stress field for dislocation slip, leading to higher mobility of dislocations under stress [108, 170]. When a dislocation slips under stress, the hydrogen atmosphere can be dragged with the moving dislocation if the temperature of environment is sufficiently high for hydrogen diffusion to keep up. In this case, the shielding effect of hydrogen for dislocation slip continues. This HELP can then lead to the intensified formation of micro-voids, and the subsequent coalescence of micro-voids can facilitate the crack tip to propagate [166]. Recently, the use of advanced in-situ E-TEM enables direct observations of the effects of hydrogen on dislocations. Figure 2.14 shows a recent result from in-situ cyclic mechanical straining to α-iron pillars, which demonstrated the reduced stress required for the bow-out of an individual screw dislocation in the presence of hydrogen [171], providing experimental support of the HELP theory.

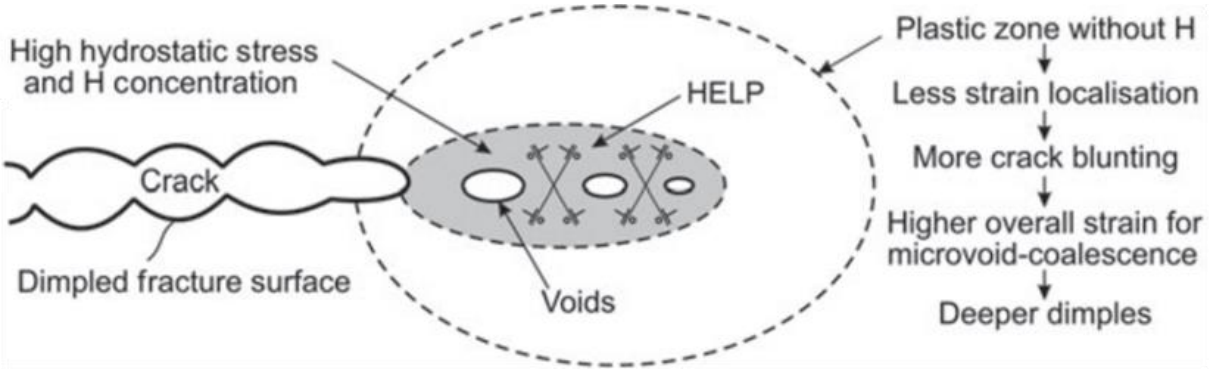

Figure 2.13. Schematic illustration of HELP mechanism [172].

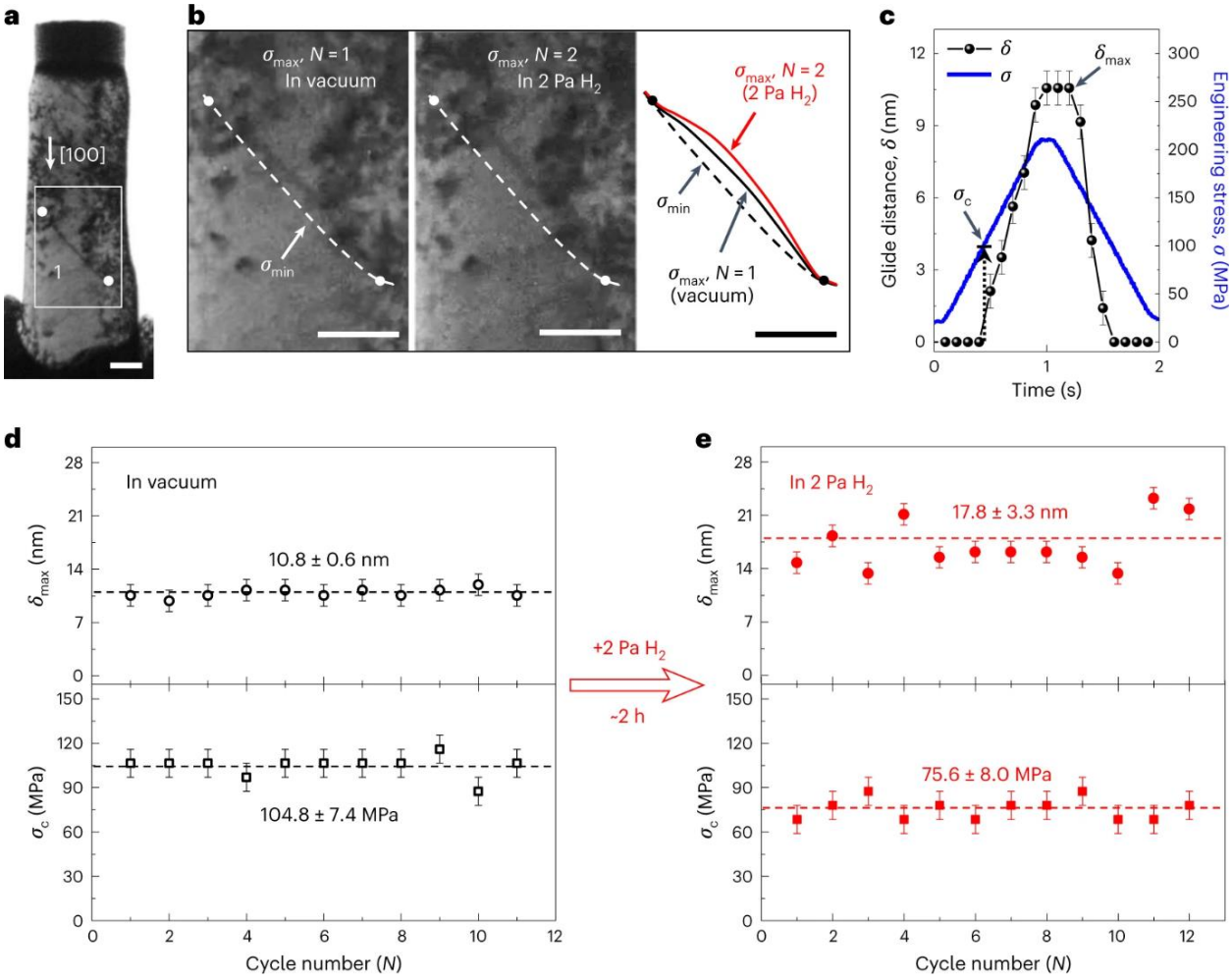

Figure 2.14. Hydrogen effects on bowing-motion of a screw dislocation. (a) Bright-field image of the α-iron pillar with a screw dislocation. (b) Comparison of the screw dislocation bowing-motion in vacuum and hydrogen circumstance. (c) Loading profile with corresponding projected glide distance of the screw dislocation. Measurements of the activation loads of bowing with corresponding projected glide distance in (d) vacuum and (e) hydrogen [171].

In the context of pipeline steels, HELP explains characteristic quasi-cleavage fracture surfaces with ridged features (Figure 2.15a). Cross-sectional observation reveals intense dislocation slip beneath the ridge (Figure 2.15b) [173]. This intense dislocation activity close to the fracture surface is quite different from what would be expected for brittle fracture, where the main contribution to strain should be directly from displacement due to brittle cracking. In fact, some pseudo-brittle fractures were also found to have a buried dislocation structure, as predicted by HELP [173, 174]. The earlier association of brittle fracture with HELP is now blamed on the low spatial resolution of early-generation microscopes, which did not allow identification of fine dimples on fracture surfaces. An example analysis that demonstrates the

importance of the spatial resolution of microscopic analysis is shown in Figure 2.15c (in low magnification) with brittle-like features and Figure 2.15d (in high magnification) with fine dimples.

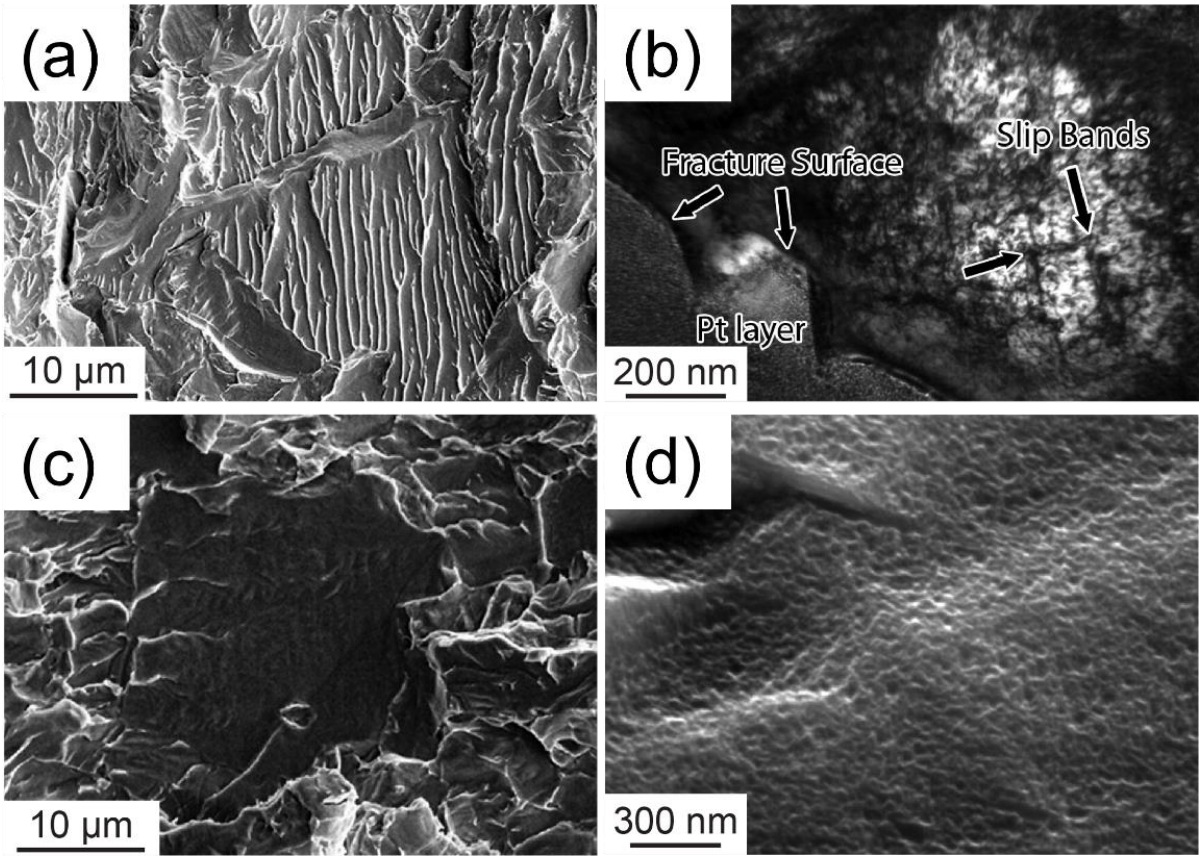

Figure 2.15. Quasi-cleavage (a, b) and flat (c, d) fracture surface of hydrogen-charged X60 hydrogen-embrittled pipeline steel: (a) SEM image showing river markings decorated on the fracture surface; (b) Bright-field TEM observation of the microstructure beneath the ridges on the fracture surface [174]; (c) Low-magnification SEM image; (d) High-magnification SEM image showing the dimple surface [173].

2.4.2 Hydrogen-enhanced decohesion

In some cases where premature fracture was observed in the presence of hydrogen, failure was found to initiate as brittle cleavage within the microstructure (Figure 2.16). This hydrogen-induced brittle cracking is attributed to hydrogen-enhanced decohesion (HEDE). HEDE was originally proposed by Troiano [175] and further developed by Oriani [176], with the postulation that hydrogen solute in lattice can directly reduce the cohesion energy of atomic bonds. However, experimental evidence of transgranular HEDE in an iron lattice has been lacking in the literature. Most of the fractographic and/or post-mortem observations of HE

samples relating to HEDE have been found to be along phase boundaries and grain boundaries (GBs) [177, 178]. In particular, the martensite-austenite interface in steels is known to be prone to brittle cracking after hydrogen charging (Figure 2.16a) [179, 180], and this has been attributed to the HEDE at the interface between matrix and MnS, a common impurity inclusion in pipeline steels (Figure 2.16b) as well as at prior austenite GBs (PAGBs) [129, 181]. Nowadays HEDE is usually used to explain the brittle failure along various interfaces in the presence of hydrogen, rather than for rationalizing the HE of pipeline steels, which is often transgranular with ductile fracture surfaces.

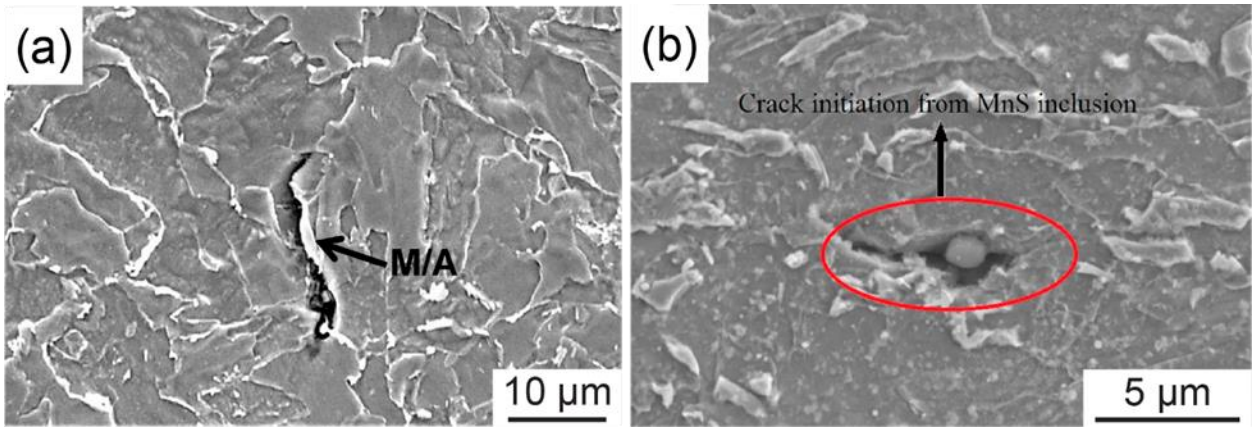

Figure 2.16. SEM images of interface cracking based on the HEDE mechanism in pipeline steels: (a) HE along martensite/austenite stringer in X65 pipeline steels [180]; (b) HE nucleation at from MnS inclusion in ferrite matrix for X60 pipeline steels [129].

2.4.3 Adsorption-induced dislocation emission

Lynch [182] first proposed the adsorption-induced dislocation emission (AIDE) theory, highlighting the role of hydrogen absorption at surface crack and the "dislocation emission" from the crack tip. Unlike hydrogen solute in the lattices for HELP and HEDE mechanisms, hydrogen in the AIDE mechanism is absorbed from the surface of materials (within first or second atomic layers beneath the surface) due to the strong traps over there [183]. As illustrated in Figure 2.17, the dislocation emission is a result of dislocation nucleation and subsequent movement away from the surface [172]. When dislocation activity is high enough to generate voids at the plastic zone ahead of cracks, cracks can propagate as a result of micro-void coalescence at the crack tip [182, 184]. The fracture surface resulting from AIDE can display both ductile (small, shallow dimples and quasi-cleavages) and brittle features (smooth intergranular facets) [183].

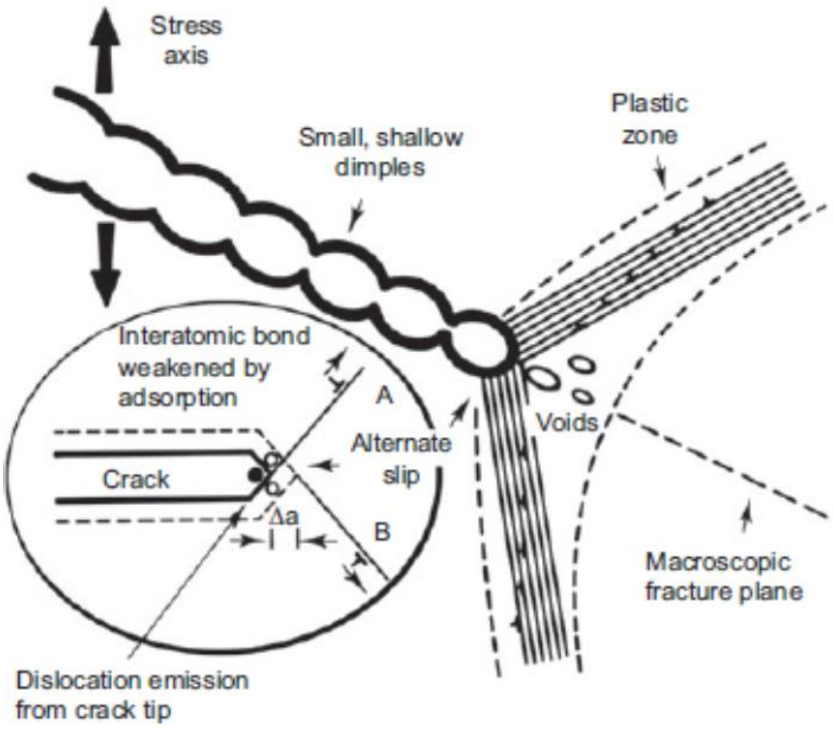

Figure 2.17 Schematic illustrations of the AIDE mechanism [172].

2.4.4 Hydrogen-enhanced strain-induced vacancies

Nagumo et al. [185, 186] first proposed the hydrogen-enhanced strain-induced vacancies (HESIV) theory that emphasized the role of enhanced vacancy formation in the presence of hydrogen. During the plastic deformation, vacancies can be generated from the dynamic dislocation interactions, like moving dislocation jogs [187] and dislocation annihilation [188] (Figure 2.18). As hydrogen reduces the formation energy of the vacancy, vacancies tend to agglomerate to form clusters as micro-void coalescence in highly strained areas in the presence of hydrogen (Figure 2.19a) [114, 115]. As hydrogen atoms prefer to trap at vacancies to generate hydrogen-vacancy complexes, the general approach to identify strain-induced vacancies is through TDA measurement on hydrogen as a tracer for vacancies (Figure 2.19b) [189].

Figure 2.18 Schematic illustrations of the HESIV mechanism for the creation and clustering of vacancies forming microcracks in the strain-concentrated area close to a barrier for slip extension [47].

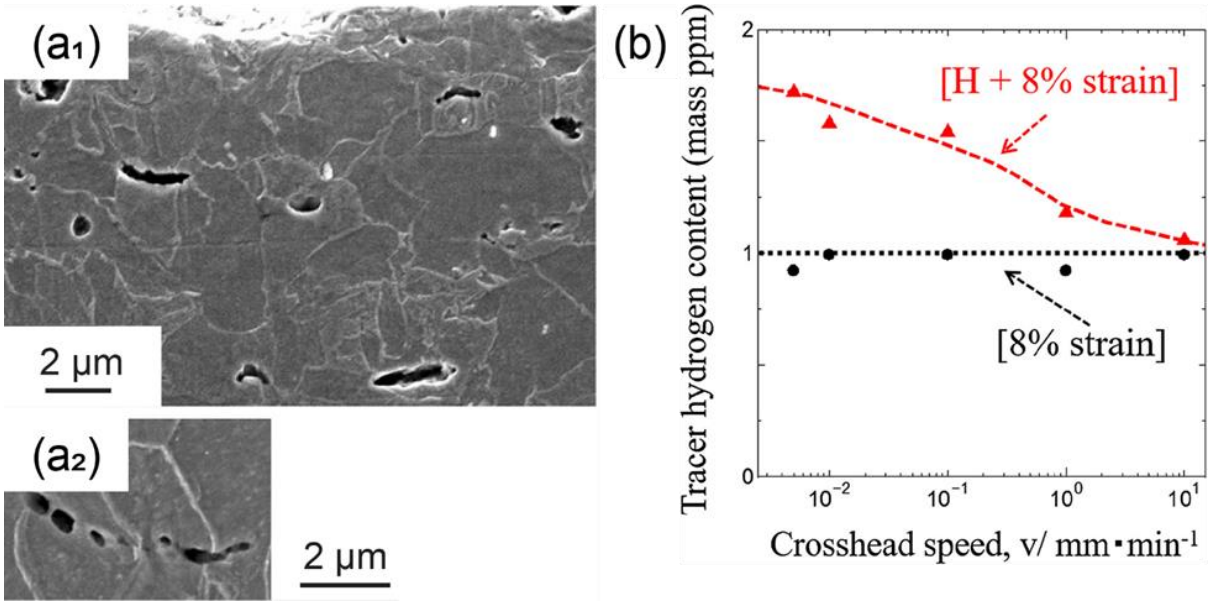

Figure 2.19 Results of slow strain rate test on pre-charged X80 pipeline steel: (a1), (a2) SEM images of lateral surfaces of fractured hydrogen-charged specimens at a crosshead speed of 0.005 mm/min; (b) Relationship between tracer hydrogen content and a crosshead speed of specimens applied at 8% plastic strain with/without hydrogen [189].

2.5 Mechanical testing for characterizing hydrogen embrittlement

2.5.1 Macroscopic testing methods

Slow strain rate tests (SSRT) and constant loading tests with hydrogen charging are standard mechanical testing methods for examining the HE susceptibility of pipeline steels [190]. One drawback of constant loading is the long time required to induce observable failures [122, 191], so SSRT is more frequently used in the literature. SSRT tests can be undertaken with either hydrogen ex-situ pre-charged specimens or in-situ hydrogen charging on the specimens during straining; the use of these two methods corresponds to the examinations for internal and environmental HE, respectively. Ex-situ hydrogen charging is less demanding in instrumentation; one can use a simple electrolytic charging unit separate from the SSRT instrument [192]. However, hydrogen solute atoms in a BCC steel lattice generally are highly diffusive, and this characteristic can lead to significant desorption of charged hydrogen immediately after the charging is completed. In contrast, in-situ charging SSRT ensures the constant presence of hydrogen in specimens by attaching a hydrogen charging rig to the SSRT specimens.

Both SSRT and constant loading tests can be conducted on either smooth or notched specimens. Using different specimen geometries allows to distinguish the localized or universal effects of hydrogen-induced strain. SSRT can give straightforward information about HE-related mechanical properties such as threshold stress for hydrogen-induced failure, plastic strain to fracture, and ductility loss [193]. Examples of hydrogen-induced ductility loss and strength (Figure 2.20b) measured by SSRT in an X80 pipeline steel in hydrogen are shown in Figure 2.20a and b, respectively [194]. In addition to SSRT, fatigue tests can be useful to determine HE susceptibility [164, 195], as shown in Figure 2.20c and d, which demonstrate the increased crack propagation rate and the reduced number of cycle to failure in hydrogen, respectively [194].

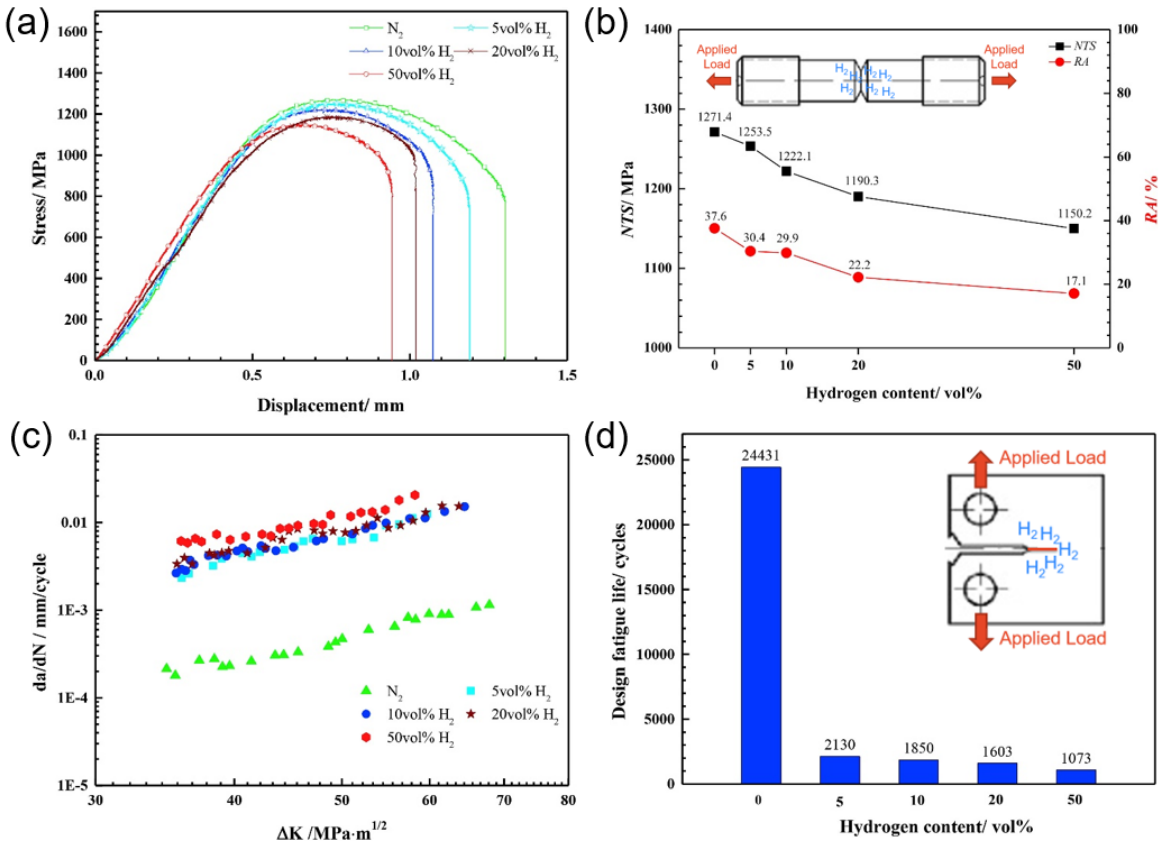

Figure 2.20. Results of SSRT for mechanical responding of X80 pipeline steels: (a) the relationship between hydrogen concentration and tensile properties of the notched samples, (b) collected data from the tensile testing (NTS: notch tensile strength, RA: reduction of area); (c) the relationship between hydrogen concentration and fatigue behaviors of the notched samples, (d) The fatigue life of the pipeline steels samples regarding hydrogen concentration [194].

Linearly increasing stress test (LIST) is another macroscopic mechanical testing technique established by Atrens et al. [196]. LIST applies a gradually increased load to measure

the threshold failure stress of the specimen. One can compare this critical stress in the presence and absence of hydrogen to determine the HE susceptibility [197, 198]. As compared to SSRT, which is a displacement-control technique and can take a long time before sample failure, LIST is a load-control technique that can reach the threshold stress within a definite time, increasing the overall data yield [199].

2.5.2 Microscopic testing methods

In addition to macroscopic methods, nowadays mechanical testing can be miniaturized and conducted in microscopes to measure the mechanical response of a specific microstructure of interest at the microscale. This micromechanical approach allows the extraction of the intrinsic property of one or a few specific microstructures, deconvoluting the contributions of individual microstructural components. The recent development of environmental micromechanics allowed tests to be conducted in certain gas environments such as in hydrogen [200, 201]. Environmental scanning electron microscopy (E-SEM) and E-TEM allow the exposure of the specimen to hydrogen during micro-straining experiments, which can be done by direct gas injection [202], hydrogen plasma bombardment [203], or in-situ electrochemical charging [204]. These experimental platforms provide real-time analysis on the material deformation behaviors in the presence of hydrogen, leading to the observation of increased dislocation mobility [167, 205], facilitated crack propagation [206] and the changes of fracture modes [207, 208]. An example is shown in Figure 2.21, where single crystalline microcantilevers of Fe with 3 wt.% Si were bent in an E-SEM in under the exposure of hydrogen plasma, resulting in the reduced yield loads (Figure 2.21a) and accelerated crack propogation (Figure 2.21b-c) [209].

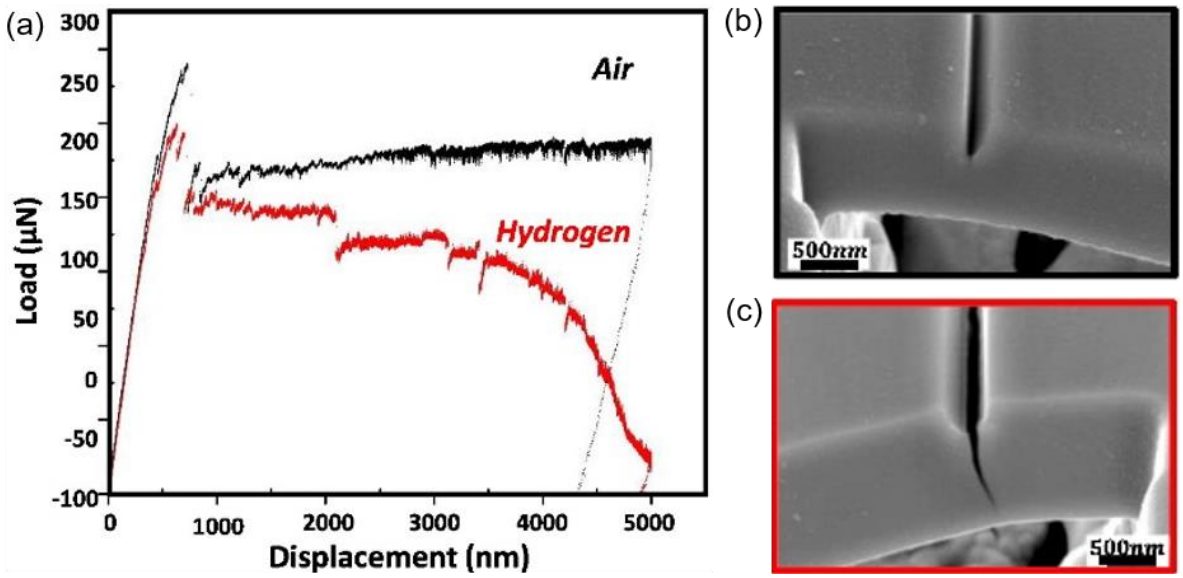

Figure 2.21. Micro-bending tests on single crystalline Fe–3wt.% Si microcantilevers. (a) Representative load–displacement curves of microcantilevers; SEM images from the side view at the crack region in (b) the absence and (c) the presence of hydrogen [209].

2.6 Summary

Conventional pipeline steels such as X42, X52, and X60 have microstructures that are predominantly ferrite and pearlite. These materials have been widely used for gas transmission applications, which have pearlite as the main strengthening/load-bearing microstructural component. Literature has demonstrated these steels are susceptible to HE, and the presence of hydrogen can change the cracking mode of pearlite. However, a fundamental view of how hydrogen-induced cracking initiates in pearlite has been lacking, and this knowledge gap limits the advance of knowledge for developing new cost-effective steels with microstructures that are less susceptible to HE and hence lead to long life in hydrogen service. With the development of emerging characterization techniques such as in-situ micromechanical testing in SEM, new insight is possible. This thesis thus focuses on developing new experimental methods and using them to generate microscale insight into how hydrogen influences the structural integrity of pearlite. We shed light on the changes of pearlite and ferrite deformation behaviors because of hydrogen introduction, using a combination of several advanced microscopy techniques to study the hydrogen-material interaction at a fundamental scale.

3 Material and methods

3.1 Model pearlite steel

A model material with a high proportion of pearlite was used, as this thesis is focused on the effects of hydrogen on pearlite, which contains cementite lamellae in a ferrite matrix. This requires more carbon alloying, so the composition, specified in Table 3.1, was chosen after consulting with our industry partner CITIC Metal. The bulk steel specimen was first cast with consideration of desulphurization and vacuum degassing. As illustrated in Figure 3.1, the specimens underwent a series of heat treatments including pre-heating (< 900 °C), heating (950 ~ 1020 °C), and homogenizing (1080 ~ 1120 °C). Then the plate steel was hot-rolled (1100 ~ 850 °C) into sheets from 40 mm to 6 mm in thickness before water-cooling to 600 °C and air-cooling to 350 °C. This heat treatment allows the specimen to contain mostly undeformed pearlite with pristine pearlitic microstructure. Finally, the steel sheet was cut into 10 × 10 mm pieces with a thickness of about 1 mm as the as-received samples. The material's yield strength, ultimate tensile strength, elongation, reduction of area, hardness, and Charpy impact energy are 580 MPa, 900 MPa, 15%, 45%, 260–320 HB, and 42 J, respectively.

Table 3.1 Composition of the model steel

Element	**C**	**Si**	**Mn**	**Cr**	**V**	**Zn**	**Al**
wt.%	0.44	0.44	1.39	0.18	0.085	0.03	0.011
Element	**S**	**Cu**	**Ni**	**P**	**N**	**Fe**	
wt.%	0.038	0.031	0.013	0.011	0.004	Balance	

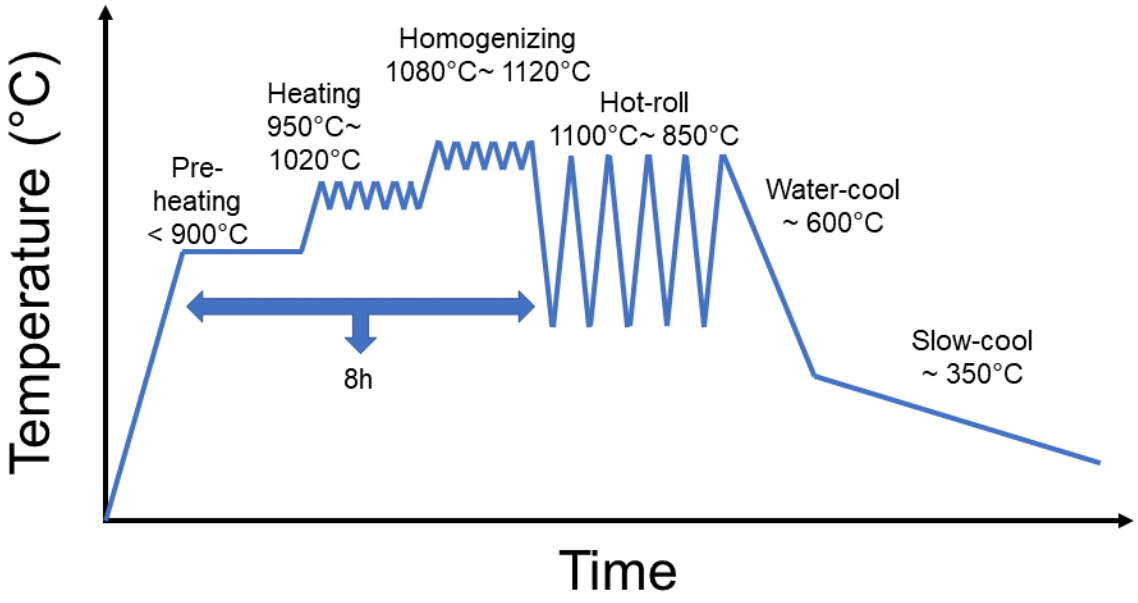

Figure 3.1 Heat treatment for the model steel specimen

3.2 Scanning electron microscope and focused ion beam

3.2.1 Interaction of electron beam with specimens

When a specimen is exposed to the electron beam in an electron microscope, the beam can have a variety of interactions with the specimen as summarized in Figure 3.2. These include direct penetration, elastic scattering, and inelastic scattering [210]. In a scanning electron microscope (SEM), elastic scattering can generate backscattered electrons (BSE) which can be used to create electron backscattering diffraction (EBSD) maps for identifying the constituent phases in a specimen [211]. Specimens under an electron beam can also generate secondary electron signals that lead to secondary electron images in common SEM surface morphology observations. In addition to these common interactions, electron beams can generate elementally characteristic X-rays that allow energy dispersive X-ray (EDX) analyses [212]. In a transmission electron microscope (TEM), the penetrated electron beam with an inelastic interaction with specimen can be used for electron energy loss spectroscopy (EELS) [213]. In TEM, specimen thickness plays a significant role in electron-specimen interactions as thicker specimens induce multi-time scattering of electrons and reduce signal intensity and data quality [214].

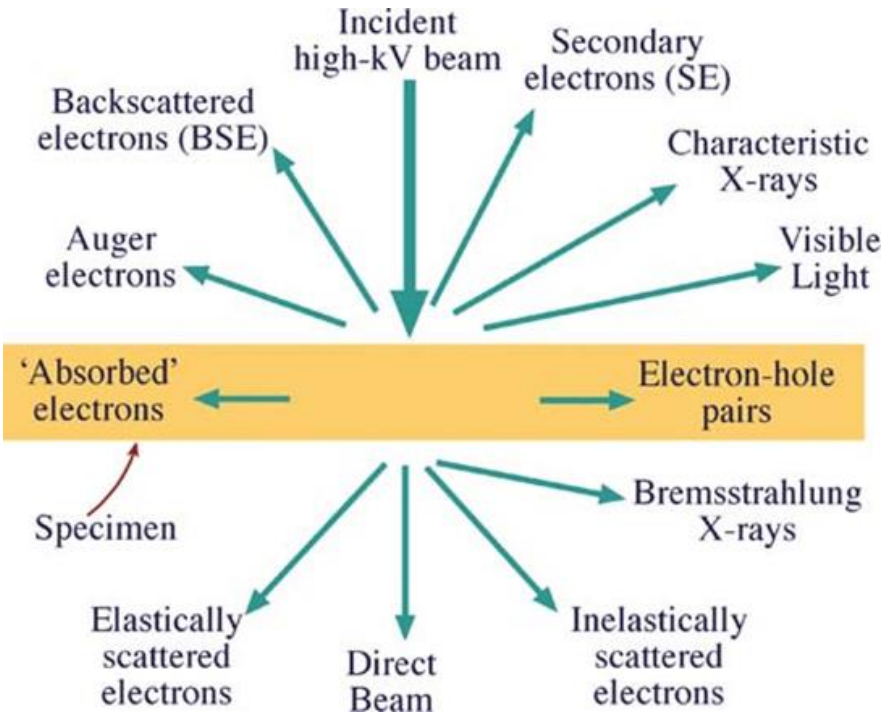

Figure 3.2 A schematic illustration of the incident electron beam-matter interaction. The collection of different electron signals via detectors represents corresponding material characterization technique [214].

3.2.2 Scanning electron microscope and focused ion beam

SEM is the core platform technique used for the experiments in this thesis. SEM was used to establish the surface morphology and phase constitution of steel specimens. A schematic illustration of SEM instrumentation is shown in Figure 3.3a. To generate SEM images, an accelerated electron beam is first emitted by an electron gun (which can be either thermionic or field-emission) and then passed through multiple electromagnetic lenses for beam convergence and scanning before reaching specimen surface [215]. SEM is a versatile platform that can be combined with other accessories to achieve advanced functionalities. A range of 5 to 30 kV can be applied for electron acceleration with various purposes. The use of which is subject to the imaging modes prefers low beam voltage (5 kV). EBSD and transmission Kikuchi diffraction (TKD) analysis generally requires a high-energy electron beam (e.g., 30 kV) to generate sufficient back-scattered electron signals in form of Kikuchi bands that indicate the lattice planes diffracting the electron beam. A Zeiss Ultra SEM with an EBSD detector, as shown in Figure 3.4a, was used for the EBSD in this thesis.

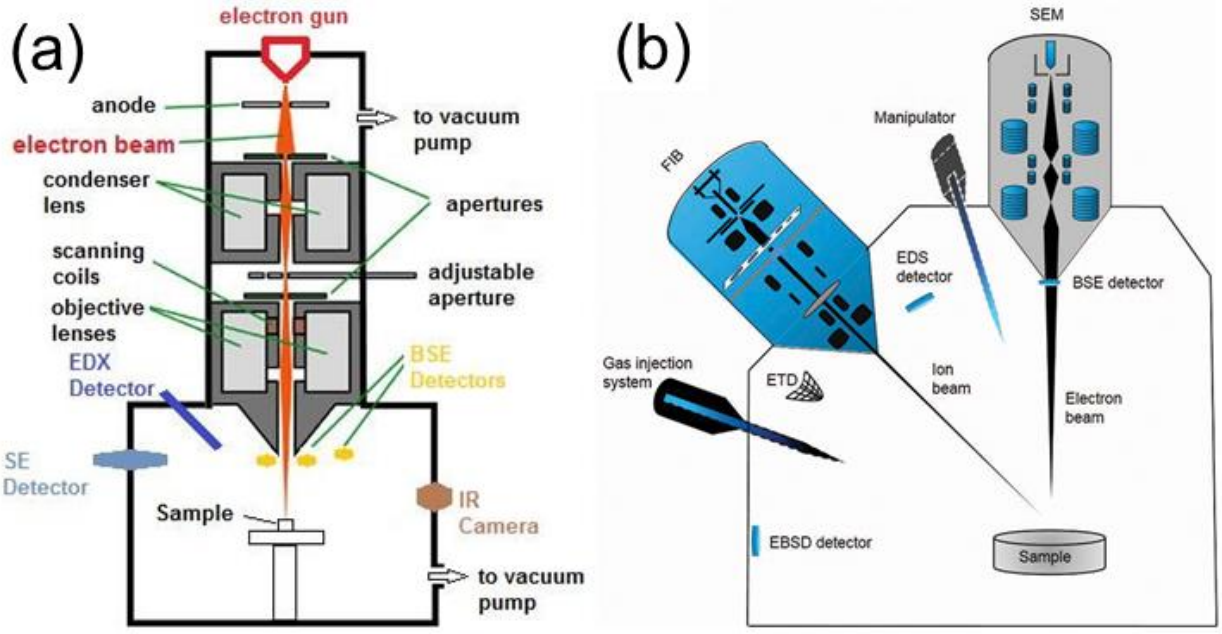

Figure 3.3 (a) Schematic illustration of main components of a scanning electron microscope and common accessories. EDX: energy-dispersive X-ray spectroscopy, BSE: backscattered electrons, SE: secondary electrons [216]. (b) Focused ion beam instrumentation [217].

Instead of electrons, the FIB uses energized ions, which are heavier than electrons, to sputter off and mill the specimen into the desired shape for subsequent analyses [218]. This ion-sputtering/milling process can also generate secondary electrons, which can be used for

imaging specimens during ion milling. As shown in Figure 3.3b, a typical dual beam FIB-SEM has a vertical electron gun and a titled ion gun (by 50° to 55° with respect to the electron beam) [217]. Common FIB ion sources include liquid metal (Ga) and plasma (Xe). Liquid gallium source can provide better spatial accuracy, but it has a lower ion milling efficiency [219]. By contrast, Xe^+ in plasma FIB (PFIB) is competent in larger cuts prepared more efficiently, whereas the different focusing methods pose challenges for precise milling [220]. The ThermoFisher Helios G4 Xe PFIB used in this thesis is shown in Figure 3.4b. It is important to note ion beam can damage the intrinsic microstructure of samples as milling regardless of ion source type [221]. To protect the target region for samples, one can apply a deposition layer (platinum or carbon coating) on the region of interest (ROI) to minimize the exposure of specimen to high-energy ion beam, and one can also consider multi-step milling using low ion voltage as the last step [222]. After shaping the specimen, our instrument allows using a micro-manipulator to lift out micro-sized samples from the bulk sample substrate. In this thesis, TEM specimens are prepared by this lift-out method after micromechanical experiments.

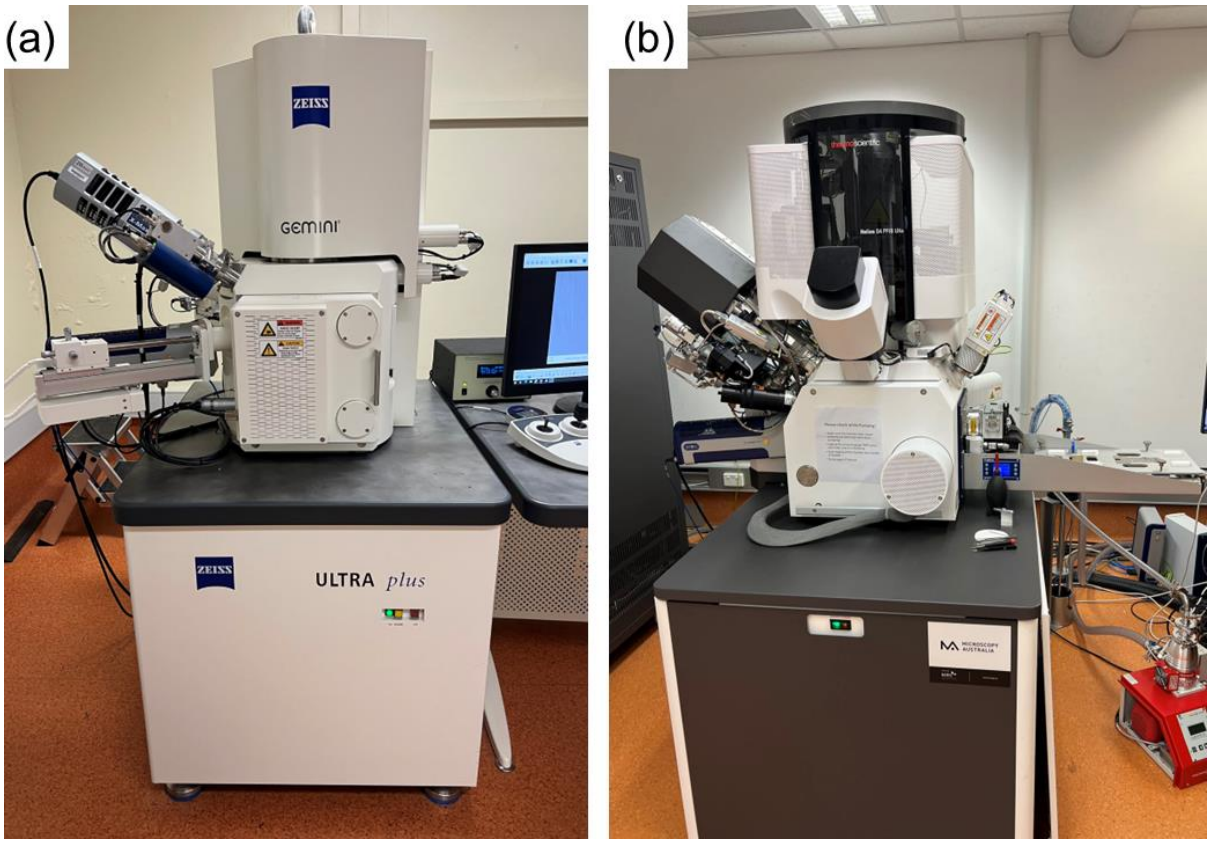

Figure 3.4 Microscopes used for specimen preparations: (a) Zeiss Ultra plus field emission SEM with EBSD and EDS detectors, (b) ThermoFisher Helios G4 plasma focused ion beam scanning electron microscopy system.

3.2.3 SEM sample preparation

The as-received steel samples were 10 × 10 × 1 mm^3 sheets and were polished to remove rust on the surface. Then the sheet was cut into small blocks of 3 × 3 × 1 mm^3 using a Struers Accutom-50 cutter (Figure 3.5a) before mounting onto a carbon stub (Figure 3.5b). For further surface preparation, samples were applied with a layer of epoxy (Figure 3.5c) to prevent the blocks from damaging the polishing pad. A 7-step preparation procedure was applied as summarized in Table 3.2. Grinding (Step 1 and 2) was conducted on a Struers RotoPol-22 polisher. Step 1 grinding was used until the sandpaper and the sample surface were in full contact. Step 2 was applied until all the epoxy covering on the sample was removed. Polishing (Steps 3-6) then was conducted on a Struers TegraPol-25 polisher. After polishing, the samples were transferred to a Buehler VibroMet 2 vibratory polisher for Step 7 using 0.05 µm colloidal silica solution. After polishing, samples were detached from carbon stubs using an ultrasonic vibrator in acetone solution. The sample was then carefully cleaned before attaching onto SEM stubs for imaging and FIB sample fabrication.

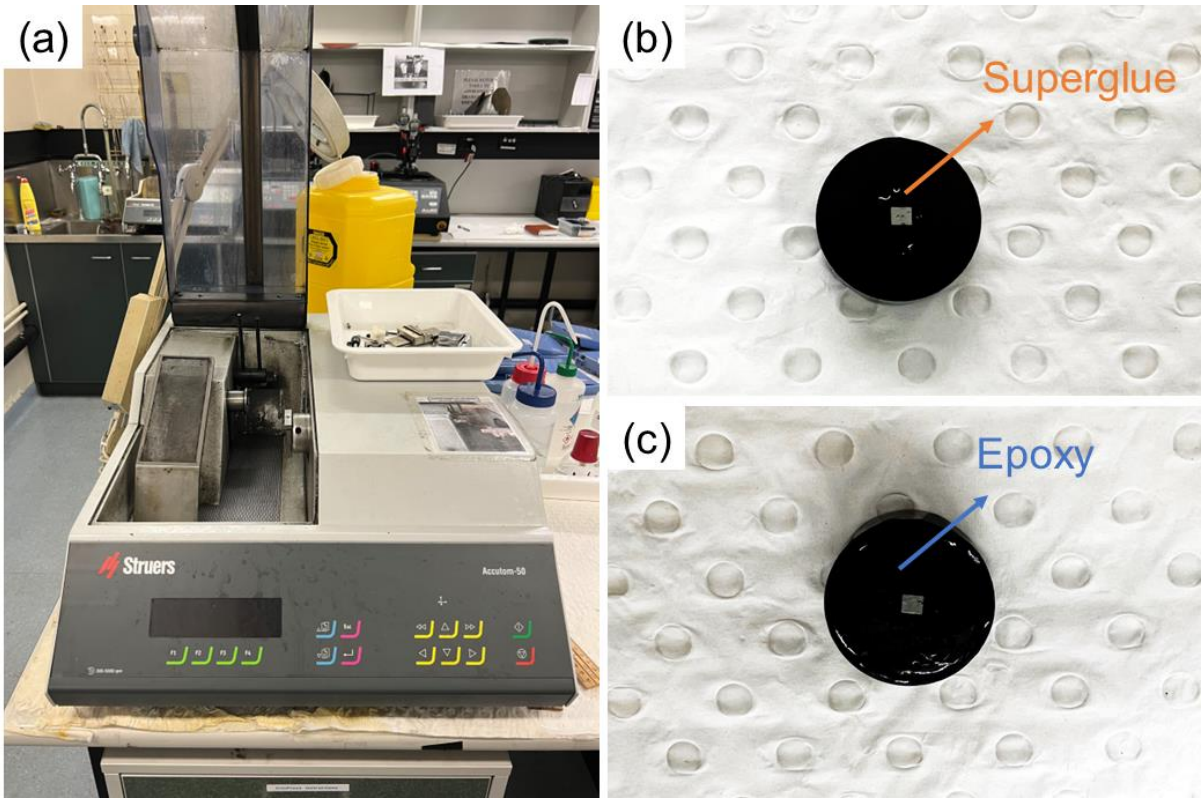

Figure 3.5 Instrument for bulk material cutting and preparation for polishing: (a) Struers Accutom-50 cutter, (b) sample attached on carbon stub with superglue, (c) sample covered by epoxy and ready for polishing.

Table 3.2 Grinding/polishing sequence for SEM-EBSD samples

Sequence No.	Size of particle on grinding/polishing media	Grinding/polishing time
Grinding		
1	30 µm	30 s/time
2	16 µm	60 s/time
Polishing		
3	8 µm	5 min
4	5 µm	8 min
5	3 µm	10 min
6	1 µm	10 min
Vibratory polishing		
7	0.05 µm	2 hrs

3.3 In-situ micromechanical testing

3.3.1 Micromechanical testing in SEM

Micromechanical testing combines nanoindentation technology and SEM to perform testing on a micro-sized specimen observed in-situ, to provide real-time measurement of the applied load as a function of its displacement [223]. This technique allows the examination of the behavior of specific microstructural features under stress and the characterization of the mechanical properties of an individual or only a few microstructures, enabling the deconvolution of their mechanical property contributions. This technique is commercially available from Bruker with their Hysitron PicoIndenter product series [224]. A PI85 PicoIndenter compatible with Zeiss Ultra SEM was used for this thesis (Figure 3.6), which consists of a sample stage to position mounted samples (blue arrow) and a transducer to control the indentation (red arrow). The sample-positioning stage can load samples with thicknesses up to 10 mm. The stage has a moving range of 3 mm along lateral and longitudinal dimensions. The PI-85 can generate a load of up to 10 micro-newton (mN) and accommodate displacement up to 5 µm. The instrument control and data acquisition can be achieved in a dedicated software, TriboScan. Photos of the experimental setup are shown in Figure 3.7.

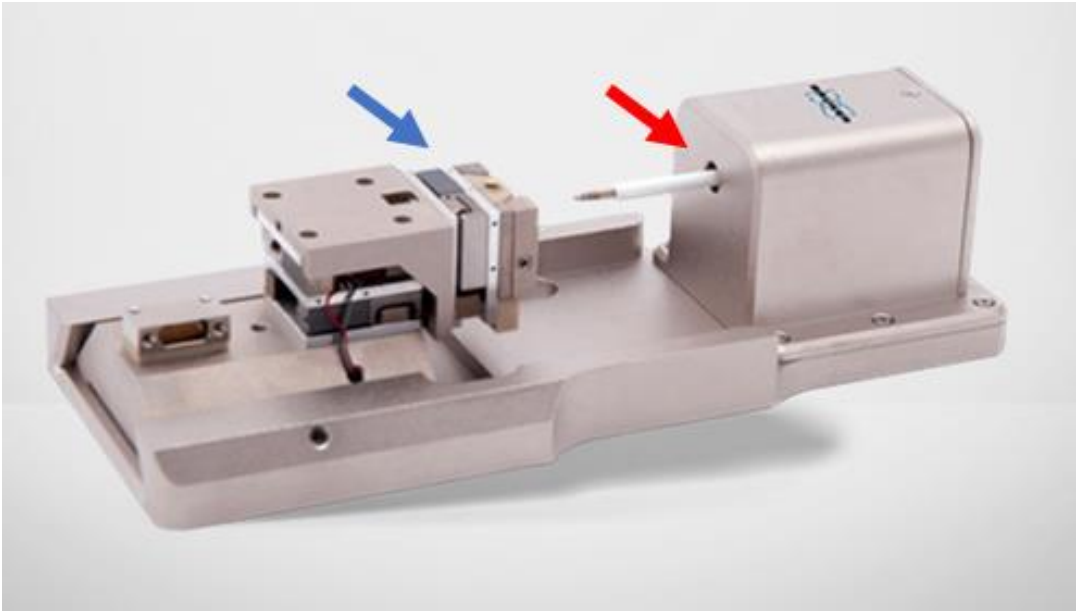

Figure 3.6 Hysitron PI85 PicoIndenter for this research consisting of a sample stage (blue arrow) and a control transducer red arrow) (https://www.bruker.com/en.html).

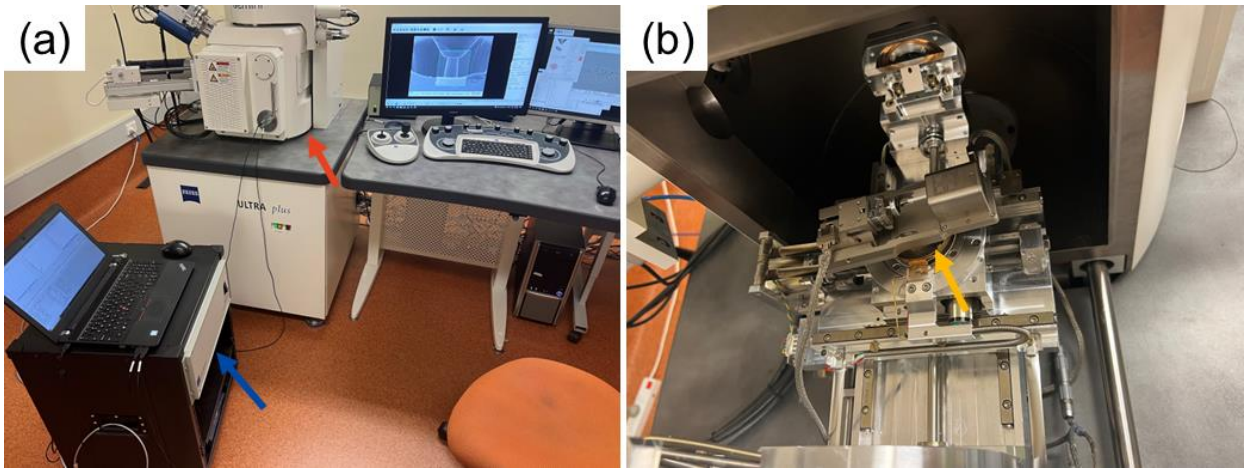

Figure 3.7 Micromechanical experiment setups: (a) the control center of Hysitron PI85 PicoIndenter (blue arrow) connected to a SEM (red arrow); (b) Hysitron PI85 PicoIndenter (yellow arrow) attached in the SEM chamber.

For general SEM micromechanical testing, three types of indenters are available: sharp tip, flat punch, and gripper corresponding to three types of FIB prepared samples involving micropillars for compression, microcantilevers for a bending test, and micro-dog-bones for tensile tests. Micropillar compression using a flat punch tip of 2 μm in diameter is adapted in this thesis, as a setup shown in Figure 3.8 with a micropillar of 1 μm in diameter and 3 μm in height. This type of microscale testing is useful for investigating slip behaviors in materials, which is dominated by dislocation activities [223]. This setup was adapted considering the HE

susceptibility is strongly related to the effect of hydrogen on dislocation mobility, which can provide insight relevant to material failures due to HELP. In addition, this setup is convenient to incorporate specific microstructures within a micropillar to study its response to load.

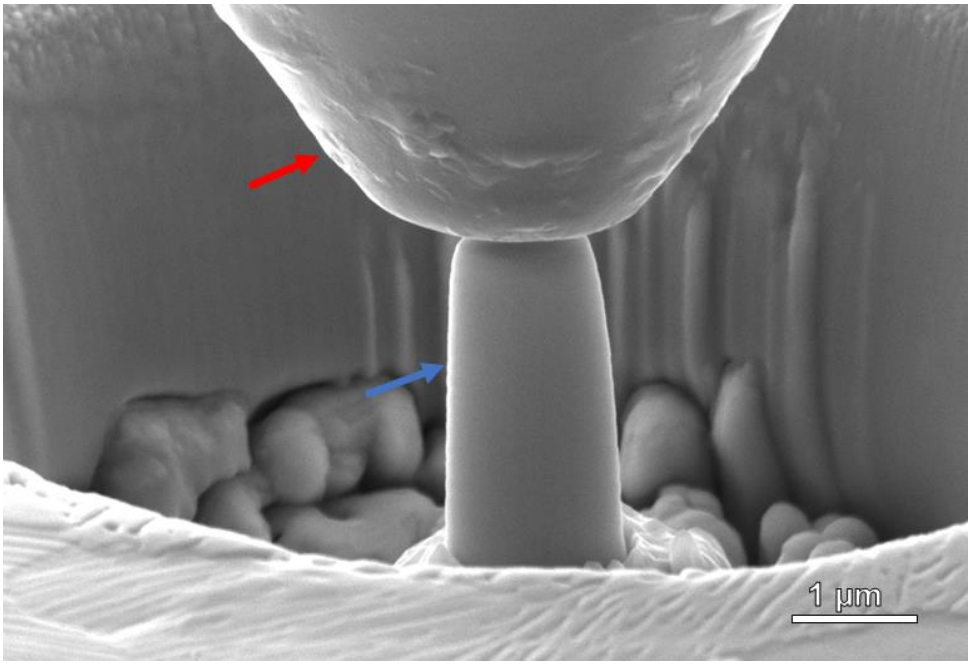

Figure 3.8 An example SEM image of a micropillar (blue arrow) and a flat punch (red arrow)

Before and after hydrogen charging (Section 3.4), low-magnification inspections of specimen surface conditions were conducted to ensure the quality of the surface is not affected by hydrogen-induced blisters (Figure 3.9a). During the micro-compression experiments, the SEM was operated at 10 kV of electron accelerating voltage, and the PI85 module was tilted for 26.4 degrees to allow the best imaging perspective for recording the entire compression process (Figure 3.9b). The micro-compressions were conducted at a rate of 3 nm/s which is equivalent to a quasi-static loading at a strain rate of 10^{-3}. Experiments slower than this setting were attempted, which may be more comparable with the macroscale mechanical testing protocols for hydrogen embrittlement, e.g., ISO11114-4 [225]. However, slow-strain experiments inevitably introduced concerns around system stability (a typical experiment at such a rate requires at least 4 hours) as well as hydrogen desorption from specimens. As such, a fixed displacement rate of 10^{-3} was used to achieve the most meaningful results. All deformed specimens undertook at least 450 nm of displacement to guarantee sufficient material straining. All the micromechanical tests were conducted at room temperature. When applicable, load-displacement data in this thesis were converted to stress–strain curves considering the geometry and angle of cementite lamellae with respect to the load direction.

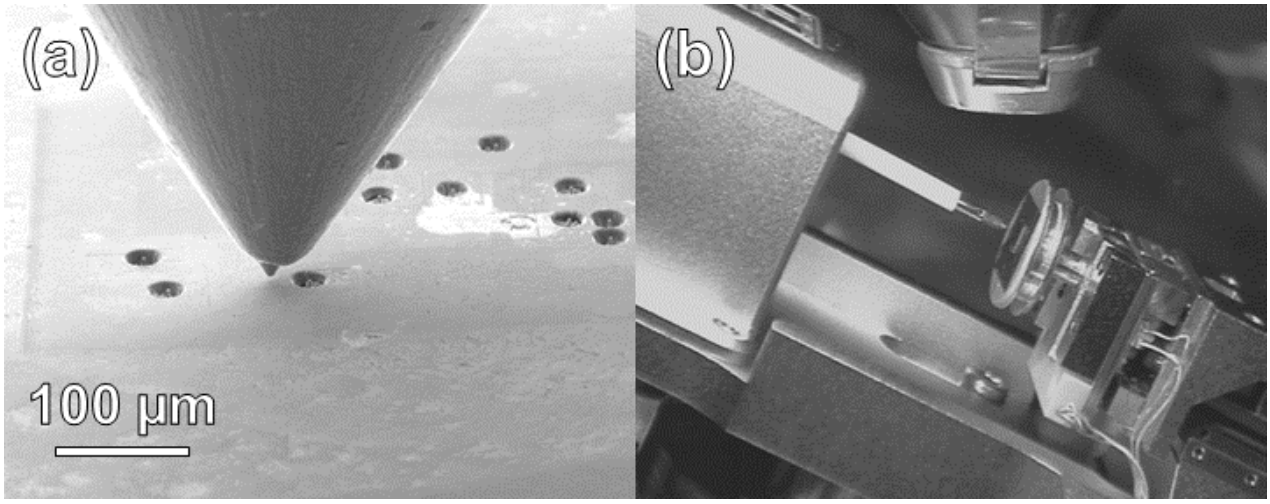

Figure 3.9 In-situ mechanical testing setup: (a) a SEM image of the alignment of tip and hydrogen-charged micropillars before testing; (b) the setup of micromechanical testing platform tilted by 26.4° in the SEM chamber.

3.3.2 Micropillar fabrication in FIB

Common in-situ compression tests can be performed on micropillars prepared on bulk samples [226] or free-standing lamellae on the edge of sheet samples [227]. In this thesis, FIB-fabricated micropillars remain attached on the surface of polished bulk samples, which can function as hydrogen reservoirs to continue supplying hydrogen and inducing HE of micropillars during testing. The micropillar fabrication for this thesis started from selecting the grains with the crystal orientation, size, and morphology of interest using EBSD via a Zeiss Ultra plus field emission SEM (Figure 3.4a). The EBSD experiments were conducted on the bulk specimens mounted on a 70° pre-tilt holder with using 20 kV acceleration voltage and 60 µm aperture. The EBSD detector was placed at 148 mm from the entry and – 4 mm in elevation. The EBSD experiment was carried out again after the micropillar fabrications to verify the micropillars have the crystal orientation desired (Sections 4.1 and 5.1). The EBSD was conducted by using the Aztec 4.2 software. The detection was conducted with 5 milliseconds of acquisition duration for each beam, 2 µm of step size for coarse scans, and 0.1 µm for fine scans. EBSD data were analyzed in the AztecCrystal software for developing the grain orientation and phase compositions. To ensure specimen quality with low ion damage, FIB micropillar shaping/milling on the selected grain was done in three steps:

1) Rough milling was conducted to effectively prepare a base stage at high ion beam energy and current (30 kV, 4nA). A ring pattern of 10 µm outer diameter and 4 µm

inner diameter with 3 μm height was used, which is applied from outside to inside. An example image of the specimen geometry of this step is shown in Figure 3.10a.

2) Low ion beam energy and current (30 kV, 30pA) were then used to shape the micropillar from the base stage. A ring pattern of 4 μm outer diameter and 1.6 μm inner diameter was used from outside to inside. This process was required to finish in "one pass" whose milling parameters were achieved by multiple trials until the height of the micropillar was reached.
3) Fine shaping was then performed to achieve a low taper angle of the pillar. The ion beam energy and current as Step 2 were used but the ion beam was applied inside out. The milling was iterated until the taper angle was less than 3 degrees with respect to the ion beam direction, as exhibited in Figure 3.10b. The final height-to-diameter ratio of each micropillar was set within the range between 2.5 and 3 [226].

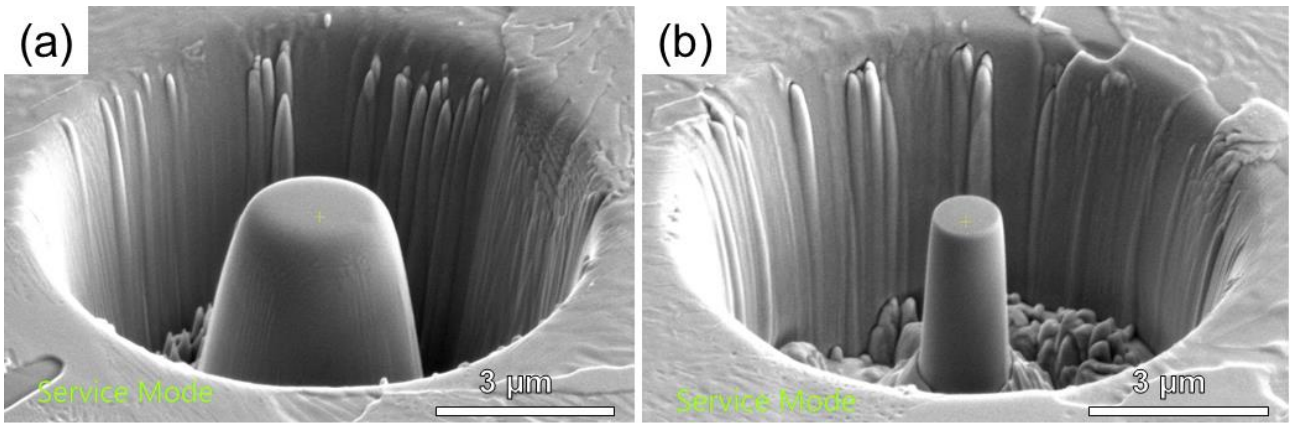

Figure 3.10 Micropillar milling processes via FIB: (a) stage, (b) micropillar.

To investigate the effects of hydrogen on the deformation behaviors of ferrite-cementite interfaces in pearlites, in-situ compression testing was conducted on both uncharged and hydrogen-charged micropillars. Samples with certain crystal structure typically deform along particular slip planes, which is often the close-packed planes [228]. In BCC ferrite matrix, the slip planes can be {110}, {112}, and {123}, and slip directions are <111> [229]. This aspect of possible slip planes was also considered during the micropillar fabrication, given the load being applied from the top flat surface of the micropillar. In addition, Critical resolved shear stress (CRSS) was used in the micro-compression data analyses to consider slipping at certain angles within the micropillars, instead of simple load-displacement data.

3.4 Hydrogen charging

In-situ hydrogen charging in an E-SEM for micromechanical testing can sometimes be useful. However, literature has demonstrated that the amount of hydrogen that can be introduced by this in-situ charging is small compared to that of ex-situ electrolytic charging [230]. Ex-situ electrolytic hydrogen charging was thus used in this thesis. Figure 3.11 shows the hydrogen charging setup, which was developed in previous work by our research group [231]. Electrolytic hydrogen charging was conducted at room temperature, in 0.1 M NaOH in H_2O at -2200 mV, powered by Keysight 2901A, for 1 hour to enable the surface hydrogen uptake in the SEM bulk specimen. The specimen was placed downward and incorporated the pre-fabricated micropillars in contact with the electrolyte, as shown in Figure 3.11. The sample acted as the cathode of the electric circuit, which is in company with a gold stripe as the anode. After charging, the sample surface was carefully cleaned without damaging the micropillars before amounting to the PI-85 and started evacuating in the Zeiss Ultra SEM within 20 minutes after the completion of hydrogen charging.

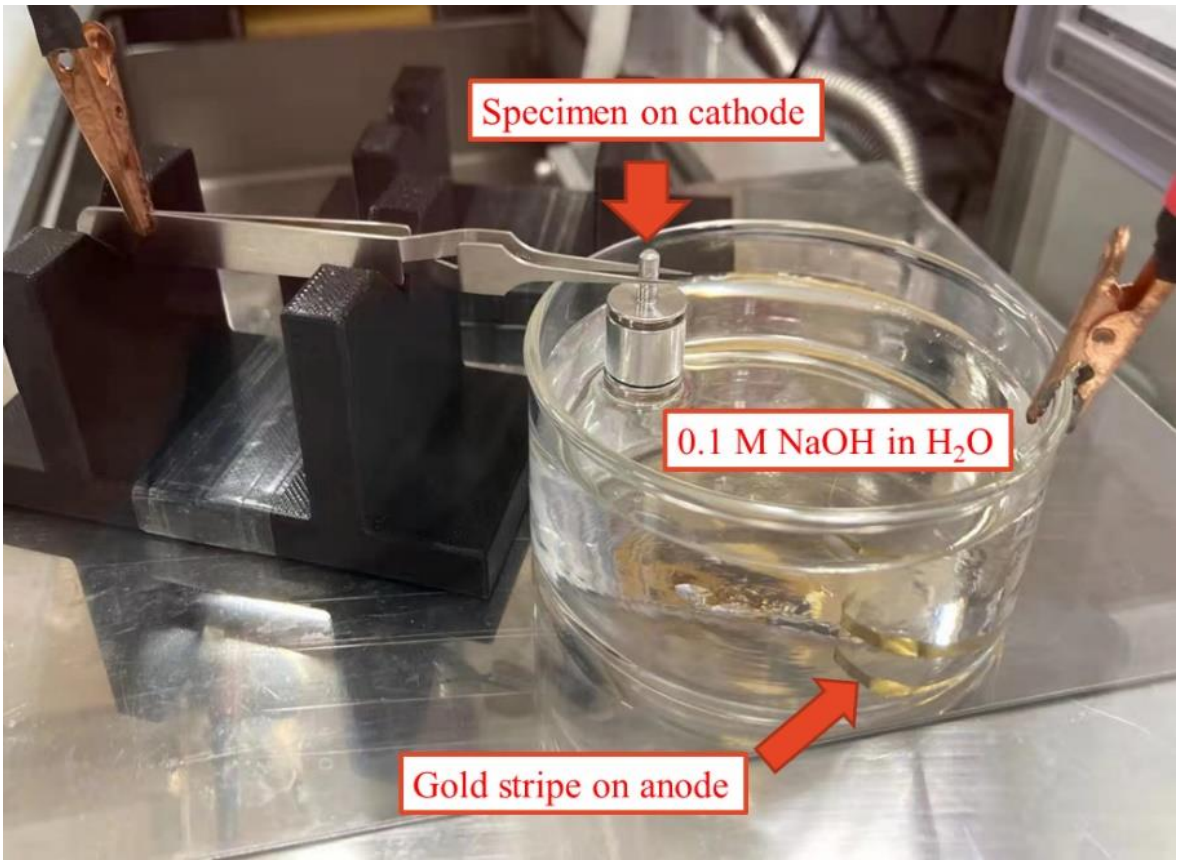

Figure 3.11 Electrolytic hydrogen charging setup for SEM specimens in this thesis.

3.5 Transmission electron microscopy

3.5.1 Transmission electron microscope

After micromechanical deformation, micropillar specimens were examined in a TEM for post-mortem analyses. Contrasting to SEM, which examines the surface morphology and near-surface electron-material interactions, TEM is a different type of electron microscope that uses a high-energy electron beam to transit a specimen and to acquire information on the interior structure of the specimen in high resolution. The control of the electron beam and the distillation of electron-specimen interaction are achieved by the cooperation of magnetic lenses, stigmators, and apertures, leading to various imaging modes that can provide different information about the material structure. The path of the electron beam after its interaction with the specimen contributed to the two most common modes of operation, i.e., diffraction mode and imaging mode, shown in Figure 3.12a and b, respectively [214]. Diffraction patterns (DP) can be obtained when the back focal plane of the objective lens is the object plane for the intermediate lens (Figure 3.12a), which provides information on the crystalline structure of the specimen. Imaging mode is achieved when intermediate lenses are adjusted to make their object plane function as the image plane of the objective lenses (Figure 3.12b). The absence and use of objective apertures at the back focal plane allow the selection of a direct beam and a diffracted beam after the electron beam passing specimen, leading to the generations of bright-field and dark-field images, respectively. Bright-field imaging provides the most common unfiltered information in TEM, while a dark-field image is used when electron beam filtration for better contrast of specific features with certain crystal structures is required, such as stacking faults, dislocations, and twins [232, 233].

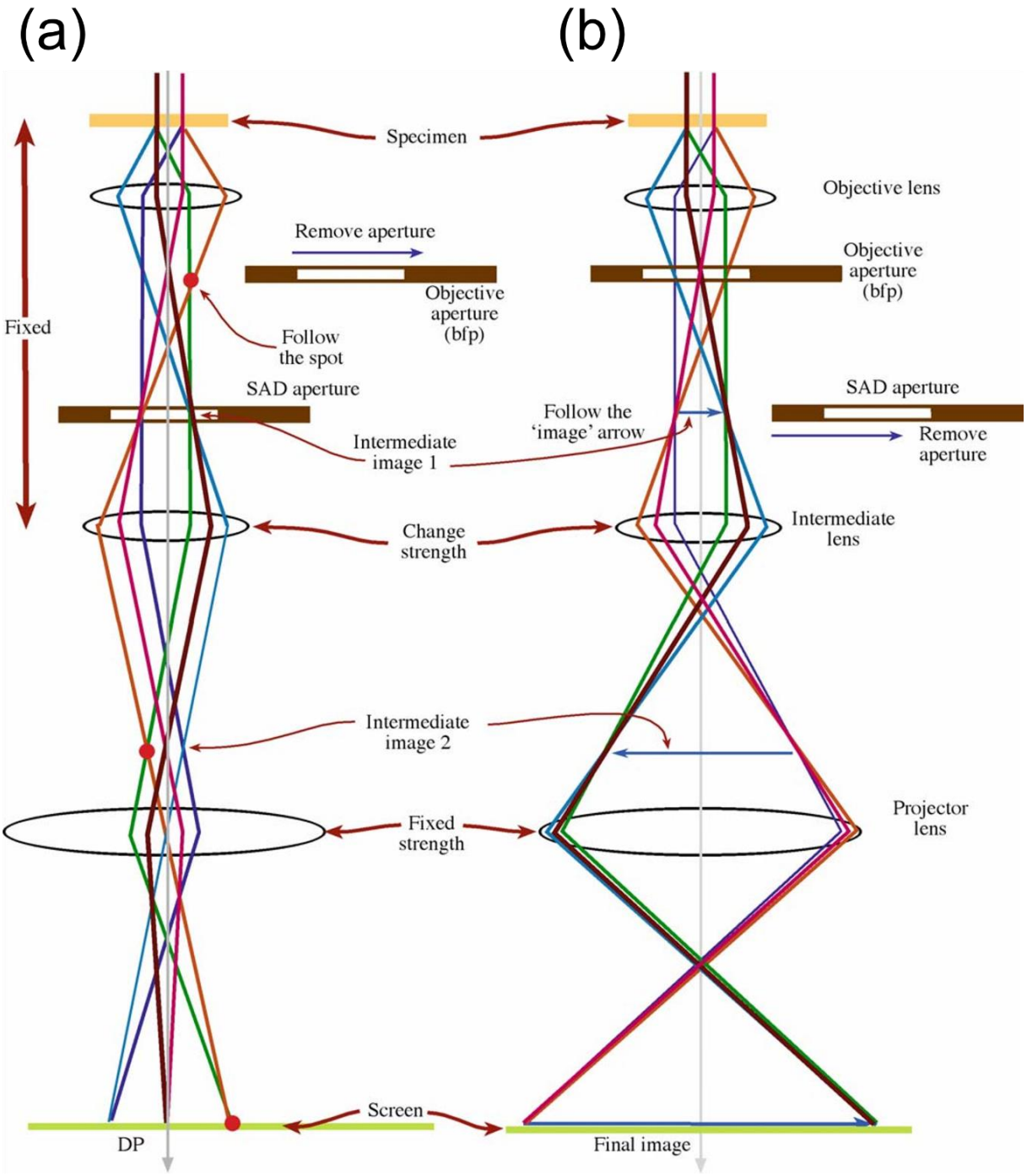

Figure 3.12 Two modes of TEM: (a) diffraction mode where the diffraction patterns are projected on the screen; (b) image mode where the specimen morphology is projected onto the screen [214].

Scanning TEM (STEM) imaging uses a convergent electron beam to conduct a point-by-point scan on a thin foil sample and collects the scattered electrons via an annular detector [214]. As shown in Figure 3.13, the use of different annular detectors leads to different imaging modes, such as annular bright-field (ABF) detector to collect unscattered electrons, annular

dark-field (ADF) and high-angle ADF (HAADF) detectors to collect scattered electrons. ABF images provide the best diffraction contrast, whereas HAADF image is good for resolving mass-thickness contrast (or Z-contrast).

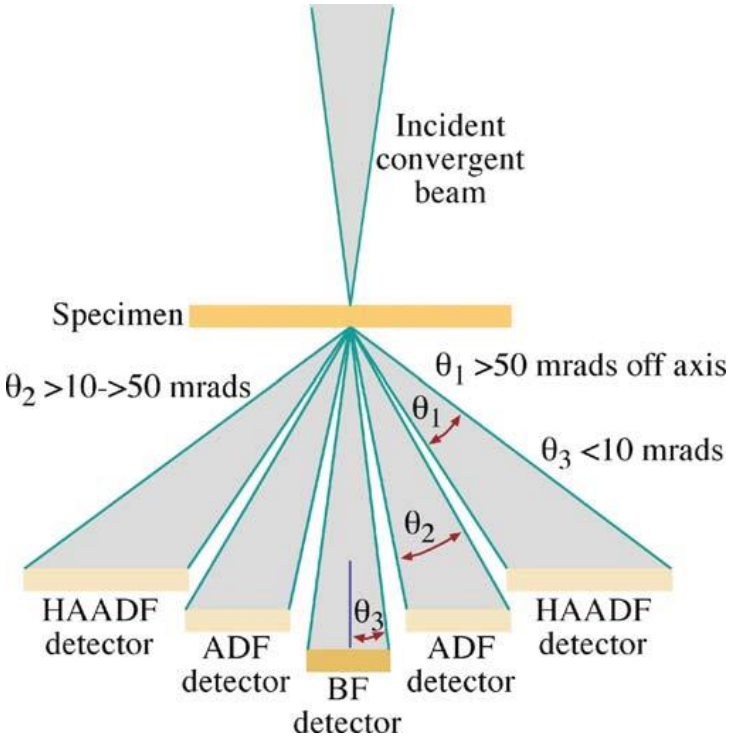

Figure 3.13 Schematic of an annular detector for STEM imaging [214].

Two TEMs were used in this thesis, i.e., JEOL JEM-2100 TEM operated at 200 kV (Figure 3.14a) and Thermo-Scientific Spectra 300 (S)TEM operated at 300 kV (Figure 3.14b). Bright-field imaging, selected-area diffraction, and the determination of the crystal orientation of the specimen were conducted on the JEOL 2100. STEM images were taken in Spectra 300 using a convergence angle of 17.9 mrad and collection angles of 109 – 200 and 0 – 44 mrad for HAADF and ABF, respectively.

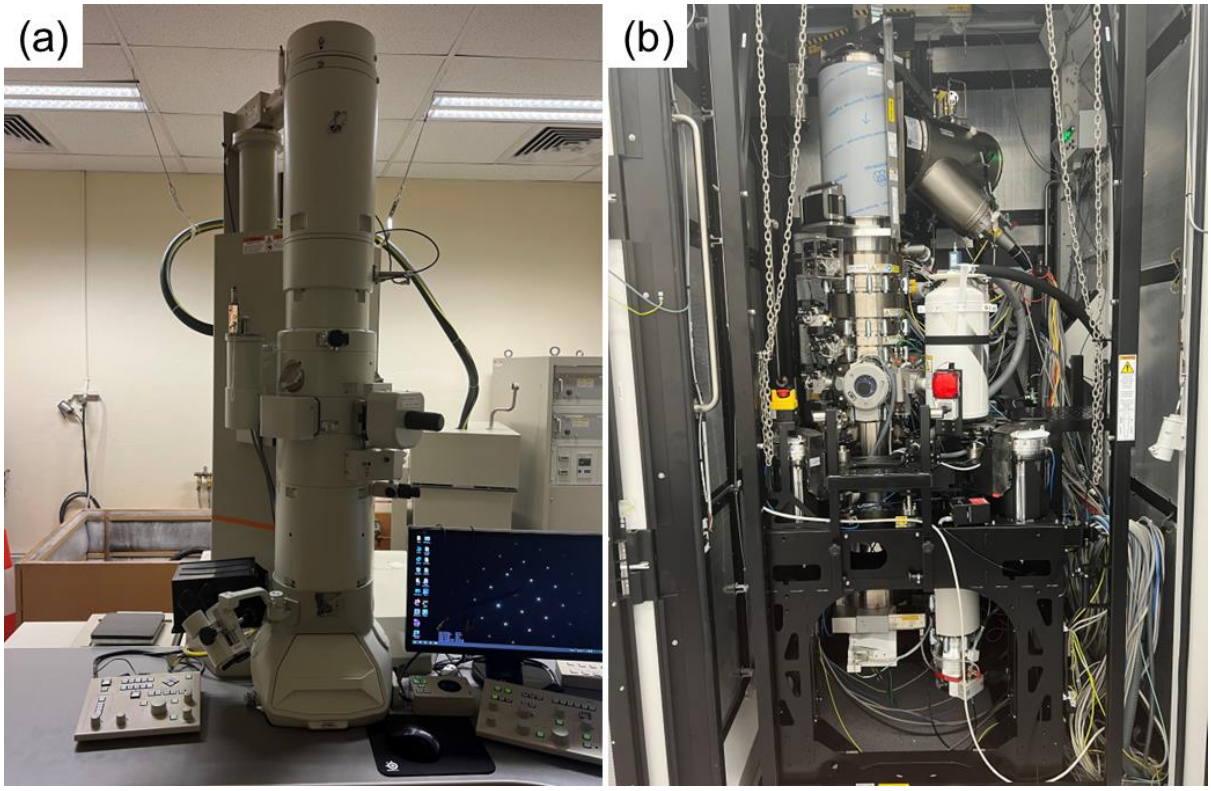

Figure 3.14 Transmission electron microscopes used in this thesis: (a) JEOL JEM-2100 TEM operated at 200 kV, (b) Thermo-Scientific Spectra 300 (S)TEM operated at 300 kV.

3.5.2 Cross-sectional TEM sample preparation after deformation

After the micromechanical experiments, cross-section specimens were prepared from the compressed micropillars for (S)TEM by using FIB to fabricate and lift out thin-foil samples. The cross-section specimens were prepared using either the ThermoFisher Helios G4 PFIB-SEM (Figure 3.4b) or the Zeiss Auriga Ga FIB-SEM (Figure 3.15a). All the cross sections of micropillars were prepared in directions that were normal to the nominal slip planes in the micropillars, as shown in Figure 3.15b. The determination of the milling direction is assisted by the measurement tools in the control software of FIB-SEM under the FIB view. After confirming the crystal orientation, Pt deposition was sometimes used to protect the features of interest from ion beam damage, as shown in Figure 3.15c. The detailed milling steps and ion beam conditions are summarized in Table 3.3.

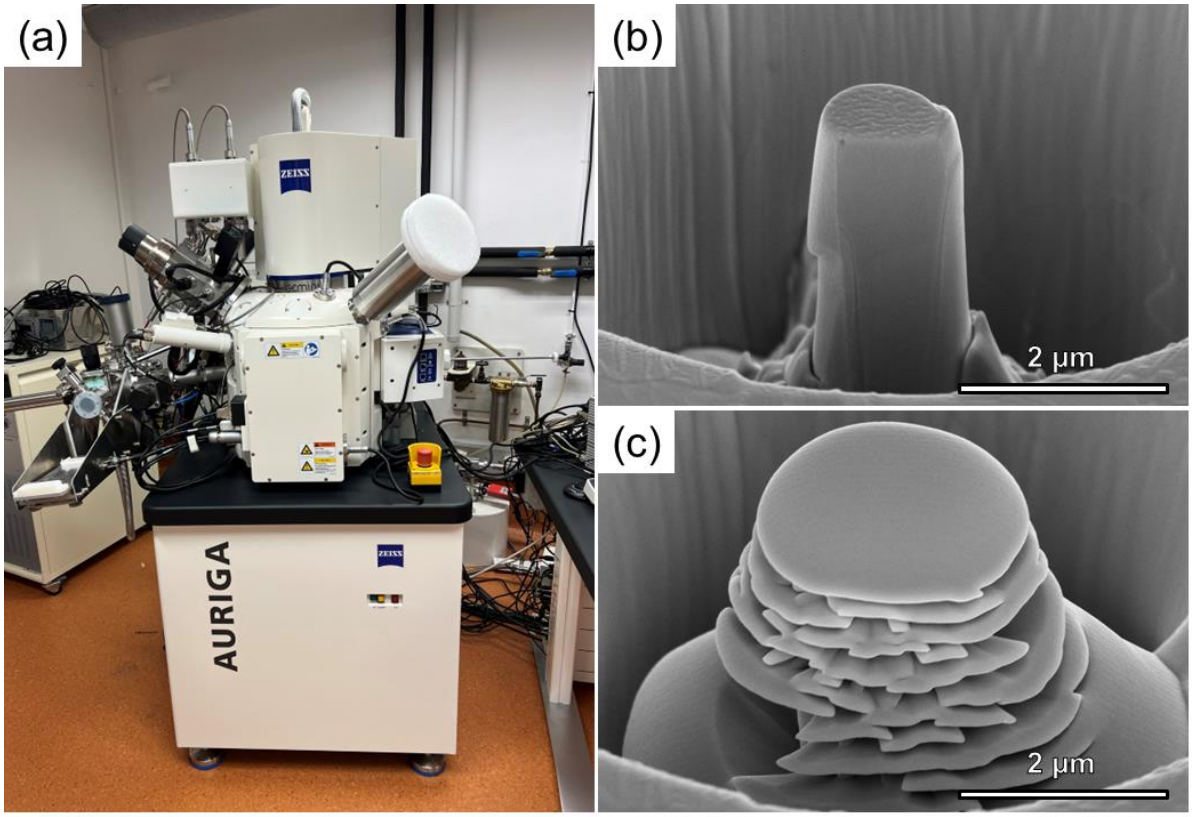

Figure 3.15 Cross-section milling after compression testing. (a) the Zeiss Auriga Ga FIB-SEM used in this thesis. (b) Cross-sectional view of a specimen after one side of FIB milling. (c) Pt deposition on a buried micropillar.

Table 3.3 Milling parameters of thinning the lift-out sample for post-mortem TEM analysis.

Steps	Sample thickness	Stage tilt angle	Beam voltage	Beam current
1	> 2 µm	52°±1.5°	30 kV	1 nA
2	< 2 µm and > 1 µm	52°±1.5°	30 kV	300 pA
3	< 1 µm and > 0.5 µm	52°±1.7°	30 kV	100 pA
4	< 0.5 µm and > 0.1 µm	52°±1.7° (may vary to ±1.9°)	30 kV	30 pA
5	~ 50 nm	52°±1.7° (may vary to ±1.9°)	12 and 5kV	30 pA
6	< 50 nm	52°±4°	2 kV	30 pA

3.6 Thermal desorption analysis

In-situ SEM imaging needs to occur in vacuum (approximately 10^{-3} Pa), and this experimental environment can lead to the desorption of hydrogen during the micromechanical tests. As such, thermal desorption analysis (TDA) was used to measure the amount of residual hydrogen in the bulk specimens in the environment approximating SEM observation. In a TDA experiment, a specimen pre-charged with hydrogen is heated in a furnace at a controlled rate, and the

desorbed hydrogen can be quantitatively measured by a mass spectrometer as a function of testing time, which can be used to link with specimen temperature [47]. The configuration of the TDA used in this thesis is shown in Figure 3.16, which is based on the setup of previous work, using a heating rate of 400 °C per hour and a 10^{-3} Pa vacuum environment without background gas flow [234]. The geometry of bulk samples and hydrogen charging parameters in TDA are consistent with those for in-situ micromechanical tests. The hydrogen charging for TDA is the same as the one for micromechanical experiments. All surfaces of TDA specimens were well polished and cleaned before TDA measurement.

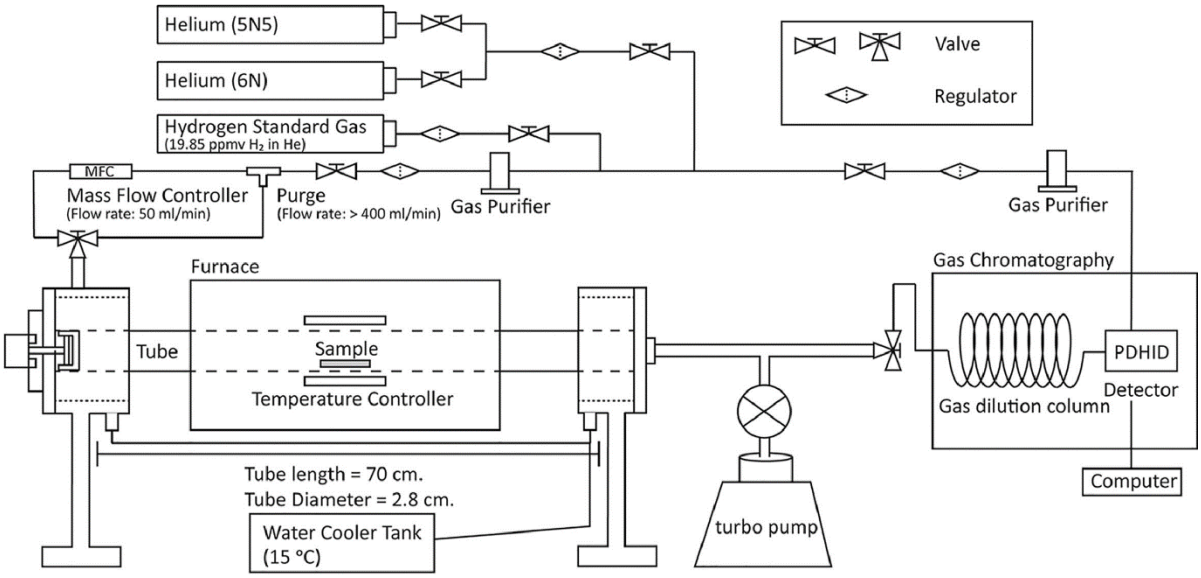

Figure 3.16 Schematic illustration of the thermal desorption analysis instrumentation [234].

3.7 Atom probe tomography

In order to measure the hydrogen distribution in steel specimens, atom probe tomography (APT) was used. APT is a mass spectroscopic technique with high spatial and elemental resolutions. As illustrated in Figure 3.17, APT applies a strong electric field on a tip specimen, the diameter of which needs to be less than 100 nm to generate a sufficiently strong field to evaporate the constituent atoms at the apex. The time-of-flight of the evaporated atoms can be measured by a detector that is sensitive to both time and position of incoming signals in combination with the knowledge of when the evaporation is triggered by pulsed voltage or laser beam on the tip [235]. Given a fixed ion flight path in an APT instrument and the energy conservation between the kinetic energy of atoms and the potential energy given by the electric field, the time-of-flight can be used to deduce the mass-to-charge ratios of the ions, providing the elemental information of the constituent atoms from specimens. The evaporation and detection of

constituent atoms are equally sensitive to all elements, and this allows precise determination of the location of the light hydrogen atoms in the tip-shaped specimens. After collecting the time-of-flight and position information of atoms, a commercial APT algorithm is used to reconstruct the data into a 3D atom map that includes hydrogen [236]. The collected data can also be configured as a mass spectrum with the quantities of the constituent atoms.

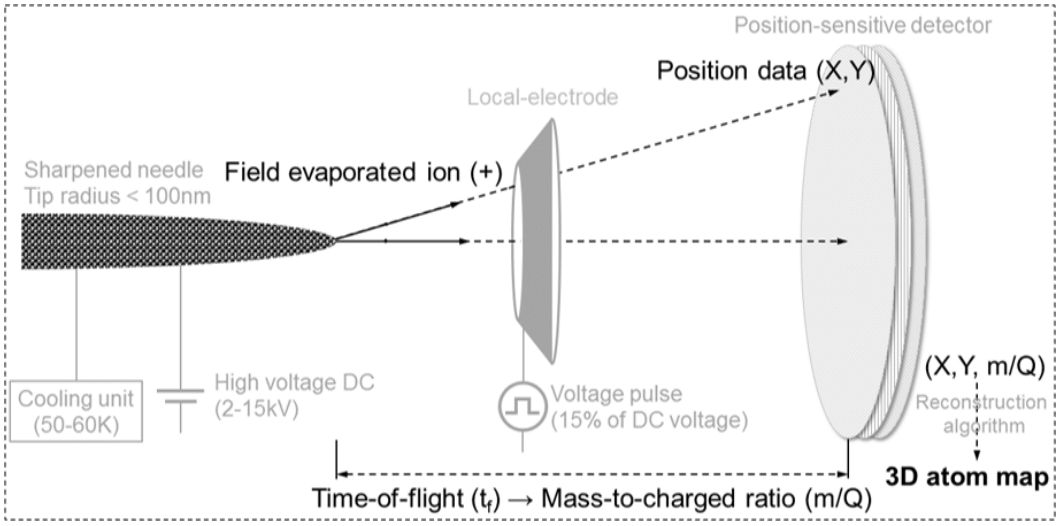

Figure 3.17 Schematization of APT principle [237].

To deliver a quality APT hydrogen analysis, a protocol combining voltage-pulsing APT, deuterium charging, and an APT-dedicated cryogenic-sample-transfer technique was used for this thesis, which has been developed in our group's previous research [231, 238]. Deuterium (^{2}H or D) charging is employed to introduce unambiguous signals into the specimen in the form of 2 mass-to-charge ratio (Da) in voltage-pulsing APT mass spectra (Figure 3.18a). Since natural hydrogen contains mostly protium (^{1}H), which results in signals at 1 Da (Figure 3.18b), the use of deuterium allows the separation of real signals from background noise generated from the residual hydrogen in the APT vacuum chamber [239]. Deuterium charging for APT samples was undertaken in 0.1 M NaOH in D_2O for 30 seconds. In this thesis, only APT experiments used deuterium, but we use mixed wording of hydrogen and deuterium, subject to the context. In addition, specimens were quenched in liquid nitrogen immediately after the completion of electrolytic deuteration. This cryogenic treatment can reduce hydrogen mobility and desorption from the samples. After quenching, the samples were kept at low temperatures (< 150 Kelvin, K) by using a cryogenic chain until the APT experiment, as specified in [231]. An experiment without this cryogenic chain was also conducted, resulting in the data shown in Figure 3.18c that does not have a detectable deuterium peak at 2 Da. Figure 3.18 also shows the ion labelling protocol used in this thesis.

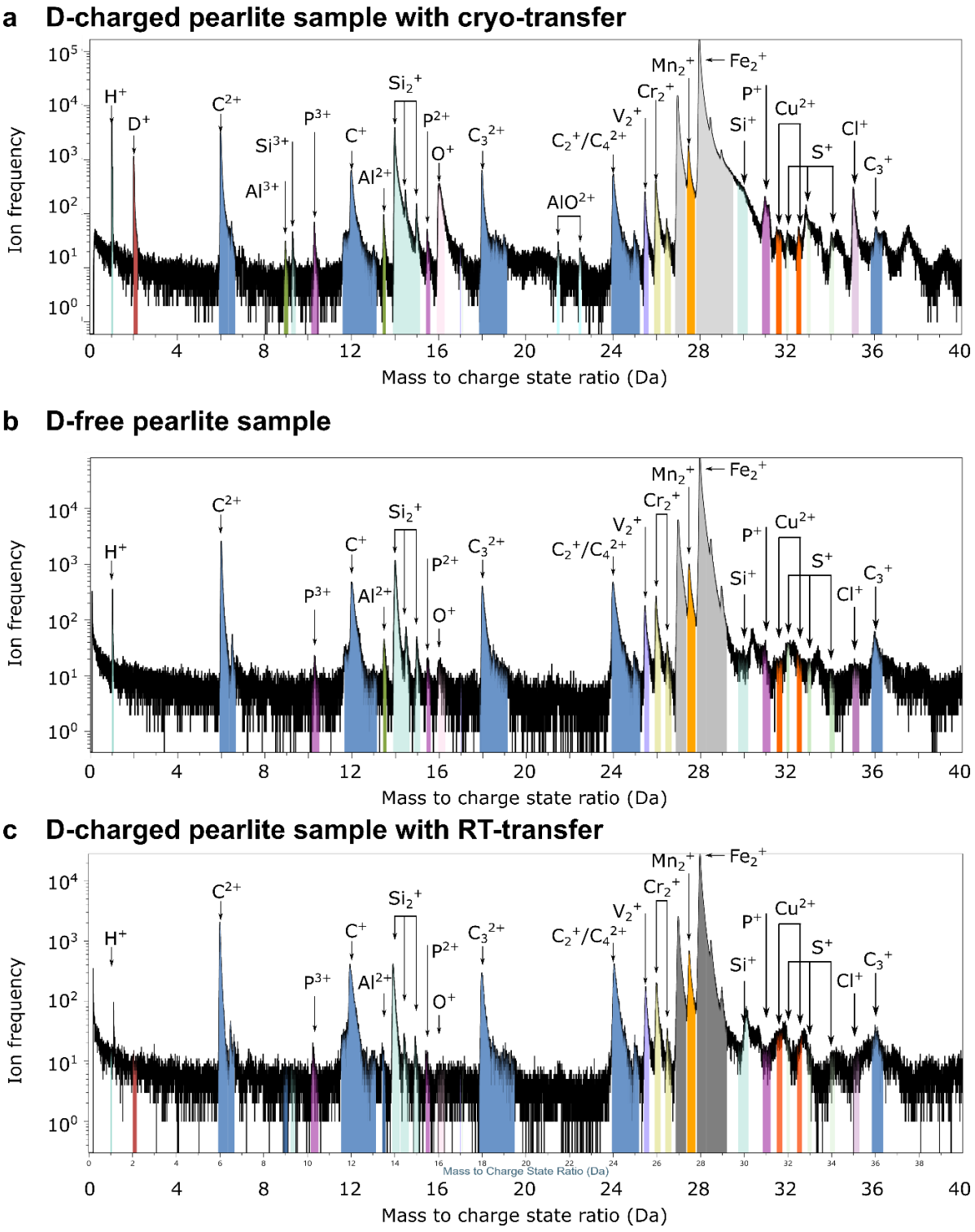

Figure 3.18 Mass spectra in logarithmic scale with ion peaks and ranges labelled from (a) the cryo-transferred D-charged pearlite sample, with a significant peak at 2 Da and (b) the D-free pearlite sample, with no 2 Da peak. Note that the peak at 24 Da were all assigned to C4, to evaluate the maximum C concentration in our APT data. Mass spectrum (c) no 2 Da peak in a D-charged pearlite sample, which was transferred at room temperature. Data credit: Dr Ranming Niu

APT tip specimens were prepared by using a two-step process, which includes a pre-sharpening electropolishing stage followed by FIB annular milling. The APT specimens were first cut into 15 × 1 × 1 mm matchstick bars. The matchstick bars were then roughly electropolished at the center of the bars, using 10 - 30 V and 25 volume percent perchloric acid in acetic acid to obtain two needle-shape specimens from each bar. Fine electropolishing using 2-volume percent perchloric acid in butoxyethanol solution under the observation of an optical microscope was conducted on each tip. To ensure the presence of cementite within the small APT field of view (approximately 200 - 300 nm from the apex), FIB annular milling was applied as illustrated in Figure 3.19. APT tips with inclined cementite lamellae were targeted to ensure the APT data yield and the deuterium mapping with the best spatial resolution, considering the tips with horizontal lamellae are subject to fracture and the ones with vertical lamellae may lead to ambiguous locations of deuterium at the ferrite-cementite interfaces [240]. The annular milling was also conducted in the ThermoFisher Helios PFIB-SEM, with the rough milling at 30 kV, 4 nA and fine milling at 30 kV, 100 pA, followed by final shaping at 2 kV, 100 pA for targeting the region of interest (ROI) with the inclined cementite lamellae and minimal ion damage. Non-cryogenic-transfer APT experiments were carried out in a CAMECA LEAP 3000X-Si instrument, and the deuterium-charged and cryogenic-transferred specimens were tested in CAMECA LEAP 4000X-Si instrument. All APT experiments used voltage-pulsing mode with a pulse frequency of 200 kHz, a specimen temperature of 50 K, and a pulse fraction of 20%. The reconstruction was conducted in AP Suite (Version 6.1, CAMECA) with the settings of 57% detector efficiency and 1.65 image compression factor.

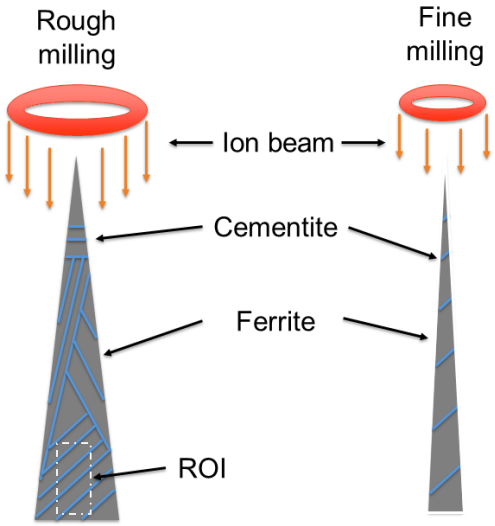

Figure 3.19 Schematic illustrations of APT specimen preparation via annular milling in FIB.

4 Effects of hydrogen on deformation near the ferrite–cementite interface

Conventional pipeline steels such as X42, X52, and X60 are widely used in the existing gas transport network, and their primary microstructures contain a combination of ferrite and pearlite [12, 147]. In these steels, pearlite functions as a strengthener and ferrite provides good ductility [241]. Pearlite contains alternating layers of ferrite and cementite, and reducing the cementite lamellae interlayer distance can effectively increase the strength of pearlite, which can reach a level equivalent to high-strength martensitic steels [34, 242]. As microstructures with higher strength can be more susceptible to HE, hydrogen-induced failure potentially occurs in pearlite, which could then lead to the overall HE of pipeline steels [135, 139]. How hydrogen affects the property of pearlite is important for developing the knowledge of HE in gas pipes, which can lead to a pipeline materials design strategy for low HE susceptibility in hydrogen transmission.

In pipeline steels, hydrogen is thought to be more likely to be trapped in pearlite than in ferrite, particularly at ferrite-cementite interfaces, since the sites were considered to have more free space to accommodate hydrogen atoms [57, 86, 87]. Despite the fact that ferrite-cementite interfaces have been reported to be weak traps, hydrogen localized at the interfaces has been considered to cause HEDE and subsequent HE of pipeline steels [140, 178]. A detailed study to clarify the role of ferrite-cementite interfaces in hydrogen trapping is required. Also, due to the presence of ferrite in pearlite, other HE mechanisms relating to ferrite, such as HELP, can play a role in the HE of pearlite. Literature has suggested it is possible that more than one mechanism can operate simultaneously [243]. As such, an in-depth analysis to clarify the origin of HE in pearlite will be valuable for a better microstructural design of pipeline steels, which is the focus of this chapter.

4.1 Characterization of pearlite sample microstructure

Characterization by SEM-EBSD, TKD, TEM, and APT was employed to measure the pearlite sample microstructure before the in-situ micromechanical specimen fabrication and testing. These analyses provide valuable information such as grain size, cementite lamellar textures, volume fraction of ferrite and cementite, their orientation relationships, the incorporated ferrite-cementite interface structure, and cementite chemical compositions. Given that crystal orientation relationships between ferrite and cementite have multiple possibilities (Table 2.1),

having a clear knowledge of how cementite lamellae are orientated in the ferrite matrix is useful for preparing the micropillars with the ability to control cementite lamellar orientation.

Figure 4.1a shows low-magnification inverse pole figure (IPF) EBSD maps of a pearlite sample using a scanning step size of 100 nm. The average grain size measured in the EBSD software is 4.1±3.0 μm, with maximum and minimum grain sizes of 31.5 μm and 1.8 μm, respectively. This means that each pearlite grain can only produce one micropillar, considering each micropillar requires a trench of 10 μm in diameter (Section 3.3.2). As per Figure 4.1a, the bulk sample has little directional grain texture, but some strain from hot rolling may be present in some grains. This can be seen by the gradually varied colors where pre-strain exists. As pre-existing strains can lead to the presence of dislocations that can introduce variance in the mechanical performance of microscale samples [244], the pearlite grains with pre-strain were not used to fabricate micropillars in this thesis. Figure 4.1b is the phase map of the pearlite specimen, which suggests the grains have BCC ferrite matrix and no large cementite (Fe_3C) or residual (FCC) austenite can be detected at this scanning resolution. Some pores were seen as in Figure 4.1b, which were avoided in the micropillar fabrication. {100}, {110}, and {111} pole figures are presented in Figure 4.1c, which agrees well with the random crystallographic orientation observed in Figure 4.1a.

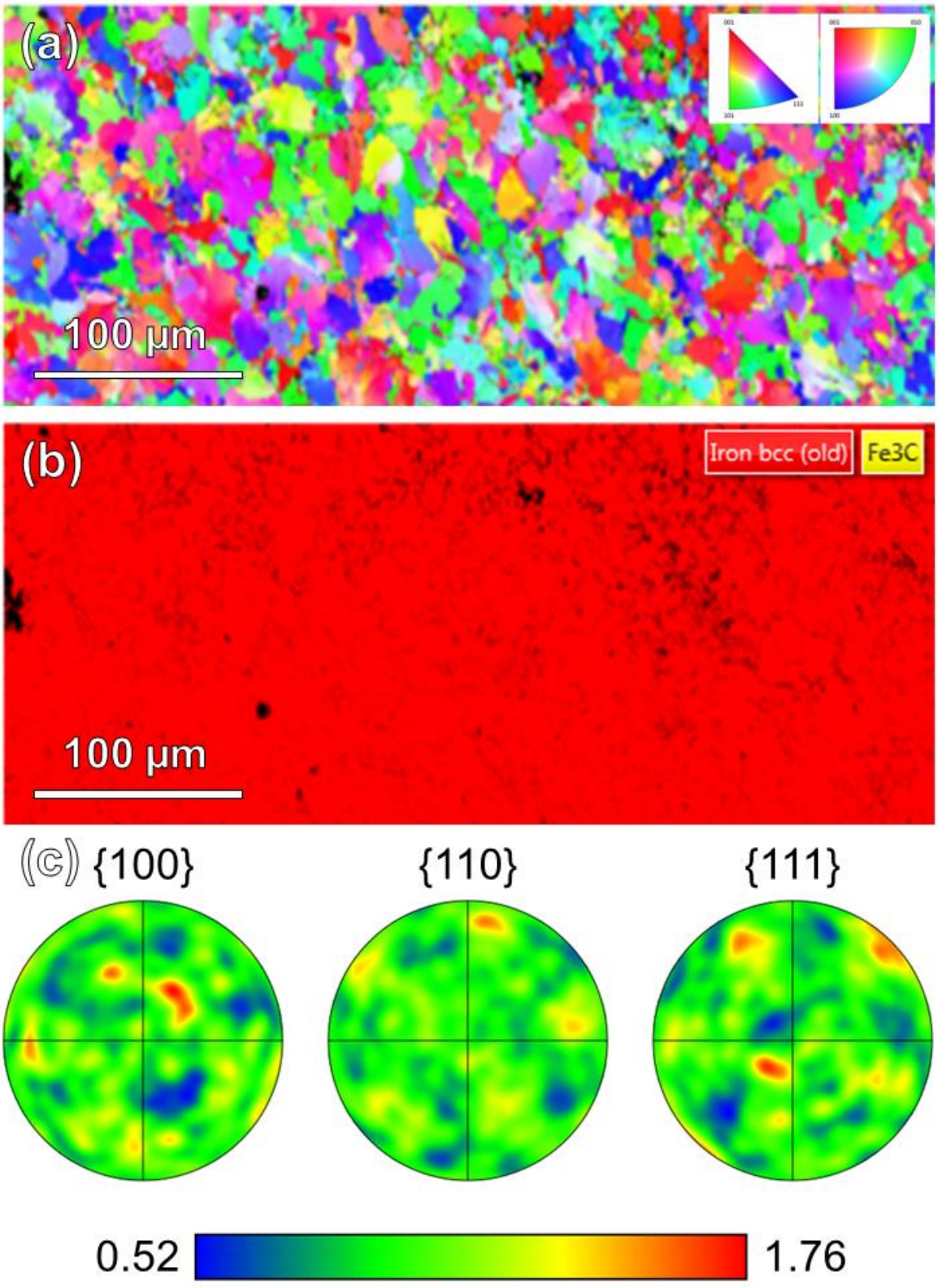

Figure 4.1 EBSD results showing the crystalline and elemental information of the bulk ferrite-pearlite sample: (a) IPF map along the z direction, (b) corresponding phase distribution map, and (c) the pole figures of {100}, {110}, and {111} directions.

Figure 4.2a is a low-magnification SEM image of the pearlite samples before the preparation of in-situ micromechanical testing micropillars, showing a large proportion of pearlite and a small proportion of proeutectoid ferrite, which are consistent with the results in Figure 4.1. This was expected since the carbon content of the sample (0.44%) is much higher than the 0.022 wt.% carbon solubility in ferrite (Figure 2.1). A higher magnification image of a pearlite grain is displayed in Figure 4.2b, which shows that the distance between cementite lamellae is approximately 100 nm. Note that the cementite lamellae are a three-dimensional (3-D) structure so the interlamellar distance measured from the surface might not represent the buried 3-D structure. For this reason, we choose the samples with the smallest spaced lamellar to describe the spacing, as these are assumed to be perpendicular to the surface, but precise measurement of interlamellar distance and the width of cementite requires using TKD or TEM. Figure 4.2a also showed that not all the cementite lamellae were continuous in the pearlite grains. Even where continuous cementite lamellae are observed on the sample surface, discontinuous lamellae can be buried in pearlite grains, evidenced by using TKD (Figure 4.3a). Discontinuous cementite lamellae are found in regions of low local carbon concentration and low transformation temperature, commonly seen in commercial ferrite-cementite steels [245]. Discontinuous cementite lamellae may facilitate the growth of lattice defects (e.g., voids or dislocation cores) and stress localization during straining experiments [246]. As such, the pearlite grains selected for micropillar preparations were those with the highest cementite continuity in the SEM image. Further examinations after FIB cross-sectioning (Section 3.3.2) were conducted to ensure the best cementite continuity in the pearlite micropillars.

TKD analysis on a thin-foil sample fabricated by FIB with a step size of 5 nm was used to better resolve the pearlitic microstructure containing fine cementite lamellae, as shown in Figure 4.3. Figure 4.3a, b, and c are the secondary electron image, the IPF, and the phase maps, respectively. Within a pearlite grain in $\{111\}_{\text{ferrite}}$ direction, although the cementite lamellae are visible in the secondary electron image (Figure 4.3a), there is very little signal of cementite detectable in the phase map (Figure 4.3c). This difficulty of indexing fine cementite lamellar using EBSD has been reported in former literature [247, 248]. Some cementite particles segregated along GBs can be detected in the yellow regions of Figure 4.3c. Figure 4.3d exhibits the stereographic projection in $[111]_{\text{ferrite}}$ and $[010]_{\text{cementite}}$ orientation, suggesting an Isaichev orientation relationship (Table 2.1), i.e., $(\bar{1}03)_{\text{cementite}}$ // $(0\bar{1}1)_{\text{ferrite}}$ as highlighted in Figure 4.3a with a red arrow.

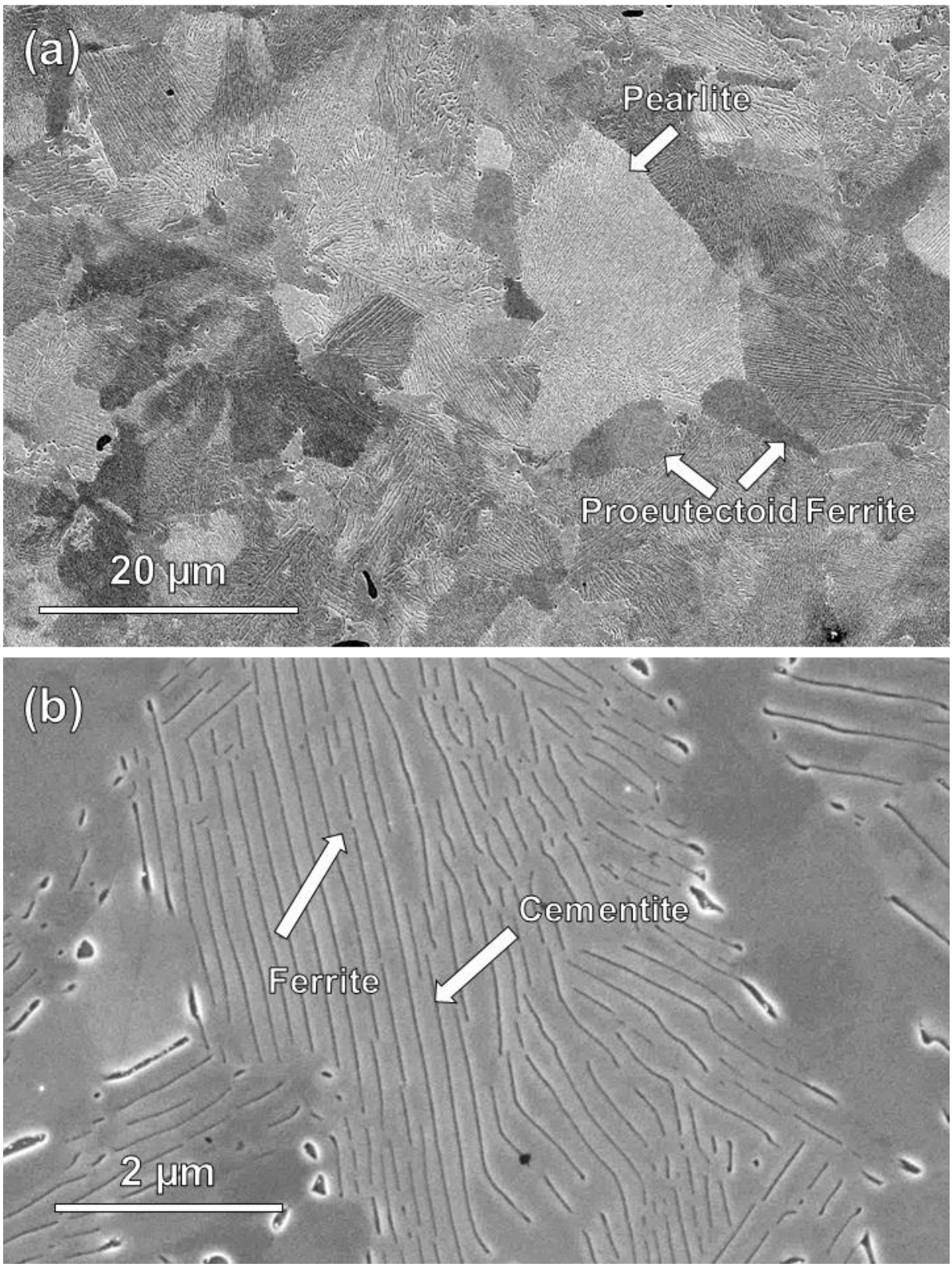

Figure 4.2 SEM images of pearlite steel samples: (a) a low-magnification image showing pearlite and some ferrite grains and (b) a high-magnification image of ferrite and cementite (dark lines) in pearlite.

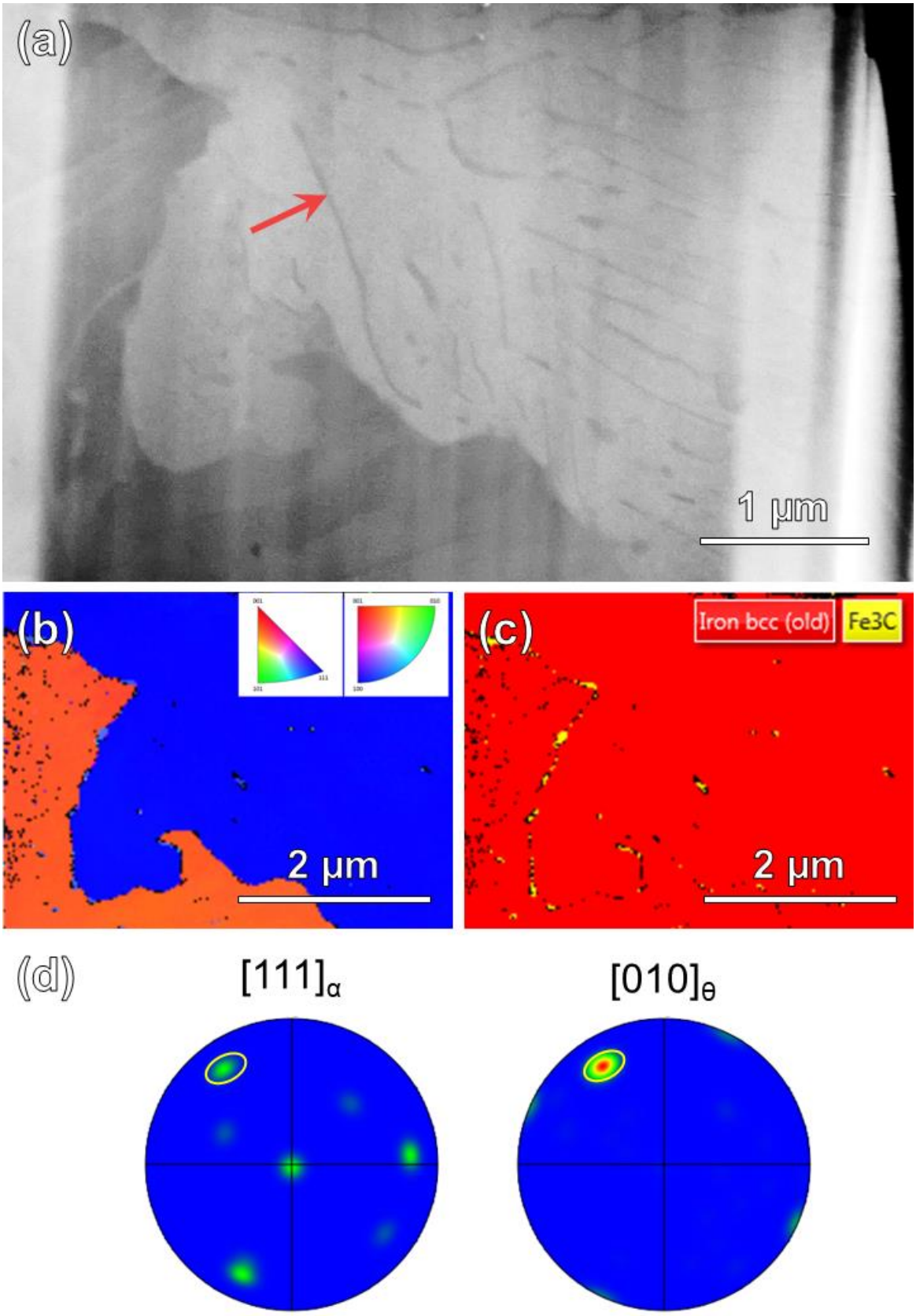

Figure 4.3 TKD maps a thin-foil pearlite sample: (a) secondary electron image of the thin-foil pearlite sample, (b) IPF map of the pearlite grain, (c) phase map, and (d) stereographic projection in the orientations of [111] of ferrite and [010] of cementite.

To better resolve the nanosized cementite lamellae, selected area electron diffraction (SAED) TEM imaging was employed, leading to the results in Figure 4.4. Figure 4.4a is a bright-field TEM image of the pearlitic microstructure, which was taken along the [111] zone-axis of ferrite. As highlighted by the white arrows, cementite strips in a darker contract than ferrite can be seen, and the thickness of cementite lamellae and interlamellar distance can be measured by combining the statistics of multiple TEM images, which are 102±3 nm and 14±2 nm, respectively. A SAED pattern is presented in the inset of Figure 4.4a, which is used to determine the orientation relationship between ferrite and cementite as $(101)_{\text{cementite}} // (11\bar{2})_{\text{ferrite}}$ and $[010]_{\text{cementite}} // [111]_{\text{ferrite}}$, i.e., the Isaichev relationship (Table 2.1). A HAADF-STEM image on a ferrite-cementite interface was also taken as shown in Figure 4.4b, suggesting a high coherency of the interface.

APT was conducted on a tip incorporating an inclined cementite lamella to measure the cementite composition. A 3-D reconstructed atom map is shown in Figure 4.5a where iron and carbon atoms are marked in grey and blue, respectively. Figure 4.5b provides a 10 nm thickness slice view along the x-z plane of the dataset from the ROI highlighted by the black dashed lines in Figure 4.5a. As shown in Figure 4.5c, a 1-D elemental concentration profile was extracted from the ROI highlighted by the grey dashed lines in Figure 4.5b. In the center region in the 1-D profile (Figure 4.5c), a decrease of iron concentration and an increase of carbon concentration were observed, corresponding to the presence of cementite in the sample. Approximately 22% carbon was measured at the peak of the concentration profile in Figure 4.5c. This carbon concentration is lower than the nominal 25% carbon content in cementite (Fe_3C), which is possibly due to a combined effect of the presence of carbon vacancies and the limit of APT on carbon quantification as reported in former literature [236, 240]. This result will be discussed in detail later in this Chapter.

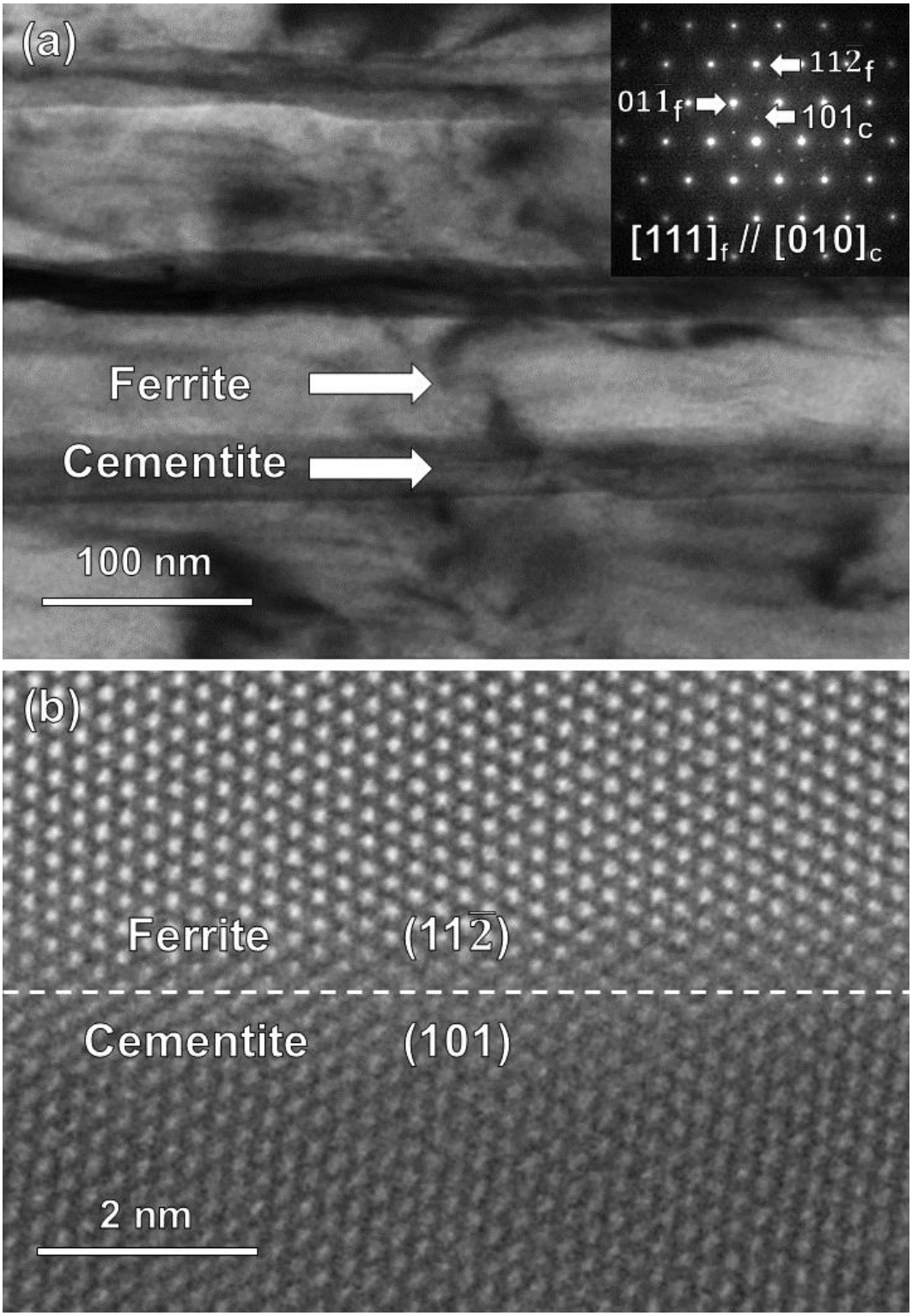

Figure 4.4 TEM observations of the ferrite-cementite interface: (a) Bright-field TEM image of a pearlite microstructure comprised of alternating ferrite and cementite lamellae. Corresponding selected area diffraction pattern of the ferrite-cementite interface along the $[111]_f$ zone axis is given in the inlet. (b) High resolution HAADF-STEM image of the ferrite-cementite interface in the pearlite.

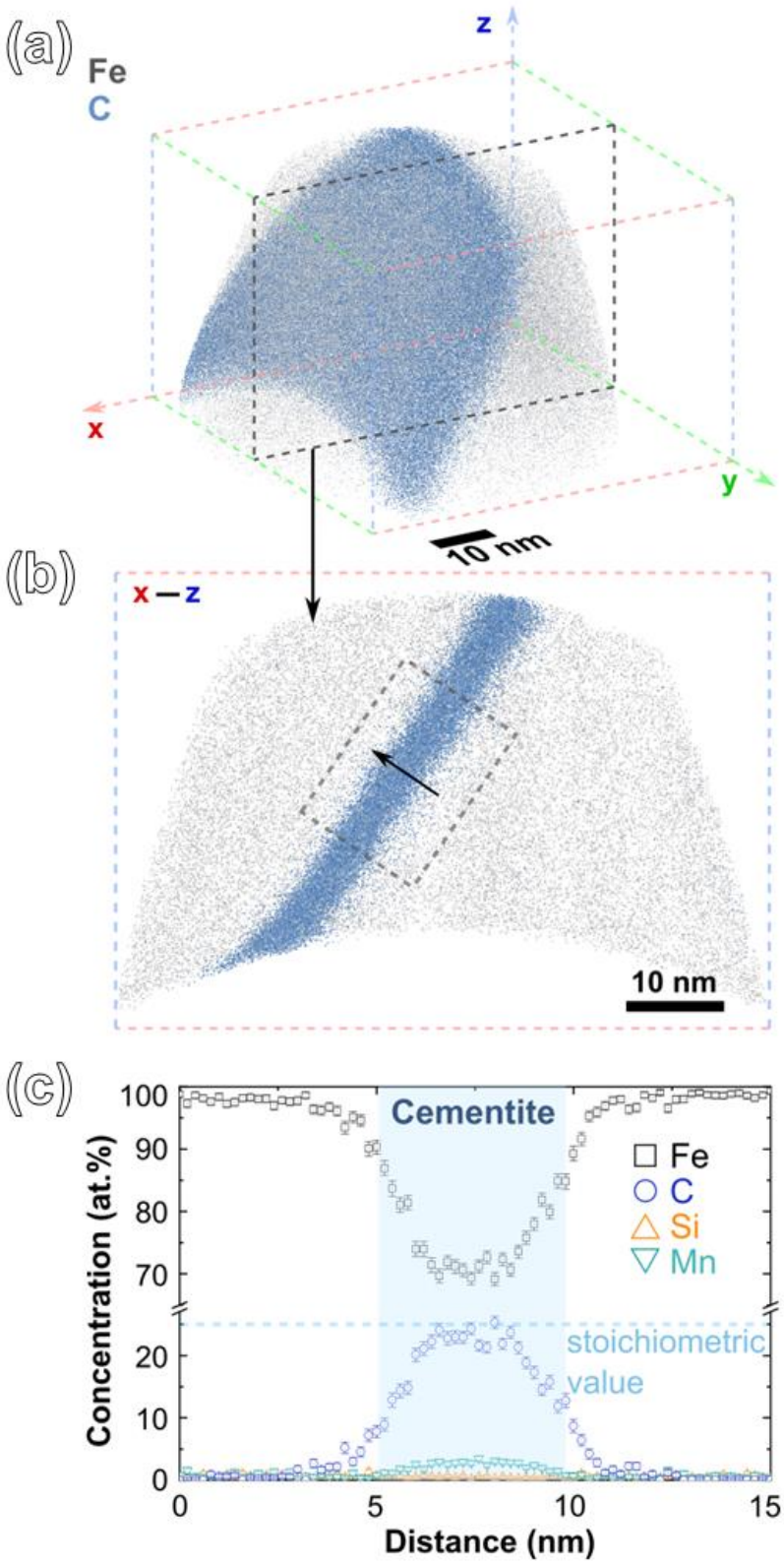

Figure 4.5 APT atom map of the pearlite: (a) APT 3D reconstruction of the ferrite-cementite interface, (b) a side x-z view with 10-nm thick slice from the region marked in (a), and (c) a 1D concentration profile from the regime marked in (b) with the size of size of 15(L) x 20(W) x 20(H) nm^3 along the direction marked with an arrow. Data credit: Dr. Ranming Niu

4.2 Fabrication of micropillars with inclined cementite lamellae

The aim of the micromechanical testing presented in this chapter is to investigate the effects of hydrogen on the ferrite-cementite interface cohesion in pearlite. It is hypothesized that hydrogen-enhanced interface decohesion (or HEDE) and/or hydrogen-enhanced slipping (or HELP) in ferrite could play a role in the hydrogen-enhanced deformation of pearlite. As such, an aim here is to compress the micropillars with 45-degree inclined cementite lamellae and to examine the deformation around the ferrite-cementite interfaces, as schematically illustrated in Figure 4.6b. This 45-degree inclination of cementite in micropillars creates the largest shear stress on the interfaces when a flat punch applies a force on a micropillar (Figure 3.8), and we expect that most of the slip is located near the interfaces.

Effective fabrication of micropillar specimens that contain 45-degree inclined cementite lamellae is the key to delivering meaningful analyses here. Given that the material contains the cementite with a certain orientation relationship with ferrite, $[010]_{cementite}$ // $[111]_{ferrite}$ (Figure 4.4), it is possible to determine the cementite lamellae direction within a ferrite grain from the crystal orientation of the ferrite grains, which can be obtained using EBSD. As shown in Figure 4.6a, which is an IPF map in the z direction, it is found that the pearlite grains with $<110>_{ferrite}$ from this view are likely to contain micropillars with the desired 45-degree cementite orientation (highlighted by a dashed line in Figure 4.6c). We examined multiple pearlite grains and found that the knowledge of the $[010]_{cementite}$ // $[111]_{ferrite}$ orientation relationship is extremely useful in the fabrication of the micropillars with any desired cementite orientations, underpinning the specimen preparation in this thesis. The flat punch setup (Figure 3.8) for this type of micropillar specimen will lead to the mechanical load applied in the direction <110> with respect to the pearlite (ferrite) matrix, and the cementite lamellae will have an angle of α with the load direction, as shown in Figure 4.6b.

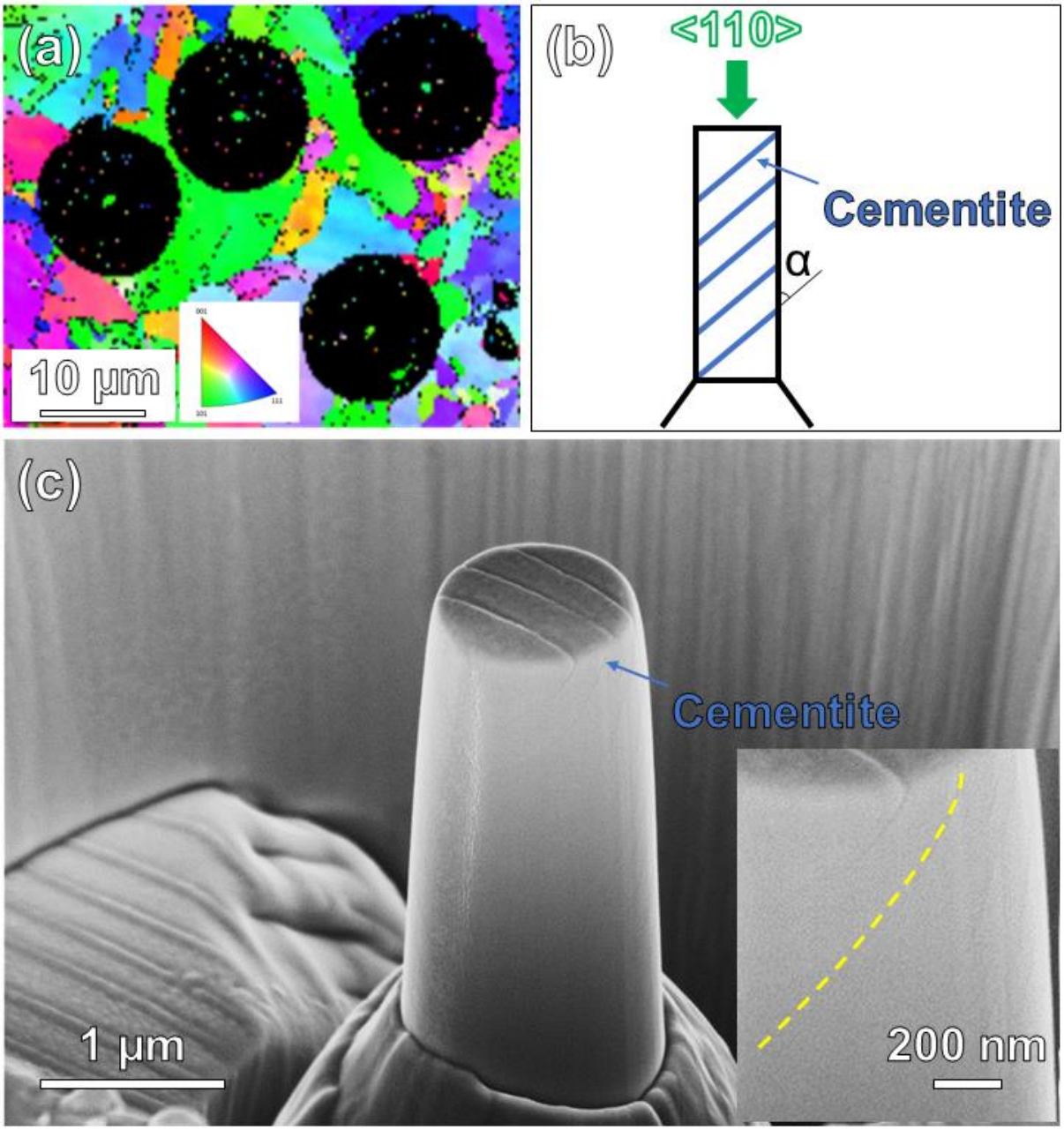

Figure 4.6 Strategy for micropillar fabrication: (a) EBSD results of the micropillars milled on a bulk sample, (b) a schematic illustration of a pearlite micropillar with desired cementite configuration., (c) a SEM image of a pearlite micropillar. The marked cementite lamella in (c) is highlighted with the yellow dashed line in the magnified inlet SEM image.

4.3 Hydrogen desorption during testing in vacuum

After electrolytic hydrogen charging of the SEM specimen with prefabricated micropillars (Section 3.4), hydrogen desorption occurs. Of course, the presence of hydrogen is required to correlate the changes of micropillar mechanical properties with HE. An important assumption

in this thesis is that the bulk specimen can function as a reservoir of hydrogen, allowing the supply of hydrogen during the micromechanical tests. As hydrogen desorption is time-sensitive, the duration of time from commencement to completion of the micromechanical experiments is a key factor in ensuring the presence of sufficient hydrogen for inducing HE in the micropillars. By conducting several dummy runs, we determined that approximately 30 minutes is required to set up the micromechanical experiments (including sample mounting and SEM chamber pumping) until the commencement of the first micropillar after 1-hour of hydrogen charging. Considering a single SEM access session is 4 hours in our laboratory, we aimed to determine the hydrogen desorption profile in the time window between 30 minutes and 4 hours. These experiments were conducted on bulk sheet specimens with identical geometry and dimensions as the sample for micromechanical testing in SEM.

Three TDA experiments were conducted to examine the presence the hydrogen in the bulk specimen (therefore micropillars) after hydrogen desorption in a vacuum environment similar to that of the SEM. The results are shown in Figure 4.7. The blue circles are the data from the 1-hour hydrogen-charged sample after 30 minutes of desorption in vacuum. The red triangles are the data from the sample that was 1-hour hydrogen-charged and placed in vacuum for 4 hours. The black squares are the data from an uncharged sample, representing a hydrogen-free reference. There are desorption peaks at about 100 °C for both the 30-minute-desorbed and 4-hour-desorbed samples. No desorption peak can be observed at a temperature higher than 350 °C. The measured hydrogen contents of 30-minute desorption, 4-hour desorption, and uncharged specimens are 0.137, 0.035, and 0.017 part per million in weight. These results suggest the bulk specimen retains a reasonable amount of hydrogen for a duration between 30 minutes and 4 hours, thought to be sufficient to influence deformation behaviour, confirming the presence of hydrogen during the micromechanical testing in the SEM.

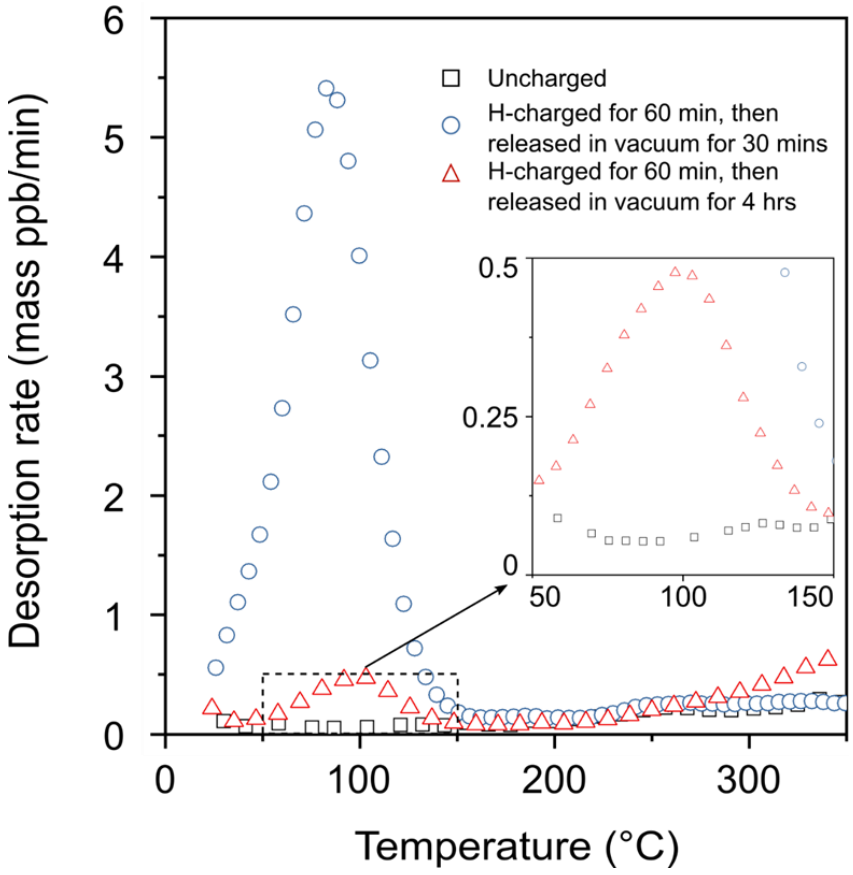

Figure 4.7 Thermal desorption analyses at bulk ferrite-cementite samples: uncharged specimen (black), a hydrogen-charged specimen (blue), and a hydrogen-charged and desorbed specimen (red) for four hours to simulate micro-compression conditions. Data credit: Mr. Pang-Yu Liu

4.4 In-situ micromechanical testing

Micro-compression tests with in-situ SEM observation were conducted on both hydrogen-charged and uncharged micropillars. The original data included load and displacement in real time, which were processed into engineering stress (σ) and strain (ε) following the formula below:

$$\sigma = \frac{F}{A} = \frac{4F}{\pi D^2}$$

$$\varepsilon = \frac{h \times k}{L} \times 100\%$$

where F and h are the load and displacement, respectively, applied in the compression tests. D and L are the diameter and height of the micropillar extracted from the SEM images of micropillars prior to the tests (such as Figure 4.6c). k is the normalized displacement based on the following formula:

$$k = \frac{h_2 - h_1}{l_2 - l_1}$$

where h_1 and h_2 are the start and end displacement in a test, respectively. l_1 and l_2 are the height of micropillars before and after a test, respectively. The engineering stress (σ) was further converted to resolved shear stress by considering the α angle between the loading direction and the nominal slip planes (Figure 4.6b), mostly likely the {112} planes of ferrite as per the result of Figure 4.4. The value of α in a test was measured in the cross-sectional images of deformed micropillars (Figure 4.14a).

Figure 4.8a is an overview of all of the stress-strain curves for uncharged (left figure) and hydrogen-charged (right figure) micropillars containing the cementite lamellae at close to a 45-degree angle with respect to the loading direction. Detecting the first deviation point in the stress-strain curves is challenging due to variations in the elastic slope caused by micropillar misalignment [249]. The yield stress is determined by selecting the stress at the first significant strain burst (≥ 0.2% plastic strain) or substantial deflection from the initial elastic stage (around 0.2% plastic strain) which aligns with the traditional criteria of 0.2% offset plastic strain [250]. The overall compression strain levels are set as 10±2% to guarantee sufficient plastic deformation. Generally, the hydrogen-charged specimens have lower yield stresses (marked by the red arrow in Figure 4.10a) than those of the uncharged specimens (marked by black arrow in Figure 4.9a). The average values of yield stress for all the shown curves in this definition are provided in Table 4.1. The yield strengths of uncharged and hydrogen-charged data are 954±99 and 498±36 MPa, respectively. The presence of hydrogen led to a decrease of yield strength of approximately 48%.

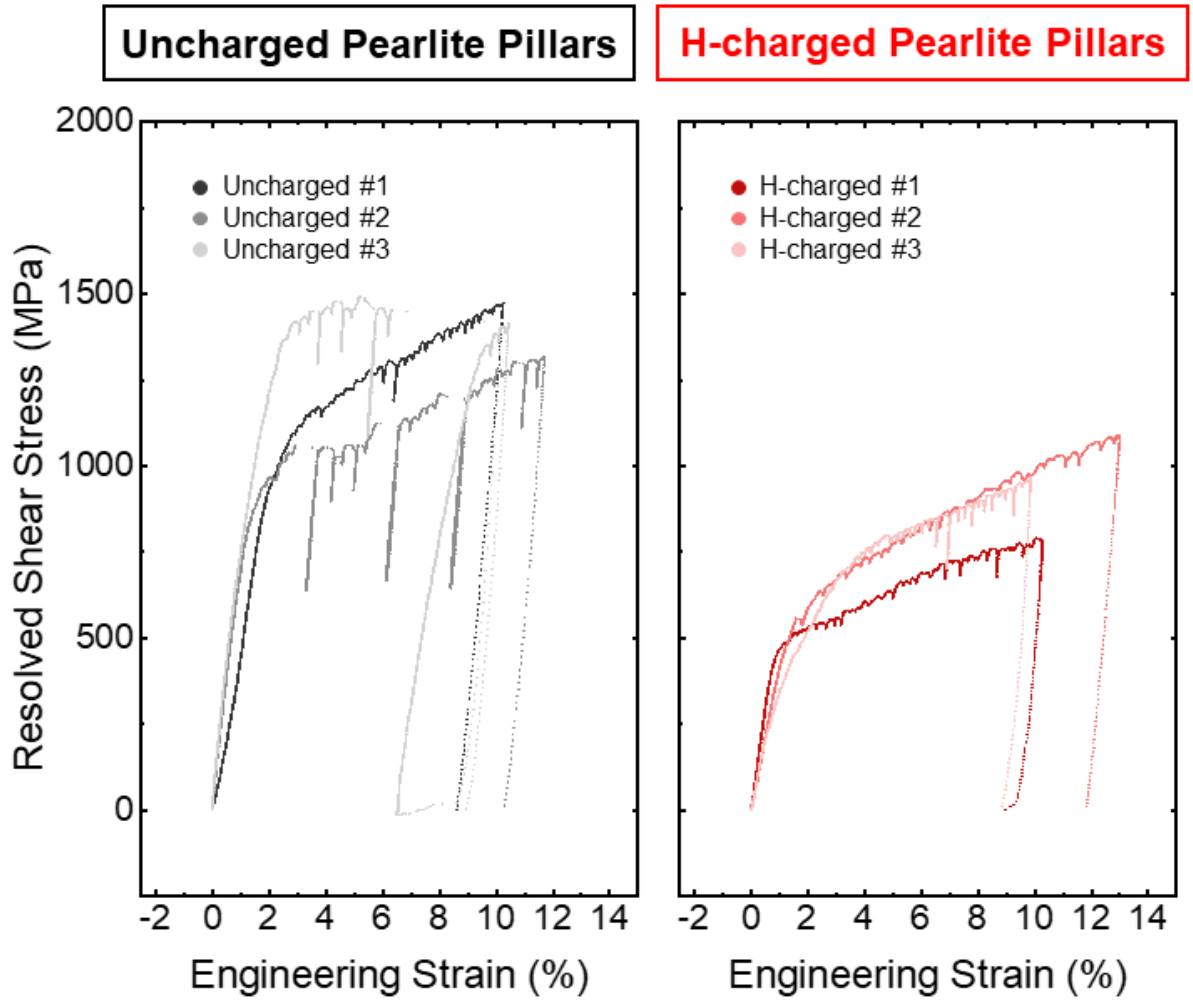

Figure 4.8 Resolved shear stress versus engineering strain dataset of three representative hydrogen-charged and uncharged micropillars.

Table 4.1 Statistics of the micromechanical testing results containing five micropillars tested for each uncharged and hydrogen-charged specimen and the errors correspond to the standard deviations (±SD) of the tests.

Charging states	**Yield stress (MPa)**
Uncharged	954±99
H-charged	498±36

Figure 4.9 and Figure 4.10 are representative stress-strain curves and low-resolution SEM images at various stages of deformation for an uncharged specimen and a hydrogen-charged specimen, respectively. In Figure 4.9a, multiple major strain bursts and corresponding reductions of load resistance are observed and marked with b, c, and d, which correspond to Figure 4.9b, c, and d, respectively. In Figure 4.9b, c, and d, one can see a few major slip regions,

highlighted by the white arrows, which contribute to the majority of the strain. The strain bursts are likely due to the accumulation and release of dislocations at slip obstacles [251]. In contrast, the stress-strain data from the hydrogen-charged micropillar, Figure 4.10a, showed a more continuous straining process with fewer sudden strain bursts (Figure 4.9a). In the observation of the pillar as strain develops(Figure 4.10b, c, and d), one can see more slip bands and less sharp ridges, which are highlighted by white arrows. This result suggests that a larger number of dislocation slip bands are activated in the presence of hydrogen. This phenomenon may be a result of the HELP mechanism in the ferrite regions. More details about deformation mechanisms are provided in the TEM analysis in a later section.

It is established that HE is a reversible phenomenon, i.e., the mechanical properties of materials can return to those in the absence of hydrogen once the hydrogen is fully desorbed [252, 253]. As such, experiments were conducted to examine the deformation behaviors of an uncharged micropillar and a hydrogen-charged and fully desorbed micropillar. The latter should behave similarly to the former if the observed property change in Figure 4.9 and Figure 4.10 is a result of HE. This helps to rule out that the effects observed are the result of surface damage or corrosion. The hydrogen-released specimen was left in the SEM vacuum chamber overnight (over 8 hours) to fully desorb the charged hydrogen. Figure 4.11a and b are cross-sectional views of compressed micropillar microstructures with similar slips from hydrogen-released and uncharged specimens, respectively. Figure 4.11c displays the stress-strain curves of both specimens, showing the yield strengths and strain bursting are very similar in the two specimens (unlike the smooth slipping seen in Figure 4.10 from the specimen containing hydrogen).

Figure 4.9, Figure 4.10, and Figure 4.11 provide evidence of the effectiveness of our electrolytic hydrogen charging, in addition to the TDA result (Figure 4.7). These results lead to the conclusion that the introduction of hydrogen can influence the stress–strain curves and deformation behaviors of the micropillars. A new technique has been established in this project that can be applied to many different materials to probe the deformation response in hydrogen for specific microstructural features or phases.

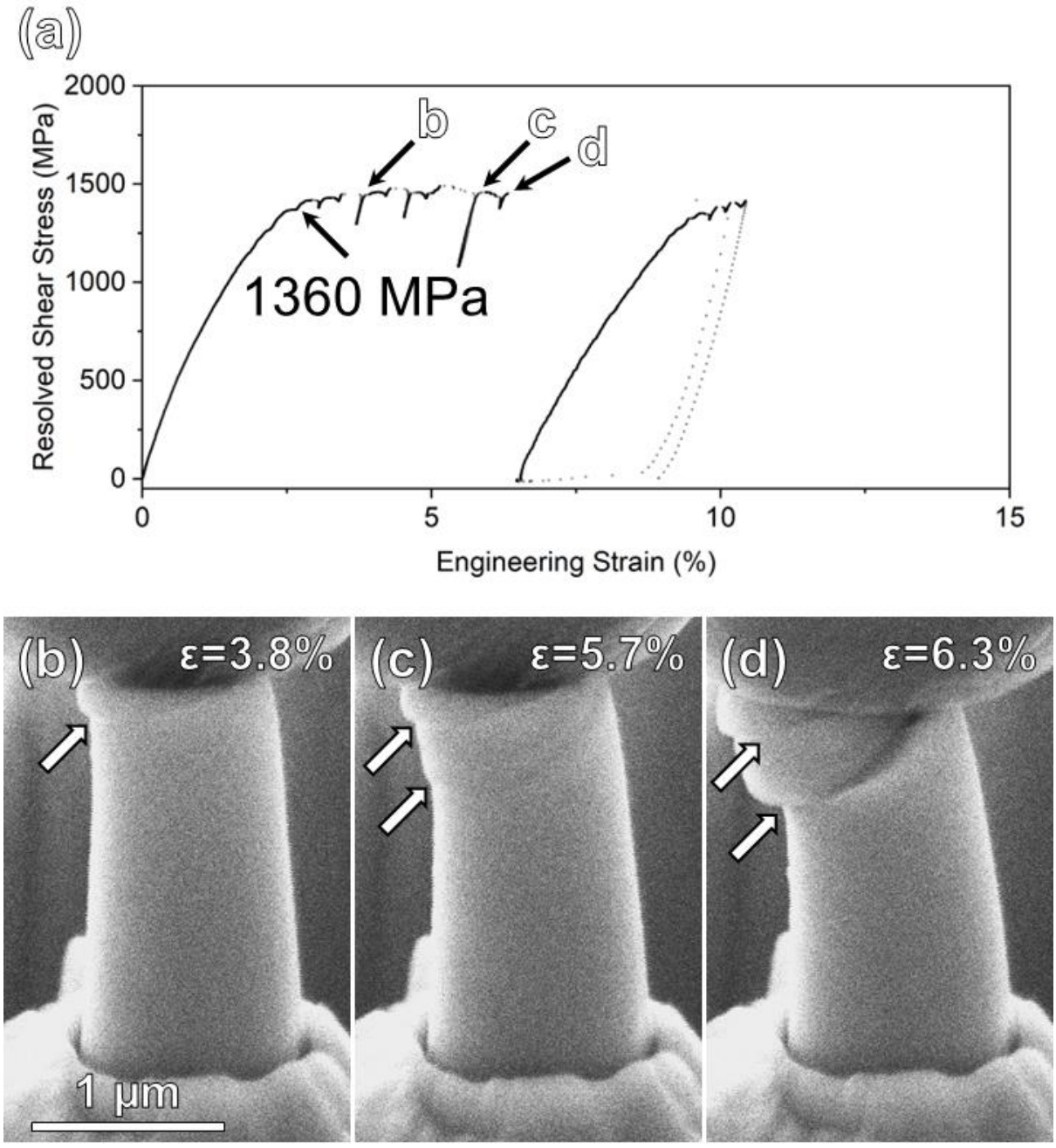

Figure 4.9 In-situ compression testing results on an uncharged pearlite micropillar, corresponding to the "Uncharged #3" curve in Figure 4.8: (a) shear stress resolved from the engineering stress as a function of engineering strain, (b), (c), (d) SEM snapshots taken from the in-situ video which are indicated on (a). The corresponding engineering strain is marked at the top-right corner. The arrows in the figures indicate slip bands at the marked strains.

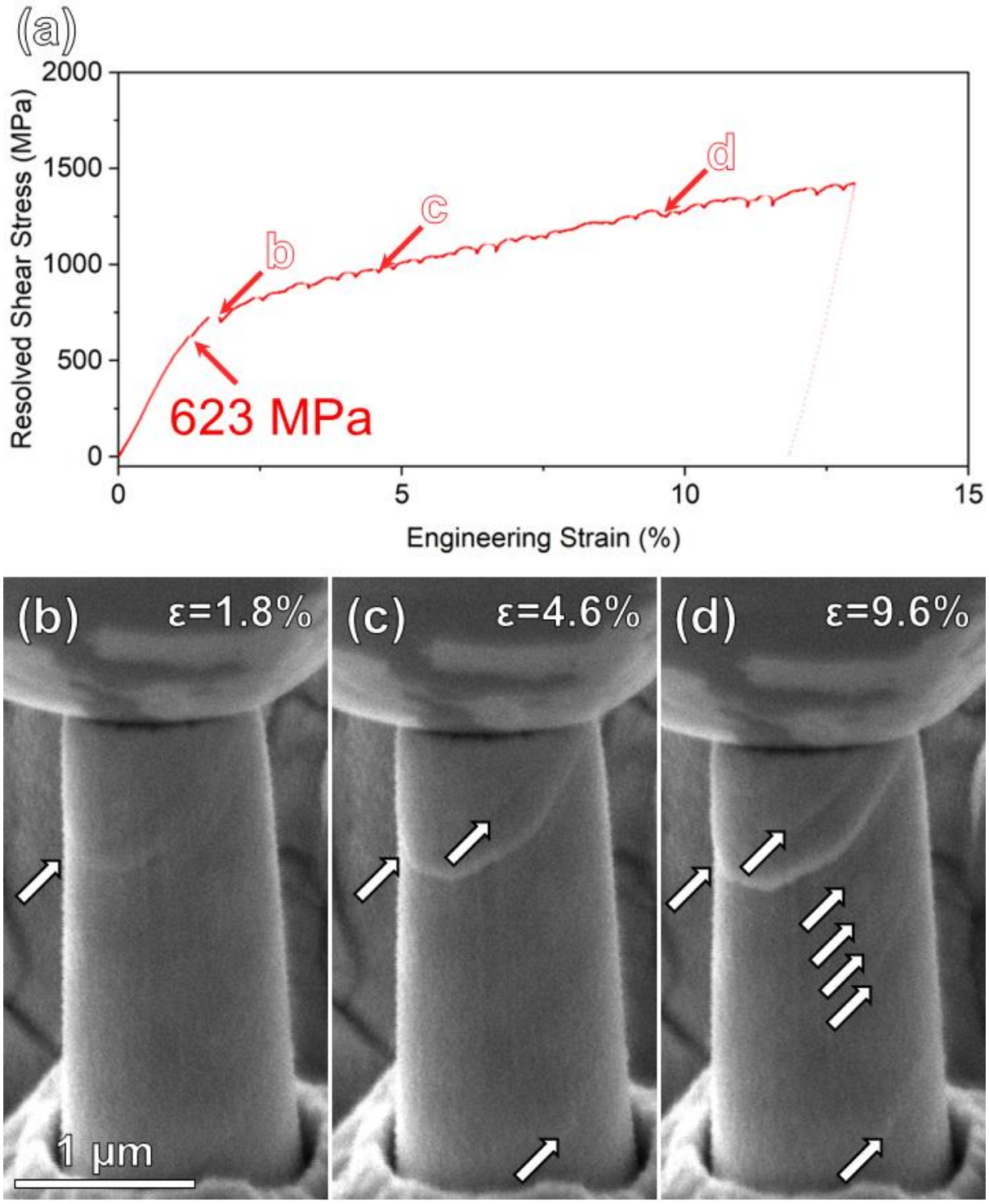

Figure 4.10 In-situ compression testing results on a hydrogen-charged pearlite micropillar, corresponding to the "H-charged #2" curve in Figure 4.8: (a) shear stress resolved from the engineering stress as a function of engineering strain, (b), (c), (d) SEM snapshots taken from the in-situ video which are indicated on (a). The corresponding engineering strain is marked at the top-right corner. The arrows in the figures indicate slip bands at the marked strains.

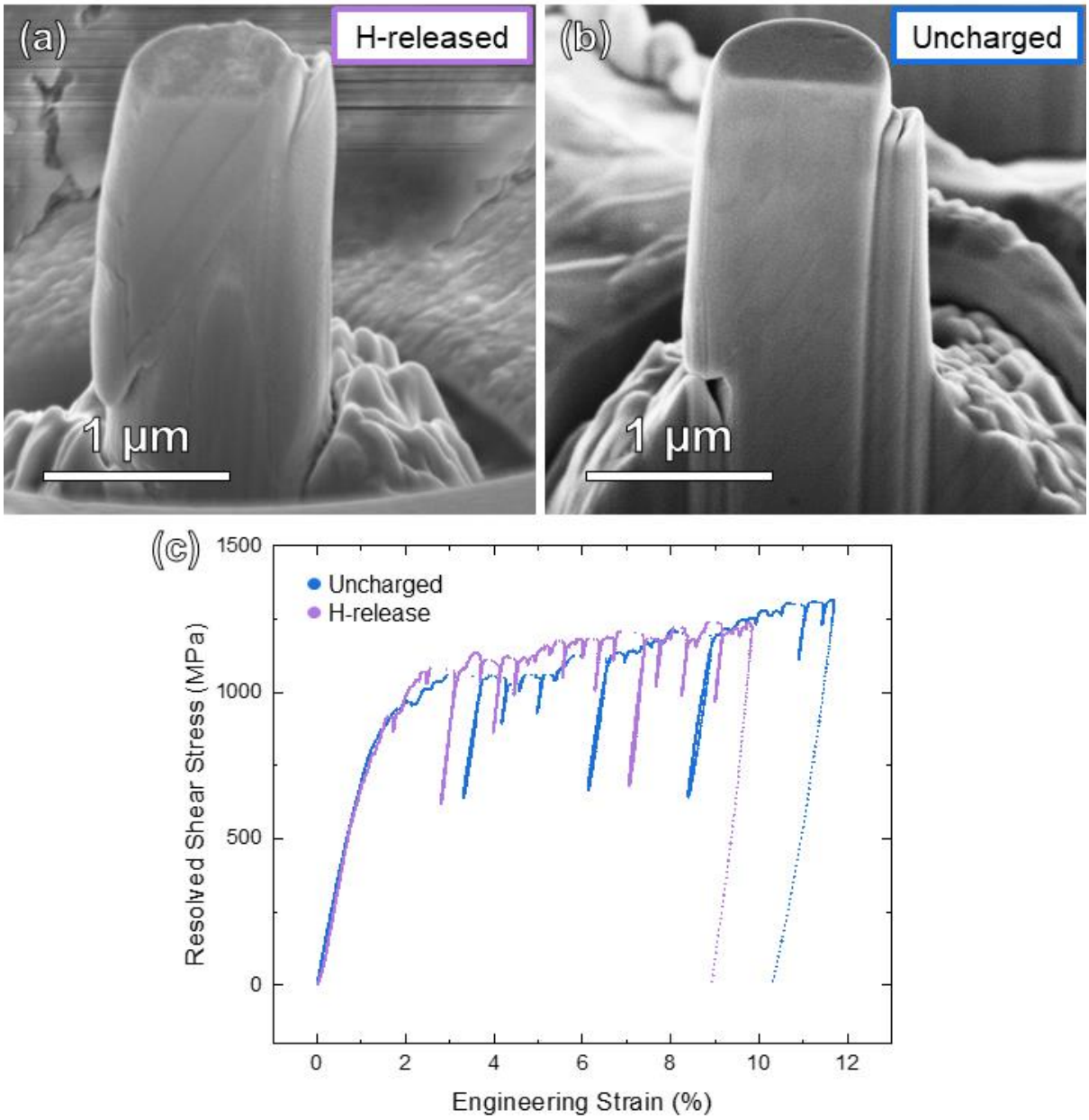

Figure 4.11 In-situ micromechanical testing on uncharged and hydrogen-released pearlite micropillars: SEM images on the cross-sections of (a) a hydrogen-released and (b) uncharged micropillars after compression. (c) are the stress-strain curves of the micropillar specimens.

4.5 Hydrogen distribution near the ferrite–cementite interface

In order to measure the distribution of hydrogen in the pearlite microstructure, for correlation with the micropillar compression results, APT using deuterium charging and cryogenic sample transfer was employed, leading to the results in Figure 4.12 and Figure 4.13. Figure 4.12a is a 3-D reconstructed atom map of a deuterium-charged tip with deuterium, carbon, and iron atoms in red, blue, and grey, respectively. The carbon-rich region corresponds to a cementite lamella

captured during FIB tip fabrication (Section 3.7) and the low-carbon region corresponds to the ferrite matrix. Figure 4.12b is a 10-nm-thick slice from the region marked by black-dashed line in Figure 4.12a, which is normal to the cementite lamella. In this view, one can see deuterium enrichment in both the cementite lamella and the ferrite region away from the interface, but not at the ferrite–cementite interface, highlighted by the black arrows.

Figure 4.12c is a 1-D concentration profile from a ROI perpendicular to the cementite lamella, marked by c in Figure 4.12a. Figure 4.12c shows a deuterium depletion area in the matrix near the interface. This indicates that there is little deuterium segregated at the ferrite–cementite interface, suggesting the interface does not trap hydrogen in this sample. In contrast, a high concentration of deuterium is found within the cementite lamella, suggesting it is a strong hydrogen trap. Deuterium is also found within the ferrite matrix, at a lower concentration than is observed in the cementite, but still three orders of magnitude higher than the hydrogen solubility in pure iron (only tens of atomic ppm). This suggests the presence of trapped hydrogen in ferrite lattice defects (most likely dislocations not otherwise visible in APT, which is a chemical mapping technique). To demonstrate data reproducibility, a repeat experiment was conducted, shown in Figure 4.13. A similar deuterium depletion was observed near the ferrite-cementite interface, confirming the lack of hydrogen trapping at these interfaces.

In summary, the hydrogen atoms are located mostly within ferrite and cementite, not at the ferrite–cementite interface. As such, the hydrogen-enhanced deformation behavior most likely takes place in either ferrite or cementite, where hydrogen is present.

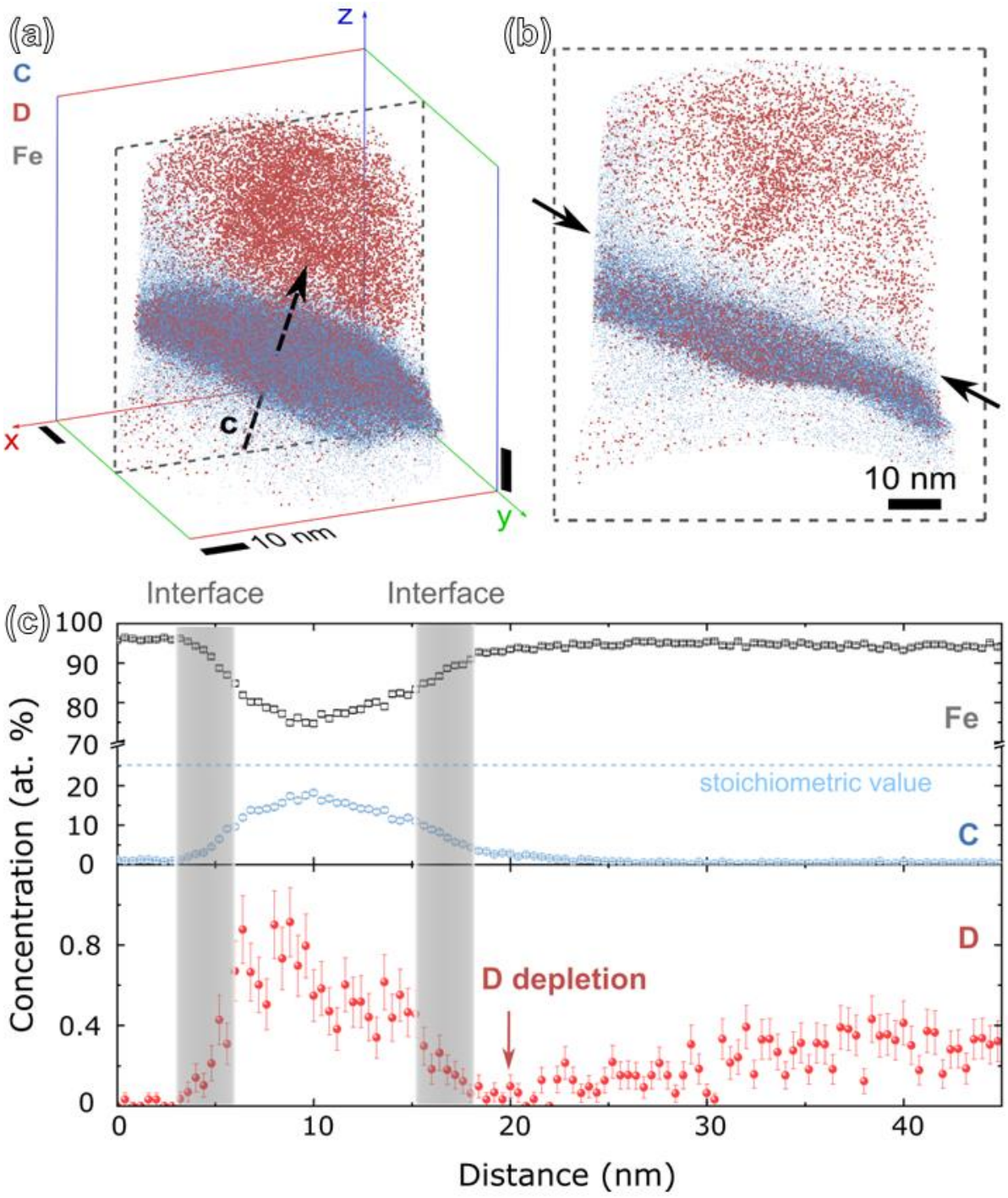

Figure 4.12 APT analysis of D-charged pearlite tip: (a) a 3-D reconstruction map of a D-charged pearlitic specimen, (b) a 10-nm-thickness slice from the region highlighted by dash line in (a), (c) a 1-D concentration profile from the region approaching the ferrite–cementite interface highlighted in (b). Data credit: Dr. Ranming Niu

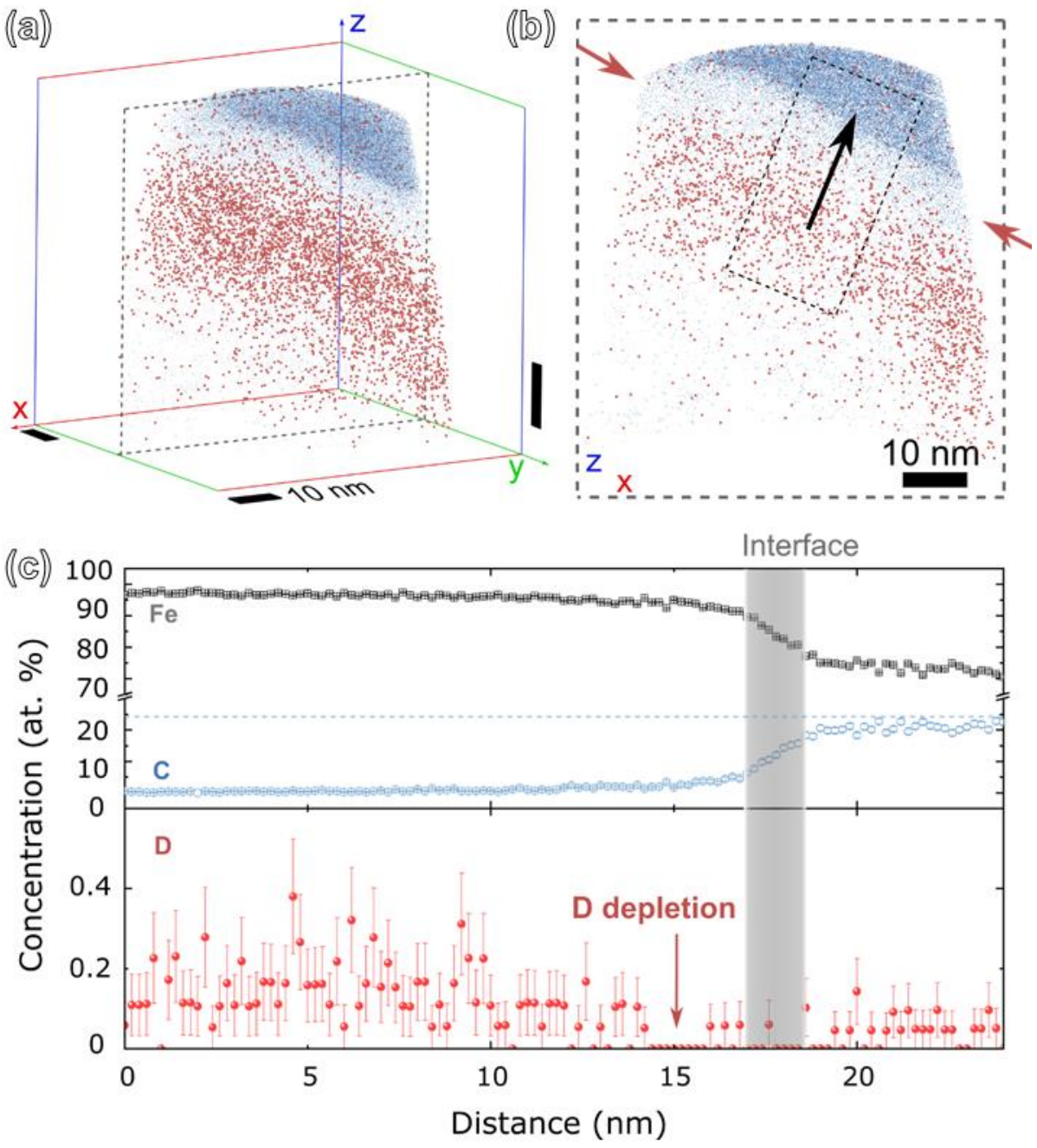

Figure 4.13 Another APT data captured the deuterium depletion zone near the cementite-ferrite interface. (a) is the 3-D reconstruction. (b) is a 2-D slice from the dashed region in (a) with a deuterium depletion zone highlighted by red arrows. (c) is the 1-D concentration profile from the direction perpendicular to the ferrite-cementite interface. Data credit: Dr. Ranming Niu

4.6 Cross-sectional observations of deformed ferrite-cementite structure

With the knowledge that i) hydrogen causes a change of deformation behavior in pearlite micropillars and ii) hydrogen is not located at the ferrite-cementite interface, SEM and STEM cross-sectional imaging was then conducted on the crystal plane that is perpendicular to the nominal slip system, i.e., {112} <111> of ferrite, in the deformed micropillars. This allows direct observations of buried defect structures that can help to understand the micropillar failures in Figure 4.9 and Figure 4.10. FIB was used to fabricate and lift out thin-foil specimens from regions that contain the surface ridges resulting from micropillar compressions. Two examples are shown in Figure 4.14. Figure 4.14a and b are from an uncharged micropillar, and Figure 4.14c and d are from a hydrogen-charged micropillar. The bright-field STEM images in Figure 4.14b and d were taken along <111> zone axis of ferrite, which allows the slip planes to be visible as highlighted by blue and orange arrows.

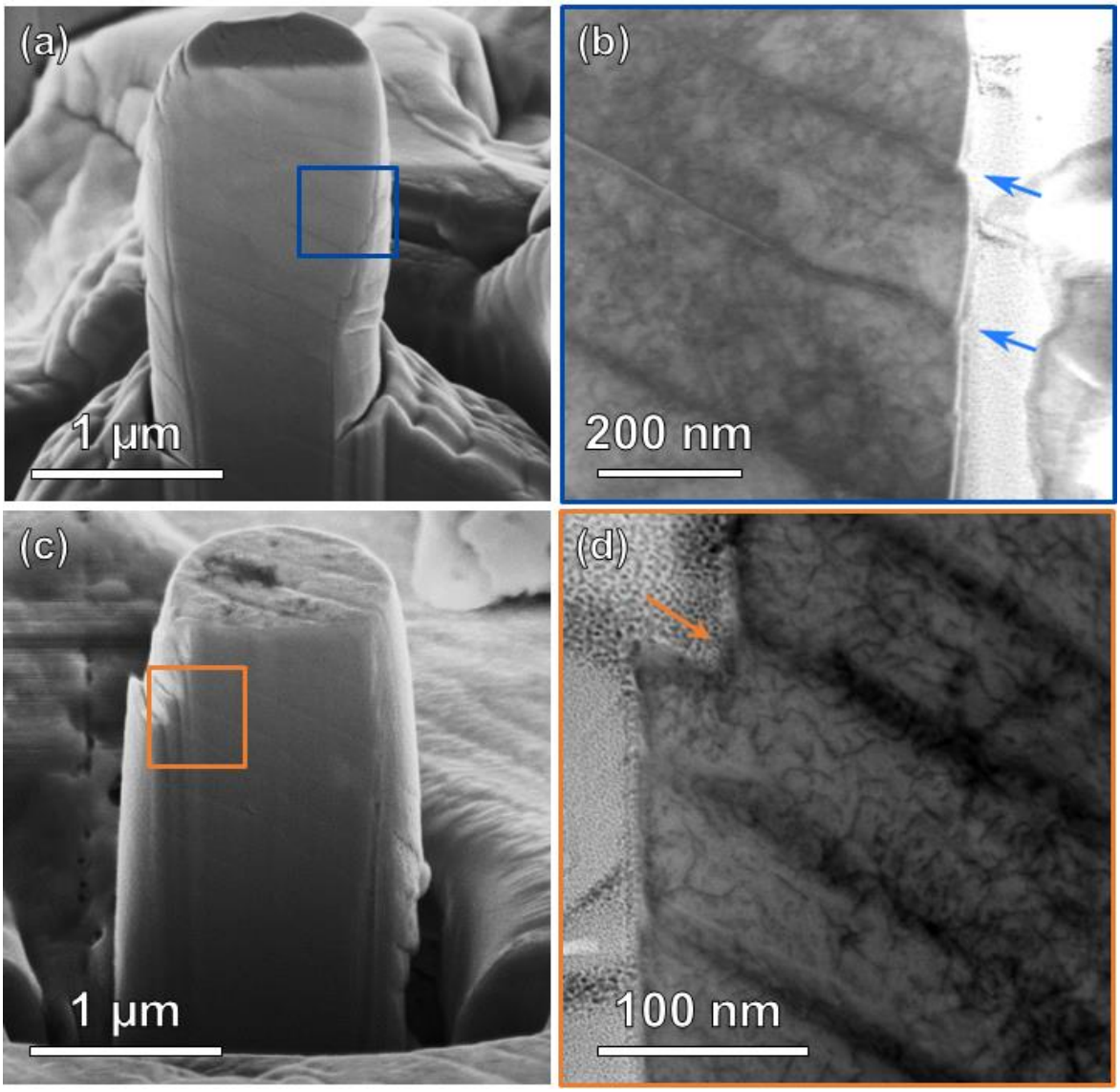

Figure 4.14 Cross-sectional images of deformed pearlite micropillars without and after hydrogen charging, corresponding to the "Uncharged #2" and "H-charged #1" curves in Figure 4.8, respectively: (a) SEM and (b) ABF-STEM images from an uncharged micropillar. (c) SEM and (d) ABF-STEM images from a hydrogen-charged micropillar. Slip planes are marked by the arrows in Figure (b) and (d) from STEM.

In Figure 4.14a and b, from an uncharged micropillar, the edge of the pillar indicates that slip occurs at the ferrite-cementite interfaces (blue arrows). According to the TEM analyses in Figure 4.4, this interface is aligned with the {112} plane of ferrite, which is also a primary slip plane. This coincidence between the strain location and the interfaces could be a result of the low bonding strength of the ferrite-cementite heterogeneous interface with respect to the intrinsic ferrite lattice metallic bond [254]. The slipping around the interface has three possible contributions. As the interfaces are located at {112} planes, it is possible that slipping was

activated along these primary slip planes. Secondly, if dislocations are activated in other slip systems (e.g., {110}<111>), the dislocation movements can be obstructed by the ferrite-cementite interfaces [255] and be locked at the interfaces. Thirdly, it is also possible dislocations can pass through the interface and the cementite lamella, causing cementite shears aligned with the slip bands in the ferrite [254]. In this sample, the critical resolved shear stress is greatest along the {112} planes, suggesting that the first of these three scenarios is the most likely.

In Figure 4.14c and d, from a hydrogen-charged micropillar, slip mainly takes place in the ferrite matrix and at a distance from the interfaces (orange arrow). This suggests that the mechanism contributing to lower yield strength in pearlite is not HEDE, i.e., a decohesion along the ferrite-cementite interface due to hydrogen reducing the interfacial bonding strength [135, 256]. This result is consistent with the APT result (Figure 4.12), which shows that hydrogen solute not located at the interface. The slip directions in the ferrite matrix, as observed in Figure 4.14d for a hydrogen-charged specimen, still align with the nominal slip plane of ferrite, i.e., {112}. Deformation *within* the ferrite could be a result of hydrogen reducing the energy required for dislocation glide, enhancing the local plasticity of the ferrite matrix via HELP in this hydrogen-charged pearlite micropillar with inclined cementite lamellae [132].

The presence of hydrogen can change the failure mechanism from a ferrite-cementite failure dominated process to a hydrogen-enhanced dislocation slip process. More detailed analyses and discussion on the effect of hydrogen on this change of deformation mechanism will ensue in the following chapters.

4.7 Summary

In this chapter, a new micromechanical method combining a fabrication method able to incorporate the desired cementite orientations in micropillars and the hydrogen charging on bulk specimens with surface prefabricated micropillars is demonstrated for the investigation of HE in pearlite.

- TDA was used to show hydrogen can be retained in the bulk specimen during the micromechanical experiments in the SEM vacuum chamber.
- The distribution of hydrogen was measured by using APT, showing hydrogen trapping in cementite and ferrite, but not at the ferrite-cementite interface.

- Cross-sectional observations of the deformed pearlite micropillars confirmed that the strain in an uncharged micropillar arises from slip along the ferrite-cementite interface, whereas a hydrogen-charged micropillar deforms within the ferrite region, not right at the interface.

5 Effect of hydrogen on the anisotropic deformation of pearlite micropillars

The last chapter investigated the effect of hydrogen on the deformation mechanism of the ferrite-cementite interface by testing pearlite micropillars with cementite lamellae inclined at 45 degrees. However, pearlite has a strong anisotropy of mechanical strength [257, 258]. That is, the strength of a pearlite grain varies according to the direction of cementite lamellae with respect to the applied loading direction. How this anisotropic load resistance can be influenced in the presence of hydrogen is important when it comes to using pearlite to strengthen pipeline steels for hydrogen applications. In addition, considering pipeline steels are polycrystalline materials under constant hydrogen pressure, the properties are likely to be affected by grains with cementite orientations that are the most susceptible to hydrogen embrittlement. Ogawa et al. [140] have reported that the environmental HE in pearlitic steels can result in two cracking modes: along the ferrite-cementite interface and across the cementite (Figure 2.8), depending on the hydrogen content in the environment. This chapter thus aims to further understand this anisotropic failure by employing micromechanical testing on hydrogen-charged micropillars of various cementite orientations. Three lamellae orientations are studied, i.e., vertical, inclined, and horizontal, using uniaxial micro-compression testing on specimens with and without hydrogen charging. Experimental methods are similar to those in the previous chapter, i.e., micro-compression, electrolytic hydrogen charging, and post-mortem microscopic transmission electron microscopic and scanning electron microscopic analysis.

5.1 Micropillar fabrication

Similar to the micropillar fabrication method described in the previous chapter (Section 4.2), EBSD was used to identify pearlite grains of desired cementite lamella orientations and PFIB was used to fabricate the micropillars. As shown in Figure 5.1, the geometry of the pearlite micropillars remains 1 μm in diameter and 3 μm in height. By utilizing the Isaichev ferrite-cementite orientation relationship (Table 2.1), the micropillars with vertical, inclined, and horizontal cementite lamellae were fabricated from the pearlite grains with the <001>, <110>, and <112> orientations of ferrite identified in EBSD IPF-Z (perpendicular to the sample surface) map, as shown in Figure 5.1a, b, and c, respectively. Note that the exact cementite lamellae orientations can slightly deviate, a tolerance of ±5 degree is acknowledged in this study, from the nominal angles due to the precision limit of the FIB-SEM stage control.

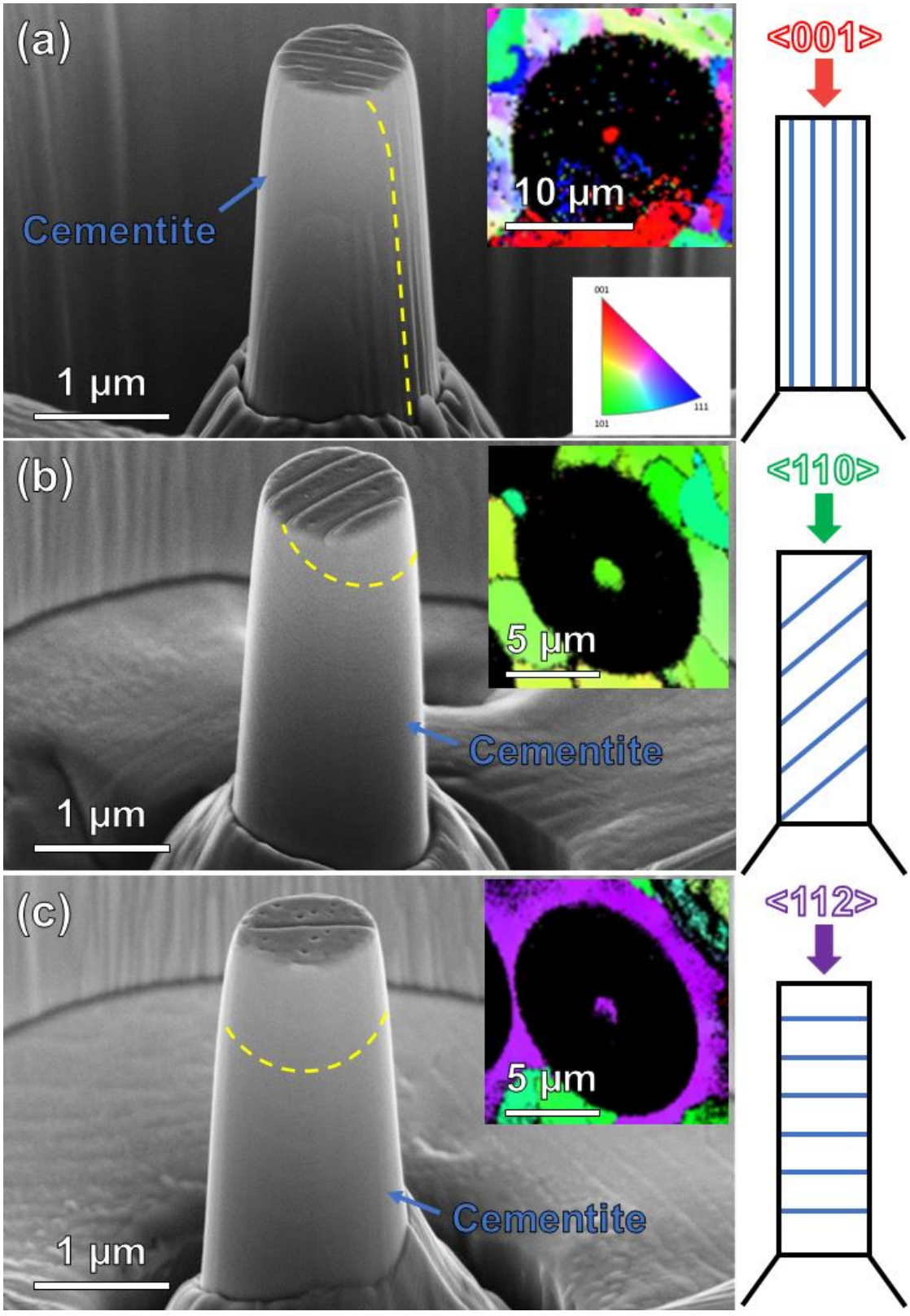

Figure 5.1 SEM images of pearlite micropillars containing (a) vertical, (b) inclined, and (c) horizontal lamellae with corresponding normal orientation identified with EBSD and schematic illustration of designed lamellae configuration. One representative cementite lamella has been highlighted with a yellow dashed line for the corresponding lamellae direction.

5.2 Overview of results

Figure 5.2 shows typical uniaxial engineering stress-strain curves from the pearlite micropillars with three different lamellae directions, in the absence (left figure) and the presence (right figure) of hydrogen, respectively. In this chapter, we opted to utilize engineering stress-strain curves (Figure 4.8, Figure 4.9, and Figure 4.10) instead of the previously employed resolved shear stress from the last chapter. This is because dislocation slip parallel to the ferrite-cementite interface is not always the dominant deformation mode. Considering the yielding behaviors were of great interest in this chapter, pillars were only compressed up to 10% of strain, allowing for the microscopic investigation of the role of cementite in the yielding behaviors and follow-up slip activities [257]. Being consistent with the analyses in the previous chapter, the onset of yield (yield strength) is defined by the occurrence of the first significant strain burst, i.e., the first sudden stress drop [250, 259].

To the left in Figure 5.2, the yield strength of the uncharged micropillars with vertical, inclined, and horizontal cementite lamellae was measured as 1.67, 1.21, and 1.72 GPa, respectively. This variance in yield strength is attributed to the orientation of the cementite lamellar. The yield strengths of the hydrogen-charged micropillars in the right of Figure 5.2 are considerably lower, at 1.02, 0.93, and 1.01 GPa for micropillars having vertical, inclined, and horizontal cementite lamellae, respectively. Analyses on each type of micropillar with and without hydrogen charging were repeated at least 5 times, leading to the statistics shown in Table 5.1. By comparing the yield strength of the uncharged and the hydrogen-charged micropillars, it can be seen that the introduction of hydrogen significantly reduces the yield strength of all micropillars, irrespective of the orientation of cementite lamellae. In addition, the yield strength became less affected by the orientation of the cementite lamellae, indicating a less anisotropic yield behavior in hydrogen-charged micropillars. Detailed analyses are presented in the following sections.

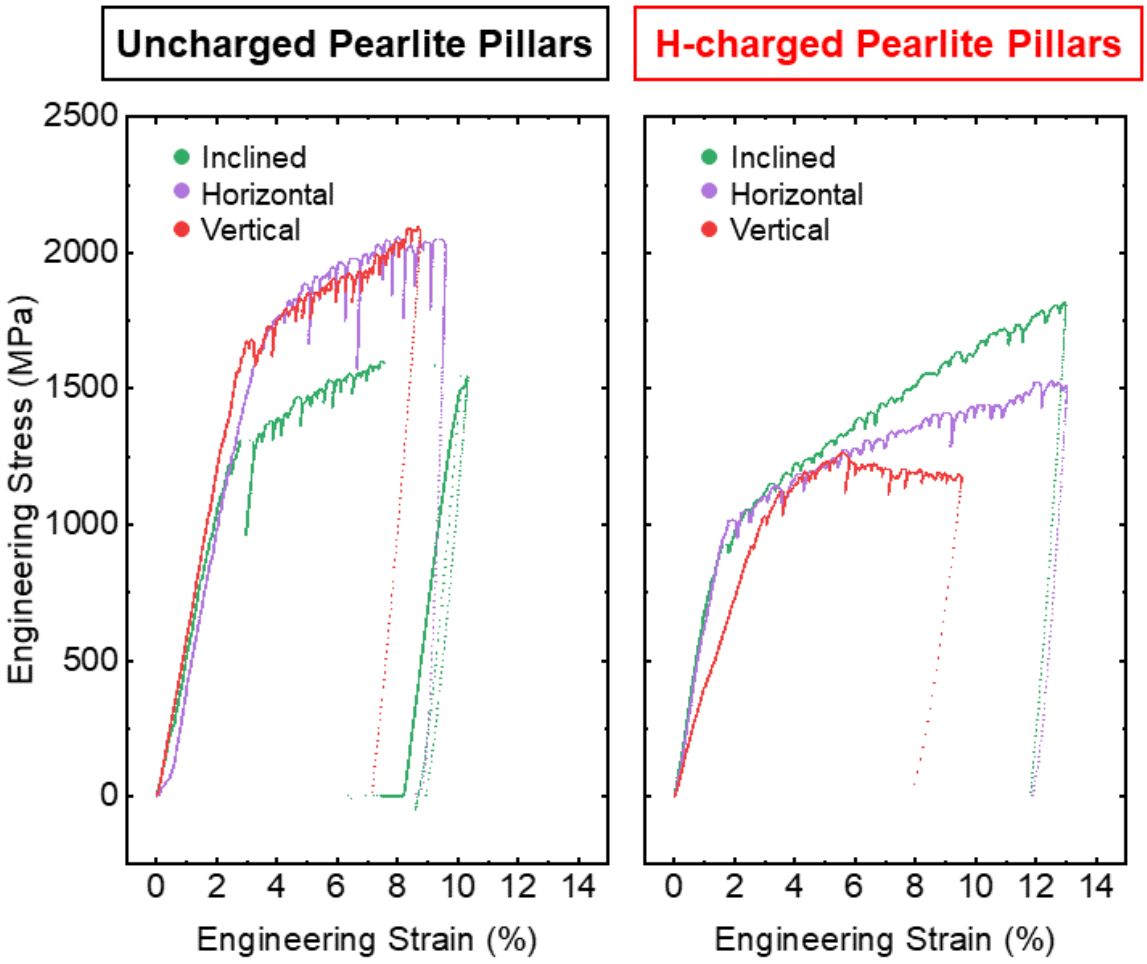

Figure 5.2 Micropillar load resistance comparison between different cementite lamellae directions in both uncharged and hydrogen-charged states.

Table 5.1 Statistics of micromechanical testing containing five tested micropillars with horizontal, inclined, and vertical lamellae under either uncharged or hydrogen-charged states and the errors corresponding to the standard deviations (±SD) of the tests.

Charging states	Lamellae directions	Yield stress (GPa)
Uncharged	Horizontal	1.53±0.14
	Inclined	1.17±0.06
	Vertical	1.48±0.14
H-charged	Horizontal	0.92±0.08
	Inclined	0.89±0.08
	Vertical	0.92±0.01

In materials with a laminate structure consisting of alternating hard and soft phases, plastic deformation typically initiates in the soft phase and is constrained by the hard phase [260]. Echoing this principle, this study also observed that minor plastic deformation was initiated in the ferrite phase, even before the yielding of the entire sample. The cementite lamellae limited the expansion of this so-called microplasticity [261, 262], until a drastic

deformation was observed, marking the yield of the entire sample [263]. In the absence of hydrogen, yield strength is highly related to the orientation of the cementite lamellar, as might be expected for an anisotropic microstructure. An example of another similar system is an Al-SiC nanolaminate composite [264]. This type of system also displays a yield strength of the vertical pillar that is approximately the same as the horizontal pillar, while both of them are higher than the inclined pillars.

5.3 Micropillars with inclined cementite lamellae

There was some scatter in the response of micropillars with inclined cementite. Two main classes of deformation took place. The first type contained pillars in which deformation occurred only along the direction of the cementite lamellar. The second type involved pillars in which shearing across the cementite lamellae was observed. These are treated separately in this section.

5.3.1 Deformation without cementite lamella shearing

The deformation process of an uncharged pearlite micropillar with inclined lamellae and corresponding engineering stress–strain curve is shown in Figure 5.3. An uncharged pillar yielded at 1.13 GPa, as shown from the engineering stress-strain curve in Figure 5.3a. The strain at which the SEM snapshot was taken is indicated on the curve and the corresponding SEM image. At 2% strain, the first large burst was activated, corresponding with a significant slip at the top of the pearlite micropillar (Figure 5.3b). Another burst occurred at 5% strain, corresponding to a new slip region observed at the bottom of the pillar that was parallel to the former slip plane (Figure 5.3c). However, the plastic deformation was mainly accommodated by the first slip plane, and the following slip planes were deformed less (Figure 5.3d). Figure 5.3e is a cross-sectional image of the compressed micropillar, perpendicular to the slip plane. The slip was activated at the ferrite–cementite interface, consistent with weak phase boundaries [254]. The sequential snapshot images confirm that the slip plane at the top of the micropillar dominated the whole straining process. The secondary slip plane at the bottom contributes less to the overall strain.

Figure 5.4 provides micromechanical testing results from a representative hydrogen-charged pearlitic pillar with inclined cementite lamellae. The yield strength of the pillar decreases to 0.78 GPa, as seen from the engineering stress-strain curve in Fig. 5.4a. In addition, the hydrogen-charged pillar deforms in a different way from the uncharged one. At the initial

stage of deformation, three parallel slip planes are activated very shortly after yielding (Figure 5.4b). The activated slip planes propagate continuously until the end of the test (Figure 5.4c and d). Figure 5.4e is a cross-section SEM image of the hydrogen-charged pillar after compression. Unlike the uncharged pillar, which slips along the ferrite-cementite interface, the slip planes of the hydrogen-charged pillars are located within the ferrite matrix. The post-mortem cross-sectional SEM observations also indicate that the slip planes did not propagate as much in the charged sample. The observed deformation explains the smooth stress–strain curve of the hydrogen-charged micropillars. The induction of hydrogen into the pearlite micropillars with inclined lamellae alters the slip near the ferrite–cementite interface, from that of an interfacial failure to deformation in the ferrite matrix close to the interface. A schematic illustration of this finding is provided in Figure 5.5.

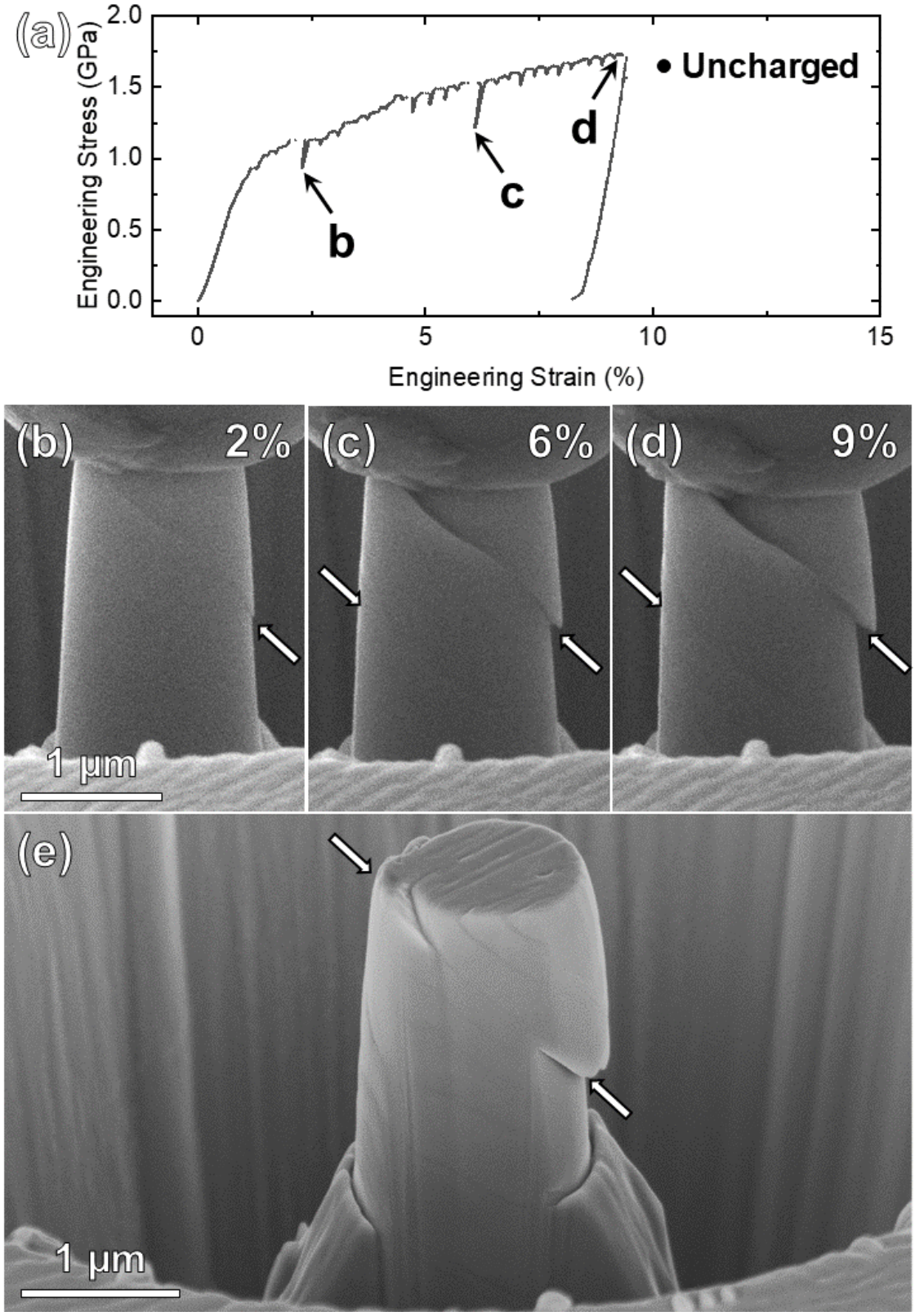

Figure 5.3 In-situ compression testing on an uncharged pearlite micropillar with inclined lamellae: (a) engineering stress-strain curve, (b), (c), (d) SEM snapshots taken from the in-situ video which are indicated on (a). (e) Cross-section SEM image of the compressed pillar milled via FIB confirming the occurrence of slipping on the pillar.

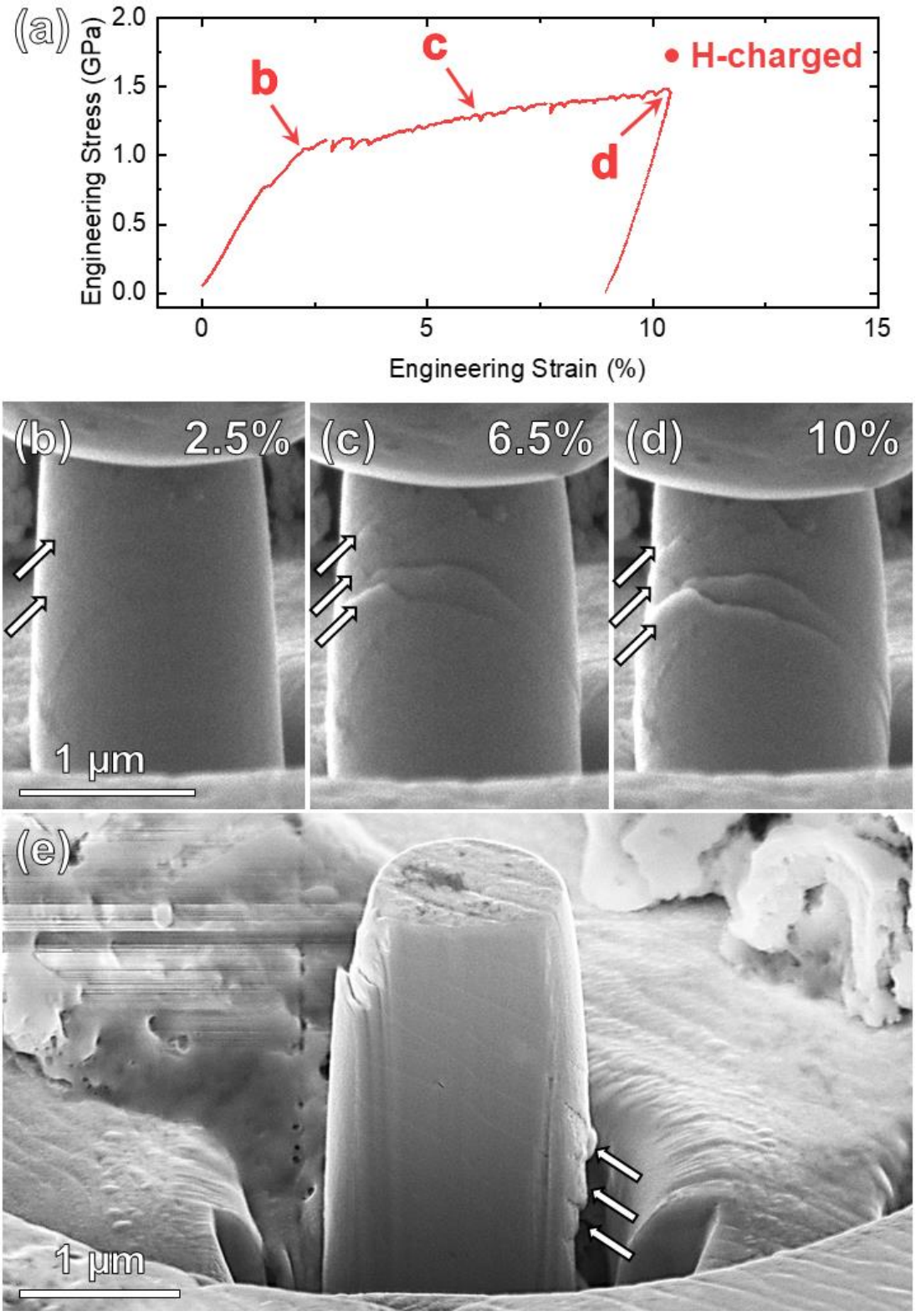

Figure 5.4 In-situ compression testing on a hydrogen-charged pearlite micropillar with inclined lamellae: (a) engineering stress-strain curve, (b), (c), (d) SEM snapshots taken from the in-situ video which are indicated on (a). (e) Cross-section SEM image of the compressed pillar milled via FIB confirming the occurrence of slipping on the pillar.

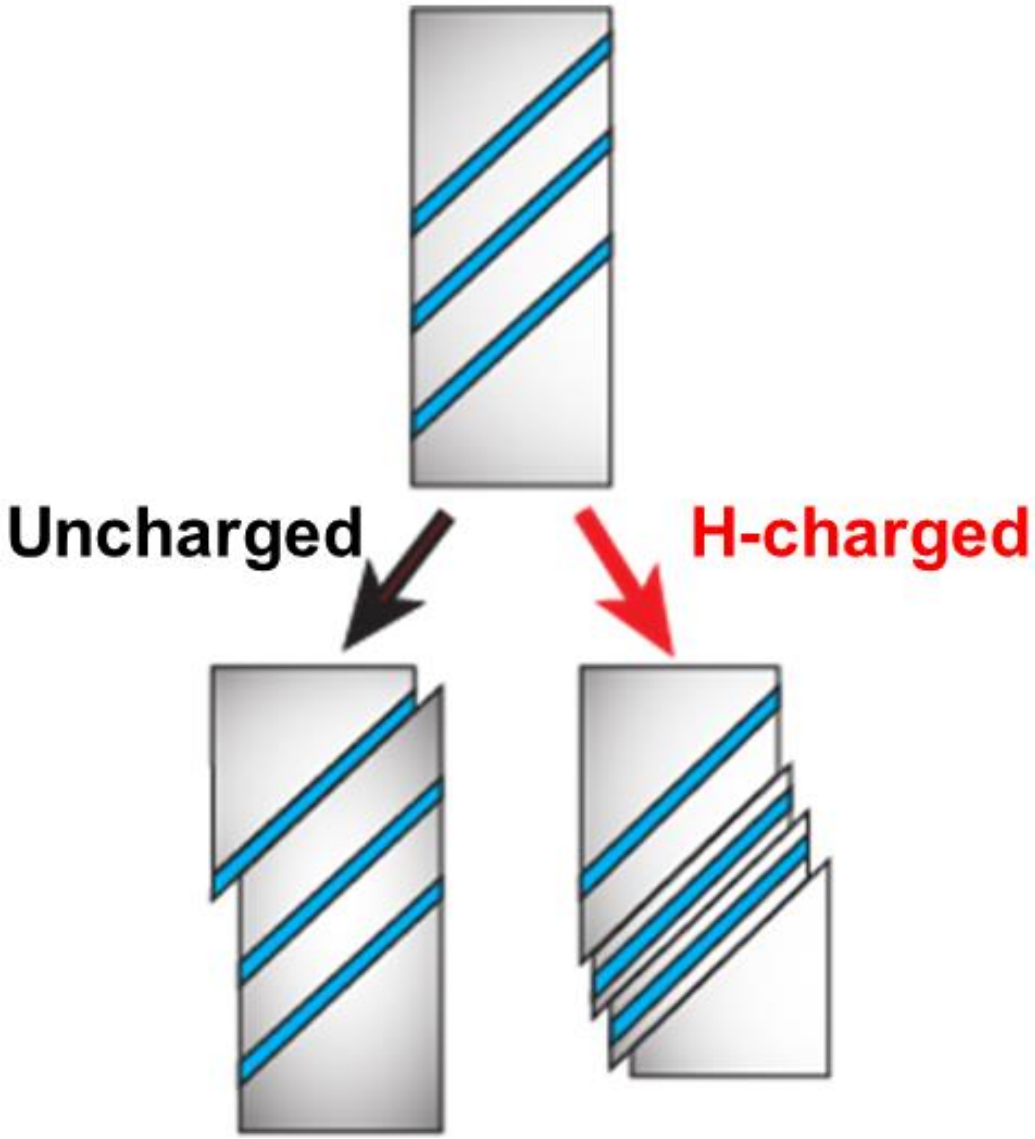

Figure 5.5 Schematic illustration of the straining areas in uncharged and hydrogen-charged micropillars

In Figure 5.6, which are ABF images of the uncharged samples after deformation, the dislocations are evenly spread throughout the ferrite phase, but there is also contrast that is consistent with dislocations along the ferrite-cementite interface. These images also suggest that the integrity of cementite lamellae was not affected, i.e., there are not many sheared or deformed lamellae. The cementite lamellae are known to be effective barriers for blocking dislocation motion [255] (Figure 5.6b highlighted by yellow arrows). Atomistic simulation on a similar type of interface has suggested that lattice dislocations approaching such an interface can adhere to the interface [265]. The adhered dislocations can then be absorbed, spread along, and finally shear over the interfaces, allowing shear straining across a cementite lamella. Kim

et al. [254] used molecular dynamics (MD) simulations, coming to a similar conclusion about the dislocation behaviors near a ferrite-cementite interface. Figure 5.6c is a high-resolution ABF image, showing dark contrast consistent with the dislocations spreading along the ferrite-cementite interface. The experimental observations on compressed micropillars are in good agreement with the theoretical calculation results.

In the hydrogen-charged pearlite micropillars (Figure 5.7), the effect of dislocation being blocked by the lamellae is not as apparent as that in Figure 5.6. By comparing Figure 5.6 and Figure 5.7, dislocations look as if they are weaving into the cementite lamellae in Figure 5.7b and c. Also, the dislocation number density is higher in the hydrogen-charged specimen. The presence of hydrogen in the micropillar seems to enhance dislocation gliding in the ferrite regions as well as penetration of the dislocations through the cementite lamellae (Figure 5.7c). This contrasts with the case without hydrogen, where dislocations in the ferrite are typically discrete from those at the interface and the cementite lamellae are mostly intact (Figure 5.6c).

When this information is combined with the APT hydrogen mapping results (Figure 4.12), it is postulated that the dislocation substructures in the hydrogen-charged specimens could result from hydrogen trapped in the dislocations in ferrite. It is also postulated that the energy required for dislocations to penetrate the cementite lamellae may be reduced in the presence of hydrogen in cementite. This enhanced cementite shearing could be another manifestation of HELP, which has not been previously defined.

Bent or rotated cementite lamellae were occasionally found in the deformed specimens. When this occurs, it could be concluded that dislocations must be emitted from the deformed cementite. They would then likely be pinned at the adjacent lamellae. This dislocation behavior is specific to laminated structures and has been described as causing material strengthening when the interlamellar spacing decreases [266, 267]. However, in the hydrogen-charged sample, the deformed cementite was found to split entirely into areas that are surrounded by a high density of dislocations (yellow dashed line region in Figure 5.7b). Again, this phenomenon can be correlated with the APT results (Figure 4.12), which show that hydrogen atoms are trapped both within the cementite lamellae and at the dislocations in the ferrite matrix, facilitating dislocations to penetrate the cementite lamellae.

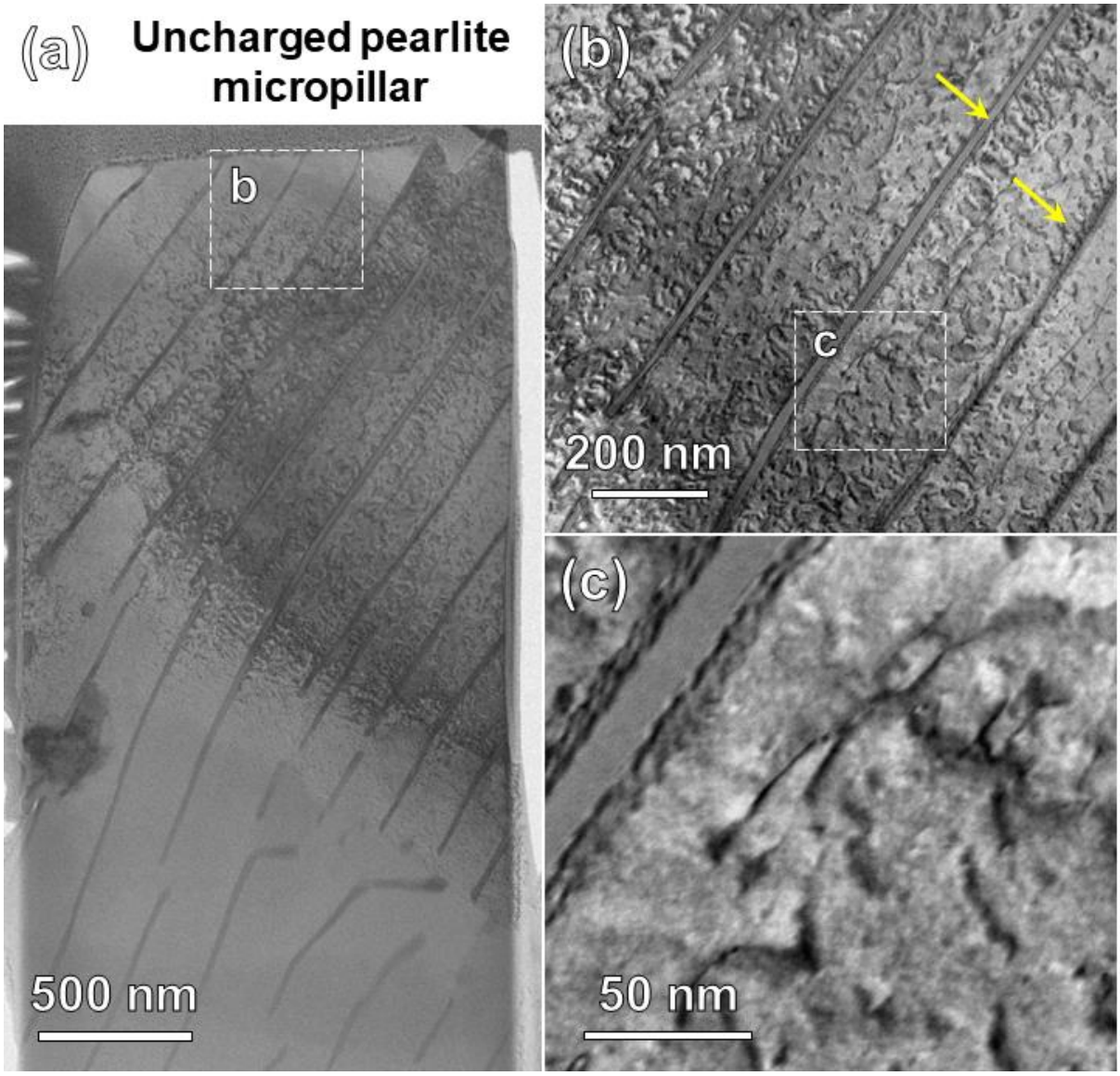

Figure 5.6 ABF-STEM images of an uncharged pearlite micropillar in the view of <111> zone axis of ferrite: (a) low-magnification overview, (b) close view of the dashed line region in (a), and (c) high-magnification view of the ferrite-cementite interface region from the dashed line region in (b). Yellow arrows highlight the dislocations pinned at the ferrite-cementite interfaces.

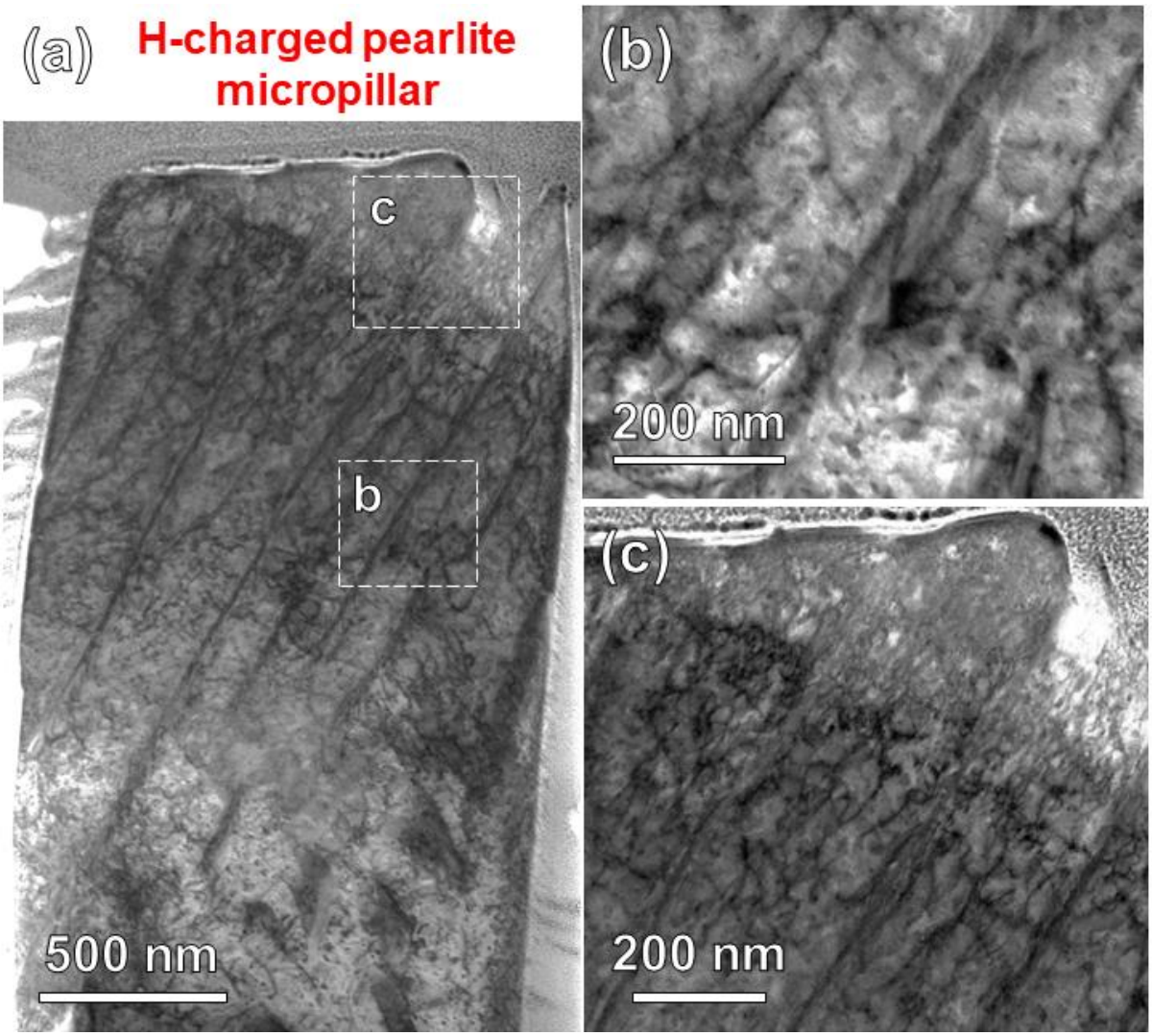

Figure 5.7 ABF-STEM images of a hydrogen-charged pearlite micropillar in the view of <111> zone axis of ferrite: (a) low-magnification overview, (b) high-magnification view from the bottom of the slip band, i.e., the dashed line region (b) in (a), (c) high-magnification view from the top of the slip band, i.e., the dashed line region (c) in (a).

5.3.2 Deformation with shearing

The pearlite micropillars with inclined lamellae were designed to induce slip along the ferrite-cementite interface. However, shearing across the cementite lamellae was sometimes observed. Figure 5.8a shows the engineering stress-strain curve of a representative pearlitic pillar with inclined cementite lamellae, which has a yield strength of 1.47 GPa. In the early stage of deformation, no significant slip or shear band was observed (Figure 5.8b). When the strain reached 8.5% (Figure 5.8c), a shear band formed (white arrow), which dominated the following straining process (Figure 5.8d). Figure 5.8e is an SEM image of the cross-section of the compressed micropillar in which a shear band traverses multiple cementite lamellae. Close

examination of the cross-section of the deformed specimen reveals that this phenomenon can correlate to the presence of non-continuous cementite lamellae (Figure 5.4e, white arrows). It is thought that the dislocations glide more easily through the gaps between non-continuous cementite lamellae, providing a stress concentration site that instigates shearing.

Figure 5.9 shows the results from a hydrogen-charged pearlite pillar with inclined, discontinuous lamellae. The yield stress is reduced to 0.97 GPa (Figure 5.9a). Shear bands in the hydrogen-charged pillar are formed immediately after yielding (Figure 5.9b, c, and d), contrasting to the initial state of yielding in the uncharged pillar (Figure 5.8b, c, and d). As the deformation proceeds, the old shear bands evolve, and a new shear band initiates continuously.

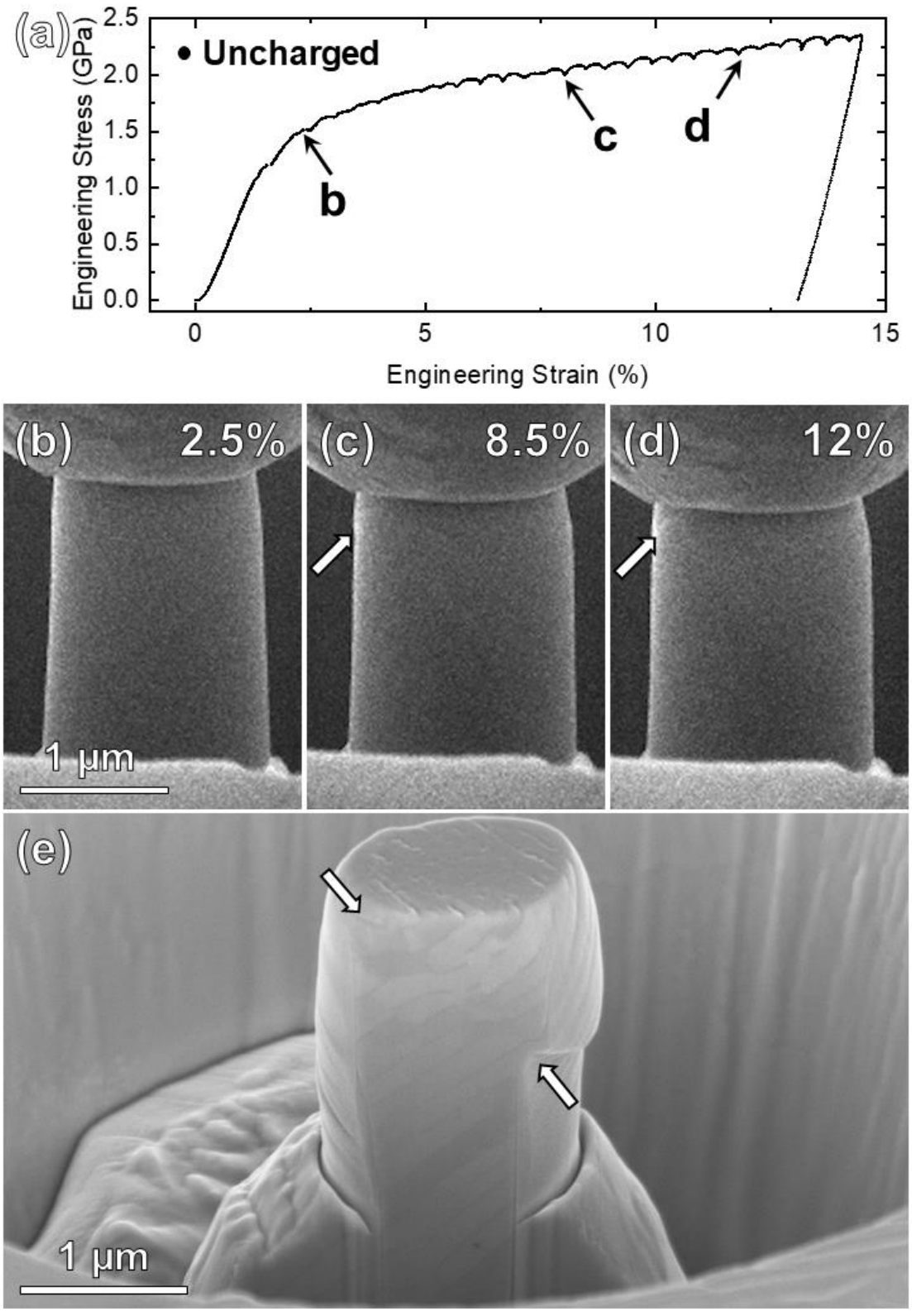

Figure 5.8 In-situ compression testing on an uncharged pearlite micropillar with several sheared inclined lamellae: (a) engineering stress-strain curve, (b), (c), (d) SEM snapshots taken from the in-situ video which are indicated on (a). (e) Cross-section SEM image of the compressed pillar milled via FIB confirming the occurrence of shearing on the pillar.

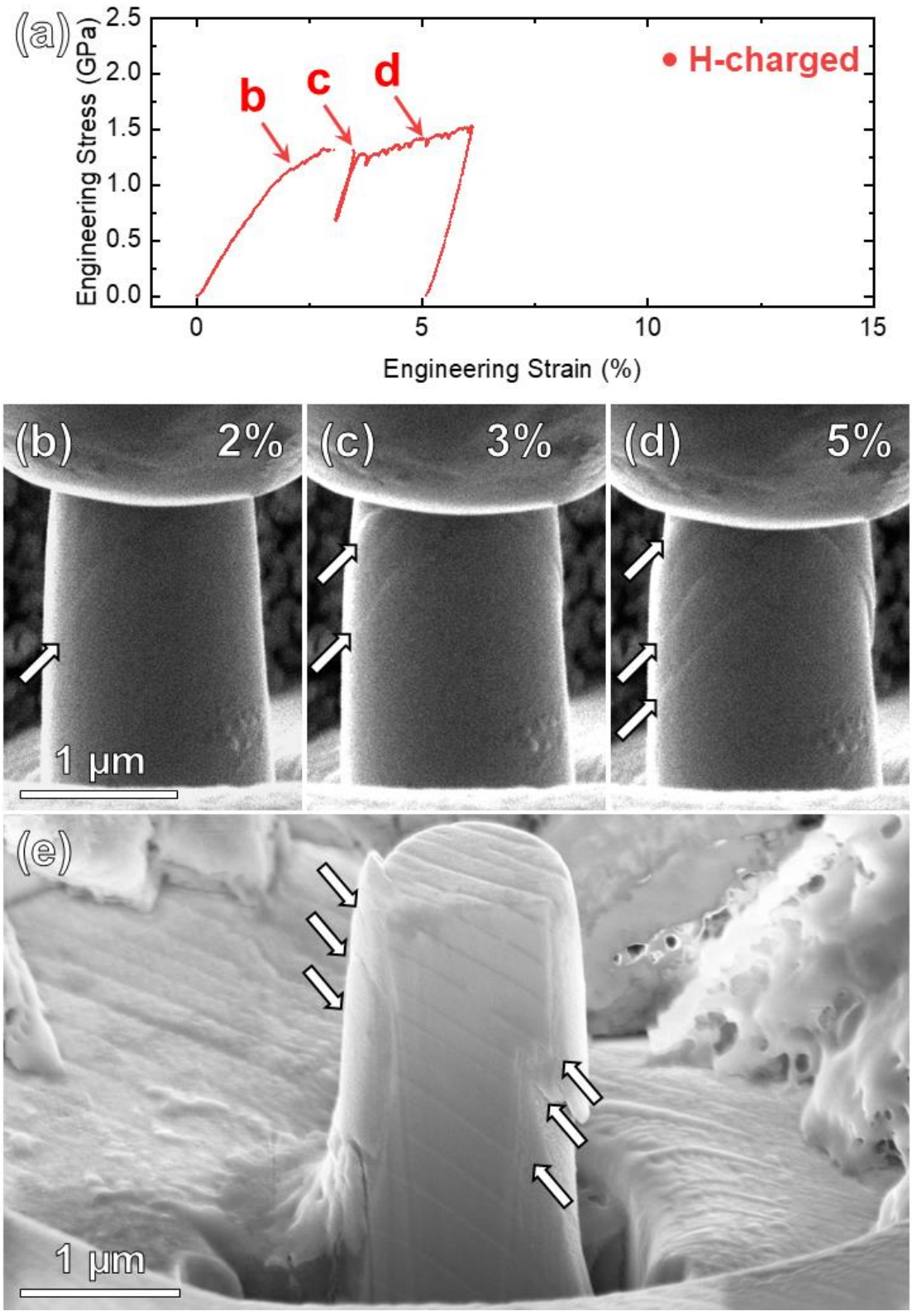

Figure 5.9 In-situ compression testing on a hydrogen-charged pearlite micropillar with several sheared inclined lamellae: (a) engineering stress-strain curve, (b), (c), (d) SEM snapshots taken from the in-situ video which are indicated on (a). (e) Cross-section SEM image of the compressed pillar milled via FIB confirming the occurrence of shearing on the pillar.

5.4 Micropillars with horizontal cementite lamellae

Applying a uniaxial load to the micropillars with horizontal lamellae can have varied consequences, specifically, shearing, barreling, and extrusion [268-271]. However, in this study, shearing was found to be the main deformation type, potentially due to the fine thickness and spacing of the cementite lamellae. Figure 5.10 shows a typical result of micromechanical testing on a pearlite micropillar with horizontal cementite lamellae. The measured yield strength of the micropillar was 1.76 GPa (Figure 5.10a). The first shear band was formed in the middle of the pillar (Figure 5.10b), which is associated with the first large burst in Figure 5.10a. The subsequent shearing occurred soon afterward (Figure 5.10c), and the third shear band took place at 10% strain (Figure 5.10d). Figure 5.10e is the cross-section SEM image with the three parallel shear bands highlighted by white arrows, corresponding to those noted in Figure 5.10a. The shear bands were seen to cross several cementite lamellae.

Figure 5.11a is a representative stress-strain curve from a hydrogen-charged pearlite micropillar with horizontal lamellae, which indicates a yield stress of 0.90 GPa. The hydrogen-charged micropillar yields at 1.8% strain and two parallel shear bands formed nearly simultaneously (Figure 5.11b). At 3.8% strain, a large strain burst occurred, associated with the second shear band near the top of the micropillar (Figure 5.11c). This shear dominated the further straining (Figure 5.11d). In the deformed micropillar cross-section (Figure 5.11e), sheared cementite lamellae were observed, as noted by the white arrows.

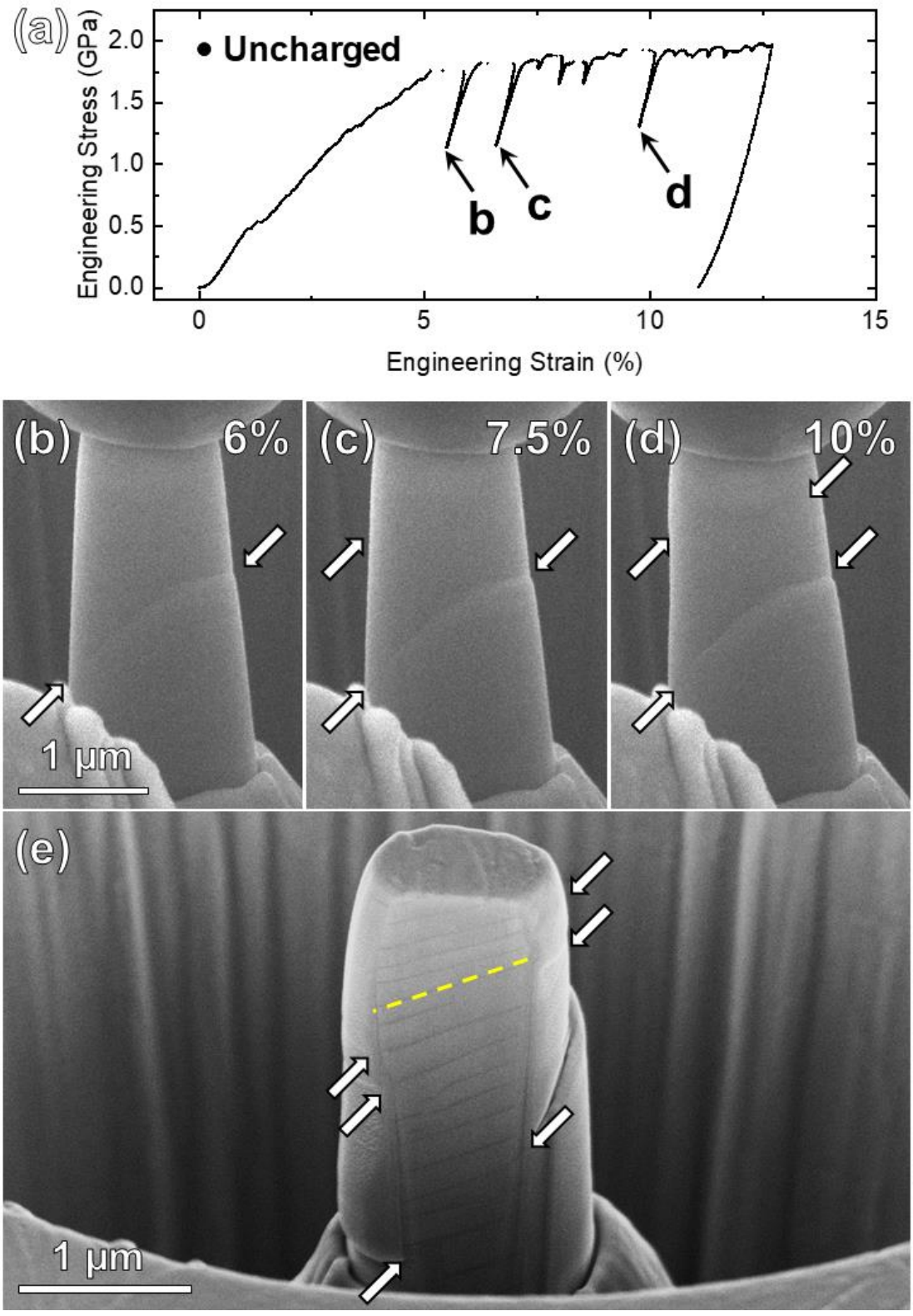

Figure 5.10 In-situ compression testing on an uncharged pearlite micropillar with near horizontal lamellae: (a) engineering stress-strain curve, (b), (c), (d) SEM snapshots taken from the in-situ video which are indicated on (a). (e) Cross-section SEM image of the compressed pillar milled via FIB. The yellow dashed line is a representative cementite.

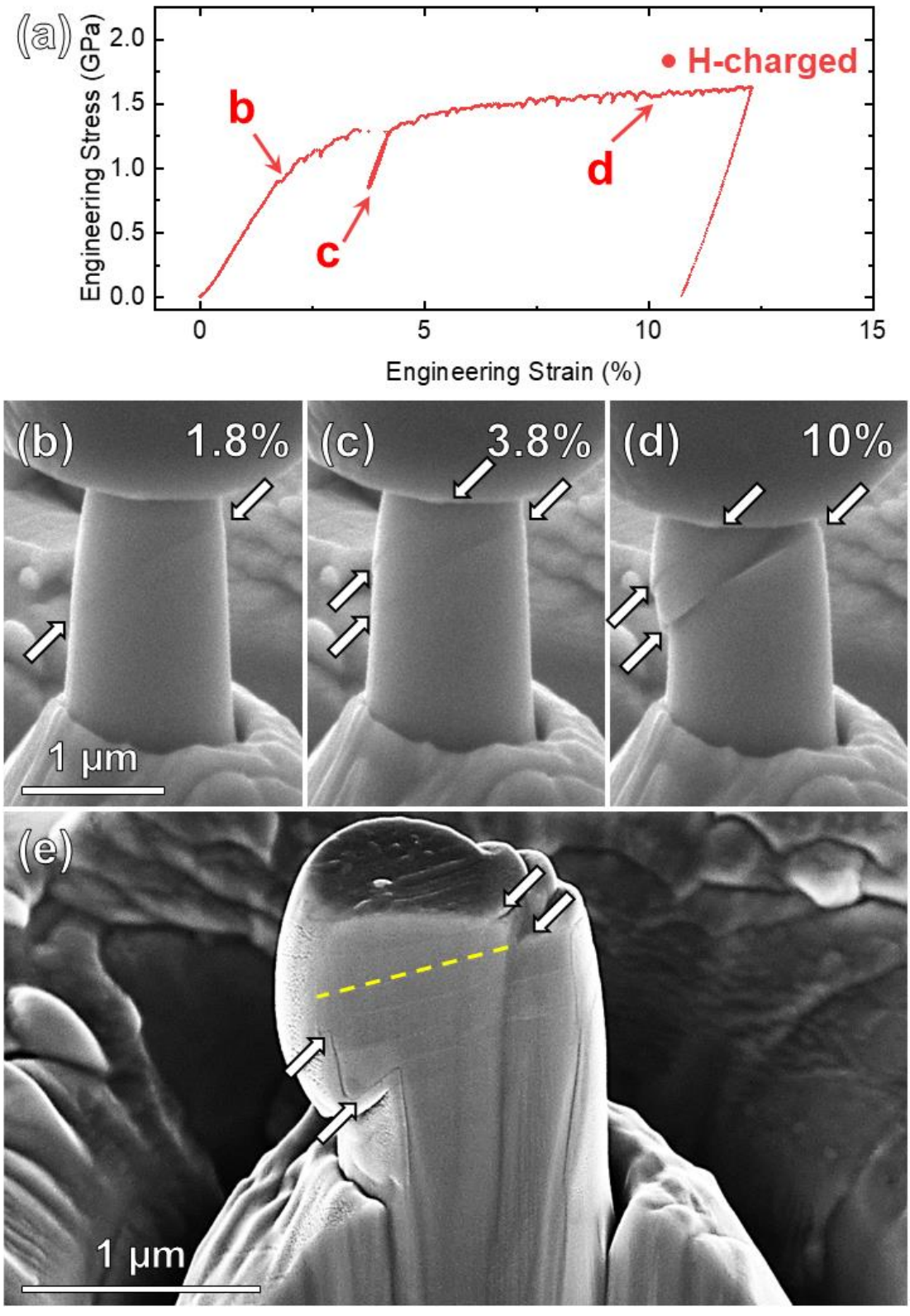

Figure 5.11 In-situ compression testing on a hydrogen-charged pearlite micropillar with horizontal lamellae: (a) engineering stress-strain curve, (b), (c), (d) SEM snapshots taken from the in-situ video which are indicated on (a). (e) Cross-section SEM image of the compressed pillar milled via FIB. The yellow dashed line is a representative cementite.

Figure 5.12a and Figure 5.13a are low-magnification post-mortem STEM images for the compressed pearlite micropillars with and without hydrogen charging, respectively. The uncharged micropillars were found to have abundant dislocations, but there were no obvious cracks in the lamellae (Figure 5.12b). The deformation in the uncharged specimen in some places results in elongated cementite lamellae (Figure 5.12b, yellow arrow) and reduced interlamellar spacing. In addition, dislocation pile-up/arrays were observed in Figure 5.12c (yellow arrow), which can be used to explain the initial work hardening in Figure 5.10a (before 5% strain).

In contrast, the hydrogen-charged micropillars were sheared, as shown in Figure 5.13b (yellow arrow) and c. The lamellae appear heavily elongated, not cracked, suggesting that the cementite has undergone substantial plastic deformation. Dislocation piling and bowing were rarely observed in the hydrogen-charged specimen. Based on the APT hydrogen mapping result (Figure 4.12), it is considered that the presence of hydrogen in cementite lamellae can lead to a change in their deformation behavior, which may indicate dislocation penetration. The introduction of hydrogen seems to disable the dislocation bows confined by the lamellae interfaces as well as dislocation piling near the interfaces.

The results in this section are consistent with the finding in the last section, suggesting that hydrogen charging can lead to a change of deformation mechanism from that dominated by cementite-lamellae-hindered dislocation gliding to that of homogeneously activated dislocation activities.

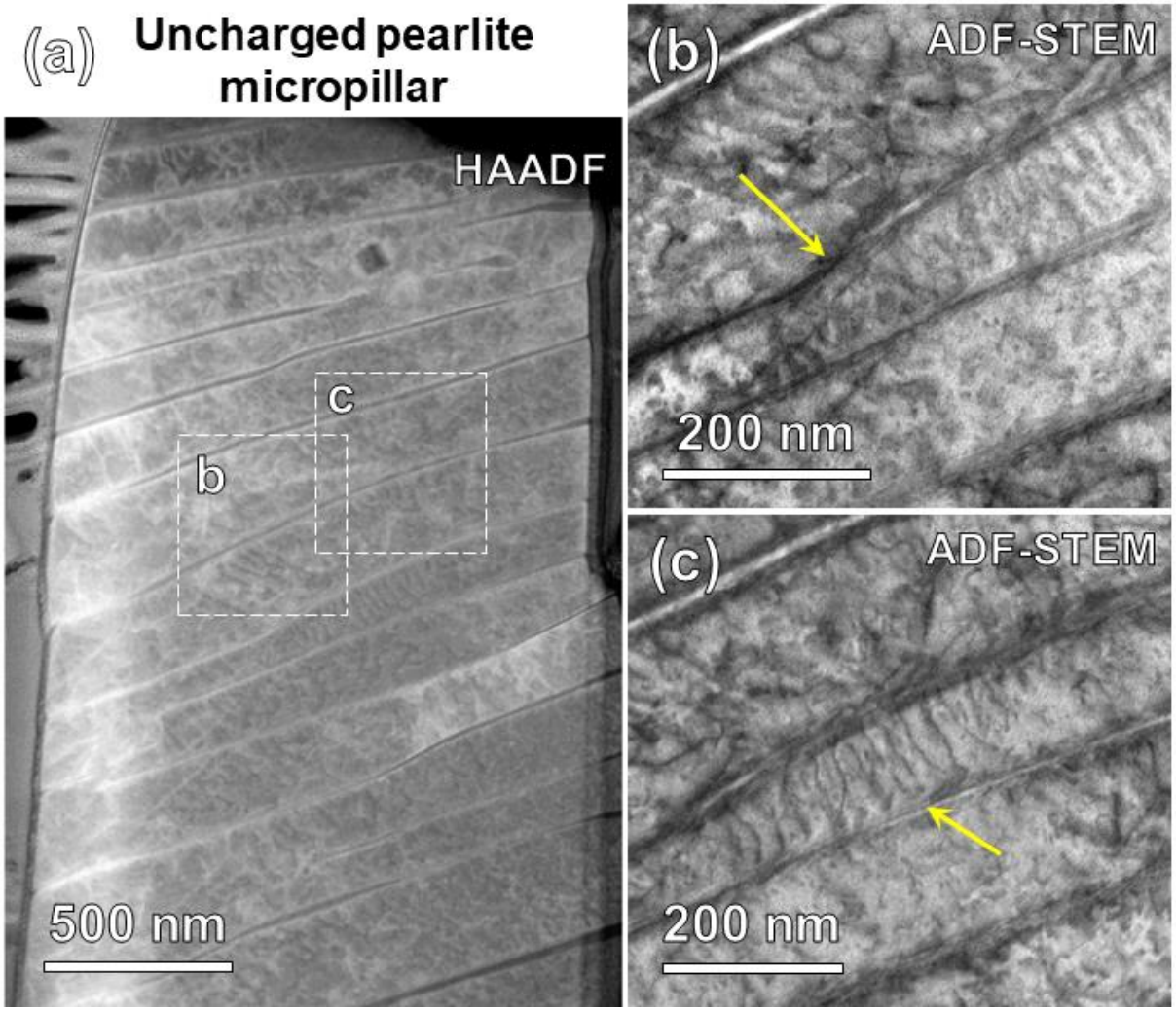

Figure 5.12 STEM images of an uncharged pearlite micropillar with horizontal lamellae in the view of <111> zone axis of ferrite: (a) overall cross-section images of the micropillar, (b) high-magnification view of deformed cementite, i.e., the dashed line region (b) in (a), (c) high-magnification view of parallel dislocations in the ferrite between adjacent cementite lamellae, i.e., the dashed line region (c) in (a).

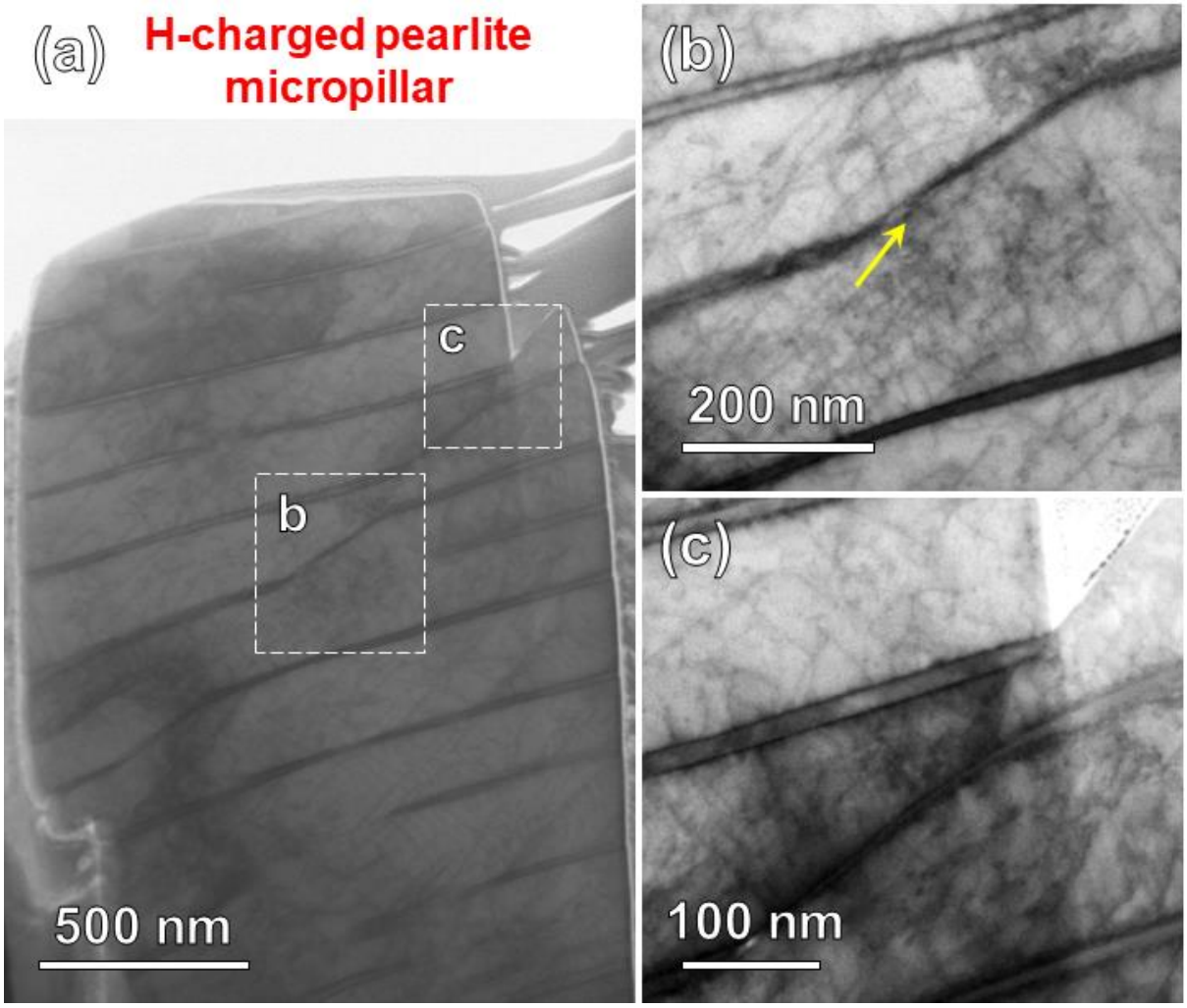

Figure 5.13 ABF-STEM images of a hydrogen-charged pearlite micropillar with horizontal lamellae in view of <111> zone axis of ferrite: (a) overall cross-section images of the micropillar, (b) high-magnification view of fractured cementite, i.e., the dashed line region (b) in (a), (c) high-magnification view of region out of shear band, i.e., the dashed line region (c) in (a).

5.5 Micropillars with vertical cementite lamellae

Literature indicates that uniaxial loading to micropillars containing vertical lamellae can lead to a variety of resulting deformation modes such as buckling, kinking, and shearing [257, 264, 271-273]. In this thesis, shearing was found to be the most common deformation mechanism for the pearlite micropillars. Buckling and kinking were only occasionally observed.

5.5.1 Micropillars with sheared cementite lamellae

A representative example of the deformation of an uncharged pearlite micropillar containing vertical cementite lamellae is shown in Figure 5.14. A yield stress of 1.46 GPa is determined using the stress-strain curve in Figure 5.14a. After a large elastic strain of around 5%, a shear band is formed at the top of the micropillar, marking the yield point (Figure 5.14b). The following plastic deformation took place mostly within the existing shear band (Figure 5.14c and d). Figure 5.14e is an SEM image of the micropillar after compression before FIB cross-sectioning. Figure 5.14f is a cross-sectional view of the deformed specimen. Although the vertical cementite lamellae were heavily sheared during the micro-compression, no cracking of the cementite lamellae was observed. Note that the blue dashed line delineates contrast from artifacts due to FIB ion milling, which is distinct from the yellow line that represents a real cementite lamella.

Figure 5.15a is a representative engineering stress-strain curve from a hydrogen-charged pearlite micropillar with vertical cementite lamellae. The yield stress is 0.93 GPa. The shear band was activated after 2% strain (Figure 5.15b). Although several large strain bursts can be seen on the stress–strain curve, most of the deformation took place in the shear bands shown in Figure 5.15c and d. In the SEM image of the micropillar after compression (Figure 5.15e), one can see that the vertical cementite lamellae in the hydrogen-charged pillar were severely sheared. Figure 5.15f provides a cross-sectional view of the deformed micropillar, showing the shear bands pass through the lamellae. The cementite lamellae are the vertical lines in Figure 5.15f. Unfortunately, fine details are obscured by the light contrast, delineated by the blue dashed lines, due to artifacts in FIB ion milling.

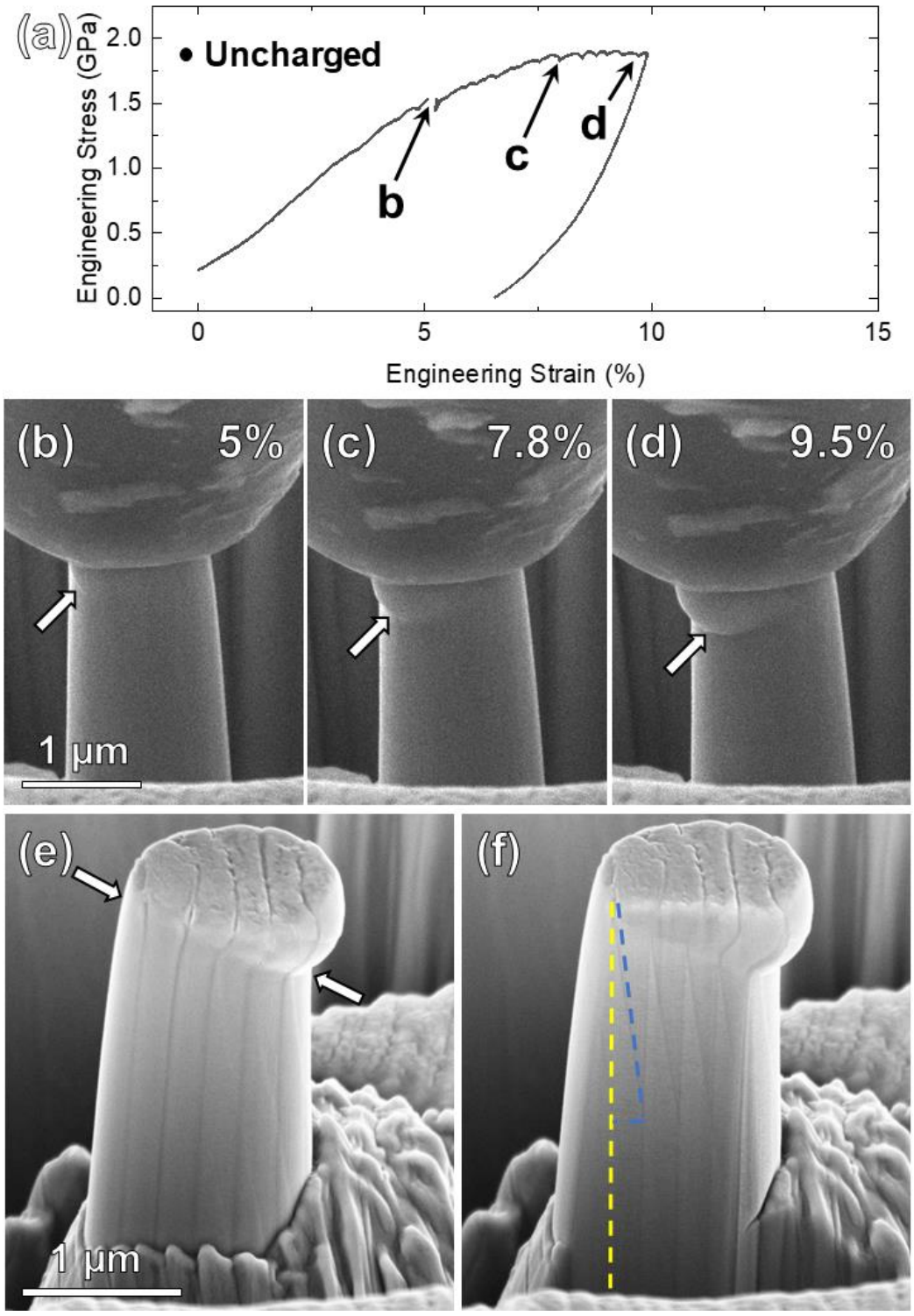

Figure 5.14 In-situ compression testing on an uncharged pearlite micropillar with vertical lamellae: (a) engineering stress-strain curve, (b), (c), (d) SEM snapshots taken from the in-situ video which are indicated on (a). (e) a post-mortem SEM image, (f) a cross-section SEM image of the compressed pillar milled via FIB. The yellow dashed line is a representative vertical cementite, and the blue dashed line shows the orientation of FIB-induced artifacts due to the different hardness of ferrite and cementite.

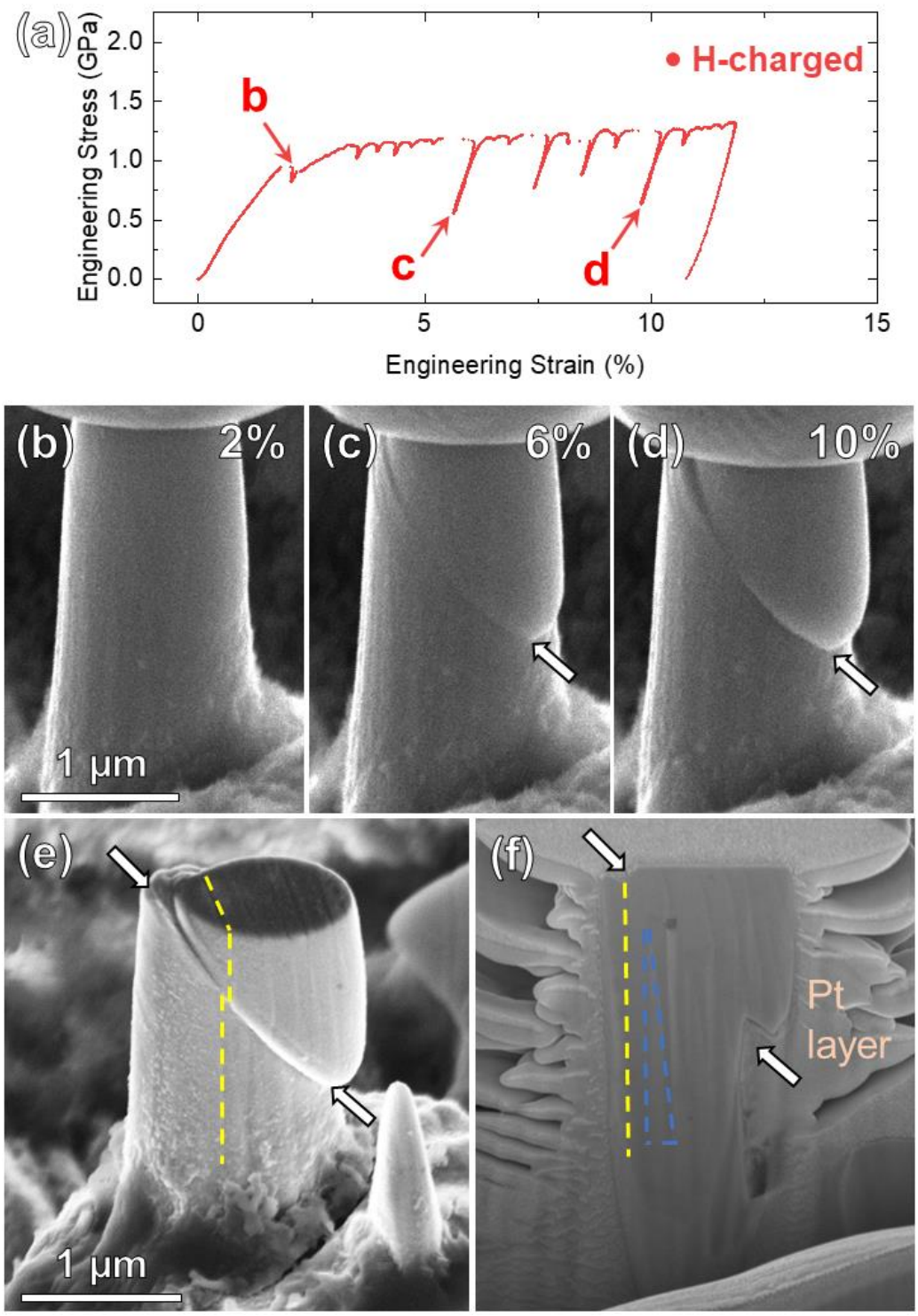

Figure 5.15 In-situ compression testing on a hydrogen-charged pearlite micropillar with vertical lamellae: (a) engineering stress-strain curve, (b), (c), (d) SEM snapshots taken from the in-situ video which are indicated on (a). (e) a post-mortem SEM image, (f) a cross-section SEM image of the compressed pillar milled via FIB. The yellow dashed line is a representative vertical cementite, and the blue dashed line shows the orientation of FIB-induced artifacts due to the different hardness of ferrite and cementite.

Figure 5.16a and Figure 5.17a contain low-magnification post-mortem ABF STEM images for the compressed pearlite micropillars with vertical lamellae before and after hydrogen charging, respectively. The cementite lamellae in uncharged micropillars showed plastic deformation without fracture in the shear band (Figure 5.16b). The lamellae themselves have not sheared. Even though highly deformed, the lamellae in the shear band still acted as barriers to avoid dislocation penetration and constrained the dislocations in the ferrite matrix between adjacent cementite lamellae. These phenomena are reproduced for other cementite lamellae in the shear band (Figure 5.16c). As a reference, an undeformed cementite lamella in the micropillar is shown (yellow arrow) in Figure 5.16d.

In contrast, the cementite lamellae in the hydrogen-charged micropillars in the vicinity of the shear band were themselves sheared/fractured, as shown in Figure 5.17b. Numerous dislocations penetrating cementite lamellae were observed in the shear band region. Similar phenomena were also observed in other parts of the pearlite micropillar (Figure 5.17c). Figure 5.17d is a representative undeformed cementite lamella in the micropillar as a reference (yellow arrow). Drawing from the APT results (Figure 4.12), the shearing of the lamella is related to either or both of the effects of hydrogen trapped at the dislocations, enhancing glide via HELP, and/or hydrogen within the cementite lamellae themselves. Hydrogen trapped in cementite may reduce the dislocation obstacle capacities of the ferrite-cementite interfaces and facilitate the approaching dislocations to penetrate the cementite lamellae. Hydrogen at the dislocations in the ferrite matrix, according to the HELP mechanism, facilitates the motion of the defects, creating cracks in the cementite lamellae, possibly due to accumulated local plasticity [274]. Given that hydrogen that travels with the dislocations can also accumulate, creating a local concentration that accelerates fracture [119], cementite lamellae may fracture in the shear band from the presence of accumulated hydrogen.

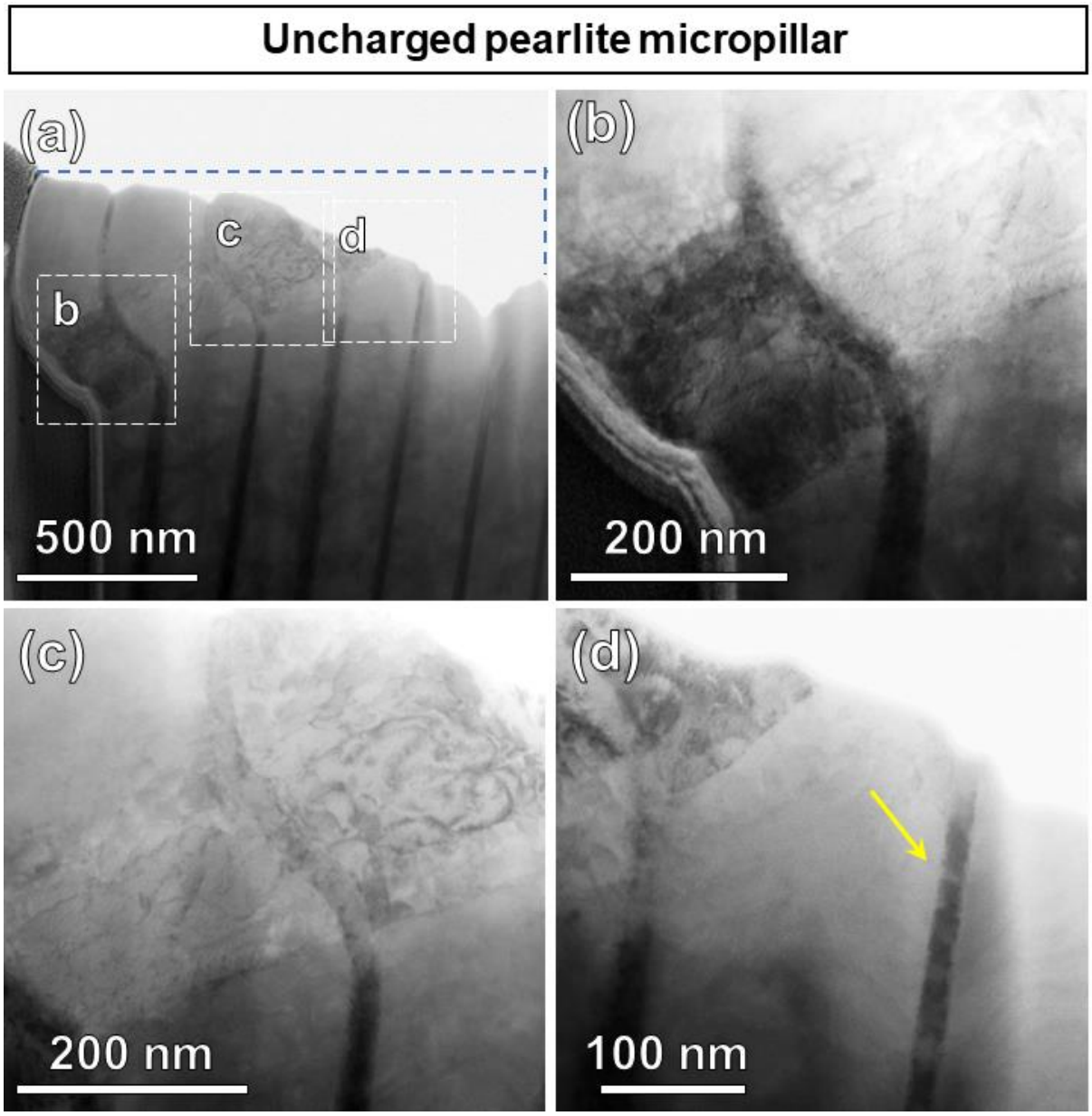

Figure 5.16 ABF-STEM images of an uncharged pearlite micropillar with vertical lamellae in the view of <111> zone axis of ferrite: (a) overall cross-section images of the micropillar, the blue dashed line delineates the shape of micropillars that was milled by FIB. (b),(c) high-magnification view of deformed cementite i.e., the dashed line region (b), (c) in (a), (d) high-magnification view of the region out of shear band, i.e., the dashed line region (d) in (a).

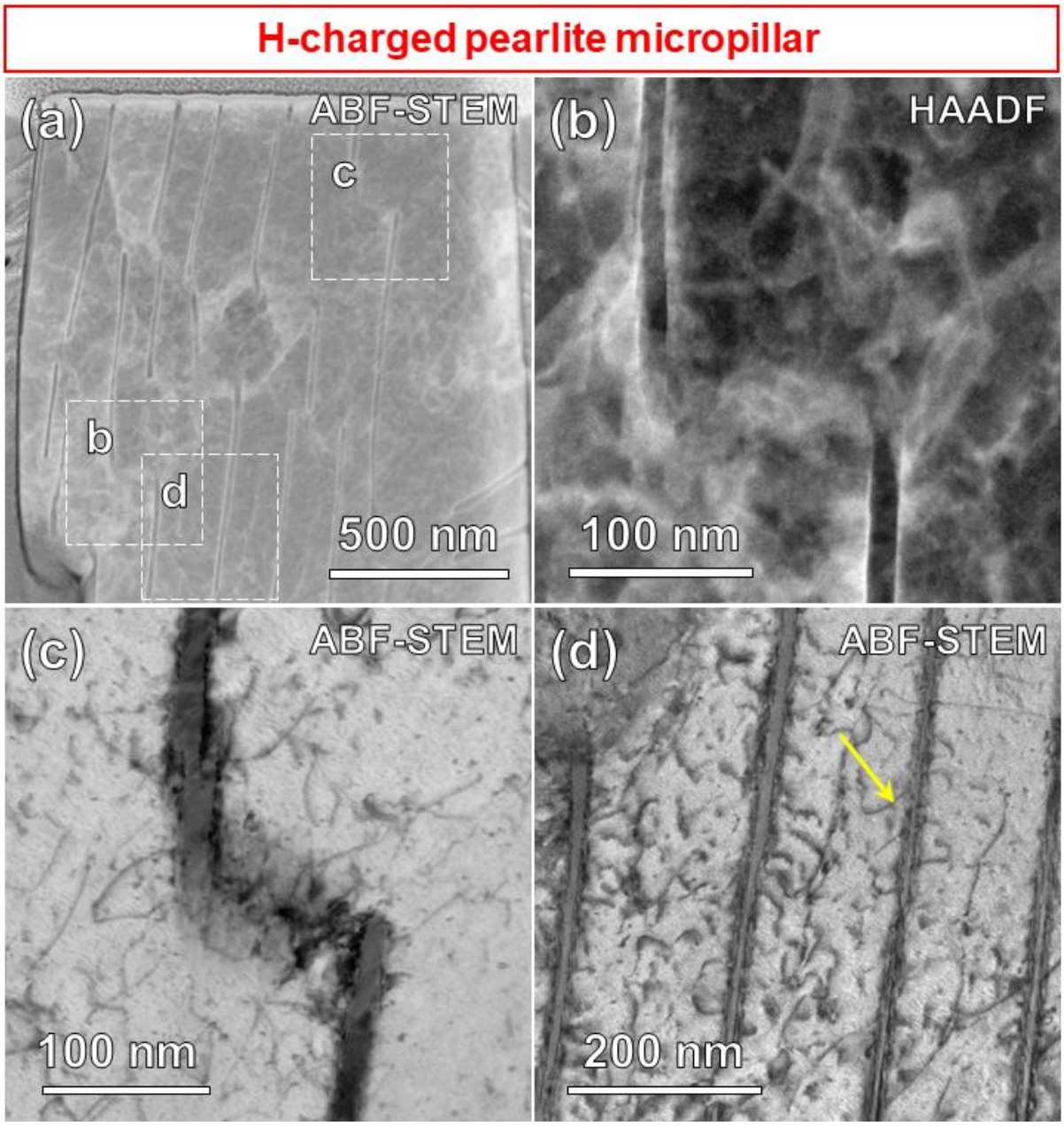

Figure 5.17 STEM images of a hydrogen-charged pearlite micropillar with vertical lamellae in the view of <111> zone axis of ferrite: (a) overall cross-section images of the micropillar, (b),(c) high-magnification view of fractured cementite i.e., the dashed line region (b), (c) in (a), (d) high-magnification view of the region out of shear band, i.e., the dashed line region (d) in (a).

5.5.2 Micropillars with buckled and kinked cementite lamellae

Out of all conducted on pearlite micropillars with vertical lamellae (over 20 successful tests), only 2-3 micropillars were observed to display deformation by buckling or kinking. Figure 5.18 provides a comparison of the mechanical responses observed during compression testing of uncharged and hydrogen-charged pillars, with the dominant mechanism being kinking. The

determination of the kinking mechanism was based on post-mortem SEM images taken after the testing (Figure 5.18b and d). In the cross-sections, the deformed cementite lamellae exhibit an 'S' shape, indicating that deformation is concentrated in the middle part while the top and bottom sections remain vertical, as shown in Figure 5.18c and e. The intensely deformed region is referred to as the kink band [275]. Figure 5.18a shows the engineering stress-strain curves for representative uncharged and hydrogen-charged micropillars with yield stresses determined as 1.46 GPa and 0.94 GPa, respectively. It is worth noting that the stress-strain curve exhibits significant strain-softening behaviors. By examining the cross-section SEM images, the presence of broken cementite lamellae provides evidence to explain this phenomenon, as dislocations are able to traverse the discontinuous parts without being blocked by the lamellae [276]. Unfortunately, it is not clear whether these broken lamellae are the result of deformation, or whether they were present in the original sample.

Figure 5.19 exhibits the results from compression testing on pearlite micropillars deformed through buckling. The introduction of hydrogen led to a reduction in yield stress, decreasing from 1.17 GPa to 0.92 GPa (Figure 5.19a). The buckling was determined based on post-mortem SEM images, which showed that the uniaxial load caused the micropillars to bow (Figure 5.19b and d). The cross-section images reveal that the integrity of the cementite lamellae in the uncharged micropillar remained after buckling. However, in the hydrogen-charged micropillar, several cementite lamellae fractured after compression testing (yellow arrows).

As buckling and kinking are rarely observed in this thesis, it is difficult to conclude what is the major factor influencing the specimen deformation with meaningful data statistics. The results in Figure 5.18 and Figure 5.19 are mainly to acknowledge the presence of variance in the micromechanical testing.

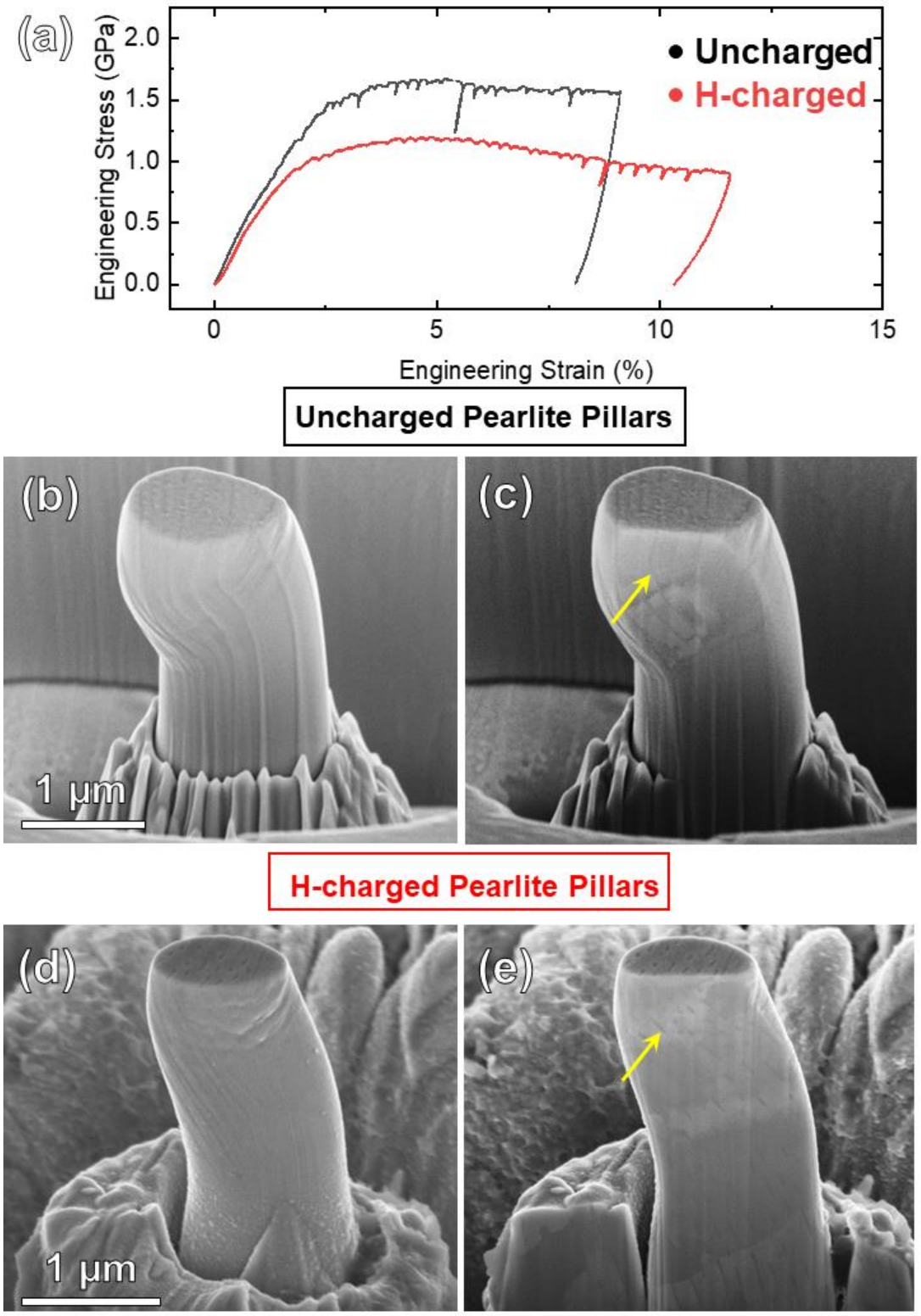

Figure 5.18 The comparison of in-situ compression testing on pearlite micropillars with vertical lamellae the deform by kinking before and after hydrogen charging: (a) engineering stress-strain curve; post-mortem SEM images for (b) uncharged and (d) hydrogen-charged pillars; cross-section SEM images of the (c) uncharged and (e) hydrogen-charged pillars milled via FIB. The yellow arrow marks a representative cementite lamella.

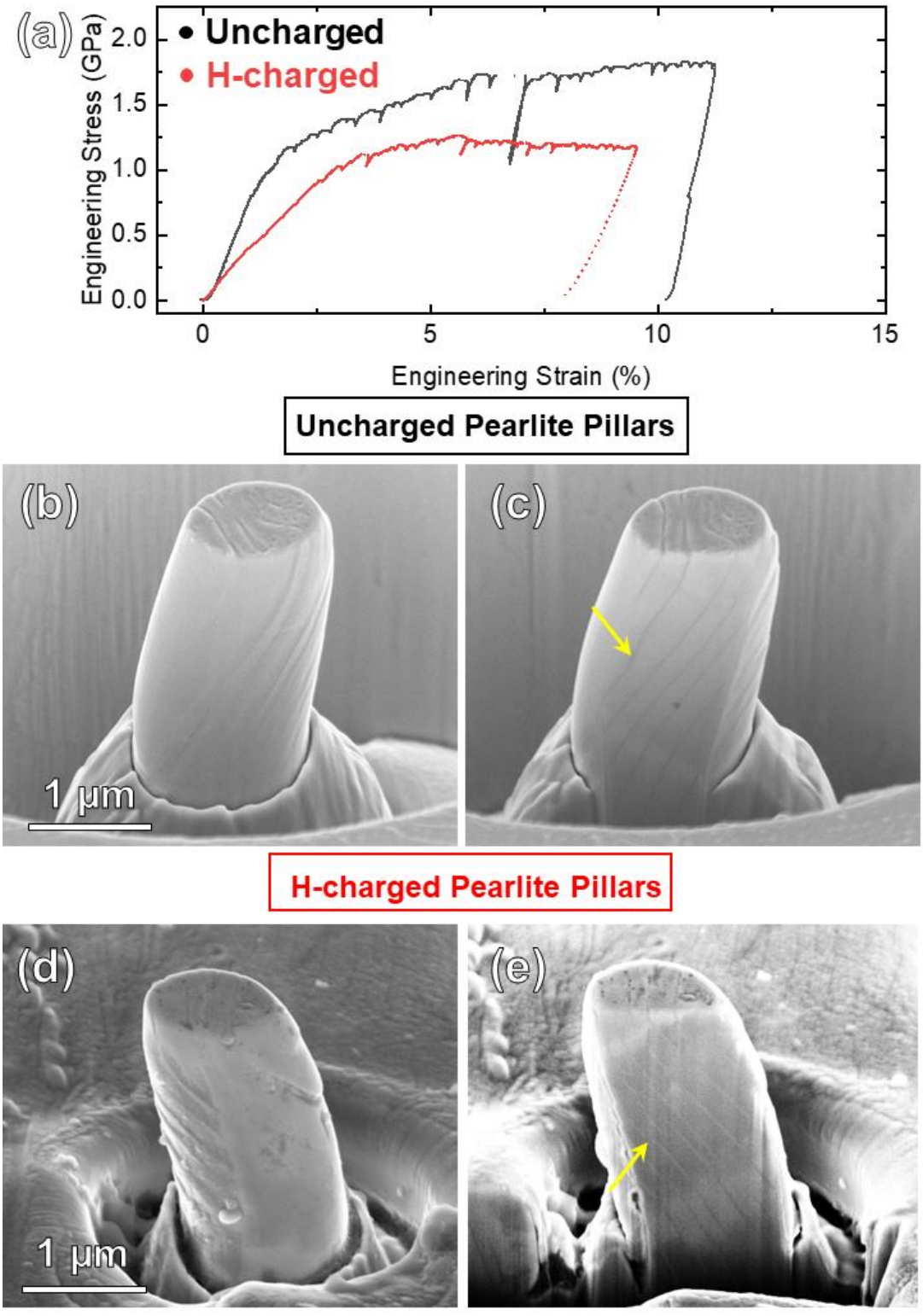

Figure 5.19 The comparison of in-situ compression testing on pearlite micropillars with horizontal lamellae dominated by buckling mechanism before and after hydrogen charging: (a) engineering stress-strain curve; post-mortem SEM images for (b) uncharged and (d) hydrogen-charged pillars; cross-section SEM images of the (c) uncharged and (e) hydrogen-charged pillars milled via FIB. The yellow arrow marks a representative cementite lamella.

5.6 Summary

In this chapter, the effect of hydrogen on the deformation of pearlite at different orientations was investigated via in-situ micro-compression testing conducted on pearlite micropillars with horizontal, inclined, and vertical cementite lamellae whose deformation behaviors have been summarized in Figure 5.20. The investigation compares the deformation of uncharged and hydrogen-charged micropillars regarding their corresponding stress–strain curves, post-mortem SEM, and post-mortem TEM and draws the following conclusions:

- The deformation behaviors vary according to the lamellae orientation, regardless of the introduction of hydrogen. Slip occurs in micropillars with inclined lamellae, while shear dominates for vertical and horizontal lamellae.
- Before charging with hydrogen, anisotropic yielding is seen. Pillars with inclined lamellae have the lowest yield strength and those with vertical and horizontal lamellae have similar yield strength.
- Hydrogen charging reduces the yield strength of pearlite micropillars regardless of lamellae orientation. Anisotropy in the yield strength is also reduced.
- Hydrogen weakens the ability of the ferrite–cementite interface which acts as an obstacle blocking dislocation motion. This could be a result of HELP, the result of hydrogen in the cementite, or both.
- Hydrogen charging changes the dislocation substructures (leading to less complex structures), by affecting their slipping and piling behaviors near the cementite lamellae.

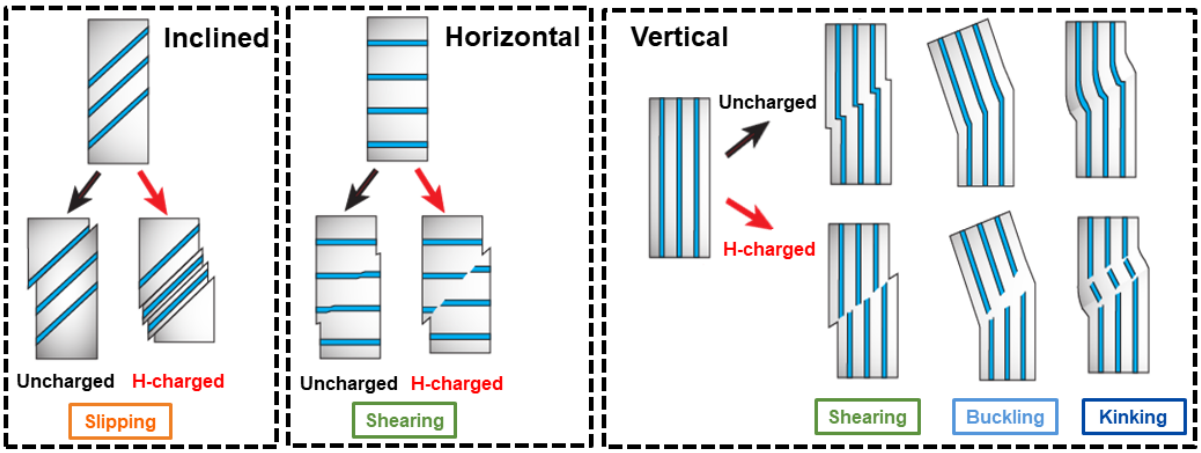

Figure 5.20 An illustration summary of deformation behaviors of pearlite micropillar with various cementite directions with/without hydrogen charging.

6 The effect of hydrogen on the deformation behavior of single-crystalline ferrite micropillars

To better understand the behaviour of pearlite, it is useful to also examine the behaviour of ferrite alone. Of course, the study of ferrite is useful in its own right. In the realm of large-scale hydrogen-based energy distribution, steel-based hydrogen infrastructure plays a crucial role, with ferrite-based steels dominating the market due to their high cost-effectiveness [277, 278]. However, ferritic steels are susceptible to HE, leading to significant risk in the transition to a hydrogen-fueled society [279-281]. Previous studies have focused on the relationship between HE susceptibility and microstructural features such as grain boundaries [282, 283], interfaces [284, 285], and secondary precipitates [231, 286]. The role of single crystal ferrite matrix has not yet been well defined by using micromechanical approaches. This is possibly due to the high diffusivity of hydrogen in ferrite lattice, restricting the study to bulk scale investigations where hydrogen retention is less challenging. Based on the successful analyses demonstrated in the previous chapters for investigating the effect of hydrogen charging on the mechanical property of pearlite micropillars, attempts were made to study the effect of hydrogen charging on ferrite micropillars.

To iterate, in-situ hydrogen charging during mechanical testing in environmental SEM is a good experimental method [287, 288], but it can lead to other uncertainties such as whether surface hydrogen can enter the bulk and cause HE effectively. Also, this project did not have access to the ESEM facility. Here an ex-situ hydrogen charging method was used, proven to be effective in previous chapters, to investigate the effect of hydrogen in ferrite micropillars. The bulk specimens on which ferrite micropillars were prepared were kept the same as those used in previous chapters and each ferrite micropillar was fabricated on a single ferrite grain. The microstructures of the bulk samples, such as ferrite-cementite interfaces and grain boundaries, are able to trap hydrogen and thus act as “hydrogen reservoirs” during the micromechanical testing. The micromechanical tests were conducted along the <001> orientation of ferrite. Other experimental methods are identical to those used in the last two chapters.

6.1 Overview of results

Figure 6.1 shows the results from in-situ micro-compression testing carried out on ferrite pillars. Engineering stress-strain curves are shown in Figure 6.1a and b correspond to three representative micropillars tested with and without hydrogen-charging. In the uncharged

condition, the yield strengths of the three ferrite micropillars are determined to be 0.53 GPa (#1), 0.61 GPa (#2), and 0.63 GPa (#3), while the yield strengths of the hydrogen-charged pillars reach 0.55 GPa (#1), 0.62 GPa (#2), and 0.45 GPa (#3). By comparing the results of these representative ferrite pillars, it appears that hydrogen charging has a slight influence on the yield strength. To confirm the effects of hydrogen on the yield strength, additional five tests were conducted on both uncharged and hydrogen-charged ferrite pillars, leading to the statistical analysis in Figure 6.1c, which suggests that the uncharged micropillars yield at 0.53±0.06 GPa and the hydrogen-charged pillars yield at 0.49±0.04 GPa. Similar to the results from the representative micropillars, the yield strength only experiences a reduction of approximately 7.5% after the introduction of hydrogen into the ferrite micropillars, which is technically within the range of error. Similar results have also been observed in micromechanical testing conducted on BCC vanadium micropillars with a compression direction of <100> [289]. Despite the fact that the method used here to determine the yield strength is different from the literature, the engineering stresses corresponding to the first strain burst remain within a narrow and statistically confident range, consistent with the results here.

The yield stress is determined by selecting the stress at the first significant strain burst (≥ 0.2% plastic strain) or substantial deflection from the initial elastic stage (around 0.2% plastic strain) which aligns with the traditional criteria of 0.2% offset plastic strain [250]. The results are consistent with a prior study that carried out tensile tests on bulk single-crystal ferrite, finding a slight reduction in yield strength after hydrogen charging [290]. The yield strengths of single crystalline ferrite micropillars are much higher than their bulk counterparts (around 250 MPa [291]), which is reasonable as the sample size may significantly increase the yield strength [226]. In micropillars, yielding is accommodated mainly with the nucleation of dislocations with the condition of dislocation-free. For this reason, the yield strength in micromechanical tests is measured by the activation stress for operating the dislocation sources. We therefore expected a decrease in micromechanical yield strength after hydrogen promotes the homogeneous nucleation of dislocation, as it facilitates the onset of plasticity based on the HELP mechanism [141]. However, this is not the case in Figure 6.1. A possible explanation is that HELP might not promote homogeneous nucleation in BCC ferrite at the onset of plasticity. This has also been suggested by previous atomistic simulation research [292]. As for the micropillars fabricated in the single crystalline ferrite grain, there are few defects or features, such as dislocations or vacancies, to trap hydrogen. The high diffusivity of hydrogen in ferrite leads to insignificant effects on the yielding strength.

The insignificant effect of hydrogen on the yield strength in single crystalline ferrite is in great contrast to the softening effect of hydrogen on pearlitic pillars (see Chapter 4). In the pearlite micropillars with inclined lamellae, hydrogen enhances slip in the ferrite phase near the ferrite-cementite interfaces (Figure 4.14). Table 6.1 indicates that hydrogen causes a greater reduction in yield strength in pearlite micropillars compared to ferrite micropillars. The different effects of hydrogen on both pillars imply that cementite, which is the only difference of both pillars in terms of microstructure, is playing an important role in the investigation on the effects of hydrogen on plasticity. Moreover, the APT results from pearlite have demonstrated that hydrogen is trapped in cementite lamellae, which can lead to a decreased barrier to dislocations penetrating the cementite lamellar. In other words, the obstructing effect of cementite on dislocation motion, i.e., the strengthening effect of cementite, has been weakened. Hydrogen is expected to be trapped by dislocations in both structures, so the hydrogen trapped in cementite must contribute to the reduction in yield strength. Regardless of the lamellae direction, the reduced yield strength of pearlite micropillars remains higher than that of ferrite micropillars. This suggests that the presence of hydrogen reduces, rather than eliminates, the dislocation-obstacle ability of the cementite lamellae.

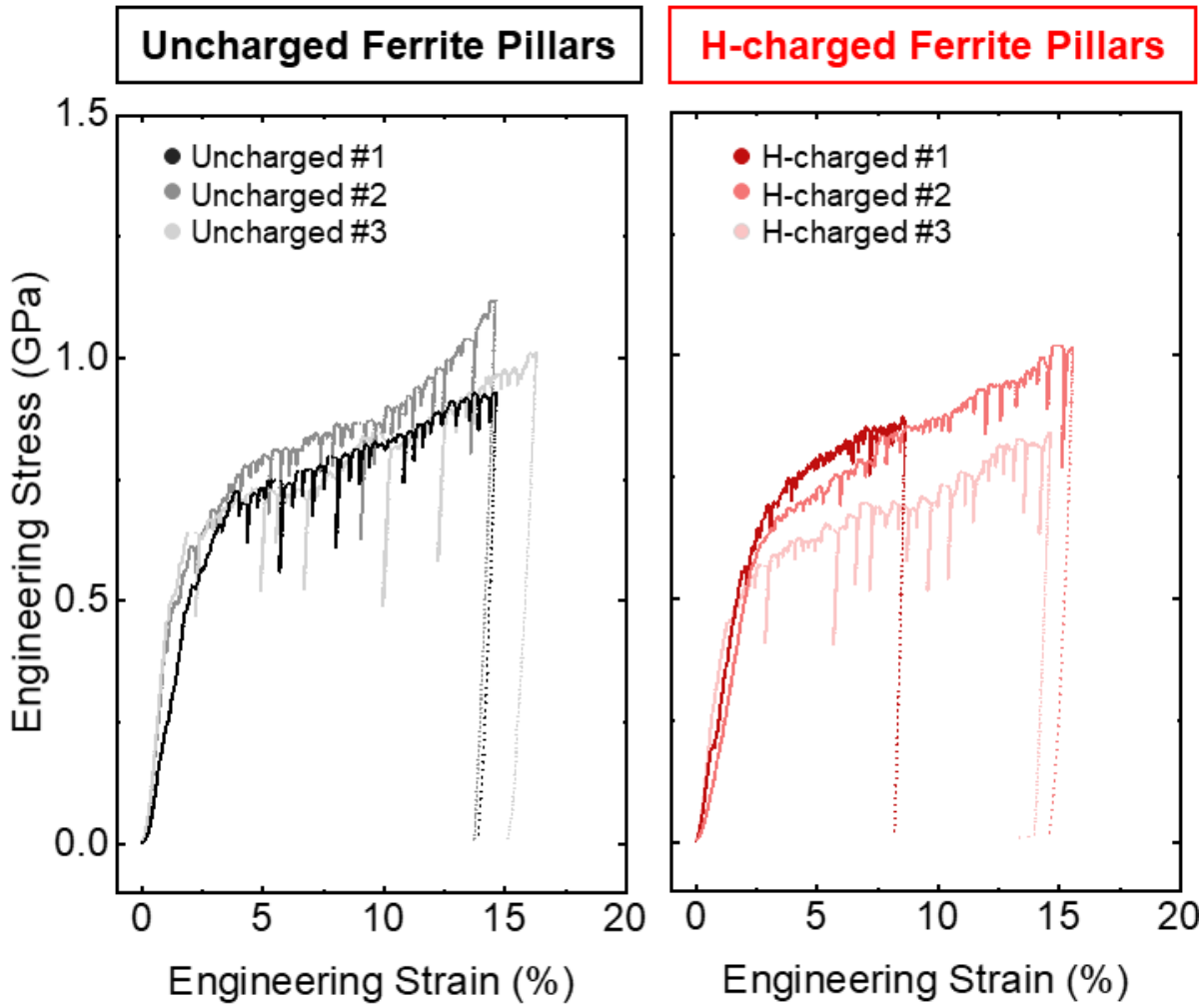

Figure 6.1 Comparison of mechanical performance of ferrite micropillars: three representative engineering stress-engineering strain curves for (a) uncharged and (b) hydrogen-charged pillars.

Table 6.1 Statistics of micromechanical testing containing five pearlite and eight ferrite micropillars tested for each condition. The errors correspond to the standard deviations (±SD) of the tests.

Microstructures	Charging states	Yield stress (GPa)
Ferrite	Uncharged	0.53±0.06
	H-charged	0.49±0.04
Pearlite (inclined lamellae)	Uncharged	1.17±0.06
	H-charged	0.89±0.08

6.2 Slip

Next, we examine the effect of hydrogen on the slip mechanism in ferrite. As a typical BCC metal, the potential slip systems are {110} <111>, {112} <111>, and {123} <111> according to Schmid´s law [293]. In this thesis, the trace of slip planes of each ferrite micropillar is based

on the combined analysis of crystalline orientation obtained from EBSD and post-mortem SEM images. After the analysis, the slip behaviors before and after hydrogen charging still follow Schmid´s law and no {123} <111> slip system was observed for the micropillars. In the <001> compression direction, the Schmid factors are calculated as 0.47 and 0.41 for the {112} and {110} slip planes, respectively.

Figure 6.2 and Figure 6.3 show the deformation processes of representative ferrite micropillars compressed without and with hydrogen, respectively, and corresponding engineering stress-strain curves. For uncharged ferrite micropillars, the yield strength was identified as 0.71 GPa from the stress-strain curve in Figure 6.2a. The first significant slip plane was found to be {110} plane (marked as a red dash line in Figure 6.2b) and then the second slip was on {112} plane (marked as a green dash line in Figure 6.2c). The following strain took place along the two activated slip systems (Figure 6.2d). The representative hydrogen-charged ferrite micropillars yielded at 0.61 GPa (Figure 6.3a), which is slightly lower than that of the uncharged specimen. The first visible slip was initiated when the applied strain reached 6%, identified as a {112} slip plane (Figure 6.3b). With the following applied strain, multiple parallel slip planes were activated but no sharp slip bands were observed (Figure 6.3c) until the last parallel slip plane started to propagate (Figure 6.3d).

Note that due to the similar Schmid factors for {110} (m = 0.41) and {112} (m = 0.47), slip planes may result in slip initiation that is contrary to Schmid's law [293, 294]. As dislocation sources in small-sized samples are limited and stochastically distributed, considering a possible situation when a weak source exists on a slip plane with a higher Schmid factor, the triggering of this slip plane is likely, even if it contradicts the Schmid law [295]. This is more frequently seen in sub-micron-sized pillars but less seen in micropillars. For the uncharged ferrite micropillars, the primary slip planes were dominated by secondary {110} planes and {112} planes began to glide after the activation of primary {110} planes. Several factors can contribute to the sequent activation of multiple slip systems, such as the combined effects of geometry and variations in the loading conditions throughout testing, or dislocation cross-slip in BCC structures [294]. For the hydrogen-charged micropillar, slip events in (110) <110> systems were not detected, contradicting Schmid's law, similar to some other BCC materials, such as BCC vanadium [289]. In hydrogen-charged ferrite pillars, slip primarily occurred along {112} planes and sequential slip band broadening towards neighboring slip planes in the same system was also observed. This activity shows the development process for

the formation of a thick slip band, which is frequently seen in materials with medium or low stacking fault energies due to promoted planar slip propensity.

Here we consider the results are a result of HELP. That is, hydrogen reduces the formation energy of dislocations and facilitates dislocation motion [170]. This is consistent with the atomistic study that indicates dislocations on {112} planes are more sensitive to hydrogen, leading to premature dislocation nucleation and gliding [296]. Also, it was shown that the presence of hydrogen can increase slip planarity and reduce dislocation cross-slip [297]. This previous finding can be used to explain the activated multiple parallel slips of {112} planes here.

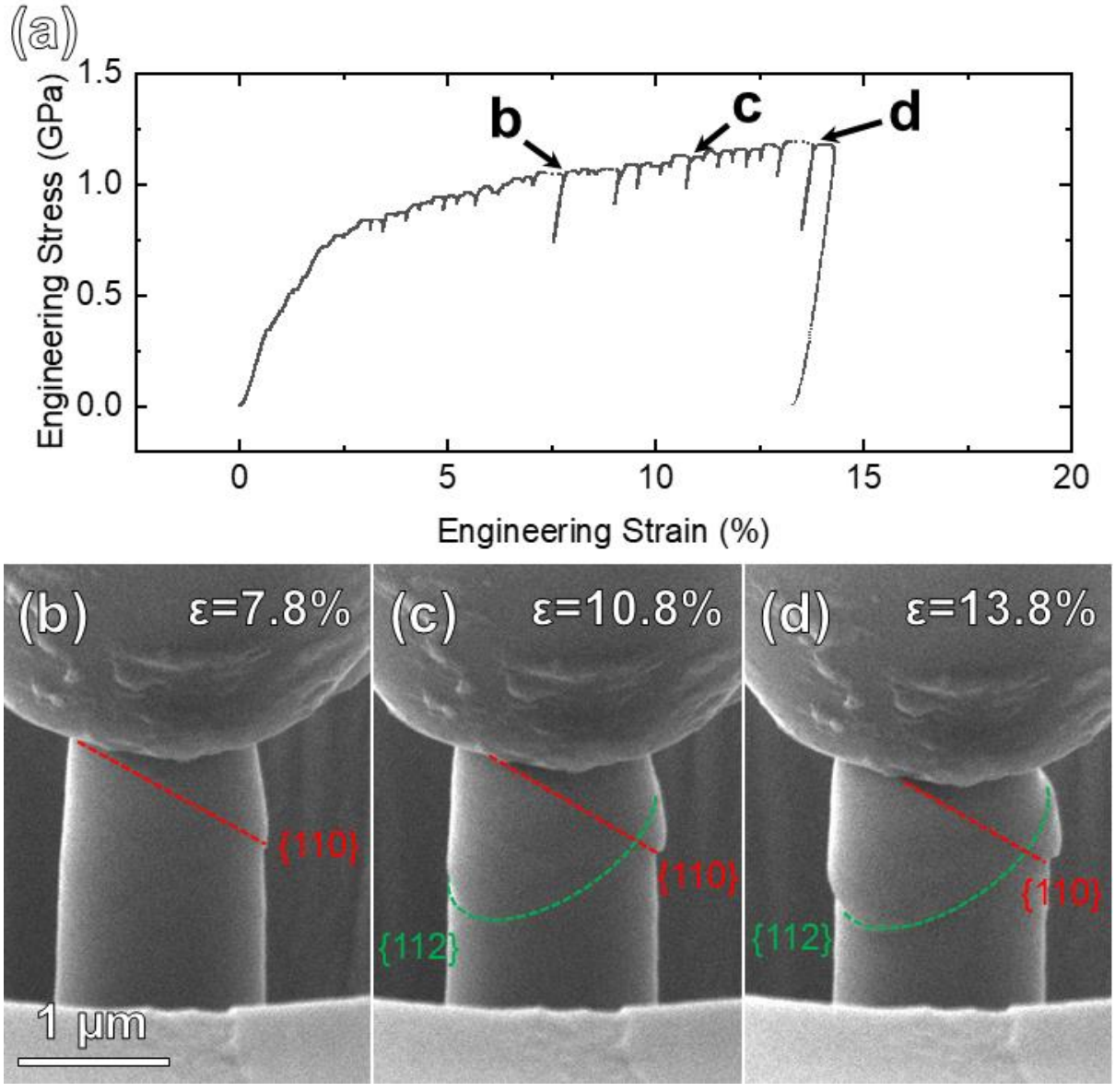

Figure 6.2 The comparison of in-situ compression testing on uncharged ferrite micropillars: (a) engineering stress-strain curve; SEM snapshots taken from the in-situ video for (b), (c), (d)

uncharged which are indicated on (a). Slip traces marked on SEM snap shots represent {110} and {112} slip planes as red and green dash lines, respectively.

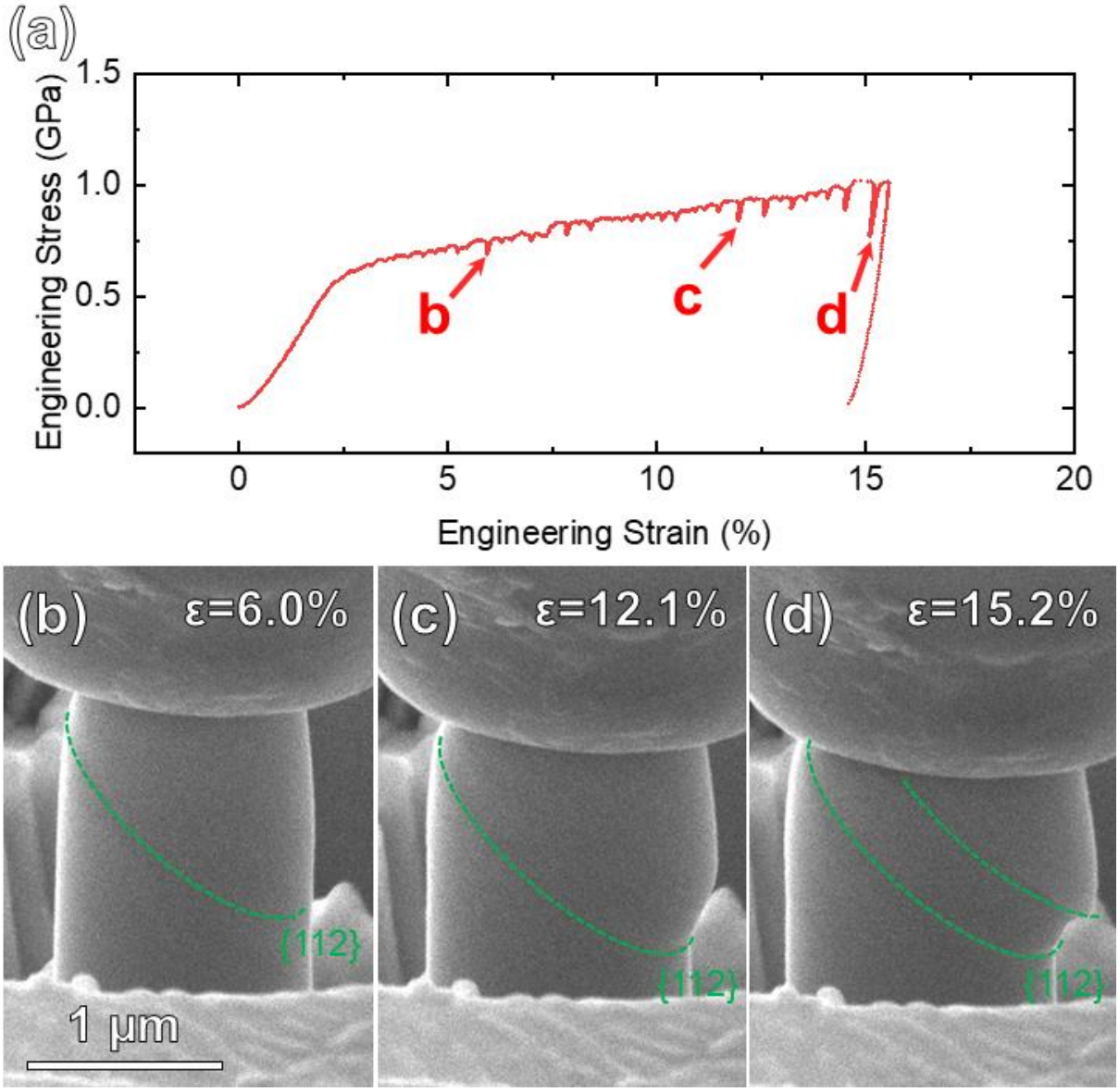

Figure 6.3 The comparison of in-situ compression testing on hydrogen-charged ferrite micropillars: (a) engineering stress-strain curve; SEM snapshots taken from the in-situ video for (b), (c), (d) uncharged which are indicated on (a). Slip traces marked on SEM snap shots represent {112} slip planes as green dash lines.

The slip behavior in ferrite micropillars can also provide evidence to explain the deformation mechanisms in the pearlite micropillars with inclined lamellae (Figure 4.14). For uncharged conditions, the dislocations in activated {110} planes are blocked by the ferrite-cementite interfaces that turn to glide along the interface resulting in slip at the interface. With

the introduction of hydrogen, if the activated {112} planes are parallel to the interfaces, slip can occur more easily. Once other {112} planes, intersecting the cementite lamellae, are activated, the slip planes will then shear the cementite lamellae, which is more likely to happen in the presence of hydrogen as the cementite is weakened by the trapped hydrogen inside cementite.

6.3 Strain hardening/softening

Hydrogen also affects strain hardening, which is an important factor for plastic deformation driven by dislocation activities. The power-law strain hardening relationship was employed, following the Ludwik-Hollomon equation:

$$\sigma_p = K_1 + K_2 \varepsilon_p^n$$

where K_1 represents the initial yield stress, K_2 is the strengthening coefficient, σ_p is the true plastic stress, ε_p is the true plastic strain, and n is the strain hardening component. The strain hardening rate (θ) can be estimated as:

$$\theta = \frac{d\theta}{d\varepsilon} = \frac{n(\sigma_p - \sigma_y)}{\varepsilon_p - \varepsilon_y}$$

where σ_y and ε_y represent yield stress and corresponding strain. Here, we applied true stress and strain at 3% in order to guarantee that the calculated results match the plastic regime. The true stress and strain are transformed from the engineering stress and strain as [272]:

$$\sigma_t = \sigma_e \times (1 - \varepsilon_e)$$

$$\varepsilon_t = -\ln(1 - \varepsilon_e)$$

where σ_t and ε_t represent true stress and strain, σ_e and ε_e are engineering stress and strain, respectively. Transferred true stress-strain curves of representative ferrite micropillars before and after hydrogen charging can be seen in Figure 6.4.

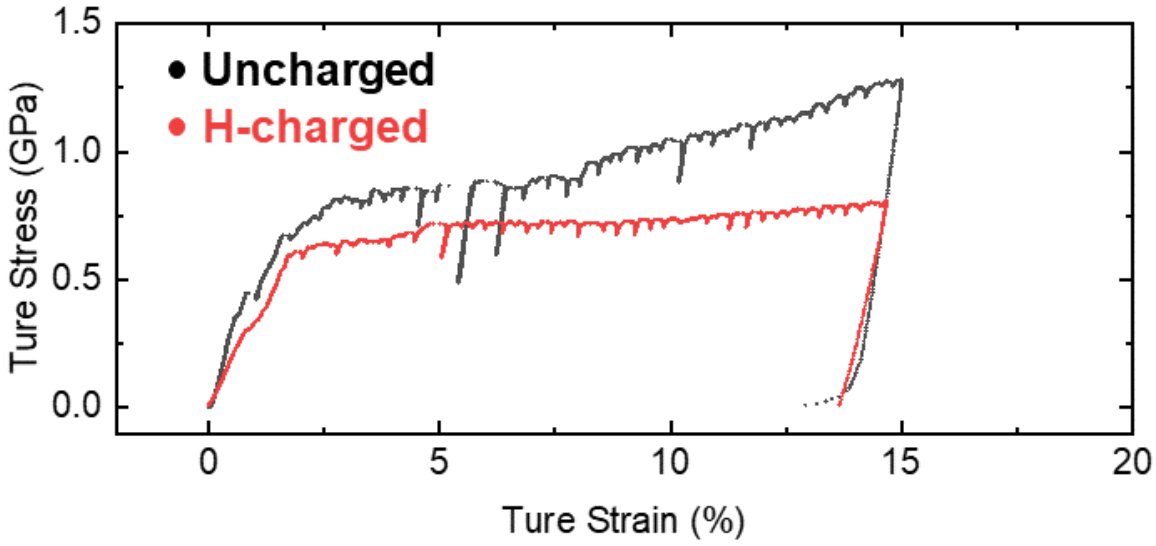

Figure 6.4 True stress-strain curves of representative uncharged/H-charged ferrite micropillars which are transferred from corresponding engineering stress-strain curves.

Figure 6.5 shows the strain hardening of ferrite micropillars with (bottom) and without (top) hydrogen charging. Eight results are incorporated in each data point. The positive and negative values indicate hardening and softening, respectively. For the uncharged micropillars (the top of Figure 6.5), the increase of applied strain reduces the strain hardening rate. This is expected since once over the initial stage of deformation, higher applied stress is required to induce more dislocation hardening. Activated dislocations resulted in primary slip, given the taper geometry of micropillar specimens, as shown in Figure 6.2b. In the following deformation, more deformation led to the stress distributing uniformly along the existing slip planes, leading to reduced hardening [227].

In contrast, in the bottom of Figure 6.5, hydrogen-charged ferrite micropillars softened in the micro-compression, which could be a result of HELP [114, 115, 298]. We postulate that the result is a sequence of the following events:

During the early stages of straining, even with lower applied stress, the escape of pre-existing dislocations and the following sufficient dislocation generated during straining, results in a relatively stable softening rate, as depicted in Figure 6.5. After that, together with the onset of the first primary slip activity initiated in the micropillar (Figure 6.3b), hydrogen then can accelerate dislocation glide and their ability to overcome obstacles under lower stress levels, leading to hydrogen-induced softening [108, 168]. Finally, the presence of hydrogen reduces the formation energy of screw dislocations, enhancing the generation of kink pairs, which

further promotes softening during plastic deformation and cross-slip dominated by screw dislocations in the BCC lattice [299]. In the H-charged pillar, it is notable to see that the softening rate remains around the same level during the entire deformation process, which implies that there is no significant change to the restriction of dislocation motion, i.e., no substantial changes to the dislocation mobility.

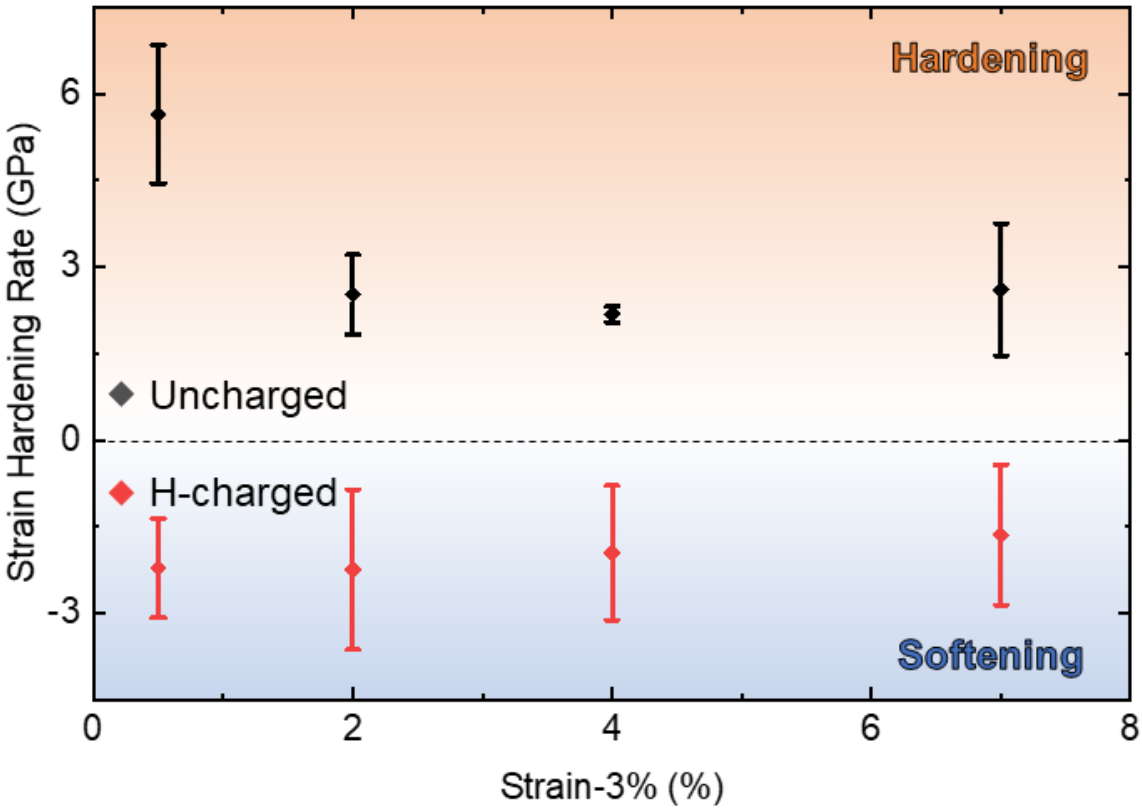

Figure 6.5 The relationship between strain hardening rate and plastic strain for uncharged and hydrogen-charged ferrite micropillars.

Table 6.2 compares the strain hardening at 10% strain for both ferrite and pearlite and both uncharged and hydrogen-charged micropillars. Pearlite micropillars exhibit strain hardening regardless of hydrogen introduction, and their corresponding hardening rate is higher than that of the ferrite micropillars. We consider the reasons below:

The presence of the cementite lamellae in pearlite plays a significant role in the strain hardening behavior. Firstly, the hard cementite lamellae may affect the activation of dislocation sources in the soft ferrite matrix, leading to changed strain hardening due to the complicated geometry [300]. Secondly, the cementite lamellae block dislocation gliding, preventing the escape of dislocations from the micropillars and simultaneously reinforcing the dislocation interactions [301], leading to a higher dislocation density, contributing to a more significant

strain hardening effect of pearlite than ferrite. In contrast, hydrogen not only weakens the strength of cementite, but it also weakens the blocking effect on dislocations moving along {112} planes (Chapter 5). The corresponding hardening effects thus become less significant.

However, the strain hardening rate of hydrogen-charged pearlite micropillars is still higher than that of uncharged ferrite micropillars. This implies that hydrogen weakens the reinforcing effects of the ferrite-cementite interface, rather than completely neutralizing them, as found in the previous chapter.

Table 6.2 Statistics of strain hardening rates containing five pearlite and eight ferrite micropillars tested for each condition. The errors correspond to the standard deviations (±SD) of the tests.

Microstructures	Charging states	Strain hardening rate (GPa)
Ferrite	Uncharged	2.61±1.14
	H-charged	-1.64±1.22
Pearlite (inclined lamellae)	Uncharged	9.11±1.11
	H-charged	5.80±1.20

6.4 Plastic stability (Strain bursting)

In contrast to the smooth stress-strain curves observed in mechanical testing conducted on bulk samples, micromechanical testing on microscale specimens reveals discrete load drops that appear as "strain bursts" along the stress-strain curves [302]. These strain bursts, characterized by intermittent plastic flow in the micropillars during compression testing, originate from dislocation avalanches [303]. Due to the high level of randomness and uncertainty associated with the plastic behavior of micropillars, it is essential to perform statistical analysis using a large database to characterize the dynamics of microscale dislocation behavior [227].

Figure 6.6 and Figure 6.7 contain statistical results of the strain burst sizes for ferrite and pearlite micropillars during micro-compression testing, respectively, both with and without hydrogen. The burst size is defined as the strain within the discrete stress drop collected from the stress-strain curve. Each case involved the collection of over 100 strain bursts for statistical analysis. In the case of ferrite micropillars, the mean burst size is larger for uncharged pillars compared to hydrogen-charged ones. Additionally, the burst sizes of uncharged pillars vary more, exhibiting a wide distribution, including large strain bursts, whereas the burst sizes of hydrogen-charged pillars are concentrated within a narrow range, primarily consisting of small strain bursts.

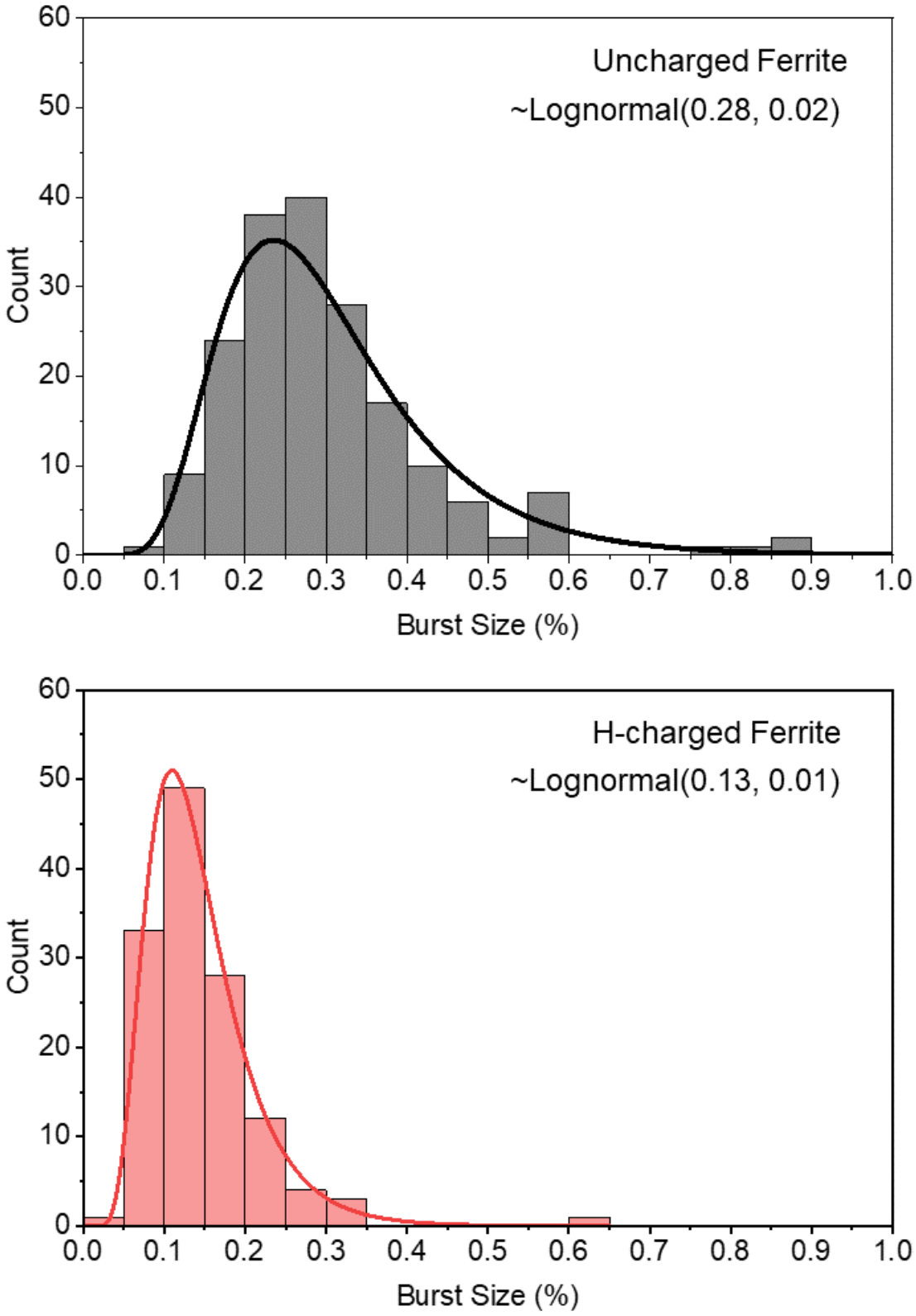

Figure 6.6 Lognormal distributions of burst size for ferrite micropillars as fitted by the solid lines with the format of "~Lognormal (μ, σ)", where μ is the mean and σ is the standard deviation of the burst size's natural logarithm.

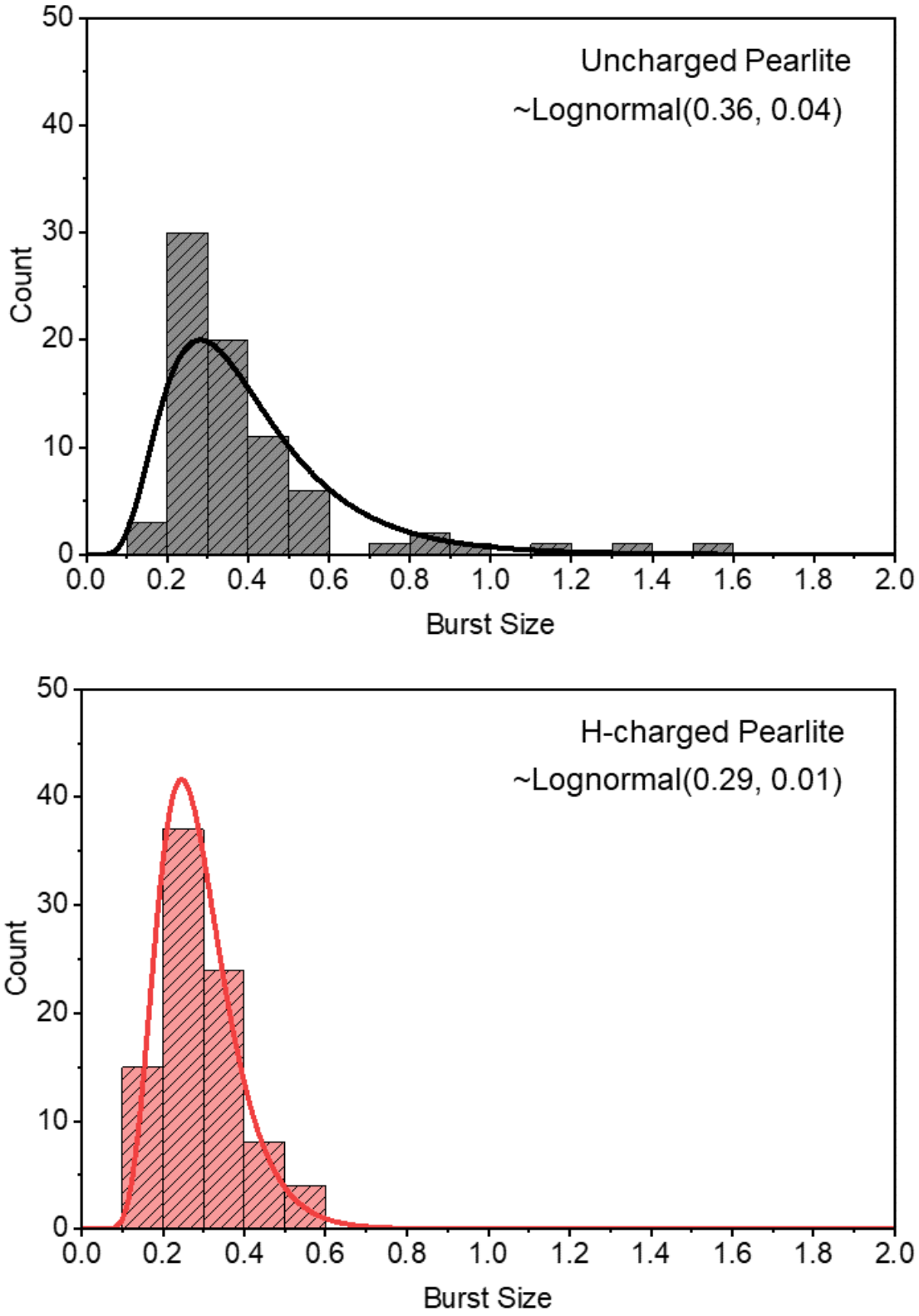

Figure 6.7 Lognormal distributions of burst size for pearlite micropillars as fitted by the solid lines with the format of "~Lognormal (μ, σ)", where μ is the mean and σ is the standard deviation of the burst size's natural logarithm.

The burst size distribution depends on several factors including the activation of dislocation sources [303], dislocation interactions [304], and dislocation speed [305]. From an energy perspective, high stress levels required to activate dislocation sources, dense dislocation interactions, and low dislocation speeds lead to the accumulation of energy during plastic deformation [306]. When the accumulated energy is released, it manifests as a strain burst whose size is determined by the magnitude of the accumulated energy. According to the HELP mechanism, hydrogen can facilitate the formation of dislocation sources, accelerate dislocation motion, and weaken dislocation-dislocation interactions. These hydrogen-induced effects decrease the energy accumulation, resulting in smaller strain burst sizes and smoother plastic behavior in the stress-strain curve.

Similar hydrogen-induced effects on strain burst size can also be observed in pearlite micropillars, as shown in Figure 6.7. Uncharged pearlite micropillars exhibit a higher mean burst size with a more dispersed distribution, while hydrogen-charged micropillars display a more concentrated distribution with a smaller mean burst size. Regardless of the presence of hydrogen, the burst sizes in pearlite pillars are larger than those in ferrite pillars. This is because the cementite lamellae in pearlite impede dislocation motion and facilitate energy accumulation. Even with the introduction of hydrogen, the weakened interface still affects dislocation behavior and energy accumulation, resulting in larger strain burst sizes compared to ferrite.

6.5 Summary

This chapter focuses on investigating the influence of hydrogen on the deformation behaviors of ferrites through in-situ micro-compression testing. The analysis primarily examines various mechanical properties, including yield strength, slip mechanisms, strain hardening, and intermittent plasticity. By comparing different groups, namely uncharged vs. hydrogen-charged and ferrite vs. pearlite, we draw the following conclusions regarding the hydrogen-induced mechanical responses:

- The introduction of hydrogen leads to a slight reduction in the yield strength of ferrite micropillars, whereas significant strength degradation is observed in hydrogen-charged pearlite micropillars due to hydrogen trapped in the cementite lamellae.
- Prior to hydrogen charging, ferrite micropillars predominantly activate the {110} <111> slip system, followed by secondary slips potentially occurring on other systems such as {110} or {112} planes. In contrast, hydrogen-charged ferrite micropillars primarily exhibit slip along {112} <111> systems.

- Regarding work hardening, the presence of hydrogen softens ferrite pillars, which exhibit strain hardening behaviors prior to hydrogen charging and reduces the intermittency of plasticity. This phenomenon can be explained by the HELP mechanism, where hydrogen facilitates the formation of dislocation sources, accelerates dislocation motion, and weakens the obstacles presented by dislocation-dislocation interactions.
- Similar effects of hydrogen on mechanical performance are observed in pearlite micropillars, although the effects are not as pronounced as those observed in ferrite. Hydrogen trapped in cementite lamellae diminishes their effectiveness as obstacles to dislocation motion rather than eliminating completely the strength-reinforcement ability of the ferrite-cementite interfaces.
- The presence of hydrogen may stabilize the plastic flow which is demonstrated by much smoother and continuous stress–strain curves. This effect can be attributed to the HELP mechanism: hydrogen mobilizes the dislocation motion and hence less energy is accumulated and released during the strain bursting.

7 Conclusions and future works

7.1 Conclusions

This thesis focused on the effects of hydrogen on the mechanical behavior of ferrite-pearlite based pipeline steels at the microscale. To simplify the complexities of studying bulk steel systems, a novel protocol was developed that combined in-situ micro-compression testing in SEM with ex-situ electrochemical hydrogen charging. The following conclusions were drawn from the research, providing scientific insights into the understanding of HE mechanisms in iron and steel metallurgy, as well as their hydrogen-related applications.

i. A simple new protocol of micromechanical testing after hydrogen charging overcomes several long-standing challenges. For conventional micromechanical testing, FIB-prepared samples are often located on single-crystal or coarse-grained bulk materials, or they are prepared as lift-out single-crystal lamella. In both cases, it is not possible to prevent the escape of hydrogen entirely. Existing in-situ hydrogen charging apparatus is constrained to testing within either a nanoindenter without in-situ video to record deformation or to ESEM, which is only available in specialist laboratories. It has been demonstrated that it is possible to test the influence of hydrogen in pre-charged pearlitic steel SEM samples. The 3 × 3 mm sample traps hydrogen by acting as a reservoir that supplies sufficient hydrogen for the duration of the experiment. This ex-situ electrochemical hydrogen charging approach is compatible with the average laboratory. In-situ SEM micromechanical testing allows the recording of the whole process of deformation for further analysis. The protocol combining ex-situ hydrogen charging and in-situ mechanical testing has been shown to be a successful approach to test samples with specific microstructural features and even a single phase.

ii. The location at which hydrogen is trapped has a significant impact on the deformation behavior of pearlite. Three-dimensional APT reconstructions reveal that in undeformed pearlite, hydrogen is trapped primarily in the cementite lamellae rather than at the ferrite-cementite interfaces. Additional hydrogen was observed in the ferrite, away from the interface, presumably at dislocations. Micro-compression testing results confirm that the introduction of hydrogen significantly reduces the yield strength of pearlitic micropillars. This is attributed to hydrogen trapping in the cementite lamellae weakening the capacity of the ferrite-cementite interfaces to block dislocation motion.

According to the HELP mechanism, hydrogen facilitates dislocation nucleation and subsequent motion through the micropillars. As a result, hydrogen-induced yielding reduction is observed, with slip traces transitioning from the ferrite–cementite interfaces in uncharged conditions to the soft ferrite matrix in the presence of hydrogen.

iii. Anisotropic mechanical behaviors, characteristic of laminate materials, are influenced by hydrogen. Prior to hydrogen charging, deformation is accommodated in shear bands in pearlite micropillars with vertical and horizontal lamellae, while slip dominates in micropillars with inclined lamellae. Distinct anisotropy of yield strength is also observed, with inclined lamellae-decorated micropillars exhibiting the lowest strength, while micropillars with vertical and horizontal lamellae yield at similar stresses. The introduction of hydrogen does not alter the deformation mechanisms but reduces the yield strength to a similar level regardless of lamellae direction, resulting in a diminished anisotropic strength. Hydrogen trapped in cementite lamellae promotes the fracture of the hard lamellae, weakening the original blockage of dislocation motion and strengthening mechanisms.

iv. Through in-situ micromechanical testing on single crystalline ferrite micropillars, the effects of hydrogen on the deformation behavior of ferrites were examined. It was found that the strength of ferrite pillars is not significantly affected by hydrogen, as the introduction of hydrogen only slightly reduces their yield strength. However, hydrogen has a pronounced influence on the plastic deformation of ferrites. Hydrogen tends to activate the {112} <111> slip system in ferrite micropillars, which is different from the normal <001> direction. Additionally, hydrogen facilitates the softening of ferrite during plastic deformation by promoting the formation of kink pairs, based on the HELP mechanism. Furthermore, hydrogen weakens the intermittency of plasticity in ferrite micropillars by reducing the size of strain bursts, thereby making the microscale deformation behaviors resemble those observed at the macroscale.

v. Finally, comparing the mechanical performance of ferrite and pearlite reveals that the yield strength of hydrogen-affected pearlite is still higher than that of uncharged ferrite. Moreover, hydrogen-softened pearlite exhibits a higher strain hardening rate than ferrite (in fact, the ferrite actually strain-softens in the presence of hydrogen). These findings

demonstrate that hydrogen weakens the blocking capacity of the ferrite-cementite interfaces rather than neutralizing it.

7.2 Future works

The protocol combining in-situ SEM micromechanical testing and ex-situ electrochemical hydrogen charging has significant potential for investigating the effects of hydrogen on the mechanical performance of other specific microstructures. The study focused on pearlite and ferrite as model microstructures to examine hydrogen's influence on pipeline steel deformation behaviors. However, as this protocol is still in its early stages – there are areas for technical improvements and unresolved issues that should be highlighted for future extensions of this project.

i. First, it is possible to improve the experimental process for selecting bulk materials on which FIB-prepared micropillars are located. The mean grain size of 4 μm proved challenging in terms of selecting appropriate grains, consuming valuable time. Increasing the grain size would enhance sample preparation efficiency and experimental consistency.

ii. Secondly, while the thesis focused on compression testing of micropillars, which is good for investigating hydrogen's effects on dislocation dynamics and mechanical response, it is important to note that embrittlement phenomena cannot be observed solely through compression testing. The test is terminated based on manually scheduled compression distance rather than sample fracture. Further investigations should include additional testing modes such as bending tests on microcantilever samples with surface notches and tensile testing on microscale dog-bone specimens. In addition to microscale SSRT, fatigue testing based on the protocol would also be valuable for exploring hydrogen-induced effects on fatigue life.

iii. Thirdly, Chapter 5 examined the effects of hydrogen on the anisotropic deformation behavior of pearlite. However, the interlamellar distance, an important characteristic of pearlite, was not investigated. Decreasing the interlamellar distance while maintaining the same micropillar geometry would be useful to probe the strengthening mechanism of pearlite, as it transitions from the Hall-Petch model to the confined layer slip mechanism. The results in Chapter 5 suggested that the strengthening mechanism

transition appears to be absent in the hydrogen-charged samples. Moreover, pearlitic steels often contain significant strain from cold drawing to increase their strength, particularly for high-strength steel wires or cables. It is thus important to understand the role of hydrogen in pearlitic steels that have undergone various straining conditions. Testing focused on interlamellar distance or pre-strained conditions would confirm whether the transformation of strengthening mechanisms is delayed or non-existent.

iv. Lastly, the fraction of cementite lamellae is likely to influence the deformation mechanisms of pearlite micropillars. To investigate the effects of lamellae fraction, the size of the micropillar can be changed while keeping the interlamellar distance constant. Increasing the lamellae fraction alters the dominant strengthening mechanisms from the "small is strong" theory for single crystal ferrite to reinforced ferrite-cementite interfaces. There exists a transition zone where the "small is strong" mechanism is about to disappear while interface strengthening has not yet come into effect. This transition zone can be tested under uncharged conditions. Additionally, the introduction of hydrogen may diminish the effects of the transition zone or even weaken both strengthening mechanisms. This hypothesis might be examined through micromechanical testing on hydrogen-charged samples.

v. Overall, the findings of this thesis have confirmed the feasibility of conducting tests on single crystalline ferrite, where hydrogen exhibits its fastest diffusion. This means that the investigation of hydrogen-induced plasticity is now accessible to conventional studies on micro- or nanoscale materials. The thesis explored the involvement of hydrogen in reducing the plasticity intermittency (Chapter 6), which is characteristic of small-scale materials. Therefore, it is important to emphasize and systematically study the relationship between hydrogen and the size-effect on strength. Additionally, apart from the BCC materials examined in this thesis, other crystal structures such as FCC or HCP can also be incorporated into this protocol. With different crystal structures, it is expected that fundamental research on deformation mechanisms, such as twinning, and corresponding factors like stacking fault energy or phase transformation, could be explored as extensions of this project.

References

1. Veziroglu, T.N., *21st Century's energy: Hydrogen energy system*, in *Assessment of hydrogen energy for sustainable development*. 2007, Springer. p. 9-31.

2. Abe, J.O., et al., *Hydrogen energy, economy and storage: review and recommendation.* International journal of hydrogen energy, 2019. **44**(29): p. 15072-15086.

3. Energy, U.D.o., *The Department of Energy Hydrogen Program Plan*. 2020, US Government Printing Office Washington, DC.

4. Jia, J., et al., *Solar water splitting by photovoltaic-electrolysis with a solar-to-hydrogen efficiency over 30%.* Nature communications, 2016. **7**(1): p. 1-6.

5. Balta, M.T., I. Dincer, and A. Hepbasli, *Thermodynamic assessment of geothermal energy use in hydrogen production.* International Journal of hydrogen energy, 2009. **34**(7): p. 2925-2939.

6. Liu, H., et al., *Microbial electrolysis: novel technology for hydrogen production from biomass.* Biofuels, 2010. **1**(1): p. 129-142.

7. Kurtz, J., et al., *Renewable hydrogen-economically viable: Integration into the US transportation sector.* IEEE Electrification Magazine, 2018. **6**(1): p. 8-18.

8. Hawkins, S. and D. Joffe, *Technological characterisation of hydrogen storage and distribution technologies.* Policy Studies Institute: London, UK, 2006.

9. Moradi, R. and K.M. Groth, *Hydrogen storage and delivery: Review of the state of the art technologies and risk and reliability analysis.* International Journal of Hydrogen Energy, 2019. **44**(23): p. 12254-12269.

10. Melaina, M.W., O. Antonia, and M. Penev, *Blending hydrogen into natural gas pipeline networks: a review of key issues.* 2013.

11. Blanton, E.M., D.M.C. Lott, and K.N. Smith, *Investing in the US natiral gas pipeline system to support net-zero targets.* 2021.

12. Melaina, M.W., O. Antonia, and M. Penev, *Blending hydrogen into natural gas pipeline networks. a review of key issues*. 2013, National Renewable Energy Laboratory.

13. Vudumu, S.K., *Experimental and computational investigations of hydrogen safety, dispersion and combustion for transportation applications.* 2010.

14. Yang, F., et al., *Review on hydrogen safety issues: Incident statistics, hydrogen diffusion, and detonation process.* International Journal of Hydrogen Energy, 2021.

15. Yang, C. and J. Ogden, *Determining the lowest-cost hydrogen delivery mode.* International Journal of Hydrogen Energy, 2007. **32**(2): p. 268-286.

16. Somerday, B.P. and C.W. San Marchi, *EFFECTS OF HYDROGEN GAS ON STEEL VESSELS AND PIPELINES*. 2006, Sandia National Lab.(SNL-CA), Livermore, CA (United States).

17. Das, S.K., *Materials Solutions for Hydrogen Delivery in Pipelines.* FY 2007 Annual Progress Report, 2007.

18. Rosado, D.B., et al., *Latest developments in mechanical properties and metallurgical features of high strength line pipe steels.* International Journal of Sustainable Mechanical Engineering and Design, 2013. **4**(1).

19. DeArdo, A., et al., *On strength of microalloyed steels: an interpretive review.* Materials Science and Technology, 2009. **25**(9): p. 1074-1082.

20. DeArdo, A.J., *The metallurgy of high strength linepipe steels.* Pipelines for the 21th Century, 2005: p. 85-100.

21. Sha, Q. and D. Li, *Microstructure, mechanical properties and hydrogen induced cracking susceptibility of X80 pipeline steel with reduced Mn content.* Materials Science and Engineering: A, 2013. **585**: p. 214-221.

22. Huang, F., et al., *Effect of microstructure and inclusions on hydrogen induced cracking susceptibility and hydrogen trapping efficiency of X120 pipeline steel.* Materials Science and Engineering: A, 2010. **527**(26): p. 6997-7001.

23. Li, X., et al., *Structure–property–fracture mechanism correlation in heat-affected zone of X100 ferrite− bainite pipeline steel.* Metallurgical and Materials Transactions E, 2015. **2**(1): p. 1-11.

24. Zhou, Q., et al., *The influence of isothermal holding times on microstructural evolution of X90 linepipe steel.* Materials Research, 2019. **22**.

25. Specification, A., *5L 46th Edition, 2018.* Line Pipe, American Petroleum Institute.

26. Johnson, W.H., *II. On some remarkable changes produced in iron and steel by the action of hydrogen and acids.* Proceedings of the Royal Society of London, 1875. **23**(156-163): p. 168-179.

27. Lynch, S., *Hydrogen embrittlement phenomena and mechanisms.* Corrosion Reviews, 2012. **30**(3-4): p. 105-123.

28. Hardie, D., E. Charles, and A. Lopez, *Hydrogen embrittlement of high strength pipeline steels.* Corrosion Science, 2006. **48**(12): p. 4378-4385.

29. Krauss, G., *Steels: processing, structure, and performance*. 2015: Asm International.

30. Bhadeshia, H. and R. Honeycombe, *Steels: microstructure and properties*. 2017: Butterworth-Heinemann.

31. Puls, M. and J. Kirkaldy, *The pearlite reaction.* Metallurgical and Materials Transactions B, 1972. **3**: p. 2777-2796.

32. Joung, S., et al., *Aging behavior and delamination in cold drawn and post-deformation annealed hyper-eutectoid steel wires.* Materials Science and Engineering: A, 2013. **586**: p. 171-177.

33. Ronevich, J.A., B.P. Somerday, and C.W. San Marchi, *Effects of microstructure banding on hydrogen assisted fatigue crack growth in X65 pipeline steels.* International Journal of Fatigue, 2016. **82**: p. 497-504.

34. Li, Y., et al., *Segregation stabilizes nanocrystalline bulk steel with near theoretical strength.* Physical review letters, 2014. **113**(10): p. 106104.

35. Zhou, D. and G. Shiflet, *Ferrite: cementite crystallography in pearlite.* Metallurgical Transactions A, 1992. **23**: p. 1259-1269.

36. Isaichev, I., *Orientatsiya tsementita v otpushchennoi uglerodistoi stali.* ZHURNAL TEKHNICHESKOI FIZIKI, 1947. **17**(7): p. 835-838.

37. Bagaryatsky, Y., *Likely mechanism for the tempering of martensite.* Dokl Aksd Nauk SSSR, 1950. **73**: p. 1161-1164.

38. Petch, N., *The orientation relationships between cementite and α-iron.* Acta Crystallographica, 1953. **6**(1): p. 96-96.

39. Pitsch, W., *Der Orientierungszusammenhang zwischen Zementit und ferrit im perlit.* Acta metallurgica, 1962. **10**(1): p. 79-80.

40. Michler, T. and J. Naumann, *Influence of high pressure hydrogen on the tensile and fatigue properties of a high strength Cu–Al–Ni–Fe alloy.* international journal of hydrogen energy, 2010. **35**(20): p. 11373-11377.

41. Pourazizi, R., M. Mohtadi-Bonab, and J. Szpunar, *Investigation of different failure modes in oil and natural gas pipeline steels.* Engineering Failure Analysis, 2020. **109**: p. 104400.

42. Sakintuna, B., F. Lamari-Darkrim, and M. Hirscher, *Metal hydride materials for solid hydrogen storage: a review.* International journal of hydrogen energy, 2007. **32**(9): p. 1121-1140.

43. Schlapbach, L. and A. Züttel, *Hydrogen-storage materials for mobile applications.* Nature, 2001. **414**(6861): p. 353-358.

44. Liu, Q., et al., *Determination of the hydrogen fugacity during electrolytic charging of steel.* Corrosion Science, 2014. **87**: p. 239-258.

45. San Marchi, C., B.P. Somerday, and S.L. Robinson, *Permeability, solubility and diffusivity of hydrogen isotopes in stainless steels at high gas pressures.* International Journal of Hydrogen Energy, 2007. **32**(1): p. 100-116.

46. Hickel, T., et al., *Ab initio based understanding of the segregation and diffusion mechanisms of hydrogen in steels.* Jom, 2014. **66**(8): p. 1399-1405.

47. Nagumo, M., *Fundamentals of hydrogen embrittlement*. 2016: Springer.

48. Turnbull, A., *Hydrogen diffusion and trapping in metals*, in *Gaseous hydrogen embrittlement of materials in energy technologies*. 2012, Elsevier. p. 89-128.

49. Nagano, M., et al., *Hydrogen diffusivity in high purity alpha iron.* Scripta Metallurgica, 1982. **16**(8): p. 973-976.

50. Johnson, H.H., *Hydrogen in iron.* Metallurgical Transactions B, 1988. **19**(5): p. 691-707.

51. Wang, R., *Effects of hydrogen on the fracture toughness of a X70 pipeline steel.* Corrosion Science, 2009. **51**(12): p. 2803-2810.

52. Enomoto, M., et al., *Hydrogen absorption into austenitic stainless steels under high-pressure gaseous hydrogen and cathodic charge in aqueous solution.* Metallurgical and Materials Transactions E, 2014. **1**(4): p. 331-340.

53. Wei, F., T. Hara, and K. Tsuzaki, *Precise determination of the activation energy for desorption of hydrogen in two Ti-added steels by a single thermal-desorption spectrum.* Metallurgical and Materials Transactions B, 2004. **35**(3): p. 587-597.

54. Barrera, O., et al., *Understanding and mitigating hydrogen embrittlement of steels: a review of experimental, modelling and design progress from atomistic to continuum.* Journal of materials science, 2018. **53**(9): p. 6251-6290.

55. Michler, T. and M.P. Balogh, *Hydrogen environment embrittlement of an ODS RAF steel–Role of irreversible hydrogen trap sites.* international journal of hydrogen energy, 2010. **35**(18): p. 9746-9754.

56. Counts, W., C. Wolverton, and R. Gibala, *First-principles energetics of hydrogen traps in α-Fe: Point defects.* Acta Materialia, 2010. **58**(14): p. 4730-4741.

57. Choo, W. and J.Y. Lee, *Thermal analysis of trapped hydrogen in pure iron.* Metallurgical Transactions A, 1982. **13**(1): p. 135-140.

58. Kumnick, A. and H. Johnson, *Deep trapping states for hydrogen in deformed iron.* Acta Metallurgica, 1980. **28**(1): p. 33-39.

59. Pressouyre, G. and I. Bernstein, *A quantitative analysis of hydrogen trapping.* Metallurgical transactions A, 1978. **9**(11): p. 1571-1580.

60. Pressouyre, G., *Trap theory of hydrogen embrittlement.* Acta Metallurgica, 1980. **28**(7): p. 895-911.

61. Au, J. and H. Birnbaum, *Magnetic relaxation studies of the motion of hydrogen and deuterium in iron.* Acta Metallurgica, 1978. **26**(7): p. 1105-1116.

62. Kim, K.B. and S.I. Pyun, *EFFECT OF VACANCIES ON HYDROGEN DIFFUSIVITY AND SOLUBILITY IN PURE IRON AT ROOM TEMPERATURE.* Archiv fur das Eisenhuttenwesen, 1982. **53**(10): p. 397-401.

63. Kim, K.-T., S.-I. Pyun, and E.M. Riecke, *Vacancies as hydrogen trap sites in iron.* Journal of materials science letters, 1985. **4**(5): p. 624-626.

64. Myers, S., S. Picraux, and R. Stoltz, *Defect trapping of ion-implanted deuterium in Fe.* Journal of Applied Physics, 1979. **50**(9): p. 5710-5719.

65. Paxton, A.T., *From quantum mechanics to physical metallurgy of steels.* Materials Science and Technology, 2014. **30**(9): p. 1063-1070.

66. Lee, J. and J.Y. Lee, *Hydrogen trapping in AISI 4340 steel.* Metal Science, 1983. **17**(9): p. 426-432.

67. Paxton, A.T. and I.H. Katzarov, *Quantum and isotope effects on hydrogen diffusion, trapping and escape in iron.* Acta Materialia, 2016. **103**: p. 71-76.

68. Hagi, H. and Y. Hayashi, *Effect of dislocation trapping on hydrogen and deuterium diffusion in iron.* Transactions of the Japan institute of metals, 1987. **28**(5): p. 368-374.

69. Takai, K., et al., *Identification of trapping sites in high-strength steels by secondary ion mass spectrometry for thermally desorbed hydrogen.* Journal of the Japan Institute of Metals and Materials, 1996. **60**(12): p. 1155-1162.

70. Bernstein, I.M., *The Effect of Hydrogen on the Deformation of Iron*. 1974, CARNEGIE-MELLON UNIV PITTSBURGH PA METALS RESEARCH LAB.

71. Lin, Y.-C., et al., *Response of hydrogen desorption and hydrogen embrittlement to precipitation of nanometer-sized copper in tempered martensitic low-carbon steel.* JOM, 2019. **71**(4): p. 1349-1356.

72. Ono, K. and M. Meshii, *Hydrogen detrapping from grain boundaries and dislocations in high purity iron.* Acta metallurgica et materialia, 1992. **40**(6): p. 1357-1364.

73. Parvathavarthini, N., et al., *Studies on hydrogen permeability of 2.25% Cr–1% Mo ferritic steel: correlation with microstructure.* Journal of Nuclear Materials, 2001. **288**(2-3): p. 187-196.

74. Asaoka, T., et al., *Observation of hydrogen trapping in Fe-0.15 wt% Ti alloy by high resolution autoradiography.* Corrosion, 1978. **34**(2): p. 39-47.

75. Lee, H. and J.-Y. Lee, *Hydrogen trapping by TiC particles in iron.* Acta Metallurgica, 1984. **32**(1): p. 131-136.

76. Pérez Escobar, D., et al., *Thermal desorption spectroscopy study of the interaction of hydrogen with TiC precipitates.* Metals and Materials International, 2013. **19**(4): p. 741-748.

77. Wei, F.G. and K. Tsuzaki, *Quantitative analysis on hydrogen trapping of TiC particles in steel.* Metallurgical and Materials Transactions A, 2006. **37**(2): p. 331-353.

78. Lin, Y.-T., et al., *Role of Vanadium Carbide in Hydrogen Embrittlement of Press-Hardened Steels: Strategy From 1500 to 2000 MPa.* Frontiers in Materials, 2021: p. 432.

79. Asahi, H., D. Hirakami, and S. Yamasaki, *Hydrogen trapping behavior in vanadium-added steel.* ISIJ international, 2003. **43**(4): p. 527-533.

80. Yamasaki, S. and T. Takahashi, *Evaluation method of delayed fracture property of high strength steels.* Tetsu-to-Hagané, 1997. **83**(7): p. 454-459.

81. Wallaert, E., et al., *Thermal desorption spectroscopy evaluation of the hydrogen-trapping capacity of NbC and NbN precipitates.* Metallurgical and Materials Transactions A, 2014. **45**(5): p. 2412-2420.

82. Wei, F.-G. and K. Tsuzaki. *Hydrogen trapping character of nano-sized NbC precipitates in tempered martensite*. in *Proceedings of the 2008 International Hydrogen Conference-Effects of Hydrogen on Materials*. 2009. ASM International Materials Park Ohio.

83. Depover, T. and K. Verbeken, *Evaluation of the role of Mo2C in hydrogen induced ductility loss in Q&T FeCMo alloys.* international journal of hydrogen energy, 2016. **41**(32): p. 14310-14329.

84. Hinotani, S., Y. Ohmori, and F. Terasaki, *Effects of Fe3C and Mo2C precipitation on hydrogen diffusivity and hydrogen embrittlement in iron alloys.* Materials Science and Engineering, 1985. **76**: p. 57-69.

85. Thomas, R.L., et al., *Trap-governed hydrogen diffusivity and uptake capacity in ultrahigh-strength AERMET 100 steel.* Metallurgical and Materials Transactions A, 2002. **33**(7): p. 1991-2004.

86. Hong, G.-W. and J.-Y. Lee, *The interaction of hydrogen and the cementite-ferrite interface in carbon steel.* Journal of materials science, 1983. **18**(1): p. 271-277.

87. Wei, F.-G. and K. Tsuzaki, *Response of hydrogen trapping capability to microstructural change in tempered Fe–0.2 C martensite.* Scripta materialia, 2005. **52**(6): p. 467-472.

88. Hsu, Y.-T., et al., *Hydrogen-induced embrittlement of nickel-chromium-molybdenum containing HSLA steels.* Journal of the Chinese Institute of Engineers, 2020. **43**(1): p. 58-66.

89. Serra, E., A. Perujo, and G. Benamati, *Influence of traps on the deuterium behaviour in the low activation martensitic steels F82H and Batman.* Journal of Nuclear Materials, 1997. **245**(2): p. 108-114.

90. Esteban, G.A., et al., *Hydrogen transport and trapping in ODS-EUROFER.* Fusion Engineering and Design, 2007. **82**(15): p. 2634-2640.

91. Huang, G.-Y., X. Hu, and B.D. Wirth, *First-principles investigations of hydrogen trapping in Y₂O₃ and the Y₂O₃|bcc Fe interface.* Journal of Physics: Condensed Matter, 2020. **32**(49): p. 495001.

92. Turnbull, A. and R.B. Hutchings, *Analysis of hydrogen atom transport in a two-phase alloy.* Materials Science and Engineering: A, 1994. **177**(1): p. 161-171.

93. Lee, K., J.-Y. Lee, and D. Kim, *A study of hydrogen-trapping phenomena in AISI 5160 spring steel.* Materials Science and Engineering, 1984. **67**(2): p. 213-220.

94. Lee, J.-L. and J.-Y. Lee, *The interaction of hydrogen with the interface of AI2O3 particles in iron.* Metallurgical Transactions A, 1986. **17**(12): p. 2183-2186.

95. Araújo, D., E. Vilar, and J.P. Carrasco, *A critical review of mathematical models used to determine the density of hydrogen trapping sites in steels and alloys.* International Journal of hydrogen energy, 2014. **39**(23): p. 12194-12200.

96. Jack, T.A., et al., *Investigation of the hydrogen induced cracking behaviour of API 5L X65 pipeline steel.* International Journal of Hydrogen Energy, 2020. **45**(35): p. 17671-17684.

97. Haq, A.J., et al., *Effect of microstructure and composition on hydrogen permeation in X70 pipeline steels.* International journal of hydrogen energy, 2013. **38**(5): p. 2544-2556.

98. Mohtadi-Bonab, M., J. Szpunar, and S. Razavi-Tousi, *A comparative study of hydrogen induced cracking behavior in API 5L X60 and X70 pipeline steels.* Engineering Failure Analysis, 2013. **33**: p. 163-175.

99. Dong, C.-f., et al., *Hydrogen induced cracking of X80 pipeline steel.* International Journal of Minerals, Metallurgy, and Materials, 2010. **17**(5): p. 579-586.

100. Li, L., et al., *Effect of vanadium content on hydrogen diffusion behaviors and hydrogen induced ductility loss of X80 pipeline steel.* Materials Science and Engineering: A, 2019. **742**: p. 712-721.

101. Dong, C., et al., *Effects of hydrogen-charging on the susceptibility of X100 pipeline steel to hydrogen-induced cracking.* International journal of hydrogen energy, 2009. **34**(24): p. 9879-9884.

102. Han, Y., et al., *Hydrogen embrittlement sensitivity of X100 pipeline steel under different pre-strain.* International Journal of Hydrogen Energy, 2019. **44**(39): p. 22380-22393.

103. Myers, S., et al., *Trapping and surface permeation of deuterium in He-implanted Fe.* Journal of Applied Physics, 1982. **53**(12): p. 8734-8744.

104. Nagumo, M. and K. Takai, *The predominant role of strain-induced vacancies in hydrogen embrittlement of steels: overview.* Acta Materialia, 2019. **165**: p. 722-733.

105. Zhou, X. and J. Song, *Effects of alloying elements on vacancies and vacancy-hydrogen clusters at coherent twin boundaries in nickel alloys.* Acta Materialia, 2018. **148**: p. 9-17.

106. Matsumoto, R., et al., *Atomistic simulations of hydrogen embrittlement.* International Journal of Hydrogen Energy, 2009. **34**(23): p. 9576-9584.

107. Ferreira, P., I. Robertson, and H. Birnbaum, *Hydrogen effects on the interaction between dislocations.* Acta materialia, 1998. **46**(5): p. 1749-1757.

108. Birnbaum, H.K. and P. Sofronis, *Hydrogen-enhanced localized plasticity—a mechanism for hydrogen-related fracture.* Materials Science and Engineering: A, 1994. **176**(1-2): p. 191-202.

109. Robertson, I., *The effect of hydrogen on dislocation dynamics.* Engineering fracture mechanics, 1999. **64**(5): p. 649-673.

110. Hirth, J. and J. Lothe, *Theory of Dislocations. McGraw-Hill, New York, 600 p.* 1968.

111. Robertson, I., *The effect of hydrogen on dislocation dynamics.* Engineering fracture mechanics, 2001. **68**(6): p. 671-692.

112. Chêne, J. and A. Brass, *Hydrogen transport by mobile dislocations in nickel base superalloy single crystals.* Scripta Materialia, 1999. **42**(5).

113. Hwang, C. and I. Bernstein, *Dislocation transport of hydrogen in iron single crystals.* Acta Metallurgica, 1986. **34**(6): p. 1001-1010.

114. Kirchheim, R., *Reducing grain boundary, dislocation line and vacancy formation energies by solute segregation. I. Theoretical background.* Acta Materialia, 2007. **55**(15): p. 5129-5138.

115. Kirchheim, R., *Reducing grain boundary, dislocation line and vacancy formation energies by solute segregation: II. Experimental evidence and consequences.* Acta Materialia, 2007. **55**(15): p. 5139-5148.

116. Wen, M., S. Fukuyama, and K. Yokogawa, *Atomistic simulations of effect of hydrogen on kink-pair energetics of screw dislocations in bcc iron.* Acta materialia, 2003. **51**(6): p. 1767-1773.

117. Sirois, E. and H. Birnbaum, *Effects of hydrogen and carbon on thermally activated deformation in nickel.* Acta metallurgica et materialia, 1992. **40**(6): p. 1377-1385.

118. Tien, J., et al., *Hydrogen transport by dislocations.* Metallurgical Transactions A, 1976. **7**(6): p. 821-829.

119. Dadfarnia, M., et al., *Modeling hydrogen transport by dislocations.* Journal of the Mechanics and Physics of Solids, 2015. **78**: p. 511-525.

120. Brass, A. and J. Chene, *Influence of deformation on the hydrogen behavior in iron and nickel base alloys: a review of experimental data.* Materials Science and Engineering: A, 1998. **242**(1-2): p. 210-221.

121. Zhong, L., et al., *Charge transfer mechanism of hydrogen-induced intergranular embrittlement of iron.* Physical Review B, 2000. **62**(21): p. 13938.

122. Venezuela, J., et al., *A review of hydrogen embrittlement of martensitic advanced high-strength steels.* Corrosion Reviews, 2016. **34**(3): p. 153-186.

123. Mohtadi-Bonab, M.A., M. Eskandari, and J.A. Szpunar, *Texture, local misorientation, grain boundary and recrystallization fraction in pipeline steels related to hydrogen induced cracking.* Materials Science and Engineering: A, 2015. **620**: p. 97-106.

124. Mohtadi-Bonab, M., et al., *Effect of different microstructural parameters on hydrogen induced cracking in an API X70 pipeline steel.* Metals and Materials International, 2017. **23**(4): p. 726-735.

125. Zhao, M.-C. and K. Yang, *Strengthening and improvement of sulfide stress cracking resistance in acicular ferrite pipeline steels by nano-sized carbonitrides.* Scripta Materialia, 2005. **52**(9): p. 881-886.

126. Han, Y., et al., *Sulphide stress cracking behaviour of the coarse-grained heat-affected zone in X100 pipeline steel under different heat inputs.* International Journal of Hydrogen Energy, 2020.

127. Cui, Q., et al., *Effect of nanosized NbC precipitates on hydrogen diffusion in X80 pipeline steel.* Materials, 2017. **10**(7): p. 721.

128. Mohtadi-Bonab, M. and H. Ghesmati-Kucheki, *Important factors on the failure of pipeline steels with focus on hydrogen induced cracks and improvement of their resistance.* Metals and Materials International, 2019. **25**(5): p. 1109-1134.

129. Mohtadi-Bonab, M., et al., *The mechanism of failure by hydrogen induced cracking in an acidic environment for API 5L X70 pipeline steel.* international journal of hydrogen energy, 2015. **40**(2): p. 1096-1107.

130. Jin, T.Y., Z.Y. Liu, and Y.F. Cheng, *Effect of non-metallic inclusions on hydrogen-induced cracking of API5L X100 steel.* International Journal of Hydrogen Energy, 2010. **35**(15): p. 8014-8021.

131. Xue, H.B. and Y.F. Cheng, *Characterization of inclusions of X80 pipeline steel and its correlation with hydrogen-induced cracking.* Corrosion Science, 2011. **53**(4): p. 1201-1208.

132. Martin, M.L., et al., *Enumeration of the hydrogen-enhanced localized plasticity mechanism for hydrogen embrittlement in structural materials.* Acta Materialia, 2019. **165**: p. 734-750.

133. Sun, B., et al., *Dependence of hydrogen embrittlement mechanisms on microstructure-driven hydrogen distribution in medium Mn steels.* Acta Materialia, 2020. **183**: p. 313-328.

134. Sun, B., et al., *Chemical heterogeneity enhances hydrogen resistance in high-strength steels.* Nature Materials, 2021. **20**(12): p. 1629-1634.

135. Jiang, Y., et al., *Hydrogen-assisted fracture features of a high strength ferrite-pearlite steel.* Journal of Materials Science & Technology, 2019. **35**(6): p. 1081-1087.

136. Doshida, T. and K. Takai, *Dependence of hydrogen-induced lattice defects and hydrogen embrittlement of cold-drawn pearlitic steels on hydrogen trap state, temperature, strain rate and hydrogen content.* Acta Materialia, 2014. **79**: p. 93-107.

137. Yu, S.-H., et al., *Effects of lamellar structure on tensile properties and resistance to hydrogen embrittlement of pearlitic steel.* Acta Materialia, 2019. **172**: p. 92-101.

138. Chan, S.L.I. and J.A. Charles, *Effect of carbon content on hydrogen occlusivity and embrittlement of ferrite–pearlite steels.* Materials Science and Technology, 1986. **2**(9): p. 956-962.

139. Ogawa, Y., et al., *Pearlite-driven surface-cracking and associated loss of tensile ductility in plain-carbon steels under exposure to high-pressure gaseous hydrogen.* International Journal of Hydrogen Energy, 2021. **46**(9): p. 6945-6959.

140. Ogawa, Y., et al., *Dual roles of pearlite microstructure to interfere/facilitate gaseous hydrogen-assisted fatigue crack growth in plain carbon steels.* International Journal of Fatigue, 2022. **154**: p. 106561.

141. Barnoush, A. and H. Vehoff, *Recent developments in the study of hydrogen embrittlement: Hydrogen effect on dislocation nucleation.* Acta Materialia, 2010. **58**(16): p. 5274-5285.

142. Lovicu, G., et al., *Hydrogen embrittlement of automotive advanced high-strength steels.* Metallurgical and Materials Transactions A, 2012. **43**(11): p. 4075-4087.

143. Wang, M., E. Akiyama, and K. Tsuzaki, *Effect of hydrogen and stress concentration on the notch tensile strength of AISI 4135 steel.* Materials Science and Engineering: A, 2005. **398**(1-2): p. 37-46.

144. Nanninga, N., et al., *A review of fatigue crack growth for pipeline steels exposed to hydrogen.* Journal of research of the national institute of standards and technology, 2010. **115**(6): p. 437.

145. An, T., et al., *Influence of hydrogen pressure on fatigue properties of X80 pipeline steel.* International Journal of Hydrogen Energy, 2017. **42**(23): p. 15669-15678.

146. Nanninga, N., et al., *Comparison of hydrogen embrittlement in three pipeline steels in high pressure gaseous hydrogen environments.* Corrosion Science, 2012. **59**: p. 1-9.

147. Somerday, B.P., et al., *Enhancing safety of hydrogen containment components through materials testing under in-service conditions.* International Journal of Hydrogen Energy, 2017. **42**(11): p. 7314-7321.

148. Venezuela, J., et al., *Determination of the equivalent hydrogen fugacity during electrochemical charging of 3.5 NiCrMoV steel.* Corrosion Science, 2018. **132**: p. 90-106.

149. Nagao, A., et al., *The role of hydrogen in hydrogen embrittlement fracture of lath martensitic steel.* Acta Materialia, 2012. **60**(13-14): p. 5182-5189.

150. Alp, T., T.J. Dames, and B. Dogan, *The effect of microstructure in the hydrogen embrittlement of a gas pipeline steel.* Journal of Materials Science, 1987. **22**(6): p. 2105-2112.

151. Zhang, T., et al., *Effect of microstructure inhomogeneity on hydrogen embrittlement susceptibility of X80 welding HAZ under pressurized gaseous hydrogen.* International Journal of Hydrogen Energy, 2017. **42**(39): p. 25102-25113.

152. Pluvinage, G., *Mechanical properties of a wide range of pipe steels under influence of pure hydrogen or hydrogen blended with natural gas.* International Journal of Pressure Vessels and Piping, 2021. **190**: p. 104293.

153. Ronevich, J.A., C.R. D'Elia, and M.R. Hill, *Fatigue crack growth rates of X100 steel welds in high pressure hydrogen gas considering residual stress effects.* Engineering Fracture Mechanics, 2018. **194**: p. 42-51.

154. Hart, P. *Hydrogen cracking-its causes, costs and future occurrence*. in *Proceedings: 1st International Conference*. 1999.

155. Chatzidouros, E., et al., *Hydrogen effect on fracture toughness of pipeline steel welds, with in situ hydrogen charging.* International journal of hydrogen energy, 2011. **36**(19): p. 12626-12643.

156. Qu, J., et al., *Hydrogen-assisted crack growth in the heat-affected zone of X80 steels during in situ hydrogen charging.* Materials, 2019. **12**(16): p. 2575.

157. Gan, L., et al., *Hydrogen trapping and hydrogen induced cracking of welded X100 pipeline steel in H2S environments.* International journal of hydrogen energy, 2018. **43**(4): p. 2293-2306.

158. Capelle, J., et al., *Evaluation of electrochemical hydrogen absorption in welded pipe with steel API X52.* international journal of hydrogen energy, 2013. **38**(33): p. 14356-14363.

159. Zandinava, B., R. Bakhtiari, and G. Vukelic, *Failure analysis of a gas transport pipe made of API 5L X60 steel.* Engineering Failure Analysis, 2022. **131**: p. 105881.

160. Yue, X., *Investigation on heat-affected zone hydrogen-induced cracking of high-strength naval steels using the Granjon implant test.* Welding in the World, 2015. **59**(1): p. 77-89.

161. Tsay, L., Y. Chen, and S. Chan, *Sulfide stress corrosion cracking and fatigue crack growth of welded TMCP API 5L X65 pipe-line steel.* International Journal of Fatigue, 2001. **23**(2): p. 103-113.

162. Kah, P. and J. Martikainen, *Influence of shielding gases in the welding of metals.* The International Journal of Advanced Manufacturing Technology, 2013. **64**(9): p. 1411-1421.

163. Sharma, S.K. and S. Maheshwari, *A review on welding of high strength oil and gas pipeline steels.* Journal of Natural Gas Science and Engineering, 2017. **38**: p. 203-217.

164. Ronevich, J.A., et al., *Fatigue crack growth rates in high pressure hydrogen gas for multiple X100 pipeline welds accounting for crack location and residual stress.* Engineering Fracture Mechanics, 2020. **228**: p. 106846.

165. Beachem, C.D., *A new model for hydrogen-assisted cracking (hydrogen "embrittlement").* Metallurgical and Materials Transactions B, 1972. **3**(2): p. 441-455.

166. Robertson, I.M., et al., *Hydrogen embrittlement understood.* Metallurgical and Materials Transactions B, 2015. **46**(3): p. 1085-1103.

167. Bond, G., I. Robertson, and H. Birnbaum, *The influence of hydrogen on deformation and fracture processes in high-strength aluminum alloys.* Acta Metallurgica, 1987. **35**(9): p. 2289-2296.

168. Tabata, T. and H.K. Birnbaum, *Direct observations of the effect of hydrogen on the behavior of dislocations in iron.* Scripta Metallurgica, 1983. **17**(7): p. 947-950.

169. Sofronis, P. and H.K. Birnbaum, *Mechanics of the hydrogendashdislocationdashimpurity interactions—I. Increasing shear modulus.* Journal of the Mechanics and Physics of Solids, 1995. **43**(1): p. 49-90.

170. Birnbaum, H., et al. *Mechanisms of hydrogen related fracture--a review*. in *Second International Conference on Corrosion-Deformation Interactions. CDI'96*. 1996.

171. Huang, L., et al., *Quantitative tests revealing hydrogen-enhanced dislocation motion in α-iron.* Nature Materials, 2023.

172. Lynch, S., *Mechanisms of hydrogen assisted cracking–a review.* Hydrogen effects on material behaviour and corrosion deformation interactions, 2003: p. 449-466.

173. Martin, M., I. Robertson, and P. Sofronis, *Interpreting hydrogen-induced fracture surfaces in terms of deformation processes: a new approach.* Acta Materialia, 2011. **59**(9): p. 3680-3687.

174. Martin, M.L., et al., *On the formation and nature of quasi-cleavage fracture surfaces in hydrogen embrittled steels.* Acta Materialia, 2011. **59**(4): p. 1601-1606.

175. Troiano, A.R., *The role of hydrogen and other interstitials in the mechanical behavior of metals.* trans. ASM, 1960. **52**: p. 54-80.

176. Oriani, R., *A mechanistic theory of hydrogen embrittlement of steels.* Berichte der Bunsengesellschaft für physikalische Chemie, 1972. **76**(8): p. 848-857.

177. Takahashi, Y., et al., *Direct evaluation of grain boundary hydrogen embrittlement: a micro-mechanical approach.* Materials Science and Engineering: A, 2016. **661**: p. 211-216.

178. Koyama, M., et al., *Hydrogen-assisted decohesion and localized plasticity in dual-phase steel.* Acta Materialia, 2014. **70**: p. 174-187.

179. Park, G.T., et al., *Effect of microstructure on the hydrogen trapping efficiency and hydrogen induced cracking of linepipe steel.* Corrosion science, 2008. **50**(7): p. 1865-1871.

180. Singh, V., et al., *Hydrogen induced blister cracking and mechanical failure in X65 pipeline steels.* International Journal of Hydrogen Energy, 2019. **44**(39): p. 22039-22049.

181. Moshtaghi, M. and M. Safyari, *Different augmentations of absorbed hydrogen under elastic straining in high-pressure gaseous hydrogen environment by as-quenched and as-tempered martensitic steels: combined experimental and simulation study.* International Journal of Hydrogen Energy, 2023.

182. Lynch, S., *Environmentally assisted cracking: overview of evidence for an adsorption-induced localised-slip process.* Acta Metallurgica, 1988. **36**(10): p. 2639-2661.

183. Lynch, S., *Interpreting hydrogen-induced fracture surfaces in terms of deformation processes: A new approach.* Scripta Materialia, 2011. **65**(10): p. 851-854.

184. Lynch, S., *Metallographic contributions to understanding mechanisms of environmentally assisted cracking.* Metallography, 1989. **23**(2): p. 147-171.

185. Nagumo, M., K. Ohta, and H. Saitoh, *Deformation induced defects in iron revealed by thermal desorption spectroscopy of tritium.* Scripta materialia, 1999. **40**(3).

186. Nagumo, M., M. Nakamura, and K. Takai, *Hydrogen thermal desorption relevant to delayed-fracture susceptibility of high-strength steels.* Metallurgical and Materials Transactions A, 2001. **32**(2): p. 339-347.

187. Cuitino, A. and M. Ortiz, *Ductile fracture by vacancy condensation in fcc single crystals.* Acta materialia, 1996. **44**(2): p. 427-436.

188. Essmann, U. and H. Mughrabi, *Annihilation of dislocations during tensile and cyclic deformation and limits of dislocation densities.* Philosophical Magazine A, 1979. **40**(6): p. 731-756.

189. Hattori, M., et al., *The role of hydrogen-enhanced strain-induced lattice defects on hydrogen embrittlement susceptibility of X80 pipeline steel.* Jom, 2017. **69**(8): p. 1375-1380.

190. ANSI/CSA, C., *Test Methods for Evaluating Material Compatibility in Compressed Hydrogen Applications-Metals*. 2014, CSA Group.

191. Dietzel, W., A. Atrens, and A. Barnoush, *Mechanics of modern test methods and quantitative-accelerated testing for hydrogen embrittlement*, in *Gaseous hydrogen embrittlement of materials in energy technologies*. 2012, Elsevier. p. 237-273.

192. Chatzidouros, E., et al., *Effect of hydrogen on fracture toughness properties of a pipeline steel under simulated sour service conditions.* International Journal of Hydrogen Energy, 2018. **43**(11): p. 5747-5759.

193. Parkins, R., E. Belhimer, and W. Blanchard, *Stress corrosion cracking characteristics of a range of pipeline steels in carbonate-bicarbonate solution.* Corrosion, 1993. **49**(12).

194. Meng, B., et al., *Hydrogen effects on X80 pipeline steel in high-pressure natural gas/hydrogen mixtures.* International Journal of Hydrogen Energy, 2017. **42**(11): p. 7404-7412.

195. Briottet, L., I. Moro, and P. Lemoine, *Quantifying the hydrogen embrittlement of pipeline steels for safety considerations.* International journal of hydrogen energy, 2012. **37**(22): p. 17616-17623.

196. Atrens, A., G. Dannhäuser, and G. Bäro, *Stress-corrosion-cracking of Zircaloy-4 cladding tubes: Part 1. Threshold in the presence of iodine.* Journal of Nuclear Materials, 1984. **126**(2): p. 91-102.

197. Venezuela, J., et al., *The influence of hydrogen on the mechanical and fracture properties of some martensitic advanced high strength steels studied using the linearly increasing stress test.* Corrosion Science, 2015. **99**: p. 98-117.

198. Venezuela, J., et al., *Influence of hydrogen on the mechanical and fracture properties of some martensitic advanced high strength steels in simulated service conditions.* Corrosion Science, 2016. **111**: p. 602-624.

199. Atrens, A., et al., *Linearly increasing stress test (LIST) for SCC research.* Measurement Science and Technology, 1993. **4**(11): p. 1281.

200. Danilatos, G., *Foundations of environmental scanning electron microscopy*, in *Advances in electronics and electron physics*. 1988, Elsevier. p. 109-250.

201. Sharma, R., *An environmental transmission electron microscope for in situ synthesis and characterization of nanomaterials.* Journal of Materials Research, 2005. **20**(7): p. 1695-1707.

202. Xie, D.-G., et al., *In situ study of the initiation of hydrogen bubbles at the aluminium metal/oxide interface.* Nature materials, 2015. **14**(9): p. 899-903.

203. Deng, Y., et al., *In-situ micro-cantilever bending test in environmental scanning electron microscope: Real time observation of hydrogen enhanced cracking.* Scripta Materialia, 2017. **127**: p. 19-23.

204. Kim, J. and C.C. Tasan, *Microstructural and micro-mechanical characterization during hydrogen charging: An in situ scanning electron microscopy study.* International Journal of Hydrogen Energy, 2019. **44**(12): p. 6333-6343.

205. Bond, G., I. Robertson, and H. Birnbaum, *Effects of hydrogen on deformation and fracture processes in high-ourity aluminium.* Acta Metallurgica, 1988. **36**(8): p. 2193-2197.

206. Shih, D., I. Robertson, and H. Birnbaum, *Hydrogen embrittlement of α titanium: in situ TEM studies.* Acta Metallurgica, 1988. **36**(1): p. 111-124.

207. Lee, T., I. Robertson, and H. Birnbaum, *An HVEM in situ deformation study of nickel doped with sulfur.* Acta Metallurgica, 1989. **37**(2): p. 407-415.

208. Bond, G., I. Robertson, and H. Birnbaum, *On the mechanisms of hydrogen embrittlement of Ni3Al alloys.* Acta Metallurgica, 1989. **37**(5): p. 1407-1413.

209. Hajilou, T., et al., *In situ electrochemical microcantilever bending test: A new insight into hydrogen enhanced cracking.* Scripta Materialia, 2017. **132**: p. 17-21.

210. Krumeich, F., *Properties of electrons, their interactions with matter and applications in electron microscopy.* Laboratory of Inorganic Chemistry, disponível em http://www. microscopy. ethz. ch/downloads/Interactions. pdf, consultado em, 2011: p. 3-08.

211. Chambers, S.A., *Elastic scattering and interference of backscattered primary, Auger and X-ray photoelectrons at high kinetic energy: principles and applications.* Surface Science Reports, 1992. **16**(6): p. 261-331.

212. Shindo, D., et al., *Energy dispersive x-ray spectroscopy.* Analytical electron microscopy for materials science, 2002: p. 81-102.

213. Egerton, R.F., *Electron energy-loss spectroscopy in the TEM.* Reports on Progress in Physics, 2008. **72**(1): p. 016502.

214. Williams, D.B., et al., *The transmission electron microscope*. 1996: Springer.

215. Zhou, W., et al., *Fundamentals of scanning electron microscopy (SEM).* Scanning Microscopy for Nanotechnology: Techniques and Applications, 2007: p. 1-40.

216. Keles, H., *Mid-IR imaging and multivariate analysis of dynamic processes in pharmaceutically relevant microparticles*. 2014: Sheffield Hallam University (United Kingdom).

217. Wolff, A., *Focused ion beams: An overview of the technology and its capabilities.*

218. Lee, J.S., et al., *1.4.5 - Surface Patterning*, in *Biomaterials Science (Fourth Edition)*, W.R. Wagner, et al., Editors. 2020, Academic Press. p. 553-573.

219. Berger, C., et al., *Plasma FIB milling for the determination of structures in situ.* Nature Communications, 2023. **14**(1): p. 629.

220. Smith, N., et al., *High brightness inductively coupled plasma source for high current focused ion beam applications.* Journal of Vacuum Science & Technology B:

Microelectronics and Nanometer Structures Processing, Measurement, and Phenomena, 2006. **24**(6): p. 2902-2906.

221. Yu, J., et al., *TEM investigation of FIB induced damages in preparation of metal material TEM specimens by FIB.* Materials Letters, 2006. **60**(2): p. 206-209.

222. Wanzenboeck, H., et al., *Effects of Ga-irradiation on properties of materials processed by a focused ion beam (FIB).* MRS Online Proceedings Library (OPL), 2000. **647**.

223. Dehm, G., et al., *Overview on micro-and nanomechanical testing: New insights in interface plasticity and fracture at small length scales.* Acta Materialia, 2018. **142**: p. 248-282.

224. Corporation, B., *Hysitron PI 85L SEM PicoIndenter-Versatile In-Situ Mechanical Testing Platform*. 2017.

225. ISO, B., *11114-4, 2005:'Transportable gas cylinders-Compatibility of cylinder and valve materials with gas contents', Part 4: Test methods for selecting metallic materials resistant to hydrogen embrittlement.* British Standards Institution, London.

226. Uchic, M.D., et al., *Sample dimensions influence strength and crystal plasticity.* Science, 2004. **305**(5686): p. 986-989.

227. Niu, R., et al., *Mechanical properties and deformation behaviours of submicron-sized Cu–Al single crystals.* Acta Materialia, 2022. **223**: p. 117460.

228. Reed-Hill, R.E., R. Abbaschian, and R. Abbaschian, *Physical metallurgy principles*. Vol. 17. 1973: Van Nostrand New York.

229. Kheradmand, N., et al., *Small scale testing approach to reveal specific features of slip behavior in BCC metals.* Acta Materialia, 2019. **174**: p. 142-152.

230. Depover, T., et al., *The effect of hydrogen on the crack initiation site of TRIP-assisted steels during in-situ hydrogen plasma micro-tensile testing: Leading to an improved ductility?* Materials Characterization, 2020. **167**: p. 110493.

231. Chen, Y.-S., et al., *Observation of hydrogen trapping at dislocations, grain boundaries, and precipitates.* Science, 2020. **367**(6474): p. 171-175.

232. Liu, S., et al., *Stacking fault energy of face-centered-cubic high entropy alloys.* Intermetallics, 2018. **93**: p. 269-273.

233. Liu, J., et al., *Deformation twinning behaviors of the low stacking fault energy high-entropy alloy: An in-situ TEM study.* Scripta Materialia, 2017. **137**: p. 9-12.

234. Lin, Y.-C., et al., *Hydrogen trapping and desorption of dual precipitates in tempered low-carbon martensitic steel.* Acta Materialia, 2020. **196**: p. 516-527.

235. Miller, M.K., *Atom probe tomography: analysis at the atomic level*. 2012: Springer Science & Business Media.

236. Gault, B., et al., *Atom probe microscopy*. Vol. 160. 2012: Springer Science & Business Media.

237. Chen, Y., *Characterisation of hydrogen trapping in steel by atom probe tomography*. 2017, University of Oxford.

238. McCarroll, I.E., et al., *New frontiers in atom probe tomography: a review of research enabled by cryo and/or vacuum transfer systems.* Materials Today Advances, 2020. **7**: p. 100090.

239. Gemma, R., et al., *APT analyses of deuterium-loaded Fe/V multi-layered films.* Ultramicroscopy, 2009. **109**(5): p. 631-636.

240. Tung, P.-Y., et al., *Under-stoichiometric cementite in decomposing binary Fe-C pearlite exposed to rolling contact fatigue.* Acta Materialia, 2021. **216**: p. 117144.

241. Gonzaga, R.A., *Influence of ferrite and pearlite content on mechanical properties of ductile cast irons.* Materials Science and Engineering: A, 2013. **567**: p. 1-8.

242. Ogawa, Y. and K. Iwata, *Resistance of pearlite against hydrogen-assisted fatigue crack growth.* International Journal of Hydrogen Energy, 2022. **47**(74): p. 31703-31708.

243. Djukic, M.B., et al., *The synergistic action and interplay of hydrogen embrittlement mechanisms in steels and iron: Localized plasticity and decohesion.* Engineering Fracture Mechanics, 2019. **216**: p. 106528.

244. Gu, R. and A. Ngan, *Dislocation arrangement in small crystal volumes determines power-law size dependence of yield strength.* Journal of the Mechanics and Physics of Solids, 2013. **61**(6): p. 1531-1542.

245. Hu, J., et al., *Microstructure and mechanical properties of TMCP heavy plate microalloyed steel.* Materials Science and Engineering: A, 2014. **607**: p. 122-131.

246. Bramfitt, B.L. and A.R. Marder, *A transmission-electron-microscopy study of the substructure of high-purity pearlite.* Metallography, 1973. **6**(6): p. 483-495.

247. Saleh, A.A., et al., *A transmission Kikuchi diffraction study of cementite in a quenched and tempered steel.* Materials Characterization, 2016. **114**: p. 146-150.

248. Zaefferer, S., D. Raabe, and A. Khorashadizadeh, *Tomographic orientation microscopy (3D EBSD) on steels using a joint FIB SEM technique*. 2003.

249. Kiener, D. and A.M. Minor, *Source-controlled yield and hardening of Cu (1 0 0) studied by in situ transmission electron microscopy.* Acta Materialia, 2011. **59**(4): p. 1328-1337.

250. Zhang, J., K. Kishida, and H. Inui, *Specimen size and shape dependent yield strength in micropillar compression deformation of Mo single crystals.* International Journal of Plasticity, 2017. **92**: p. 45-56.

251. Aifantis, K., et al., *Interfaces within strain gradient plasticity: theory and experiments.* Acta Materialia, 2006. **54**(19): p. 5077-5085.

252. Kim, H.-J., et al., *Baking effect on desorption of diffusible hydrogen and hydrogen embrittlement on hot-stamped boron martensitic steel.* Metals, 2019. **9**(6): p. 636.

253. Dogan, H., D. Li, and J. Scully, *Controlling hydrogen embrittlement in precharged ultrahigh-strength steels.* Corrosion, 2007. **63**(7): p. 689-703.

254. Kim, J., H. Ghaffarian, and K. Kang, *The lattice dislocation trapping mechanism at the ferrite/cementite interface in the Isaichev orientation relationship.* Scientific reports, 2021. **11**(1): p. 1-8.

255. Shimokawa, T., et al., *A multiscale approach for the deformation mechanism in pearlite microstructure: Atomistic study of the role of the heterointerface on ductility.* Materials Science and Engineering: A, 2014. **598**: p. 68-76.

256. McEniry, E.J., T. Hickel, and J. Neugebauer, *Ab initio simulation of hydrogen-induced decohesion in cementite-containing microstructures.* Acta Materialia, 2018. **150**: p. 53-58.

257. Kapp, M., et al., *Anisotropic deformation characteristics of an ultrafine-and nanolamellar pearlitic steel.* Acta Materialia, 2016. **106**: p. 239-248.

258. Teshima, T., et al., *Local cementite cracking induced by heterogeneous plastic deformation in lamellar pearlite.* Materials Science and Engineering: A, 2017. **679**: p. 223-229.

259. Lee, S.-W. and W.D. Nix, *Size dependence of the yield strength of fcc and bcc metallic micropillars with diameters of a few micrometers.* Philosophical Magazine, 2012. **92**(10): p. 1238-1260.

260. Llorca, J., A. Needleman, and S. Suresh, *An analysis of the effects of matrix void growth on deformation and ductility in metal-ceramic composites.* Acta Metallurgica et Materialia, 1991. **39**(10): p. 2317-2335.

261. Hull, D. and D.J. Bacon, *6 - Dislocations in Other Crystal Structures*, in *Introduction to Dislocations (Fourth Edition)*, D. Hull and D.J. Bacon, Editors. 2001, Butterworth-Heinemann: Oxford. p. 102-127.

262. Maaß, R. and P.M. Derlet, *Micro-plasticity and recent insights from intermittent and small-scale plasticity.* Acta Materialia, 2018. **143**: p. 338-363.

263. Bhadeshia, H. and A. Chintha, *Critical assessment 41: the strength of undeformed pearlite.* Materials Science and Technology, 2022. **38**(16): p. 1291-1299.

264. Mayer, C.R., et al., *Anisotropy, size, and aspect ratio effects on micropillar compression of AlSiC nanolaminate composites.* Acta Materialia, 2016. **114**: p. 25-32.

265. Hoagland, R., J. Hirth, and A. Misra, *On the role of weak interfaces in blocking slip in nanoscale layered composites.* Philosophical Magazine, 2006. **86**(23): p. 3537-3558.

266. Phillips, M.A., B.M. Clemens, and W.D. Nix, *A model for dislocation behavior during deformation of Al/Al3Sc (fcc/L12) metallic multilayers.* Acta Materialia, 2003. **51**(11): p. 3157-3170.

267. Embury, J.D. and J.P. Hirth, *On dislocation storage and the mechanical response of fine scale microstructures.* Acta Metallurgica et Materialia, 1994. **42**(6): p. 2051-2056.

268. Lei, S., et al., *Intrinsic size-controlled strain hardening behavior of nanolayered Cu/Zr micropillars.* Scripta Materialia, 2012. **66**(9): p. 706-709.

269. Guo, W., et al., *Intrinsic and extrinsic size effects in the deformation of amorphous CuZr/nanocrystalline Cu nanolaminates.* Acta Materialia, 2014. **80**: p. 94-106.

270. Zhang, J.Y., et al., *Intrinsic and extrinsic size effects on deformation in nanolayered Cu/Zr micropillars: From bulk-like to small-volume materials behavior.* Acta Materialia, 2012. **60**(10): p. 4054-4064.

271. Chen, Y., et al., *Mechanical size effect of eutectic high entropy alloy: Effect of lamellar orientation.* Journal of Materials Science & Technology, 2021. **82**: p. 10-20.

272. Wang, S.J., et al., *Deformation behavior of nanoscale Al–Al2Cu eutectics studied by in situ micropillar compression.* Materials Science and Engineering: A, 2021. **800**: p. 140311.

273. Edwards, T.E.J., et al., *Transverse deformation of a lamellar TiAl alloy at high temperature by in situ microcompression.* Acta Materialia, 2019. **166**: p. 85-99.

274. Birnbaum, H.K. and P. Sofronis, *Hydrogen-enhanced localized plasticity—a mechanism for hydrogen-related fracture.* Materials Science and Engineering: A, 1994. **176**(1): p. 191-202.

275. Zhang, Y., et al., *Kink mechanism in Cu/Nb nanolaminates explored by in situ pillar compression.* Acta Materialia, 2022. **237**: p. 118150.

276. Hu, Y., et al., *Correlating micro-pillar compression behavior with bulk mechanical properties: Nanolaminated graphene-Al composite as a case study.* Scripta Materialia, 2018. **146**: p. 236-240.

277. Martin, M.L., et al., *Hydrogen embrittlement in ferritic steels.* Applied Physics Reviews, 2020. **7**(4): p. 041301.

278. Chen, Y.-S., et al., *Direct observation of individual hydrogen atoms at trapping sites in a ferritic steel.* Science, 2017. **355**(6330): p. 1196-1199.

279. Dwivedi, S.K. and M. Vishwakarma, *Hydrogen embrittlement in different materials: A review.* International Journal of Hydrogen Energy, 2018. **43**(46): p. 21603-21616.

280. Oriani, R., *Hydrogen embrittlement of steels.* Annual review of materials science, 1978. **8**(1): p. 327-357.

281. Li, H., et al., *Hydrogen in pipeline steels: Recent advances in characterization and embrittlement mitigation.* Journal of Natural Gas Science and Engineering, 2022: p. 104709.

282. Mohtadi-Bonab, M., M. Eskandari, and J. Szpunar, *Texture, local misorientation, grain boundary and recrystallization fraction in pipeline steels related to hydrogen induced cracking.* Materials Science and Engineering: A, 2015. **620**: p. 97-106.

283. Mohtadi-Bonab, M. and H. Ghesmati-Kucheki, *Important factors on the failure of pipeline steels with focus on hydrogen induced cracks and improvement of their resistance.* Metals and Materials International, 2019. **25**: p. 1109-1134.

284. Hong, G.-W. and J.-Y. Lee, *The interaction of hydrogen and the cementite-ferrite interface in carbon steel.* Journal of materials science, 1983. **18**: p. 271-277.

285. Luu, W. and J. Wu, *The influence of microstructure on hydrogen transport in carbon steels.* Corrosion Science, 1996. **38**(2): p. 239-245.

286. Takahashi, J., K. Kawakami, and Y. Kobayashi, *Origin of hydrogen trapping site in vanadium carbide precipitation strengthening steel.* Acta Materialia, 2018. **153**: p. 193-204.

287. Koyama, M., et al., *Hydrogen-assisted failure in a twinning-induced plasticity steel studied under in situ hydrogen charging by electron channeling contrast imaging.* Acta Materialia, 2013. **61**(12): p. 4607-4618.

288. Chatzidouros, E., V. Papazoglou, and D. Pantelis, *Hydrogen effect on a low carbon ferritic-bainitic pipeline steel.* International journal of hydrogen energy, 2014. **39**(32): p. 18498-18505.

289. Deutges, M., et al., *Influence of hydrogen on the deformation morphology of vanadium (100) micropillars in the α-phase of the vanadium–hydrogen system.* Scripta Materialia, 2013. **68**(1): p. 71-74.

290. Wang, S., et al., *Hydrogen effects on tensile property of pure iron with deformed surface.* Materials Science and Engineering: A, 2013. **560**: p. 332-338.

291. Jia, D., K.T. Ramesh, and E. Ma, *Effects of nanocrystalline and ultrafine grain sizes on constitutive behavior and shear bands in iron.* Acta Materialia, 2003. **51**(12): p. 3495-3509.

292. Lou, W., et al., *Atomistic Investigation of the Influence of Hydrogen on Mechanical Response during Nanoindentation in Pure Iron.* Acta Metallurgica Sinica (English Letters), 2023.

293. Tian, C., et al., *On the mechanical heterogeneity in dual phase steel grades: Activation of slip systems and deformation of martensite in DP800.* Acta Materialia, 2020. **183**: p. 274-284.

294. Rogne, B. and C. Thaulow, *Strengthening mechanisms of iron micropillars.* Philosophical Magazine, 2015. **95**(16-18): p. 1814-1828.

295. Ng, K.S. and A.H.W. Ngan, *Breakdown of Schmid's law in micropillars.* Scripta Materialia, 2008. **59**(7): p. 796-799.

296. Taketomi, S., R. Matsumoto, and N. Miyazaki, *Atomistic study of hydrogen distribution and diffusion around a {112}<111> edge dislocation in alpha iron.* Acta Materialia, 2008. **56**(15): p. 3761-3769.

297. Robertson, I.M., *The effect of hydrogen on dislocation dynamics.* Engineering Fracture Mechanics, 2001. **68**(6): p. 671-692.

298. Kirchheim, R., *Revisiting hydrogen embrittlement models and hydrogen-induced homogeneous nucleation of dislocations.* Scripta materialia, 2010. **62**(2): p. 67-70.

299. Kirchheim, R., *Solid solution softening and hardening by mobile solute atoms with special focus on hydrogen.* Scripta Materialia, 2012. **67**(9): p. 767-770.

300. Yasuda, Y., et al., *Strain-hardening characteristics of ferrite layers in pearlite microstructure.* Materials Science and Technology, 2018. **34**(7): p. 772-779.

301. Borchers, C., et al., *Partially amorphous nanocomposite obtained from heavily deformed pearlitic steel.* Materials Science and Engineering: A, 2009. **502**(1-2): p. 131-138.

302. Dimiduk, D.M., et al., *Scale-Free Intermittent Flow in Crystal Plasticity.* Science, 2006. **312**(5777): p. 1188-1190.

303. Weinberger, C.R. and W. Cai, *Surface-controlled dislocation multiplication in metal micropillars.* Proceedings of the National Academy of Sciences, 2008. **105**(38): p. 14304-14307.

304. Cui, Y., G. Po, and N. Ghoniem, *Influence of loading control on strain bursts and dislocation avalanches at the nanometer and micrometer scale.* Physical Review B, 2017. **95**(6): p. 064103.

305. Hu, Y., et al., *Dislocation avalanche mechanism in slowly compressed high entropy alloy nanopillars.* Communications Physics, 2018. **1**(1): p. 61.

306. Wang, P., et al., *Interpreting strain burst in micropillar compression through instability of loading system.* International Journal of Plasticity, 2018. **107**: p. 150-163.